

Nonlinear Seismic Analysis of Morrow Point Dam

A Study for the United States
Bureau of Reclamation

C. Noble[†]

J. Solberg[‡]

[†] Structural and Applied Mechanics Group, LLNL

[‡] Methods Development Group, LLNL

March 2004



Morrow Point Dam, Colorado

U.S. Department of Energy

Lawrence
Livermore
National
Laboratory

Disclaimer

This document was prepared as an account of work sponsored by an agency of the United States Government. Neither the United States Government nor the University of California nor any of their employees, makes any warranty, express or implied, or assumes any legal liability or responsibility for the accuracy, completeness, or usefulness of any information, apparatus, product, or process disclosed, or represents that its use would not infringe privately owned rights. Reference herein to any specific commercial product, process, or service by trade name, trademark, manufacturer, or otherwise, does not necessarily constitute or imply its endorsement, recommendation, or favoring by the United States Government or the University of California. The views and opinions of authors expressed herein do not necessarily state or reflect those of the United States Government or the University of California, and shall not be used for advertising or product endorsement purposes.

This work was performed under the auspices of the U.S. Department of Energy by University of California, Lawrence Livermore National Laboratory under Contract W-7405-Eng-48.

Nonlinear Seismic Analysis of Morrow Point Dam

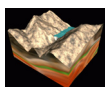
A Study for the United States Bureau of Reclamation



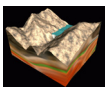
Morrow Point Dam, Colorado

Table of Contents

1.0	Objective and Background.....	13
2.0	Earthquake ground motions	18
2.1	Calculation of Force Time Histories	28
3.0	Contraction Joint Detail	35
3.1	Discrete Element Contraction Joint Model.....	40
3.2	Contact Algorithm for Beveled Contraction Joints.....	44
3.3	General Contact Mechanics	44
3.4	Modelling Small-Scale Surface Features.....	47
3.5	Modelling Friction	49
3.6	Modelling the Contraction Joint	51
3.7	Finite Element Implementation.....	54
4.0	Finite Element Verification Studies	61
4.1	Fluid Modeling	61



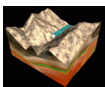
4.2	Block Sliding Test.....	65
4.3	Contraction Joint Model Tests	68
4.3.1	Two (dam-size) blocks sliding past each other.....	68
4.3.2	Comparison between discrete springs and contraction joint slide surface	71
5.0	Nonlinear Finite Element Model of Morrow Point Dam.....	73
5.1	Fluid Modeling in NIKE3D and DYNA3D	73
5.2	Contraction Joint Finite Element Model with Rigid Foundation and Westergaard Added Mass	76
5.3	Contraction Joint Finite Element Model with Flexible Foundation and Westergaard Added Mass	76
5.4	Contraction Joint Finite Element Model with Flexible Foundation and Water Explicitly Modeled	79
5.5	Contraction Joint Finite Element Model with Flexible Foundation, Water Explicitly Modeled, and Left Abutment Wedge.....	83
5.6	Homogeneous Finite Element Model	88
6.0	Finite Element Analysis Procedures of Morrow Point Dam	88
7.0	Procedure for Base Acceleration Method	88
7.1	Procedure for Force Time History Method.....	90
8.0	Natural Modeshapes and Frequencies of Morrow Point Dam.....	93
9.0	Free Vibrational Studies of Morrow Point Dam	98
9.1	Line forces ramped up over 4 seconds.....	99
9.2	Pressure at top of dam ramped up over 4 seconds	99
10.0	NIKE3D Static Initialization.....	104
11.0	Transient Response of Morrow Point Dam to Earthquake Ground Motions.....	106
11.1	Phase 1 Models	106
11.1.1	Rigid Foundation with Westergaard Added Mass.....	106
11.1.2	Flexible Foundation with Westergaard Added Mass.....	109
11.1.3	Flexible Foundation with Water Explicitly Modeled	112
11.1.4	Flexible Foundation with Water Explicitly Modeled, Abutment Wedge Modeled, and Using Deconvolved Ground Motions	114
11.2	Phase 2 Models	118
11.2.1	Model 1: Homogeneous/Monolithic Dam.....	118
11.2.2	Model 2: Model with Contraction Joints and Wedge Fixed.....	119
11.2.3	Model 3: Model with Contraction Joints and Wedge Not Fixed to Foundation.....	123
11.2.4	Model 3: Model with Contraction Joints and Wedge Not Fixed to Foundation or Dam	127
11.2.5	Model 4: Model of Foundation Only with Wedge Fixed	131
11.2.6	Model 5: Model of Foundation Only with Wedge Not Fixed	134
11.2.7	Model 6: Model of Foundation and Wedge with Uplift Modeled Between the Wedge and Foundation	136
11.2.8	Model 7: Concrete Damage Model	138
11.2.9	Model 8: Model with Tied with Failure Slide Surface at the Foundation/Dam Interface	146
11.2.10	Model 9: Model with Tied with Failure Slide Surface and Uplift at the Foundation/Dam Interface.....	149
11.2.11	Thermal Analysis.....	152



12.0	Conclusions.....	159
13.0	Acknowledgements.....	161
14.0	References.....	161

Appendix

15.0	Background.....	164
15.1	Terminology.....	165
15.1.1	Volumetric and Deviatoric Stresses and Strains.....	165
15.1.2	Stress Invariants.....	166
15.1.3	Triaxial Compression and Extension.....	166
16.0	Nonlinear Concrete Model Description.....	168
16.1	Failure Surfaces.....	168
16.2	Pressure Cutoff.....	171
16.3	Damage Evolution.....	172
16.4	Description of Third Invariant.....	176
16.5	Strain Rate Effects.....	179
16.6	Shear Dilation.....	181
16.7	Equation of State.....	182
17.0	Concrete Material Properties.....	185
17.1	WSMR-5 3/4 Concrete.....	185
17.2	SAC5 Concrete.....	185
17.3	Scaling of Existing Data.....	188
18.0	References.....	189



List of Figures

FIGURE 1.	Principal concrete dam types. a) Gravity dam; b) thin arch dam.....	14
FIGURE 2.	Morrow Point Dam overhead photos.	15
FIGURE 3.	Morrow Point Dam in southwestern Colorado, topographic setting.	16
FIGURE 4.	Colorado Seismic Hazard Map.	19
FIGURE 5.	Location of Cimarron Fault (Colorado Geological Survey).	20
FIGURE 6.	Morrow Point ground motions for Cerro Prieto time history. a) Horizontal ground acceleration; b) horizontal ground velocity; c) horizontal ground displacement.	21
FIGURE 7.	Morrow Point ground motions for Cerro Prieto time history. a) Horizontal ground acceleration; b) horizontal ground velocity; c) horizontal ground displacement.	22
FIGURE 8.	Morrow Point ground motions for Cerro Prieto time history. a) Vertical ground acceleration; b) vertical ground velocity; c) vertical ground displacement.	23
FIGURE 9.	Morrow Point deconvolved ground motions for Cerro Prieto time history. a) Horizontal ground acceleration; b) horizontal ground velocity; c) horizontal ground displacement.	24
FIGURE 10.	Morrow Point deconvolved ground motions for Cerro Prieto time history. a) Horizontal ground acceleration; b) horizontal ground velocity; c) horizontal ground displacement.	25
FIGURE 11.	Morrow Point deconvolved ground motions for Cerro Prieto time history. a) Vertical ground acceleration; b) vertical ground velocity; c) vertical ground displacement.	26
FIGURE 12.	Comparison between original and deconvolved ground motions for Cerro Prieto time history.	27
FIGURE 13.	a) Simplified finite element mesh of Morrow Point foundation; b) topographically correct finite element mesh of Morrow Point foundation.	31
FIGURE 14.	Comparison between USBR input ground motions and DYNA3D ground motions at base of dam. The DYNA3D simulation does not include damping.....	32
FIGURE 15.	Comparison between USBR input ground motions and DYNA3D ground motions at base of dam. The DYNA3D simulation includes 3.4% damping for first mode of Morrow Point Dam.	33
FIGURE 16.	Comparison between USBR input ground motions, DYNA3D ground motions at base of dam using simplified foundation, and DYNA3D ground motions using topographically correct foundation. The DYNA3D simulation includes 3.4% damping for first mode of Morrow Point Dam.....	34
FIGURE 17.	Construction photo of the Morrow Point Dam.	36
FIGURE 18.	Construction photo of the Morrow Point Dam.	37
FIGURE 19.	Morrow Point Dam elevation view.	38

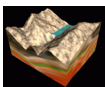


FIGURE 20.	Cross-section of a vertically extending contraction joint in Morrow Point Dam.....	39
FIGURE 21.	NIKE3D and DYNA3D vertical contraction joint modeling.....	41
FIGURE 22.	NIKE3D model of a contraction joint cycled through opening and closing in the direction tangent to the surface.	42
FIGURE 23.	NIKE3D model of a contraction joint cycled through opening and closing in the direction normal to the surface.	43
FIGURE 24.	Reference and Current Configurations for Two-Body Contact.	56
FIGURE 25.	Closest-point projection.....	57
FIGURE 26.	Closest-point projection	57
FIGURE 27.	Small-scale surface kinematics.	58
FIGURE 28.	Typical arch dam, front, showing vertical contraction joints and direction	58
FIGURE 29.	Typical arch dam contraction joints, view from top, showing direction ...	59
FIGURE 30.	Arch dam contraction joint, reference configuration.	59
FIGURE 31.	Arch dam contraction joint, displaced vertically by and horizontally by	59
FIGURE 32.	Arch dam contraction joint, displaced vertically by and horizontally by such that at certain points.....	60
FIGURE 33.	Comparison of two different possibilities for	60
FIGURE 34.	a.) Von Mises stress of steel box loaded with a hydrostatic pressure; b.) von Mises stress of steel box loaded using NIKE3D water type elements	63
FIGURE 35.	a.) Fundamental sloshing mode in DYNA3D finite element analysis; b.) vertical displacement time history of water in DYNA3D finite element analysis.....	64
FIGURE 36.	Finite element model of block sliding verification test.....	66
FIGURE 37.	a.) z displacement time history of block; b.) z velocity time history of block; c.) z acceleration time history of block.....	67
FIGURE 38.	a) Plan view of Morrow Point Dam shear keys; b) transverse displacement vs upstream-downstream displacement time history for contraction joint test problem.....	69
FIGURE 39.	Time history of dam-size blocks moving past each other (displacement scale factor in transverse direction = 5.0).	70
FIGURE 40.	a.) NIKE3D static initialization with discrete springs; b.) NIKE3D static initialization with contraction joint slide surface.....	72
FIGURE 41.	a.) Pictorial added mass for gravity dam; b). pictorial added mass for double-curvature arch dam.....	74
FIGURE 42.	Construction Plans of Morrow Point Dam.....	75
FIGURE 43.	Contraction joint finite element model with rigid foundation.	76
FIGURE 44.	IGES surface for TrueGrid mesh generation used USGS 1983 topographic map.....	78
FIGURE 45.	Contraction joint finite element model with Westergaard added mass and flexible foundation.	79

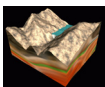


FIGURE 46.	Contraction joint finite element model with flexible foundation and water explicitly modeled.....	81
FIGURE 47.	Close-up view of contraction joint finite element model with flexible foundation and water explicitly modeled.....	82
FIGURE 48.	a.) Plan view of contraction joint finite element model with flexible foundation and water explicitly modeled; b) aerial photograph of Morrow Point Dam and Reservoir.	83
FIGURE 49.	Plan view of left abutment wedge 3.....	84
FIGURE 50.	Morrow Point Dam finite element model with flexible foundation, water explicitly modeled, and left abutment wedge.	87
FIGURE 51.	Homogeneous finite element model.....	88
FIGURE 52.	Morrow Point Dam finite element analysis procedure for base acceleration method.....	90
FIGURE 53.	Morrow Point Dam finite element analysis procedure for force time history method.	92
FIGURE 54.	Comparison between measured and computed resonant frequencies for Morrow Point Dam.	94
FIGURE 55.	Modeshapes for contraction joint slide surface model with diagonal added mass.....	95
FIGURE 56.	Modeshapes for homogeneous/monolithic model with diagonal added mass.....	96
FIGURE 57.	Measured (solid) and computed (dashed) response shapes at the first three resonances of the symmetric shake. Shown are the radial component of acceleration at the dam crest (left) and center cantilever (middle) and the hydrodynamic pressure at center block (right) [Ref 4].	98
FIGURE 58.	Finite element model and loading condition for first free vibrational analysis.....	100
FIGURE 59.	Upstream-downstream displacement time history of node at top center of dam (top) and the FFT of the upstream-downstream displacement time histories at three locations of the dam at center (bottom).	101
FIGURE 60.	Comparison of modeshapes between eigenvalue analyses and free vibrational response.	102
FIGURE 61.	Pressure loading at top of dam for second free vibration test and the corresponding FFT of the upstream-downstream displacement time history from top center of dam.....	103
FIGURE 62.	Tensile stresses at the toe of the dam after gravity initialization of the model.....	105
FIGURE 62.	Displacement time histories for rigid foundation model with Westergaard added mass.	108
FIGURE 63.	Displacement time histories for flexible foundation model with Westergaard added mass.	111
FIGURE 64.	Displacement time histories for rigid foundation model with water explicitly modeled.....	113

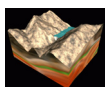


FIGURE 65.	Displacement time histories for flexible foundation model and water explicitly modeled.....	116
FIGURE 66.	Wedge displacement time histories for model with flexible foundation and water explicitly modeled.....	117
FIGURE 67.	Displacement time histories for model 1.	119
FIGURE 68.	Displacement time histories for model 2.	122
FIGURE 69.	Displacement time histories for model 3.	125
FIGURE 70.	Wedge displacement time histories for model 3.	126
FIGURE 71.	Displacement time histories for model 3.	129
FIGURE 72.	Wedge displacement time histories for model 3.	130
FIGURE 73.	Comparison between using force time histories or base accelerations at the base of the foundation. Accelerations taken at dam/foundation interface.	132
FIGURE 74.	Acceleration response spectra comparison between using force time histories or base accelerations at the base of the foundation. Accelerations taken at dam/foundation interface.....	133
FIGURE 75.	Wedge displacement time histories for model 5.	135
FIGURE 76.	Wedge displacement time histories for model 6.	137
FIGURE 77.	a). Three independent fixed failure surfaces for DTRA concrete material model; b). Uniaxial representation of concrete stress-strain curve.....	139
FIGURE 78.	WSMR-5 3/4 concrete properties: a) plot of compressive meridians; b) single element uniaxial tensile test with and without rate dependence (tensile strength = 464 psi); c) description of unconfined uniaxial compressive test and plot of damage parameter d after compressive failure; d) stress-strain plot of UUC test with and without rate dependence (compressive strength = 6500 psi).	140
FIGURE 79.	Displacement time histories for model 7.	143
FIGURE 80.	Wedge displacement time histories for model 7.	144
FIGURE 81.	Concrete damage after completion of seismic analysis.	145
FIGURE 82.	Displacement time histories for model 8.	148
FIGURE 83.	Displacement time histories for model 9.	151
FIGURE 84.	a.) Upstream temperature variation; b) downstream temperature variation.	153
FIGURE 85.	a). Upstream temperature variation ; b). downstream temperature variation.	154
FIGURE 86.	Displacement time histories for thermal model.	157
FIGURE 87.	Wedge displacement time histories for thermal model.....	158
FIGURE 88.	Description of triaxial test.....	167
FIGURE 89.	Model failure surfaces and uniaxial stress-strain response.....	170
FIGURE 90.	Description of pressure cutoff and tensile paths	172
FIGURE 91.	Effects of parameters and on softening for a single element tensile test.	175
FIGURE 92.	Three-dimensional state of stress and space diagonal	176

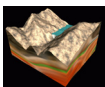
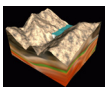
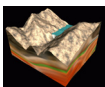


FIGURE 93.	Von Mises yield surface (plan view of π -plane).....	176
FIGURE 94.	a) Concrete deviatoric sections for increasing pressure; b) William and Warnke model.	178
FIGURE 95.	Strain rate effects on tensile and compressive strengths ([Ref 3] and [Ref 4])......	180
FIGURE 96.	Description of strength enhancement calculation.	181
FIGURE 97.	a) graphical representation of shear dilation; b) yield surface with associated flow rule; c) description of associative, non-associative, and partial associative flow rules.	182
FIGURE 98.	Pressure vs. volumetric strain curve for equation-of-state Form 8 with compaction (similarly Form 12).	183
FIGURE 99.	WSMR-5 3/4 concrete properties: a) plot of compressive meridians; b) single element uniaxial tensile test with and without rate dependence (tensile strength = 464 psi); c) description of unconfined uniaxial compressive test and plot of damage parameter d after compressive failure; d) stress-strain plot of UUC test with and without rate dependence (compressive strength = 6500 psi).	186
FIGURE 100.	SAC5 concrete properties: a) plot of compressive meridians; b) single element uniaxial tensile test with and without rate dependence (tensile strength = 363 psi); c) description of unconfined uniaxial compressive test and plot of damage parameter d after compressive failure; d) stress-strain plot of UUC test with and without rate dependence (compressive strength = 5500 psi).	187



List of Tables

TABLE 1.	Foundation Material Properties.....	29
TABLE 2.	Material properties of NIKE3D fluid elements.....	61
TABLE 3.	Material Properties for finite element models.....	80
TABLE 4.	Left Abutment Wedge Boundaries.....	85
TABLE 5.	Left Abutment Wedge Plane Orientations	85
TABLE 6.	NIKE3D and DYNA3D Left Abutment Wedge Definitions.	86
TABLE 7.	Comparison of NIKE3D calculated modes and frequencies.	97
TABLE 8.	Comparison of NIKE3D models with experimental data.	97
TABLE 1.	Comparison of NIKE3D static initialization stress state.	105
TABLE 2.	Seismic Analysis Results for Model with Rigid Foundation and Westergaard Added Mass.....	107
TABLE 3.	Seismic Analysis Results for Model with Flexible Foundation and Westergaard Added Mass.....	109
TABLE 4.	Seismic Analysis Results for Model with Flexible Foundation and Water Explicitly Modeled.....	112
TABLE 5.	Seismic Analysis Results for Model with Flexible Foundation, Water Explicitly Modeled, and Left Abutment Wedge	114
TABLE 6.	Seismic Analysis Results for Model 1	118
TABLE 7.	Seismic Analysis Results for Model 2	120
TABLE 8.	Seismic Analysis Results for Model 3	123
TABLE 9.	Seismic Analysis Results for Model 3	127
TABLE 10.	Seismic Analysis Results for Model 5	136
TABLE 11.	Seismic Analysis Results for Model 6	138
TABLE 12.	DYNA3D concrete material properties compared with Morrow Point Dam properties.....	140
TABLE 13.	Seismic Analysis Results for Model 7	141
TABLE 14.	Seismic Analysis Results for Model 8	146
TABLE 15.	Seismic Analysis Results for Model 9	149
TABLE 16.	Seismic Analysis Results for thermal model	155
TABLE 17.	Upstream-Downstream Displacement Comparison.....	160
TABLE 18.	Typical Engineering Properties of Structural Concrete	164
TABLE 19.	DYNA3D input	180
TABLE 20.	Input for equation-of-state form 12: WSMR-5 3/4 concrete	183
TABLE 21.	Input for equation-of-state form 12: SAC5 concrete	184
TABLE 22.	DYNA3D input for WSMR-5 3/4 concrete: mesh size (6 x 6 x 6 in. cube)	186
TABLE 23.	DYNA3D input for SAC5 concrete: mesh size (6 x 6 x 6 in. cube)	187



Executive Summary

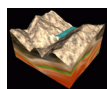
This research and development project was sponsored by the United States Bureau of Reclamation (USBR), who are best known for the dams, power plants, and canals it constructed in the 17 western states. The mission statement of the USBR's Dam Safety Office, located in Denver, Colorado, is "to ensure Reclamation dams do not present unacceptable risk to people, property, and the environment." The Dam Safety Office does this by quickly identifying the dams which pose an increased threat to the public, and quickly completing the related analyses in order to make decisions that will safeguard the public and associated resources. The research study described in this report constitutes one element of USBR's research and development work to advance their computational and analysis capabilities for studying the response of dams to strong earthquake motions. This project focused on the seismic response of Morrow Point Dam, which is located 263 km southwest of Denver, Colorado.

Studying the response of concrete dams to earthquake ground motions requires three general steps

- selecting earthquake ground motions at the site
- modeling the concrete dam, flexible foundation, and reservoir, and performing a transient analysis
- analyzing or evaluating the dynamic response, including the assessment of post-earthquake stability. Stability plays a large role in the analysis of these structures, especially Morrow Point Dam. Morrow Point Dam is a highly segmented structure that has a large "rock" or wedge defined by three foliation planes that sits directly under the dam's left abutment, which could significantly effect the structural response of the dam.

The sequence of segmented lifts typical of Morrow Point Dam's construction has a significant impact on the static stress fields induced in the dam. An analysis of a monolithic dam may show artificially high tensile stresses within the dam, especially near the abutments. The contraction joints in arch dams cannot develop tensile stresses and may open and close throughout the duration of the earthquake. Furthermore, the opening of contraction joints may reduce the tensile stresses, but may increase the compressive arch stresses in regions where the joints are closed [Ref 3].

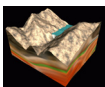
One objective of this study was to perform a detailed evaluation of the effect of various modeling idealizations, and assumptions on the predicted response of Morrow Point Dam. This included consideration of nonlinearities in the dam due to the shear keys across the vertical contraction joints, nonlinearities due to the extensive use of contact surfaces between dam/reservoir/foundation/abutment wedge, and material nonlinearities due to concrete cracking. In addition, the accurate geology topography was modeled for the foundation to study the effects of wave scattering in the canyon and a model for hydrodynamic interaction was implemented into LLNL's finite element codes for fluid representation in the three-dimensional dam system finite element model.



A large number of simulations and parameter studies were performed in this study in order to provide understanding of the significance of modeling assumptions and the differences between models of different sophistications, ranging from simple monolithic dam models to complex fully nonlinear models. The major conclusions reached during these extensive studies include:

- Using discrete elements to model the joint behavior resulted in gap openings of 0.29 inches at the dam quarter point, whereas when using a sophisticated slide surface that took into account the shear key geometry, the gap openings were only as much as 0.05 inches at the dam quarter point. However, a peak gap opening of 0.375 inches occurred near the left abutment. When the left abutment wedge was allowed to move freely from both the dam and foundation, the peak gap opening near the left abutment increased to 0.65 inches and when uplift pressures and a tied with failure slide surface was used at the dam/foundation interface, a peak gap opening near the left abutment was 0.91 inches.
- The response of the dam was highly dependent on how the input ground motions were applied to the 3-D topographically accurate flexible foundation model. It was discovered that when using non-deconvolved ground motions (motions that were not deconvolved down to the base of the foundation), the accelerations or site response at the dam/foundation interface was too high. Furthermore, when the ground motions were applied at the base of the foundation using base accelerations, which meant there was a non-transmitting boundary at that surface, the dam response was much larger than if a transmitting boundary was used.
- The accurate geology topography had the effect of reducing the site response slightly at the base of the dam.
- Two separate models studied the effects of concrete material nonlinearity and a tied with failure contact surface between the dam and foundation. Both models had similar peak upstream-downstream displacements at the top center of the dam with the model that did not include these nonlinearities. The models predicted that the dam would remain stable throughout the duration of the earthquake.
- By accounting for either the hydrostatic uplift (along the foundation) or a low temperature condition on the dam, the dam response (e.g. peak upstream-downstream displacement) was similar to the response of the models that did not include these sophistications.
- The peak upstream-downstream dam displacement predicted by this study is 2.86 inches, which is very close to the 2.9 inch value predicted by the USBR's finite element study using the code EACD3D96 [Ref 10]. In addition, the maximum cross canyon displacement of the left abutment wedge was calculated to be only 0.83 inches.

The extensive body of computational studies completed are documented herein.



Nonlinear Seismic Analysis of Morrow Point Dam

A Study for the United States Bureau of Reclamation

Charles R. Noble†

Jerome Solberg‡

† *Structural and Applied Mechanics Group*
Lawrence Livermore National Laboratory

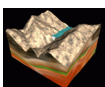
‡ *Methods Development Group*
Lawrence Livermore National Laboratory



1.0 Objective and Background

Morrow Point Dam, located in the Black Canyon of the Gunnison River in southwestern Colorado, is a thin double curvature arch dam located approximately 35 km (22 miles) east of Montrose, Colorado. A double curvature arch dam is defined as an arch dam which is curved in both “plan and elevation, with undercutting of the heel and in most instances, a downstream overhang near the crest.” In other words, it is an arch dam that is curved vertically as well as horizontally (Figure 1). The dam, which was constructed between 1963 and 1968, impounds approximately 144 million cubic meters (117,000 acre-ft) of water in the Morrow Point Reservoir. The reservoir extends approximately 19 km (12 miles) upstream. The dam structure is 143 m (468 ft) high with a crest length of 221 m (724 ft). The thin arch structure ranges in thickness from 3.7 m (12 ft) at the crest to 16 m (52 ft) at the base. The crest of the dam, at elevation 2183.9 m (7165 ft) carries a roadway across the width of the structure.

The primary objective of this project was to perform a comprehensive nonlinear seismic analysis of Morrow Point Dam for the United States Bureau of Reclamation. The project consisted of two major phases. The first phase of this research study consisted of the following:



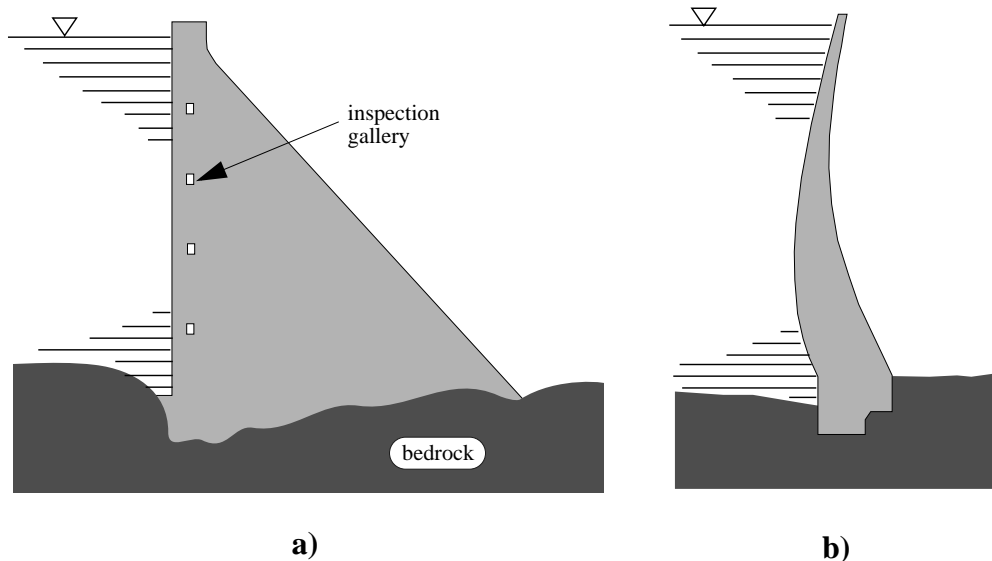


FIGURE 1. Principal concrete dam types. a) Gravity dam; b) thin arch dam.

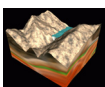
- Construct a coupled three-dimensional finite element model of the Morrow Point Dam/ Foundation Rock/Reservoir system, which includes appropriate geology topography. In addition, this will include the foundation rock with three contact surfaces to represent the abutment wedge formed by foliation plane 4, joint set 2, and joint set B.
- Complete implementation of a model for hydrodynamic interaction in the NIKE3D and DYNA3D codes. This will include implementation of nearly incompressible finite elements for fluid representation in the 3D Dam system model.
- Modify the existing NIKE3D and DYNA3D contact surfaces to allow appropriate modeling of the available shear transfer across contraction joints which contain shear keys.
- Perform nonlinear dynamic earthquake time history analyses and sensitivity studies to assess the effects of varying expansion joint characterizations on the computed system response.

The scope of Phase 2 consisted of three primary areas:

1. Finite element model verification
2. Additional finite element model development
3. Finite element analyses

In the area of model verification, the following tasks were suggested by the USBR's Consultant Review Board for Morrow Point Dam:

- Comparison with other finite element codes, such as GDAP, SCADA, or EACD.
- Free vibration study of Morrow Point Dam to determine the fundamental modes of the complex 3D finite element model and the damping in the system.
- Block sliding verification test in order to verify that the contact surfaces in DYNA3D are indeed performing as expected.



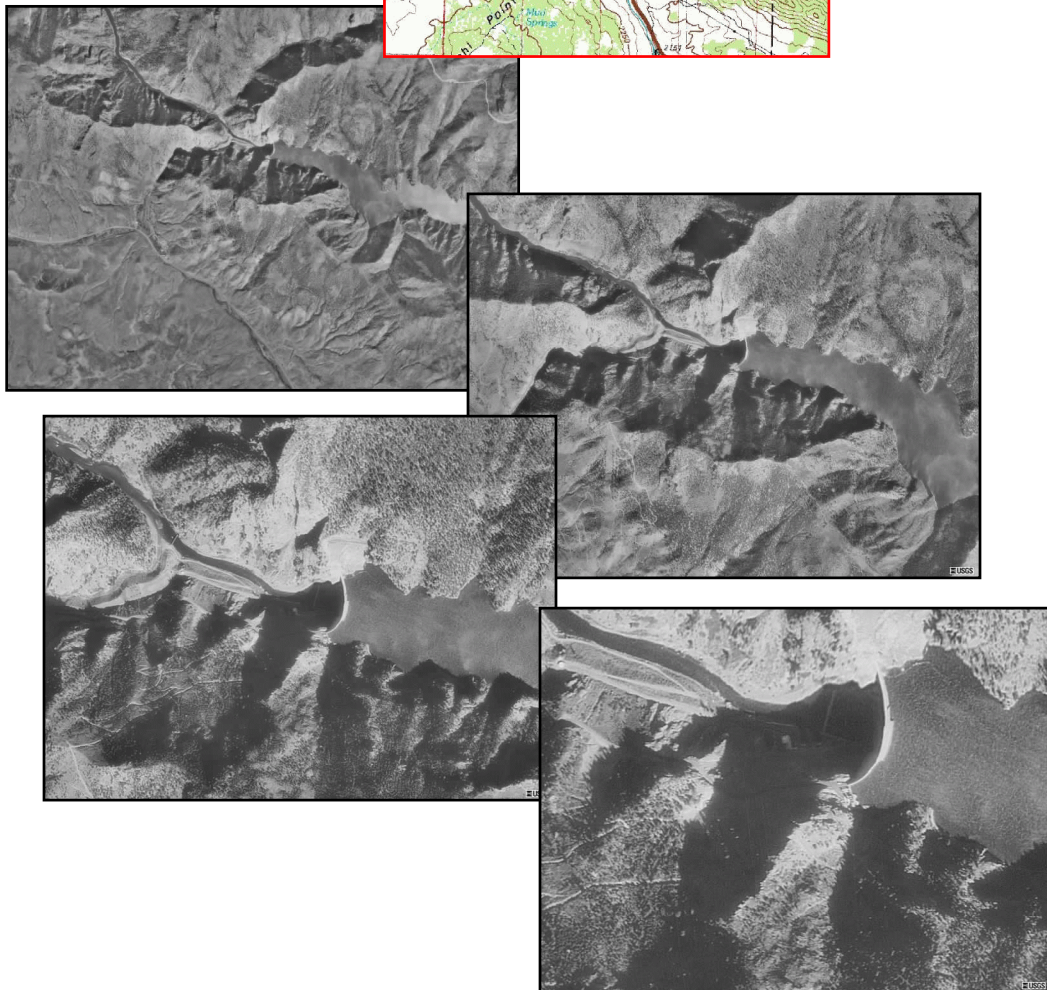
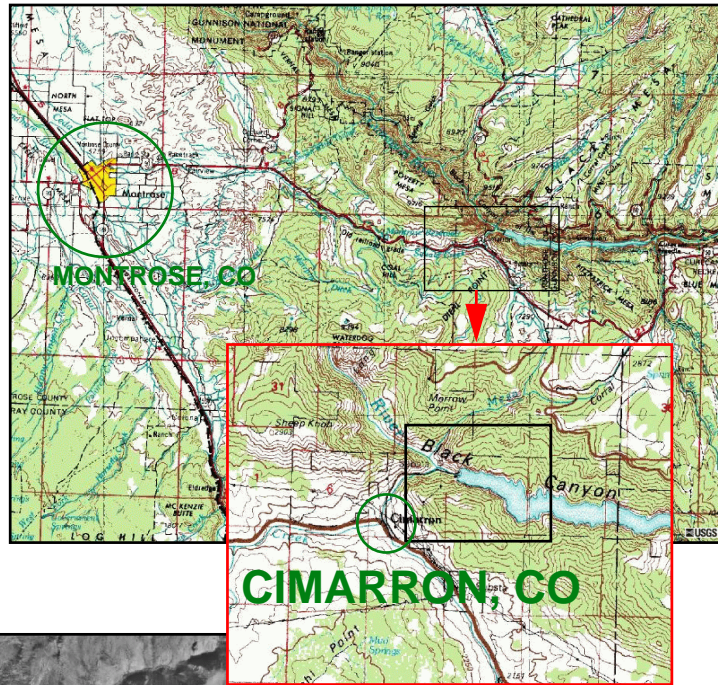
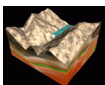


FIGURE 2. Morrow Point Dam overhead photos.



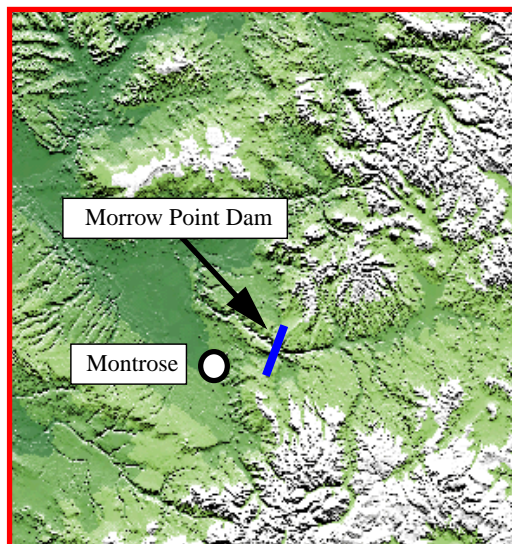
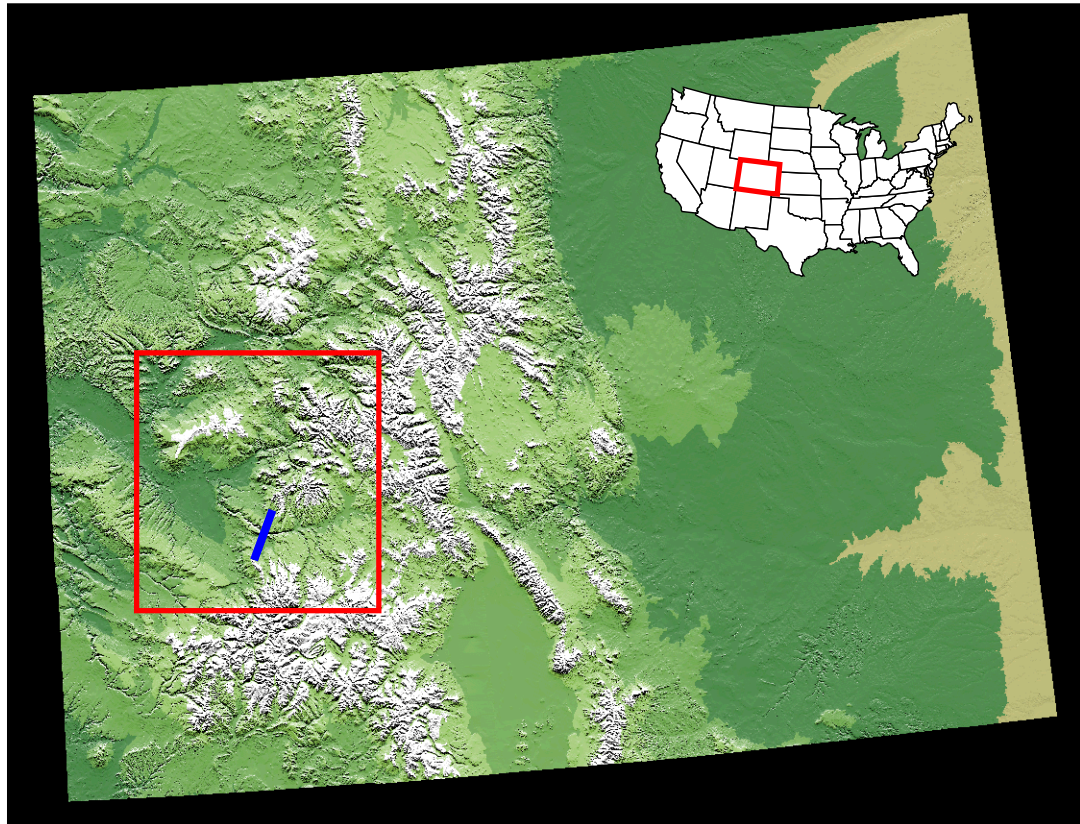
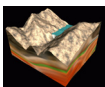


FIGURE 3. Morrow Point Dam in southwestern Colorado, topographic setting.



In the area of finite element model development, the following tasks were completed:

- Seismic input using forces were used instead of base accelerations along the base of the foundation. This allowed for a non-reflecting boundary condition to be placed on the entire boundary of the finite element model.
- A transmitting or non-reflecting boundary was added to the upstream side of the reservoir.
- A sliding contact surface was added between the reservoir and the foundation.
- The wedge geometry was modified to be closer to that found in the field.
- Hydrostatic uplift forces or pressures along the abutment wedge contact surfaces were added to the finite element model.

Nine finite element models were generated for Phase 2 of this study. The nine different finite element models are described below:

1. *Model 1: Homogeneous/Monolithic Dam*

This model has the least number of sliding contacts and will be used to validate the reservoir model, application of the ground motions, damping, sliding between the reservoir and foundation, and compare with EACD. This model will contain a flexible foundation, a homogeneous/monolithic representation of the dam, water explicitly modeled, and the abutment wedge fixed to the foundation and tied to the dam.

2. *Model 2: Model with Contraction Joints and Wedge Fixed*

This finite element model includes a flexible foundation, the dam contraction joints, the water explicitly modeled, and the abutment wedge fixed to the foundation and tied to the dam.

3. *Model 3: Model with Contraction Joints and Wedge Not Fixed*

Model 3 will be the coupled analysis with the dam and foundation wedge and will show the stability of the wedge. This model will contain a flexible foundation, contraction joints, water explicitly modeled, and the abutment wedge allowed to move freely.

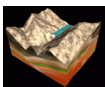
4. *Model 4: Model of Foundation Only with Wedge Fixed*

This model does not include the dam and the wedge is fixed. This finite element model will give the opportunity to study the seismic waves propagating up the foundation medium as well as assist in verifying the site response.

5. *Model 5: Model of Foundation Only with Wedge Not Fixed*

This model was constructed in order to study whether the foundation wedge will slide on its own during an earthquake without adding forces from the dam.

6. *Model 6: Model of Foundation and Wedge with Uplift Modeled Between the Wedge and Foundation*



Model 6 is the same as model 5, except that hydrostatic uplift forces have been added at the abutment wedge contact surfaces.

7. Model 7: Concrete Damage Model

This model will use a sophisticated concrete damage material model for the dam to study whether the concrete is likely to damage or crack due to the seismic response of the dam.

8. Model 8: Model with Tied with Failure Slide Surface at the Foundation/Dam Interface

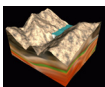
Model 8 uses a tied with failure slide surface at the foundation/dam interface in order to study the stability of the dam if the dam separates from the foundation.

9. Model 9: Model with Tied with Failure Slide Surface and Uplift at the Foundation/Dam Interface

This model is the same as model 8 except that uplift forces will be applied at the foundation/dam interface.

2.0 Earthquake ground motions

Morrow Point Dam is located in the Black Canyon of the Gunnison River, a 2,460 foot deep gorge carved into folded precambrian metamorphic and igneous rock. The foundation is entirely quartzite and mica schist that are cut by granite pegmatite dikes, shears, and joints. The Cimarron fault is approximately 1 km from the dam (Figure 5). The Cimarron fault is a west-northwest-striking fault between Montrose and Blue Mesa Reservoir. The western end of the fault is parallel to State Highway 50 and the Gunnison River. The fault begins in the Black Canyon of the Gunnison National Monument, continues southeast past Powderhorn and Iron Hill, and terminates south of the southeastern end of Huntsman Mesa. The United State Bureau of Reclamation performed site specific seismotectonic studies for Morrow Point Dam and three ground motions were developed using the results of an initial hazard calculation. Figure 4 shows a seismic hazard map for the state of Colorado. The USBR developed ground motions representing an earthquake with a return period of 1 in 50,000 years and representing a magnitude M 6.5 to M 6.7 earthquake on the Cimarron Fault. The earthquake motions that are used throughout this study are the empirical records developed from the Cerro Prieto (cpe) recording from the M 6.5 Victoria, Mexico earthquake. The cpe_045 component is the component applied in the upstream-downstream direction, the cpe_315 is the component applied in the cross-canyon direction, and the cpe_up is the vertical component of earthquake motions.



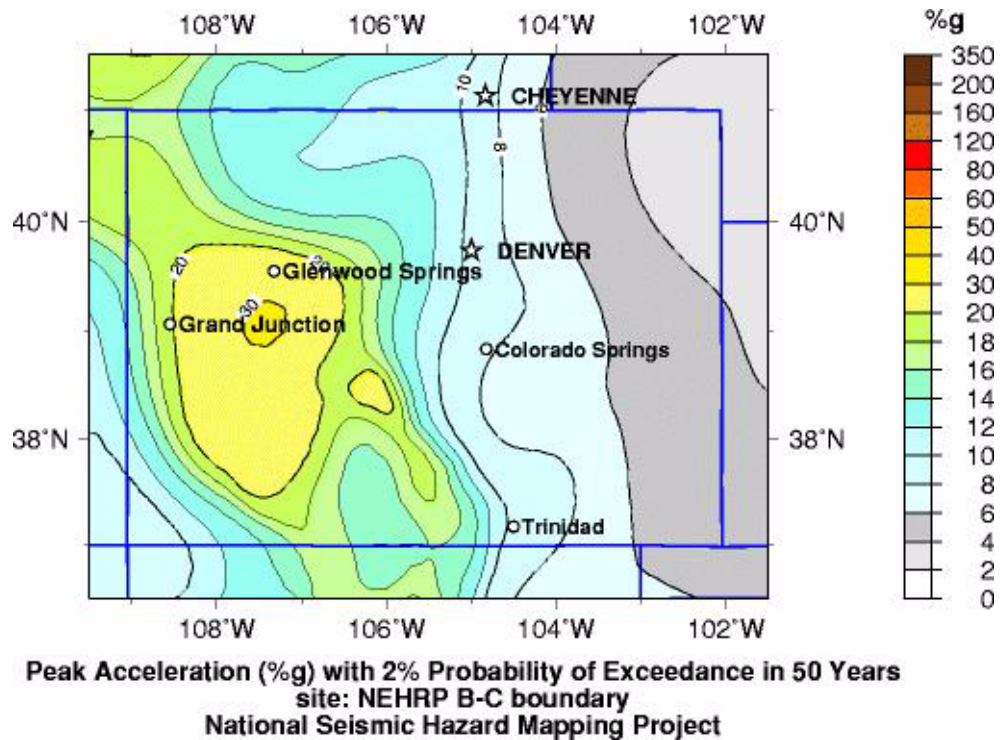
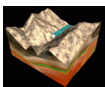


FIGURE 4. Colorado Seismic Hazard Map.

Figure 6 through Figure 8 shows the Morrow Point Cerro Prieto ground accelerations, velocities, and displacements, as well as the response spectrum for both components of horizontal ground motions and the vertical component ground motions. For this study, we also needed ground motions that were deconvolved 520 meters below the dam/foundation contact surface. These time histories were used with the finite element model that included the approximately 520 meters of earth below the dam. The USBR deconvolved the ground motions for LLNL and used 5% damping when calculating the deconvolved ground motions. Figure 9 through Figure 11 show the three components of ground accelerations, velocities, and displacements, as well as their corresponding response spectra. Figure 12 shows a comparison of the original and deconvolved ground motions for the Cerro Prieto time histories. The deconvolved ground motions are less severe than the original ground motions.



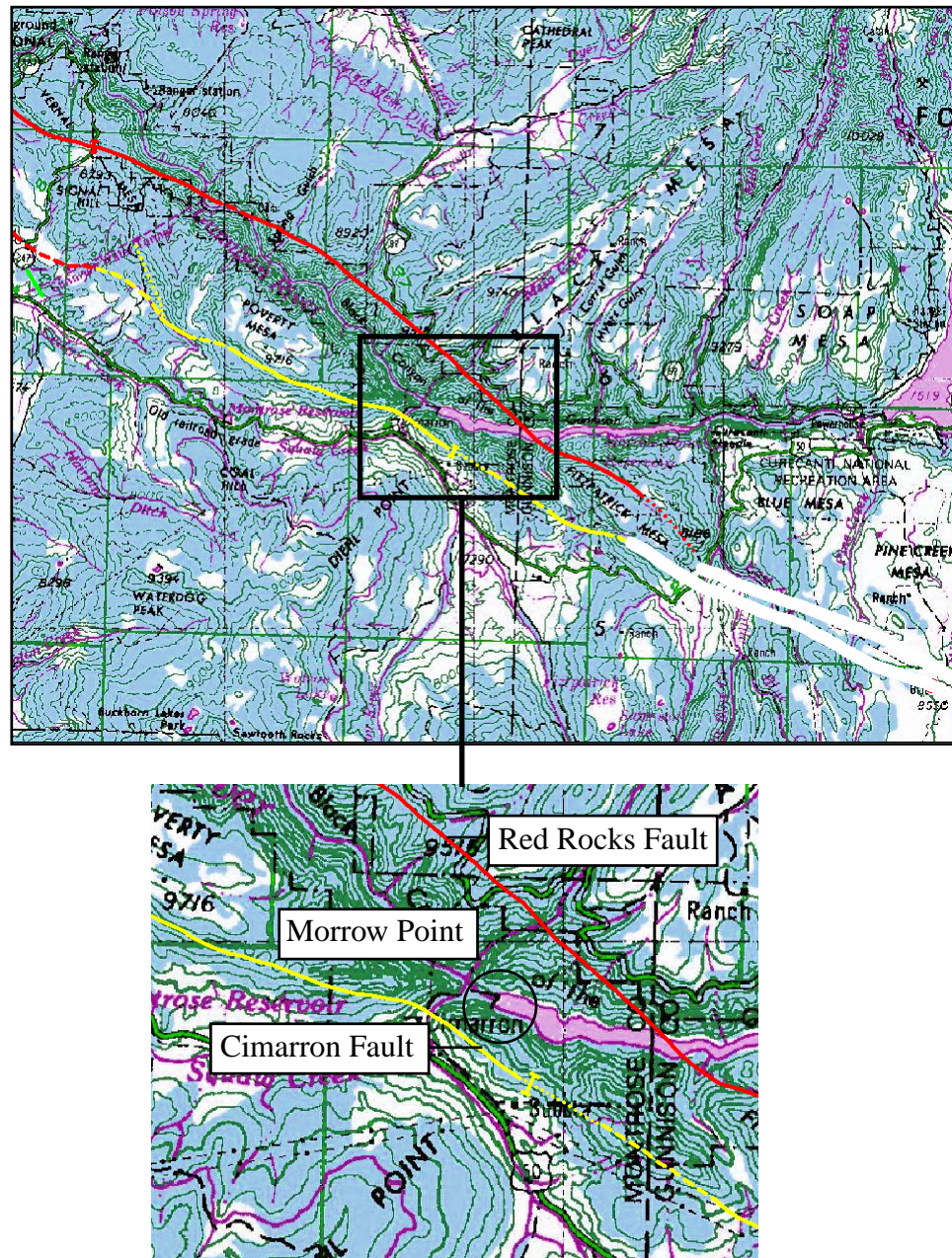
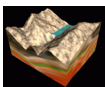


FIGURE 5. Location of Cimarron Fault (Colorado Geological Survey).



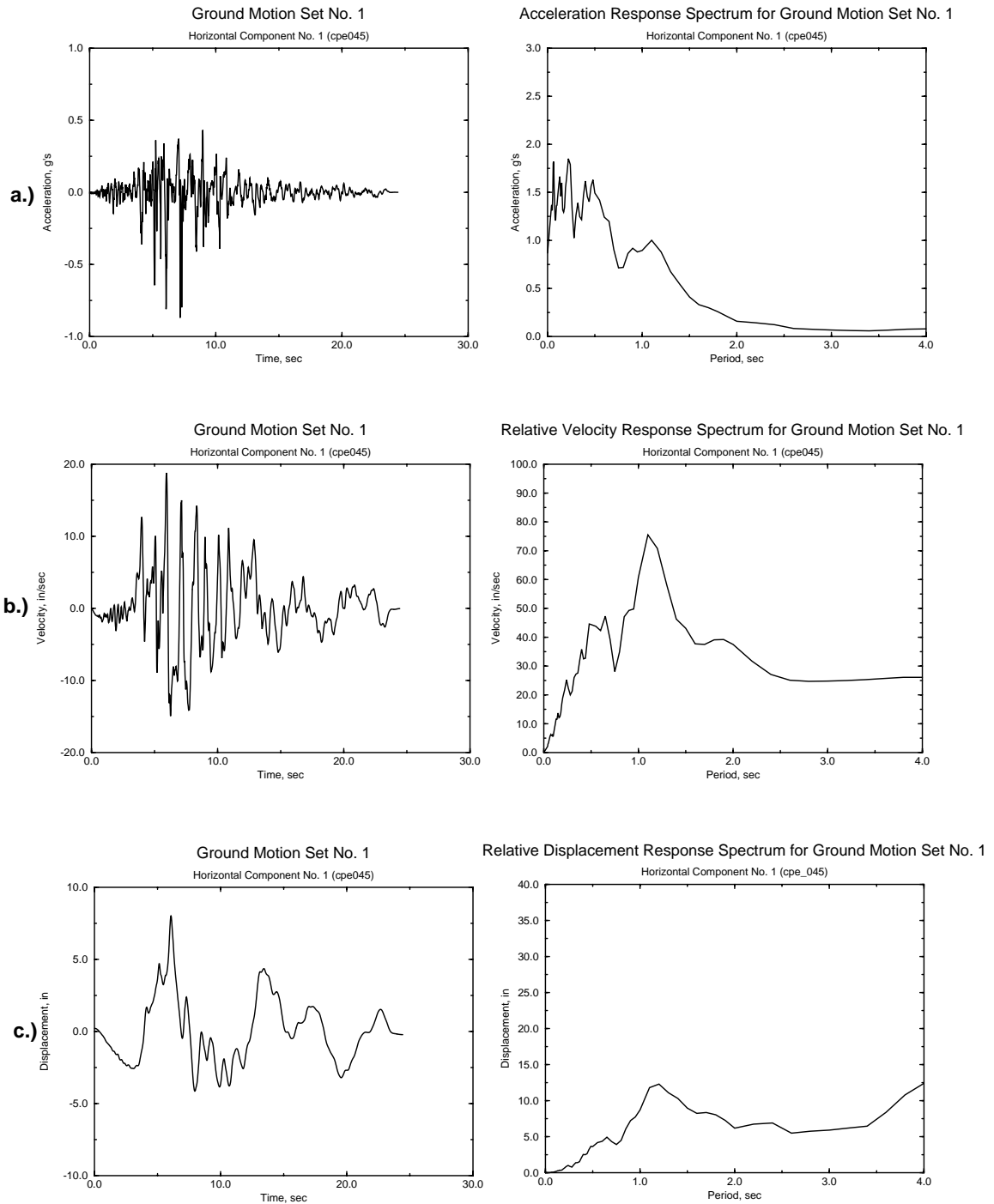
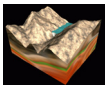


FIGURE 6. Morrow Point ground motions for Cerro Prieto time history. a) Horizontal ground acceleration; b) horizontal ground velocity; c) horizontal ground displacement.



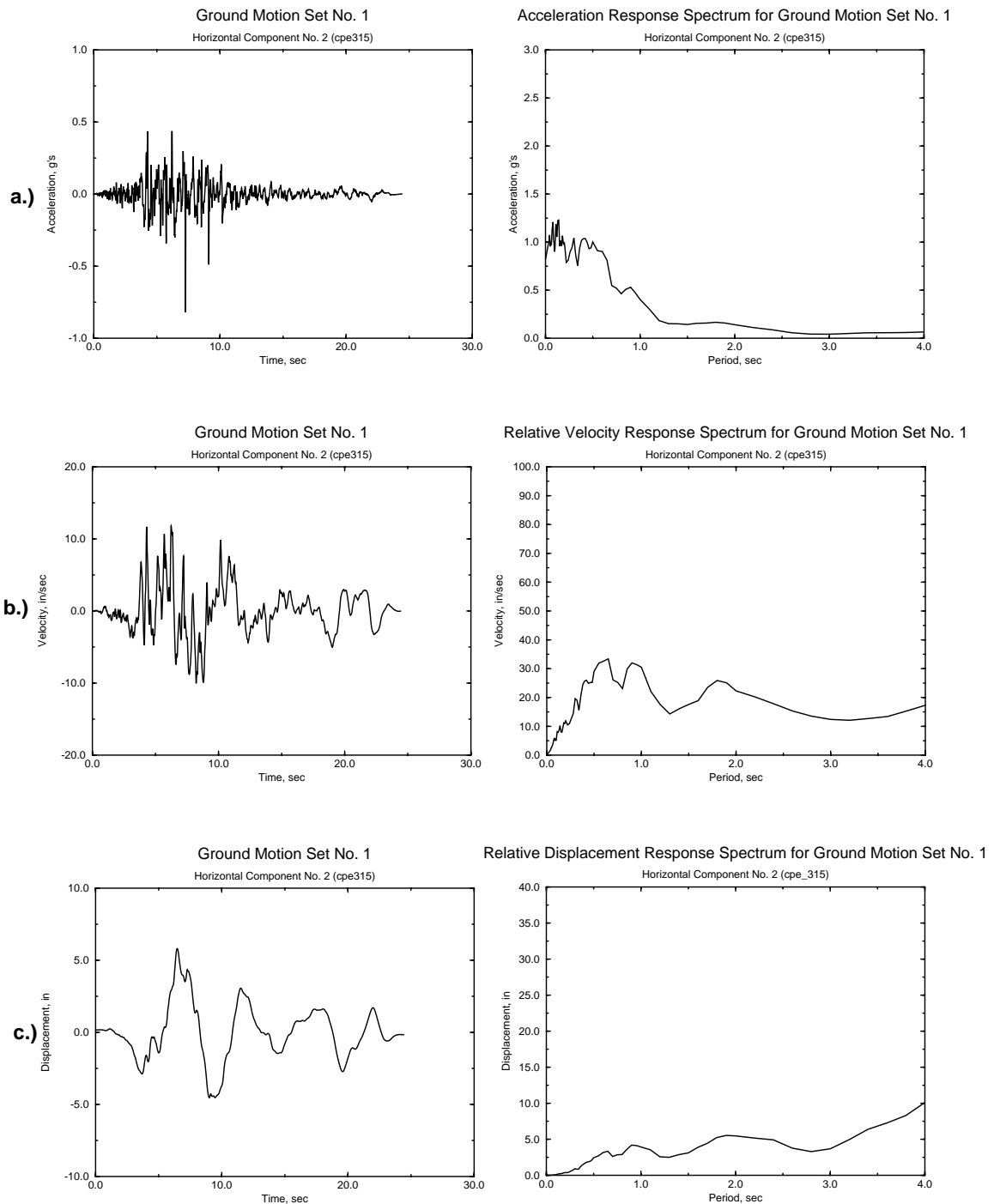
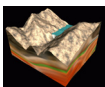


FIGURE 7. Morrow Point ground motions for Cerro Prieto time history. a) Horizontal ground acceleration; b) horizontal ground velocity; c) horizontal ground displacement.



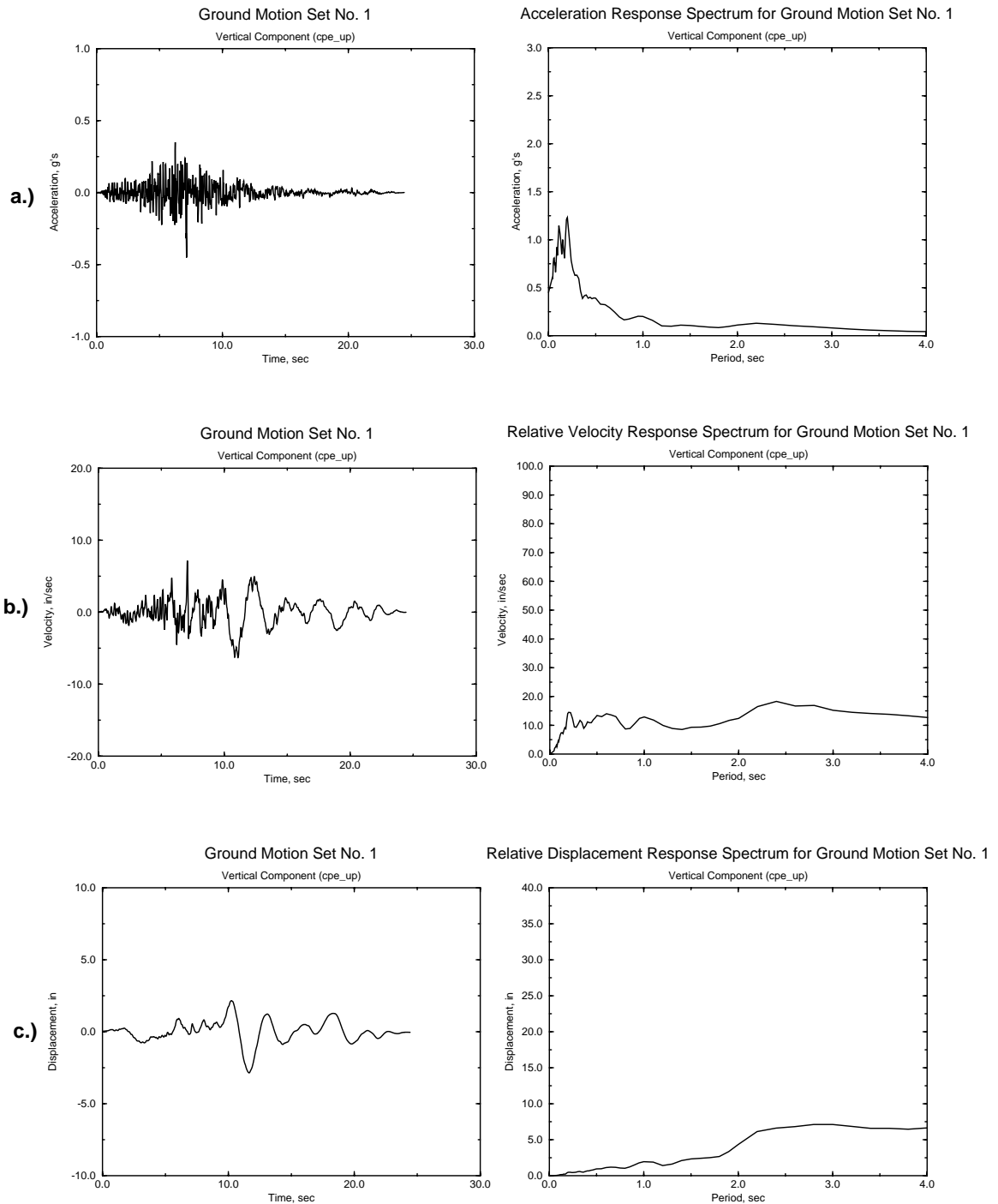
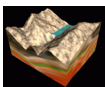


FIGURE 8. Morrow Point ground motions for Cerro Prieto time history. a) Vertical ground acceleration; b) vertical ground velocity; c) vertical ground displacement.



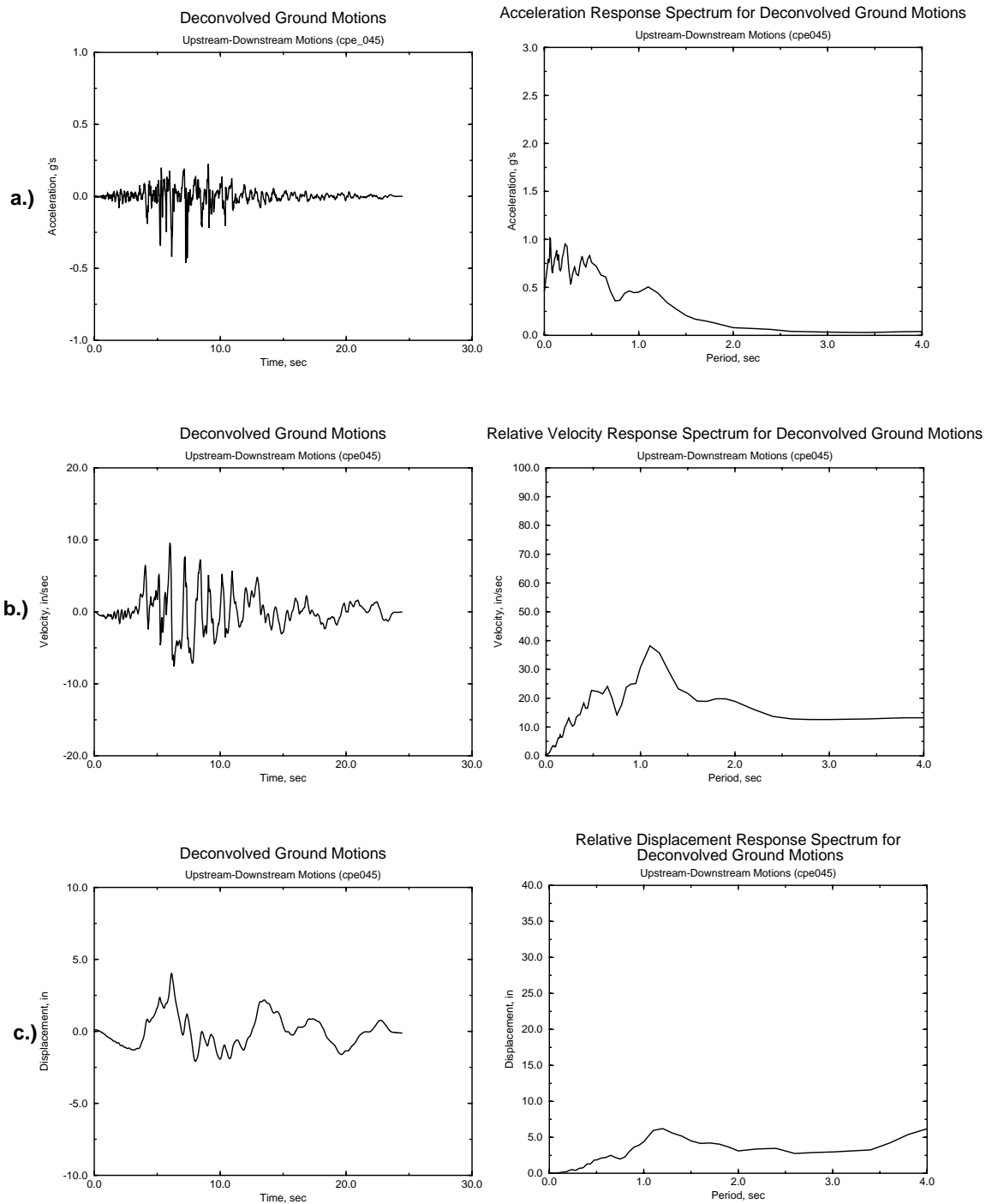
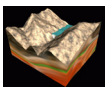


FIGURE 9. Morrow Point deconvolved ground motions for Cerro Prieto time history. a) Horizontal ground acceleration; b) horizontal ground velocity; c) horizontal ground displacement.



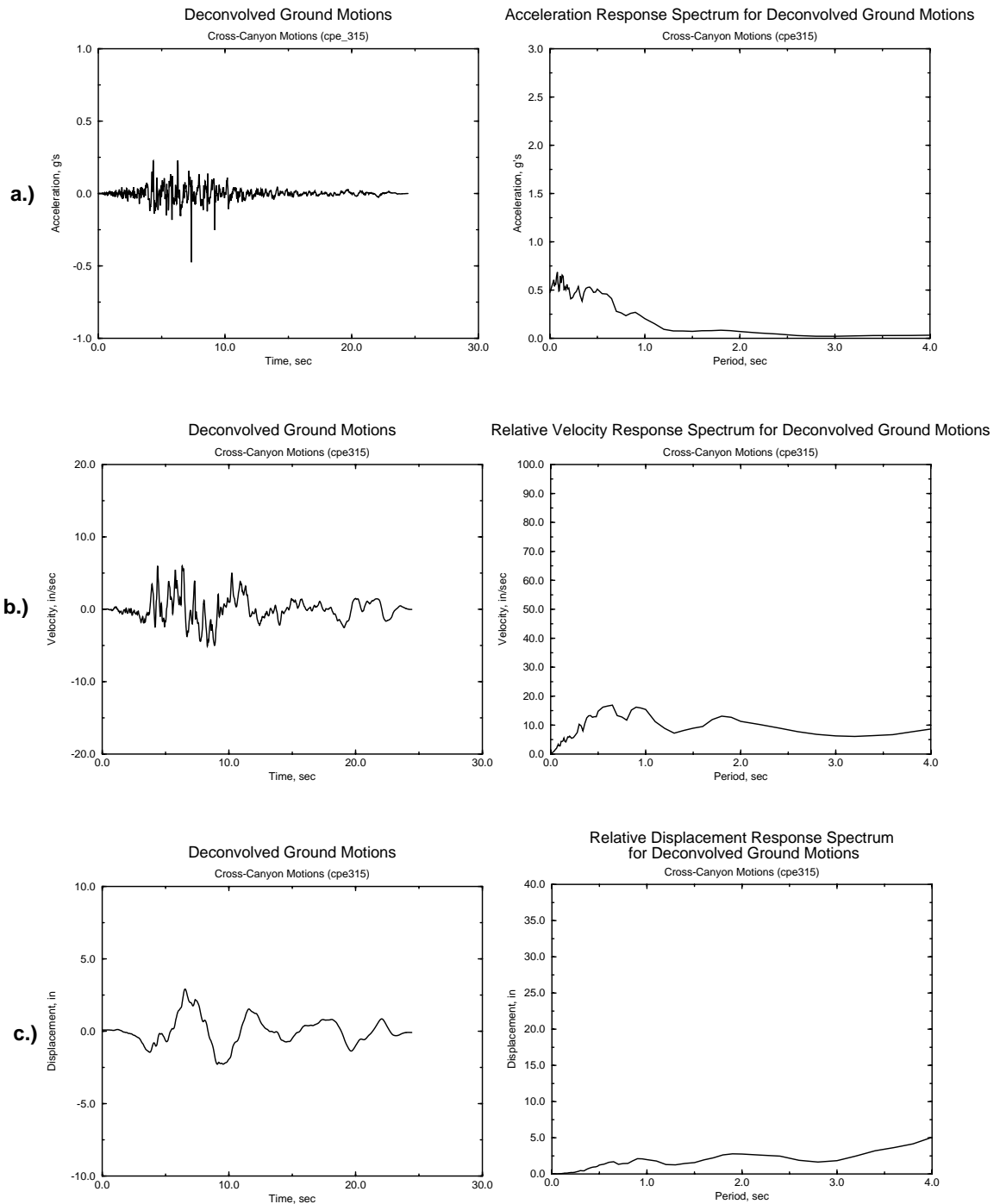
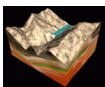


FIGURE 10. Morrow Point deconvolved ground motions for Cerro Prieto time history. a) Horizontal ground acceleration; b) horizontal ground velocity; c) horizontal ground displacement.



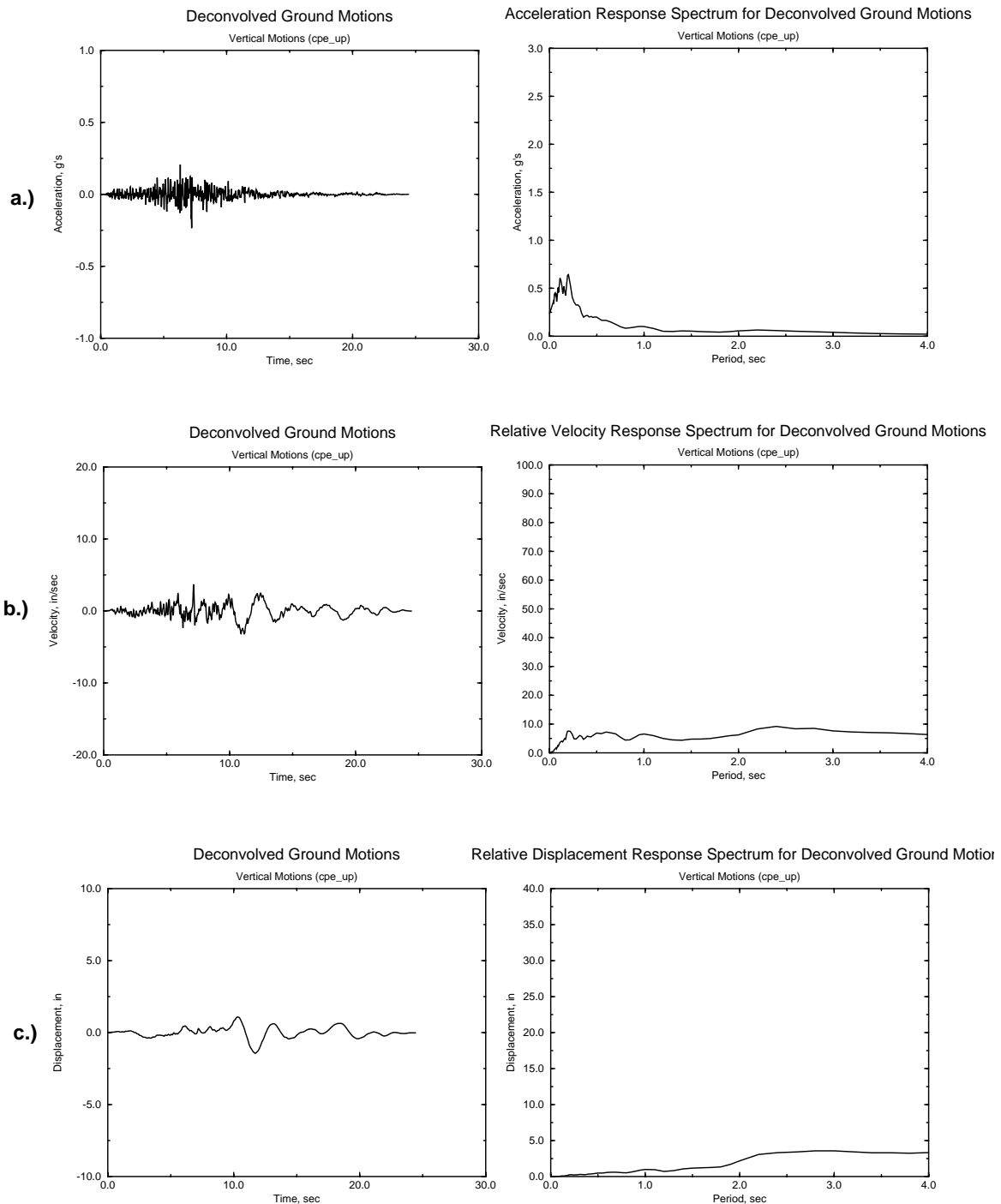
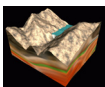
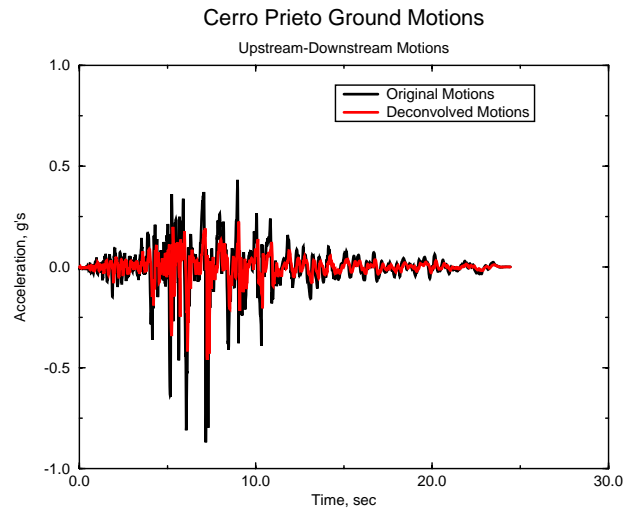


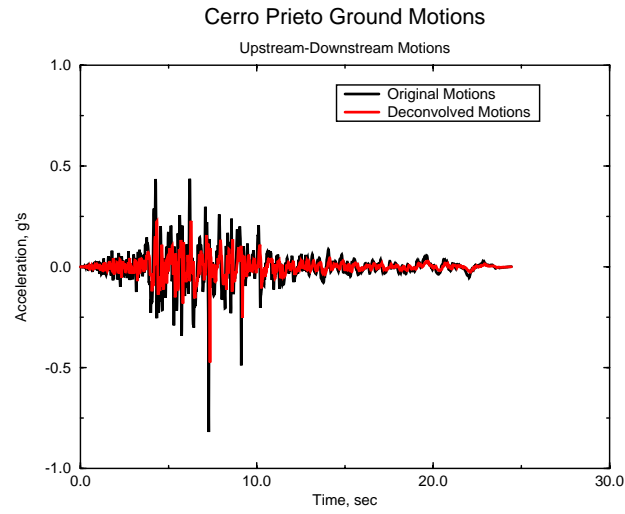
FIGURE 11. Morrow Point deconvolved ground motions for Cerro Prieto time history. a) Vertical ground acceleration; b) vertical ground velocity; c) vertical ground displacement.



a.)



b.)



c.)

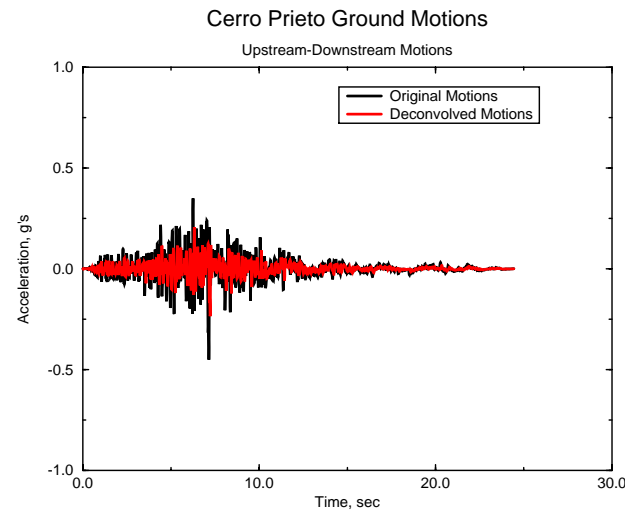
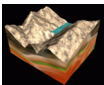


FIGURE 12. Comparison between original and deconvolved ground motions for Cerro Prieto time history.



2.1 Calculation of Force Time Histories

In LLNL's explicit code DYNA3D, there are two methods for applying earthquake ground motions. One can either apply the ground motions as accelerations (and velocities) or as nodal forces. The easiest method is to apply the ground motions as base accelerations. However, if one wants a non-reflecting boundary condition at the same location as the earthquake ground motions are to be applied, base accelerations may not be used. Therefore, Hall [Ref 11] suggested using nodal forces.

To convert the base accelerations into force time histories, one must first integrate the 3 components of deconvolved ground accelerations to obtain 3 components of deconvolved ground velocities. Knowing the deconvolved ground velocities, one can then calculate the forces at node i using the following relationships:

$$F_y = 2 \cdot E \cdot A_i \cdot \dot{y}_{gc}(t) / C_p \quad (\text{EQ 1})$$

$$F_x = 2 \cdot G \cdot A_i \cdot \dot{x}_{gc}(t) / C_s \quad (\text{EQ 2})$$

$$F_z = 2 \cdot G \cdot A_i \cdot \dot{z}_{gc}(t) / C_s \quad (\text{EQ 3})$$

where

$\dot{y}_{gc}(t)$ = y deconvolved ground velocity (y is considered to be in the vertical direction)

$\dot{x}_{gc}(t)$ = x deconvolved ground velocity

$\dot{z}_{gc}(t)$ = z deconvolved ground velocity

A_i : tributary area of node i

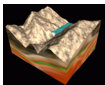
E : Young's Modulus

G : Shear Modulus

C_p : P-wave speed

C_s : S-wave speed

When using the non-reflecting boundary conditions in DYNA3D, one must modify the force time histories to account for the dampers at the input location. In the finite element models presented here, the force time histories were input at the base of the foundation geometry. This is also the location of a non-reflecting boundary. Any forces placed at the same location as a non-reflecting boundary, will be lowered due to the dashpots or dampers at that same node. For the vertical motions, the following forces must be added to EQ. 1:



$$F_y = \dot{y}_{gc}(t) \times A_i \times \rho \times \sqrt{\left(\frac{K + \frac{4}{3}G}{\rho} \right)} \quad (\text{EQ 4})$$

For the horizontal motions, the following forces must be added to EQ. 2 and EQ. 3:

$$F_x = \dot{x}_{gc}(t) \times A_i \times \rho \times \sqrt{\frac{G}{4 \cdot \rho}} \quad (\text{EQ 5})$$

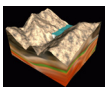
$$F_z = \dot{z}_{gc}(t) \times A_i \times \rho \times \sqrt{\frac{G}{4 \cdot \rho}} \quad (\text{EQ 6})$$

The material properties that were used to calculate the force time histories are given in the following table:

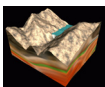
TABLE 1. Foundation Material Properties

Foundation Property	Value Used
Elastic Modulus	3.338E+06 psi
Shear Modulus	1.391E+06
Poisson's Ratio	0.2
Mass Density	2.47E-04 lbs-sec ² /in ⁴
P-wave Speed	188,070.86 in/sec
Shear-wave Speed	115,157.48 in/sec

To verify that the dam would be loaded with the correct ground accelerations, the three components of force time histories were applied to the base of a 520 meter deep rectangular box of foundation material. Acceleration time histories were gathered at the top of the foundation box for comparison with the USBR non-deconvolved ground accelerations. In addition, the force time histories were also applied to the base of the topographically correct foundation model to see what effect the topography would have on the ground accelerations at the Morrow Point Dam location. Figure 13 shows the simplified finite element mesh and the topographically correct finite element mesh of the Morrow Point Dam foundation. In addition, this figure shows where the 3 components of time histories are applied to the model as well as the location of the node where the ground accelerations were gathered for comparison with the USBR calculated Cerro Prieto ground motions. Figure 14 compares the USBR input ground motions and the DYNA3D ground motions at the base of the dam. The vertical ground motions compare very well, but the DYNA3D ground



motions appear to be larger for the horizontal components, especially between 0.5 and 1 second period. When deconvolving the ground motions, the USBR used damping in the horizontal directions. Therefore, mass proportional damping was placed into the DYNA3D finite element model in an attempt to get a better comparison. 3.4% damping for the first mode of Morrow Point Dam was used. Figure 15 compares the USBR input ground motions with the DYNA3D ground motions gathered from the finite element model with mass proportional damping. A better agreement occurs for the horizontal components. Figure 16 compares the USBR ground motions with the DYNA3D ground motions gathered from the simplified foundation model and the topographically correct foundation model. The topography tends to lessen the response across the entire spectrum at the base of the dam. This tends to be especially true for the horizontal components.



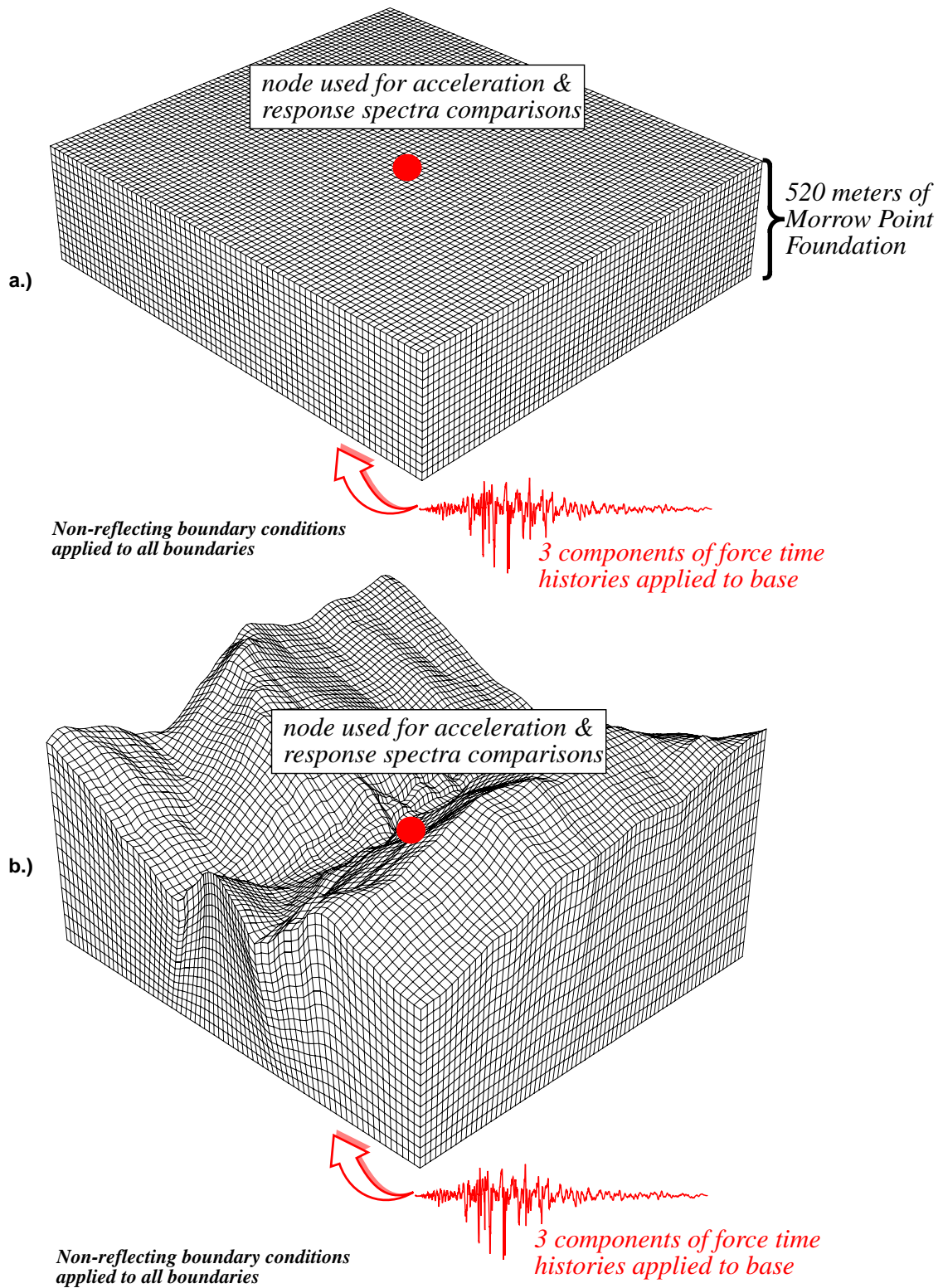
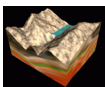


FIGURE 13. a) Simplified finite element mesh of Morrow Point foundation; b) topographically correct finite element mesh of Morrow Point foundation.



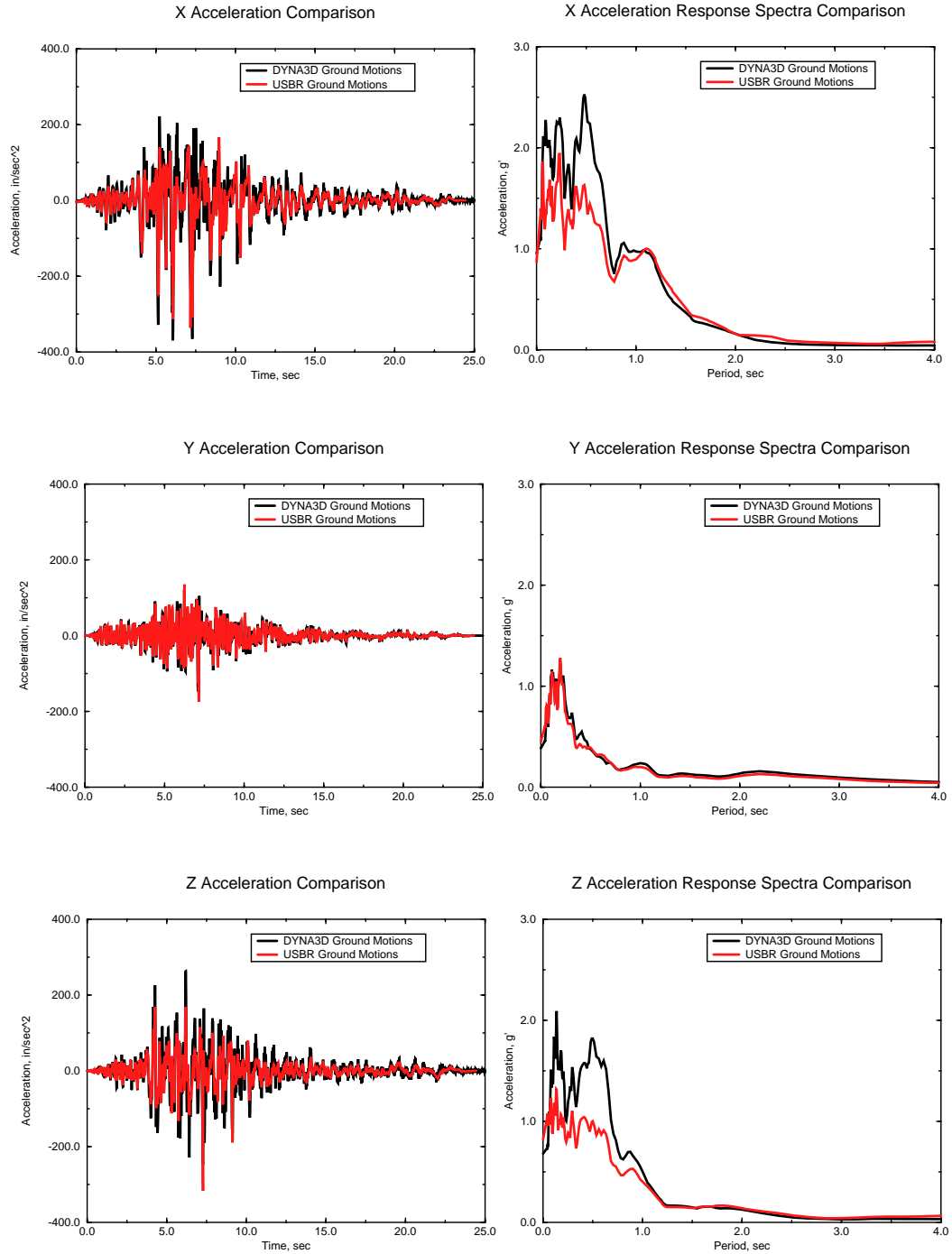
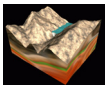


FIGURE 14. Comparison between USBR input ground motions and DYNA3D ground motions at base of dam. The DYNA3D simulation does not include damping.



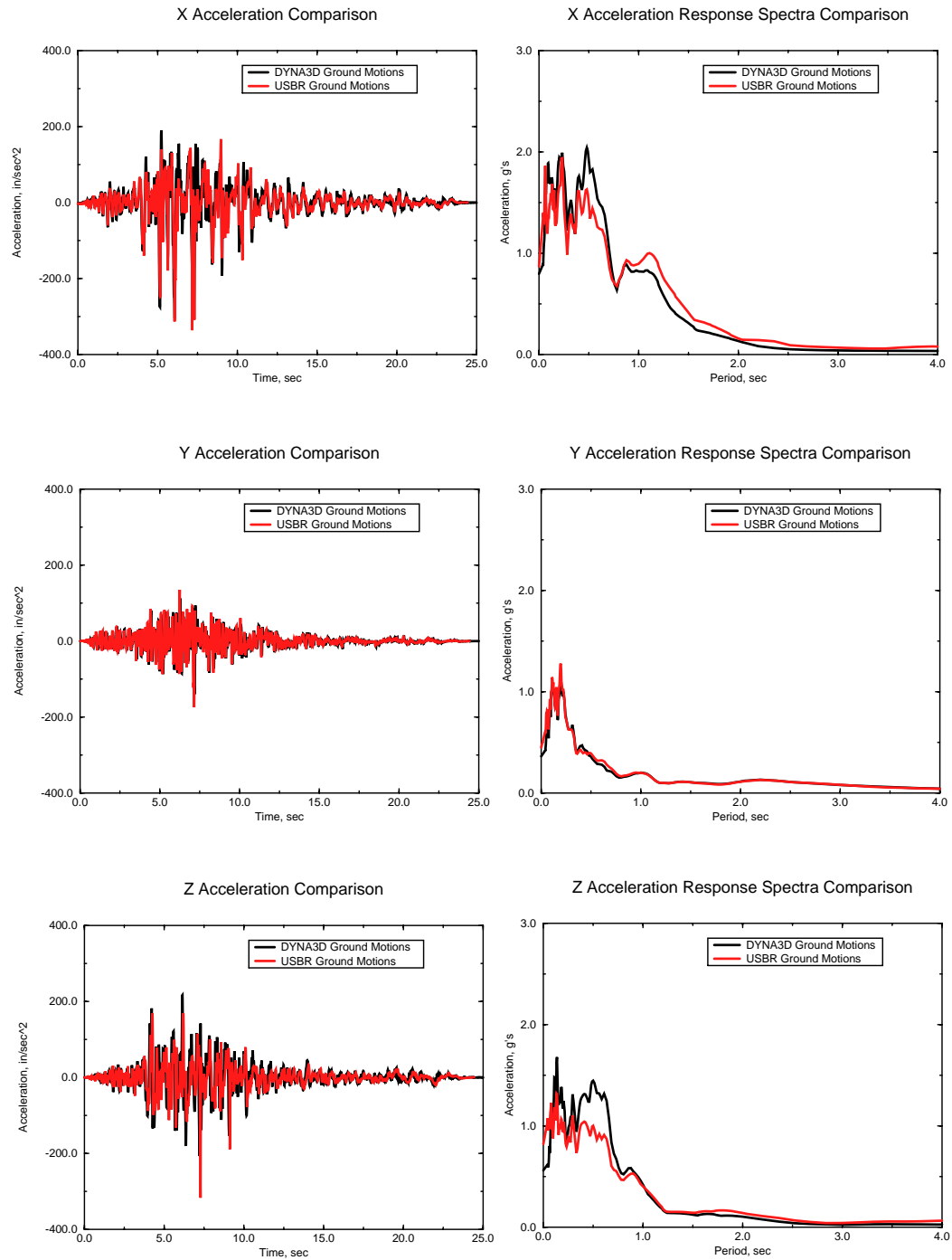
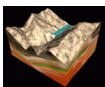


FIGURE 15. Comparison between USBR input ground motions and DYNA3D ground motions at base of dam. The DYNA3D simulation includes 3.4% damping for first mode of Morrow Point Dam.



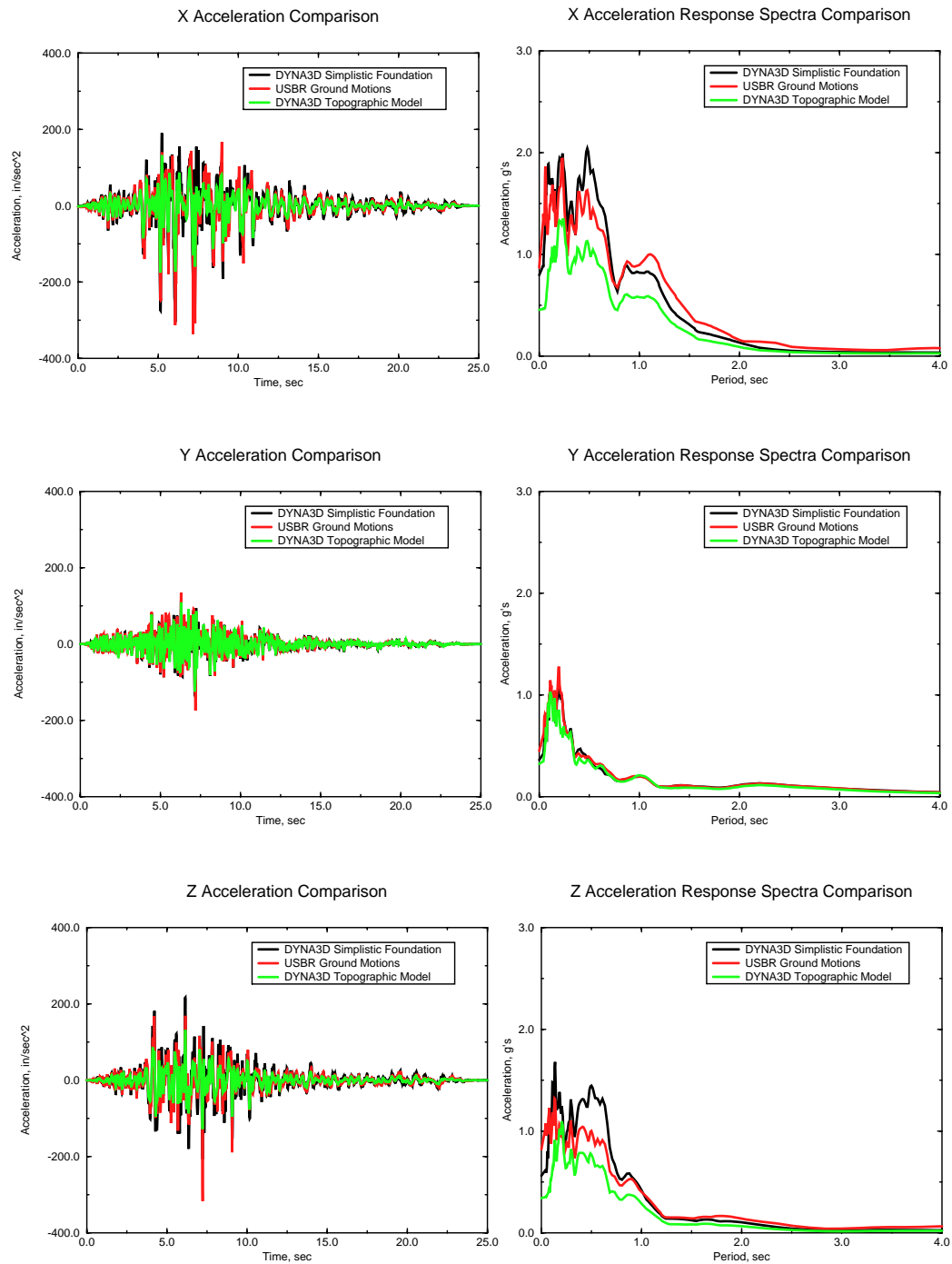
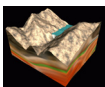


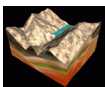
FIGURE 16. Comparison between USBR input ground motions, DYNA3D ground motions at base of dam using simplified foundation, and DYNA3D ground motions using topographically correct foundation. The DYNA3D simulation includes 3.4% damping for first mode of Morrow Point Dam.



3.0 Contraction Joint Detail

The computational model must be initialized to represent the existing dead loads on the structure, and the stress field caused by the dead loads. To achieve the correct dead load stress field due to gravity and hydrostatic load, the computer model must account for the manner in which the dams were constructed. Similar to the situation of modeling cable supported bridges, construction of a dam finite element model with the correct as-built geometry of the dam structure and simply “turning on” gravity in the computer model will generally lead to an incorrect initial stress field in the structure. The sequence of segmented lifts typical of dam construction has a significant impact on the static stress fields induced in the dam. For the Morrow Point Dam for example, the structure was constructed with alternating concrete lifts (Figure 17 and Figure 18). The dam is a highly segmented structure with the vertical segments of the dam in contact across vertical contraction joints. The global dam model must adequately represent the construction sequence and it must also account for the interaction between the adjacent dam segments across the dam contraction joints.

The dimensions of the Morrow Point Dam are shown in Figure 19. Morrow Point is a very thin arch with double curvature. The dam thickness at the crest is 3.7 m (12 ft.) and the thickness at the base is 16 m (52 ft.). The dam structure consists of a number of vertical blocks which are in contact across the vertically extending contraction joints in the dam. The vertical contraction joints of the dam are keyed to enhance shear transfer normal to the face of the dam. A typical contraction joint detail is shown in Figure 20. Under service load conditions of gravity and hydrostatic loading, the contraction joints are under a state of high compression.



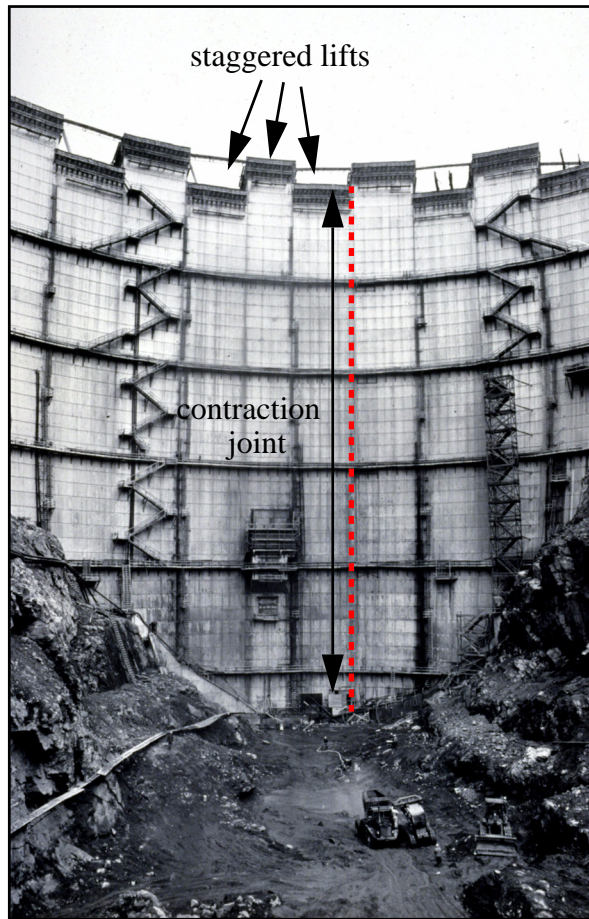
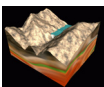


FIGURE 17. Construction photo of the Morrow Point Dam.



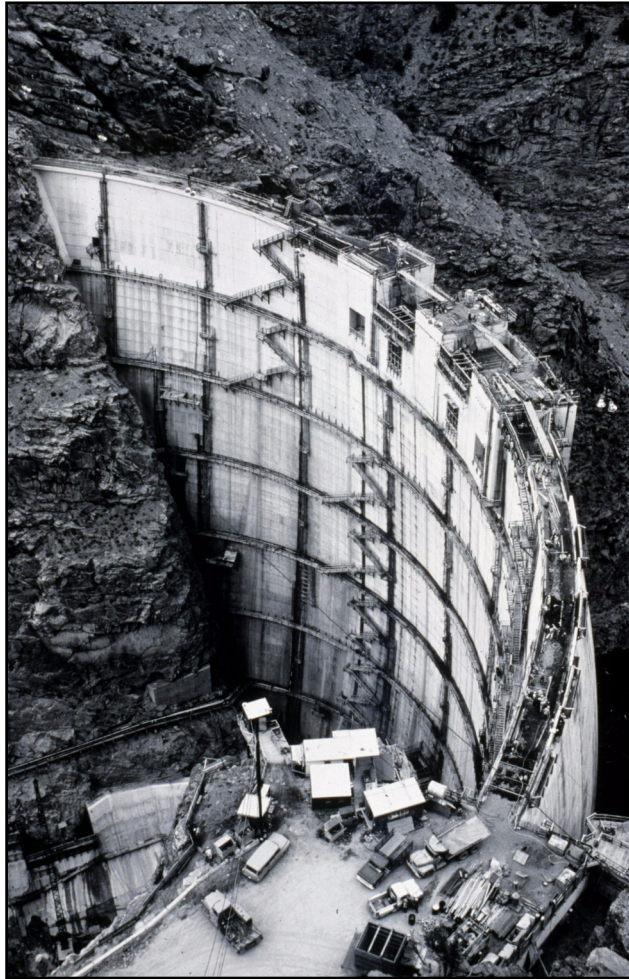
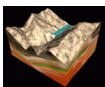
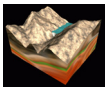
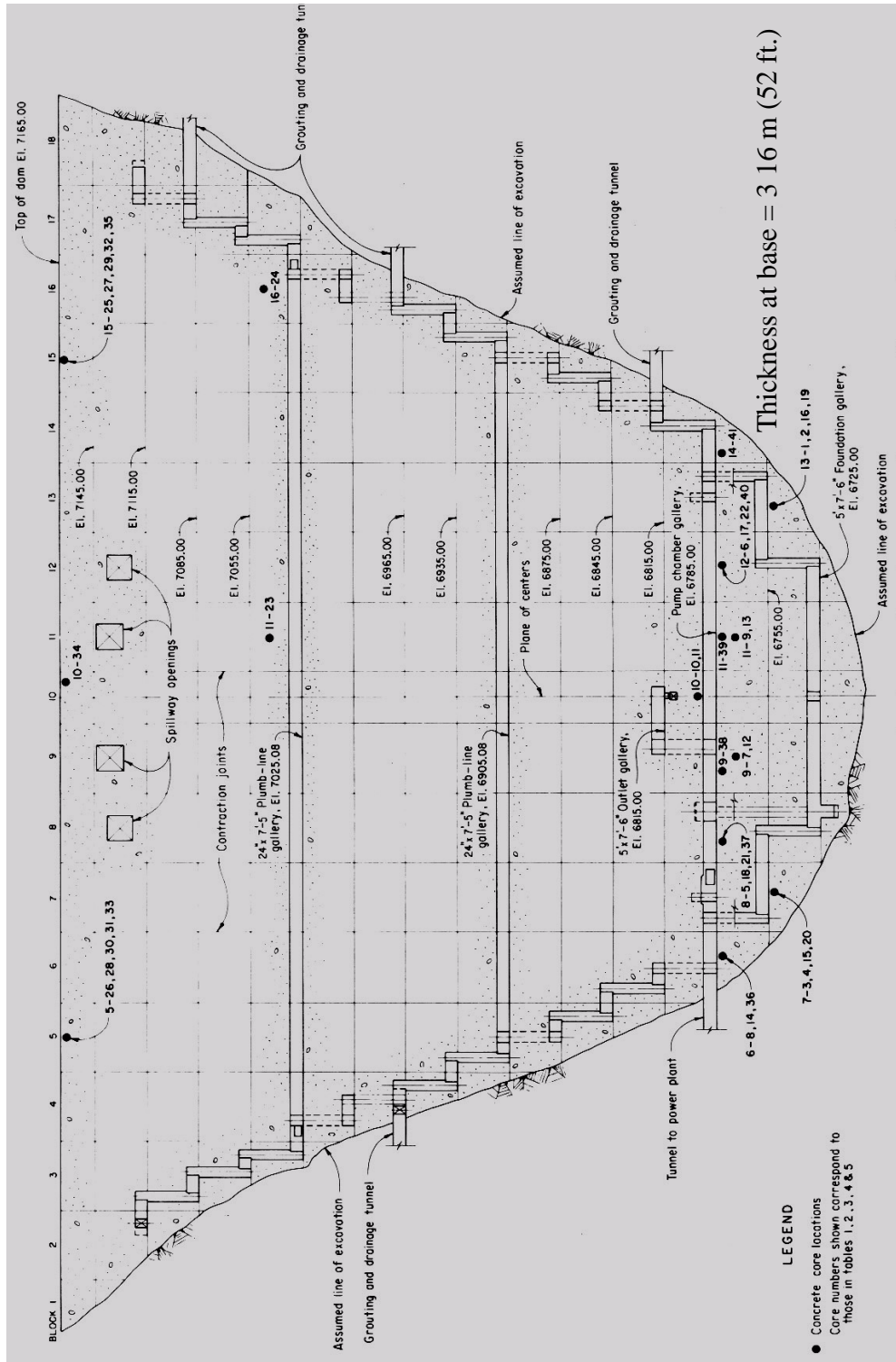


FIGURE 18. Construction photo of the Morrow Point Dam.





Thickness at height = 3.7 m (12 ft.)



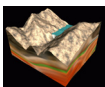
143 m
(468 ft.)

FIGURE 19. Morrow Point Dam elevation view.

3.1 Discrete Element Contraction Joint Model

During the first phase of this study, the modeling of the contraction joints included utilizing various combinations of contact surface models and discrete elements (i.e. essentially a two force member which applies a user specified force - displacement relationship between two specified nodes) to model the contact and connectivity across the expansion joint. A requirement of the contraction joint model was that the contraction joints allow free relative motion in a vertical direction between adjacent dam segments as the gravity dead load was applied. This relative motion prevents the generation of large vertical direction shear stresses which transfer large loads to the upper abutment region of the dam - which the actual construction process prevents. For the dead load initialization, a model was constructed for the NIKE3D implicit finite element program. The contraction joints were modeled with frictionless contact surfaces for the NIKE3D initialization. This prevents friction between adjacent blocks as the dead loads are applied and does not allow inter-block vertical shears to develop. To obtain displacement compatibility in the direction normal to the dam, discrete elements were placed across each interface to transfer stresses between blocks in the normal direction. The discrete elements only allowed compression, so that tensile forces were not generated across the contraction joints if they were to open. Figure 21 describes in detail how the discrete elements were used in conjunction with the sliding interfaces for both the NIKE3D and DYNA3D models. Ten discrete springs - five for each side - were modeled approximately every 30 vertical feet along each vertical contraction joint. In addition, during the NIKE3D static initialization, a “sliding with voids” interface without friction was used along the contraction joints. The springs were modeled such that they could not resist loads in tension, but they could resist loads in compression. In compression, they were given an extremely high stiffness of $1.0\text{E}+09$ lbs/in. in order to resist the compression forces when the dam blocks or contraction joints were placed in shear. The sliding interface was used so that penetration of the contraction joints would not occur. During the seismic analysis, a friction value of 0.3 was used between the vertical joints.

Small deformation contact problems can be numerically challenging for implicit programs with penalty based contact algorithms. Careful validation must be carried out for a particular problem to ensure the contact surface can open freely, without sticking, and that appropriate compatibility between adjacent segments is obtained when the surfaces come into contact. The ability of the NIKE3D contact surfaces to perform as intended was carefully validated with a series of push-pull tests for segments of the dam structure. The contact surfaces were subjected to a series of opening and closing cycles to validate the performance as indicated in Figure 23. With appropriate penalty stiffnesses and nonlinear iteration convergence tolerances, the NIKE3D contact surfaces worked quite well for normal contact. The performance of the joint model in the direction tangent to the joint is shown in Figure 22, and the appropriate compatibility in the direction tangent to the surface is correctly represented.



NIKE3D/DYNA3D Joint Model

- Slide Surface Type 3: Sliding with Gaps
- Slide Surface Friction: 0.0 for NIKE3D and 0.3 for DYNA3D
- Discrete Springs modeled between joints: 10 springs modeled every 30 ft. (vertically)

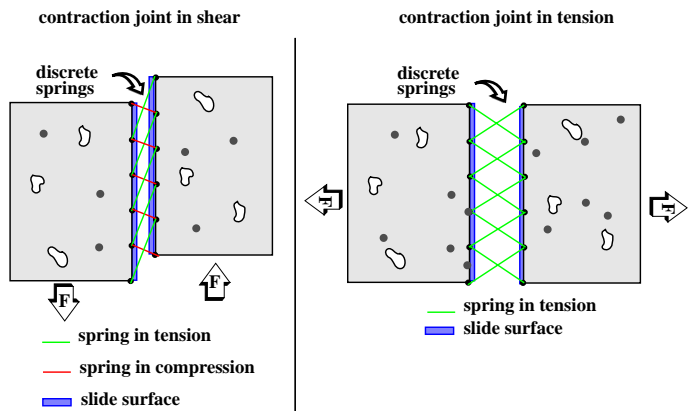
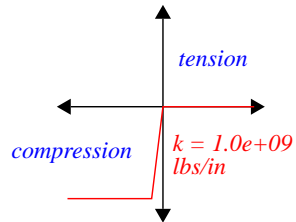
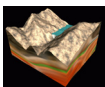


FIGURE 21. NIKE3D and DYNA3D vertical contraction joint modeling.



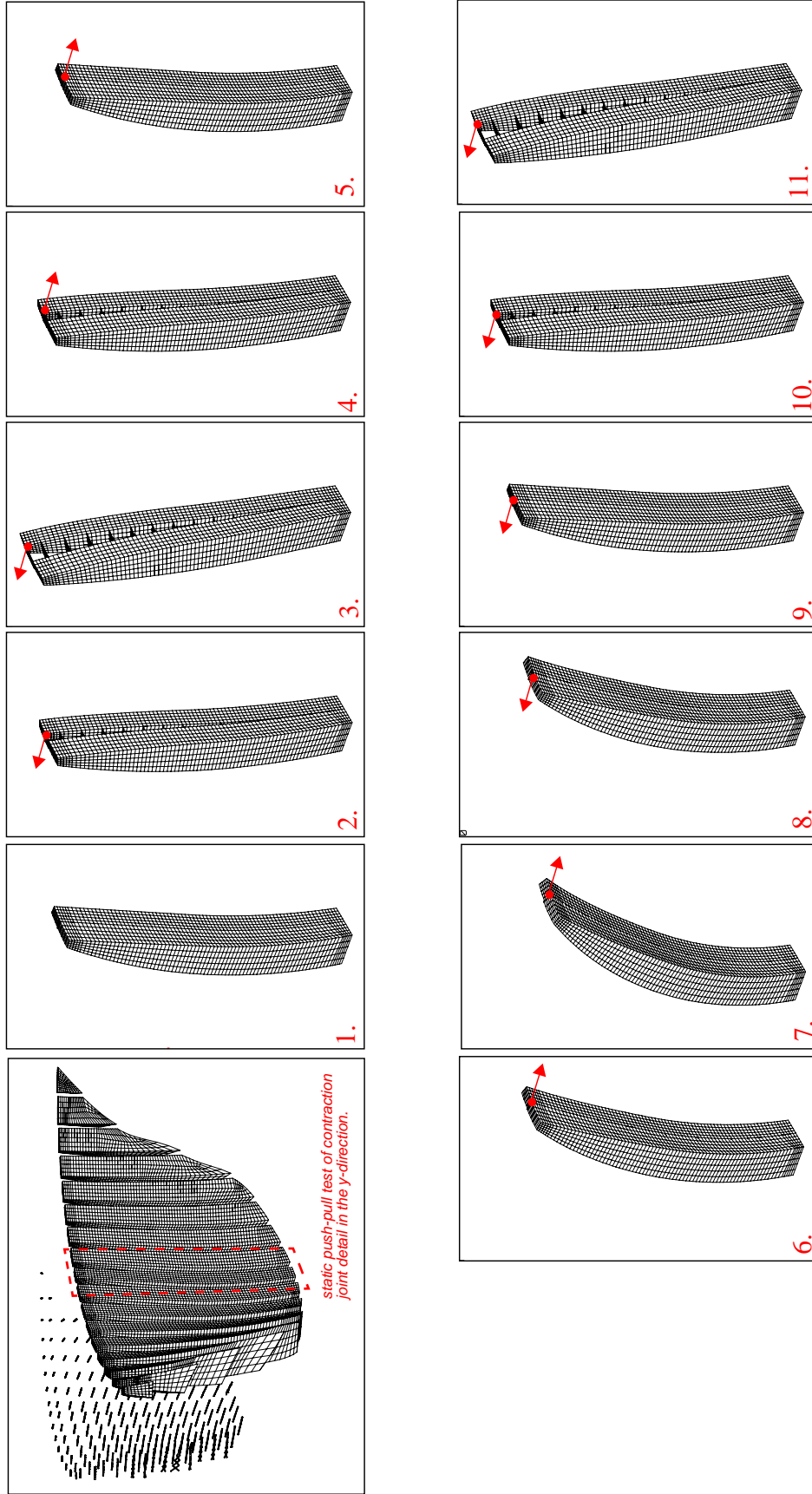
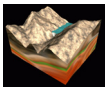


FIGURE 22. NIKE3D model of a contraction joint cycled through opening and closing in the direction tangent to the surface.

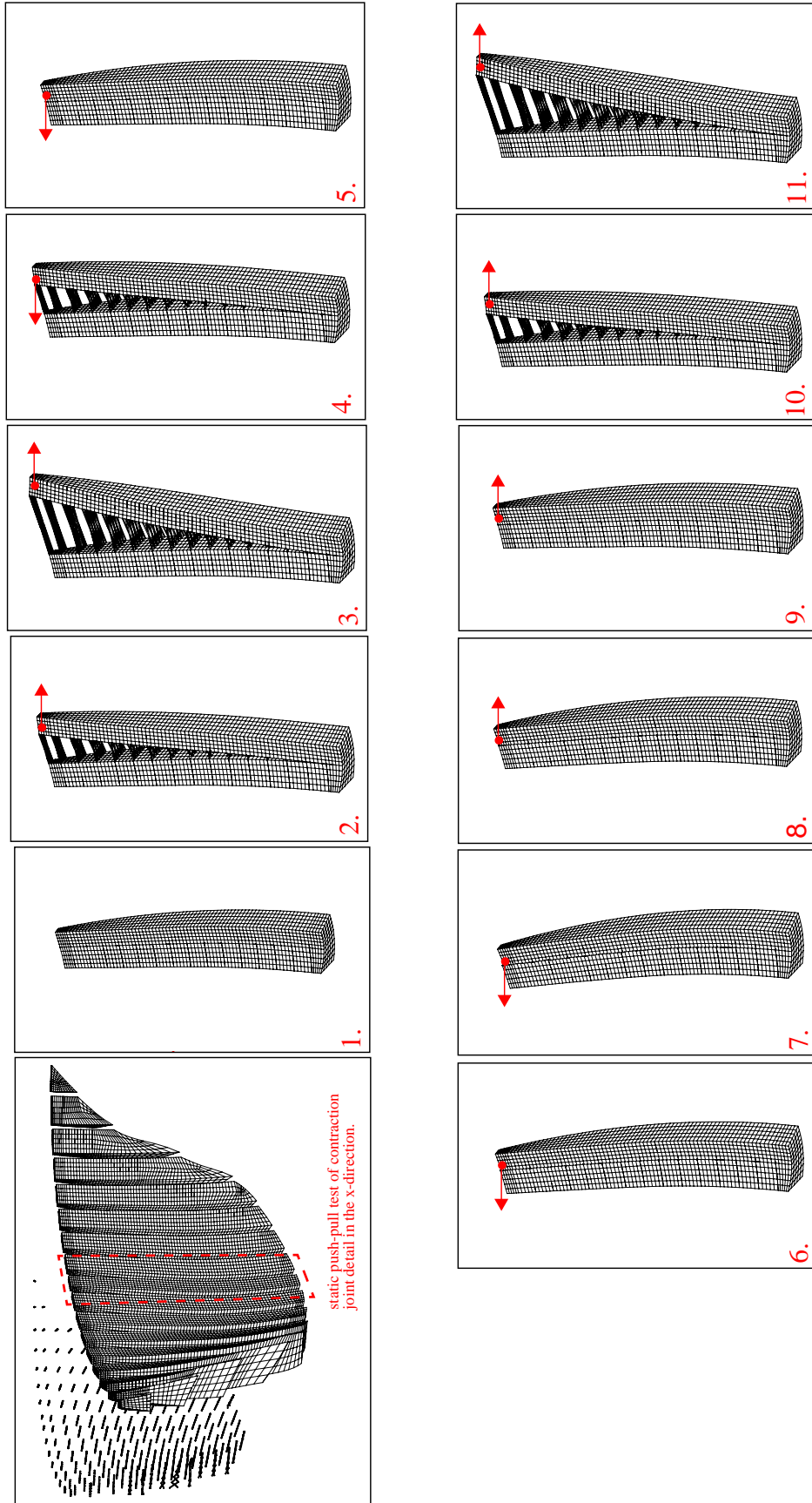
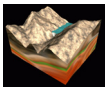


FIGURE 23. NIKE3D model of a contraction joint cycled through opening and closing in the direction normal to the surface.

3.2 Contact Algorithm for Beveled Contraction Joints

Although the discrete element representation for the contraction joints worked very well, they still could not represent the true behavior of the contraction joints. Due to the geometry of the shear keys, if a slight opening formed along a contraction joint, the vertical blocks could move in the upstream-downstream direction only a little before contacting the shear keys again. In reality, a 6 inch opening would have to occur before the joints could freely move in the upstream-downstream direction. The discrete elements could not model this behavior. If an opening occurred along a joint, the blocks were virtually free to move in the upstream-downstream direction. Therefore, one of the objectives of Phase 1 was to modify the existing NIKE3D and DYNA3D contact surfaces to allow appropriate modeling of the available shear transfer across the contraction joints.

A finite element formulation has been proposed and implemented by Lau, et. al. [Ref 7] for the case of rectangular cross-section keys. For keys of rectangular cross-section, the kinematics are much simplified because lateral motion is prohibited even when the joint is partially open. In the case of beveled cross-sections, the joint may move a restricted amount laterally as a function of the joint separation.

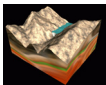
The following presents the formulation of a contraction joint model for the analysis of beveled contraction joints, based upon the general mechanics and resulting finite element implementation used in NIKE3D.

3.3 General Contact Mechanics

Consider contact between two bodies B^α , α running from 1 to 2. Let the position of a material point in the reference configuration for body B^α be denoted by X^α . One has that $X^\alpha \subset \Omega_0^\alpha$, where Ω_0^α is open on set of points in \mathfrak{R}^n ($n = 2$ or 3) defining the reference configuration at time t_0 .

The motion $x^\alpha = \chi^\alpha(X^\alpha, t)$ maps points in the reference configuration Ω_0^α into points in the current configuration Ω^α , another open set of points in \mathfrak{R}^n , at time t . The motion is assumed to be smooth and invertible, that is $J^\alpha = \det(\mathbf{F}^\alpha) > 0$, where $\mathbf{F}^\alpha = \frac{\partial}{\partial X^\alpha} \chi^\alpha(X^\alpha, t)$. The boundary of each body is denoted by $\partial\Omega^\alpha$ with outward unit normal \mathbf{n}^α .

The bodies are equipped with a mass density ρ^α and a constitutive response σ^α , which is a function of $\chi^\alpha(X^\alpha, t)$ its derivatives, and its time history. It is assumed that mass is conserved, such that $\rho_0 = \rho|_{t_0} = \rho J$. For each body the boundary may be partitioned into



sections Γ_t^α and Γ_u^α where $\Gamma_t^\alpha \cup \Gamma_u^\alpha = \partial\Omega^\alpha$. Note that one does not have necessarily that $\Gamma_t^\alpha \cap \Gamma_u^\alpha = \emptyset$.

Given prescribed boundary tractions \mathbf{t}^α on Γ_t^α , prescribed displacements $\bar{\mathbf{u}}^\alpha$ on Γ_u^α , and a prescribed body force \mathbf{b}^α over Ω^α the equations of motion can be written

$$\begin{aligned} \operatorname{div}(\boldsymbol{\sigma}) + \rho \mathbf{b} &= \rho \dot{\mathbf{x}}^\alpha \in \Omega^\alpha \\ \boldsymbol{\sigma}^\alpha \cdot \mathbf{n}^\alpha &= \mathbf{t}^\alpha \quad \text{on} \quad \Gamma_t^\alpha \\ \mathbf{x}^\alpha &= \bar{\mathbf{x}}^\alpha \quad \text{on} \quad \Gamma_u^\alpha \end{aligned} \quad (\text{EQ 7})$$

A weighted-residual form of the above equations can be written, for \mathbf{x}^α satisfying EQ. 7a a-priori, as

$$\int_{\Omega^\alpha} -\boldsymbol{\sigma}^\alpha \cdot \operatorname{grad}(\mathbf{w}^\alpha) + \rho^\alpha \mathbf{b}^\alpha \cdot \mathbf{w}^\alpha d\Omega + \int_{\Gamma_t^\alpha} \mathbf{t}^\alpha \cdot \mathbf{w}^\alpha d\Gamma = \int_{\Omega^\alpha} \rho \dot{\mathbf{x}}^\alpha d\Omega \forall \mathbf{w}^\alpha \quad (\text{EQ 8})$$

For certain choices of boundary tractions and constitutive laws, EQ. 8 is derivable from an energy functional by setting $\mathbf{w}^\alpha = \delta \mathbf{x}^\alpha$, the first variation of the motion.

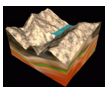
The contact constraint arises from the principle of impenetrability of matter, which states that one must have $\Omega^\alpha \cap \Omega^\beta = \emptyset$ for all time. However, one may have $\partial\Omega^\alpha \cap \partial\Omega^\beta \neq \emptyset$. Define $\Gamma_c = \partial\Omega^\alpha \cap \partial\Omega^\beta$.

General contact mechanics constructs a function g^α upon each surface $\partial\Omega^\alpha$ to measure the relative satisfaction of the constraint at a particular point $\mathbf{x}^\alpha \in \partial\Omega^\alpha$. There are various ways of defining such a function. In general the function must satisfy:

$$\begin{aligned} g^\alpha > 0 &\leftrightarrow (\Omega^\alpha \cap \Omega^\beta = \emptyset, \partial\Omega^\alpha \cap \partial\Omega^\beta = \emptyset) (\text{out-of-contact}) \\ g^\alpha = 0 &\leftrightarrow (\Omega^\alpha \cap \Omega^\beta = \emptyset, \partial\Omega^\alpha \cap \partial\Omega^\beta \neq \emptyset) (\text{contact}) \\ g^\alpha < 0 &\leftrightarrow (\Omega^\alpha \cap \Omega^\beta \neq \emptyset) (\text{penetration}) \end{aligned} \quad (\text{EQ 9})$$

One typical choice (and that used here) is the “closest-point projection”

$$g^\alpha = (\mathbf{x}^\alpha - \mathbf{x}^\beta) \cdot \mathbf{n}^\beta \text{ such that } (\mathbf{x}^\alpha - \mathbf{x}^\beta) \times \mathbf{n}^\beta = 0. \quad (\text{EQ 10})$$



The point \mathbf{x}^β projected from the surface point \mathbf{x}^α along the normal \mathbf{n}^β is called the normal projection from \mathbf{x}^α and denoted by $\mathbf{x}^\beta = \pi^\alpha(\mathbf{x}^\alpha)$. Note that one has the referential material coordinate \mathbf{X}^β defined by the projection π^α (holding \mathbf{X}^α fixed) as

$$\mathbf{X}^\beta = \chi^{-1}(\pi^2(\mathbf{x}^1), t) \quad (\text{EQ 11})$$

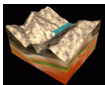
The portion of the boundary where $g^\alpha = 0$ is denoted by Γ_c^α . Note that

$$\begin{aligned} \mathbf{x}^1 \neq (\mathbf{x}^1)' &= \pi^\beta(\pi^\alpha(\mathbf{x}^1)) \text{ when } g^\alpha \neq 0 \text{ (in general),} \\ g^\alpha(\mathbf{x}^1) &\neq g^\beta(\pi^\alpha(\mathbf{x}^1)) \text{ when } g^\alpha \neq 0 \text{ (in general),} \\ \mathbf{x}^1 &= (\mathbf{x}^1)' = \pi^\beta(\pi^\alpha(\mathbf{x}^1)) \text{ when } g^\alpha = 0, \\ g^\alpha(\mathbf{x}^1) &= g^\beta(\pi^\alpha(\mathbf{x}^1)) \text{ when } g^\alpha = 0. \end{aligned} \quad (\text{EQ 12})$$

Note that $\Gamma_c^\alpha = \Gamma_c^\beta$. In general Γ_c^α is not known beforehand. A portion of Γ_t^α is denoted by Γ_p^α , the region of “potential contact” such that it is assumed that $\Gamma_c^\alpha \subset \Gamma_p^\alpha$ always. Note that because Γ_c^α is unknown beforehand, and is in general a function of time, Γ_p^α . Note that $\Gamma_p^\beta \neq \Gamma_p^\alpha$ unless it is possible to set $\Gamma_p^\alpha = \Gamma_c^\alpha = \Gamma_c$ a-priori, that is Γ_c is known beforehand.

A pressure p^α is developed over Γ_p^α that resists penetration, and satisfies (in the absence of cohesion) $p^\alpha > 0$, $p^\alpha g^\alpha = 0$, that is the pressure is always positive, and is zero outside Γ_c^α , the actual region of contact. The resulting surface traction vector is $-p^\alpha \mathbf{n}^\alpha$. Balance of linear momentum across $\Gamma_c = \Gamma_c^\alpha = \Gamma_c^\beta$ implies that here $p^\alpha = p^\beta = p$, because when $g = g^\alpha = g^\beta = 0$ it can be shown for smooth surfaces that $\mathbf{n}^\alpha = -\mathbf{n}^\beta$. Because of the relationship between g^α and g^β , one can similarly construct a single pressure function p that satisfies $p g^\alpha = p g^\beta = 0$.

If friction is present, a tangential traction t_T is also developed to resist relative sliding. Typically t_T is modelled using a constitutive law similar to that used for plasticity. Up until some threshold value, t_T acts as a Lagrange multiplier to prevent relative sliding.



Define V_T , the referential velocity of X^2 as it slides past the contact point defined by X^1 , and the corresponding referential tangential stress T_T

$$\begin{aligned} V_T &= \frac{d[\chi^{-1}(\pi^1(x^1), t)]}{dt} \Big|_{x^1} \\ T_T &= t_T \cdot F \end{aligned} \quad (\text{EQ 13})$$

In the friction theory presented in [Ref 9] and utilized in NIKE3D, the following constitutive assumption is made, where a penalty regularization of the frictional stick constraint is implemented:

$$\begin{aligned} \|\Phi\| &= \|T_T\| - \mu p \geq 0 \\ V_T - \zeta \frac{T_T}{\|T_T\|} &= \frac{1}{\varepsilon} \left(\frac{dT_T}{dT} \right) \\ \zeta &\geq 0 \\ \Phi \zeta &= 0 \end{aligned} \quad (\text{EQ 14})$$

Define δX^2 as the variational change in X^2 , the material point on surface 2 determined by the projection $\pi^1(x^1)$, that is

$$\delta X^2 = \delta t V_T = \delta[\chi^{-1}(\pi^1(x^1), t)] \Big|_{x^1} \quad (\text{EQ 15})$$

Then, as in [Ref 9], the variational form for the equations of motion can be written

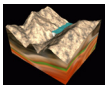
$$\begin{aligned} \sum_{\alpha=1}^2 \int_{\Omega^\alpha} -\sigma^\alpha \cdot \text{grad} \delta x^\alpha + \rho b^\alpha \cdot \delta x^\alpha d\Omega^\alpha - \int_{\Gamma_t^\alpha} \dot{t}^\alpha \cdot \delta x^\alpha d\Gamma &= \int_{\Gamma_p} p \delta g + T_T \delta X^2 d\Gamma \\ \int_{\Gamma_p} \delta p g d\Gamma &\geq 0 \end{aligned} \quad (\text{EQ 16})$$

3.4 Modelling Small-Scale Surface Features

When it is not desirable, either because of computational limitations or in the quest for simplification, to model interface geometry directly, one may replace the constraint function g in equations EQ. 16 with some other constraint function. In this way, one can model the gross geometry of the contact interface as a smooth body. In general, one would have

$$\hat{g} = f(g, x^1, X^1, F^1, x^2, X^2, F^2, t) \quad (\text{EQ 17})$$

The function \hat{g} may serve to model the evolution and/or interaction of asperities, the behavior of surface layers (gaskets, etc.), and/or the presence of boundary lubrication. For



instance, one may model the presence of a (comparatively) hard thin layer of constant thickness d covering a (comparatively) soft interior by modelling the deformation of the soft interior and setting

$$\hat{g} = g - d \quad (\text{EQ 18})$$

The enforcement of $\hat{g} = 0$ effectively forces the two surfaces to be separated by a constant amount d .

One complicating factor in the introduction of a function \hat{g} is the fact that one may or may not have (depending on the form of \hat{g})

$$\hat{g}(x^\alpha) = 0 \leftrightarrow \hat{g}^\beta(\pi^\alpha(x^\alpha)) = 0 \quad (\text{EQ 19})$$

Unfortunately, in general except when the surfaces are parallel, the projection $\pi^1(x^1)$ is not one-one (see EQ. 12). Effectively, then, the requirement of EQ. 19 restricts the function \hat{g} to the form of EQ. 18.

Since this is too restrictive, it is necessary to choose \hat{g} to be based explicitly on either g^α or g^β . For subsequent developments, it will be assumed that the choice of surface 1, $g = g^1$, and the projection $x^2 = \pi^1(x^1)$ has been made. Explicit reference to g^1 , \hat{g}^1 will henceforth not be made for simplicity. Define

$$\Gamma_k \subset \Gamma_p^1 \text{ such that } \hat{g} = \{\hat{g}(g^1(x^1), X^1, X^2), x^1 \in \Gamma_k\} \quad (\text{EQ 20})$$

where subsequent attention is focused on a function of the form,

$$\hat{g}^1 = f(g^1, X^1, X^2, t) \quad (\text{EQ 21})$$

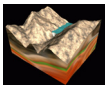
The dependence on the reference coordinates X^1, X^2 provides the ability to model surface asperities, and t allows these asperities to evolve as a function of time.

With \hat{g} of the form of EQ. 21 the weighted-residual form (without friction) follows as

$$\sum_{\alpha=1}^2 \int_{\Omega^\alpha} \Omega^\alpha - \sigma^\alpha \cdot \text{grad} \delta x^\alpha + \rho b^\alpha \cdot \delta x^\alpha d\Omega^\alpha - \int_{\Gamma_t^\alpha} i^\alpha \cdot \delta x^\alpha d\Gamma = \int_{\Gamma_k} p \left(\frac{\partial}{\partial g} \hat{g} \delta g + \frac{\partial}{\partial X^2} \hat{g} \delta X^2 \right) d\Gamma \quad (\text{EQ 22})$$

$$\int_{\Gamma_k} \delta p \hat{g} d\Gamma \geq 0$$

In the above δX^2 represents the change in the reference coordinate X^2 arising from the projection $x^2 = \pi(x^1)$:



$$\delta X^2 = \delta[\chi^{-1}(\pi^1(x^1), t)]|_{x^1} \quad (\text{EQ 23})$$

Assuming \hat{g} is formulated with respect to surface 1, $\delta X^1 = 0$ a-priori.

3.5 Modelling Friction

In order to incorporate friction into the model, it is necessary to consider slip tangential to the $\hat{g} = 0$ plane. Therefore, it is necessary to define this tangent plane. Again restricting attention to \hat{g} of the form of EQ. 21, fix attention to a particular material point X^1 . Assume that $\hat{g} = 0$ initially, and take the variation of \hat{g} using EQ. 21:

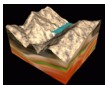
$$\delta \hat{g} = \frac{\partial f}{\partial g} \delta g + \frac{\partial f}{\partial X^2} \delta X^2 \quad (\text{EQ 24})$$

where δX^2 is determined by EQ. 23. Note that $\delta X^1 = 0$ a-priori because \hat{g} is defined with respect to material points on surface 1.

Let

$$\|\partial f\| = \left(\left(\frac{\partial f}{\partial g} \right)^2 + \left\| \frac{\partial f}{\partial X^2} \right\|^2 \right)^{\frac{1}{2}} \quad (\text{EQ 25})$$

Now define the tangent variational directions \hat{T}^γ and the normal variational direction \hat{N} with reference to $(\delta g, \delta X^2)$:

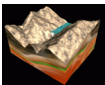


$$\begin{aligned}
\hat{T}^1 &= \frac{\left[0, N^2 \times \frac{\partial f}{\partial X^2} \right]}{\left\| \frac{\partial f}{\partial X^2} \right\|} \\
\hat{T}^2 &= \frac{\left[-\left\| \frac{\partial f}{\partial X^2} \right\|, \left(\frac{\partial f}{\partial g} \right) \frac{\partial f}{\partial X^2} \right]}{\left(\left\| \frac{\partial f}{\partial X^2} \right\|^2 \left(1 + \left(\frac{\partial f}{\partial g} \right)^2 \right) \right)^{\frac{1}{2}}} \\
\hat{N} &= \frac{\left[\frac{\partial f}{\partial g}, \frac{\partial f}{\partial X^2} \right]}{\left\| \frac{\partial f}{\partial g} \right\|}
\end{aligned} \tag{EQ 26}$$

Note that

$$\begin{aligned}
[D\hat{g}, \delta\lambda\hat{T}^1] &= \delta\lambda \left[\frac{\partial f}{\partial g}, \frac{\partial f}{\partial X^2} \right]^T \hat{T}^1 = 0 \\
[D\hat{g}, \delta\lambda\hat{T}^2] &= \delta\lambda \left[\frac{\partial f}{\partial g}, \frac{\partial f}{\partial X^2} \right]^T \hat{T}^2 = 0 \\
[D\hat{g}, \delta\lambda\hat{N}] &= \delta\lambda \left[\frac{\partial f}{\partial g}, \frac{\partial f}{\partial X^2} \right]^T \hat{N} = \delta\lambda \neq 0 \\
[\hat{T}^1, \hat{T}^1] &= 1 \\
[\hat{T}^2, \hat{T}^2] &= 1 \\
[\hat{N}, \hat{N}] &= 1 \\
[\hat{T}^1, \hat{T}^2] &= 0 \\
[\hat{T}^1, \hat{N}] &= 0 \\
[\hat{T}^2, \hat{N}] &= 0
\end{aligned} \tag{EQ 27}$$

Remembering from EQ. 16, in a friction scheme for standard contact the contribution by the frictional tractions is $T \cdot \delta X^2 = \delta t T \cdot V_T$. Analogous to this, define the two components of the referential slip velocity as (fixing the material point X^1) as



$$\begin{aligned}\hat{V}^1 &= [\dot{g}, \dot{X}^2]^T \hat{T}^1 \\ \hat{V}^2 &= [\dot{g}, \dot{X}^2]^T \hat{T}^2\end{aligned}\tag{EQ 28}$$

Then one can write the variational slip distances with \hat{s}_γ as

$$\begin{aligned}\delta \hat{s}_1 &= \delta t \hat{V}_1 = [\delta g, \delta X^2]^T \hat{T}^1 \\ \delta \hat{s}_2 &= \delta t \hat{V}_2 = [\delta g, \delta X^2]^T \hat{T}^2\end{aligned}\tag{EQ 29}$$

Now, in the same fashion as T_T in EQ. 13 one can introduce \hat{T}_T with components \hat{T}_1 and \hat{T}_2 and norm $\|\hat{T}\| = (\hat{T}^1)^2 + (\hat{T}^2)^2$ such that a frictional law analogous to EQ. 14 can be written

$$\begin{aligned}\|\Phi\| &= \|\hat{T}\| - \mu \|\partial f\| p \geq 0 \\ \hat{V}_\gamma - \zeta \frac{\hat{T}_\gamma}{\|\hat{T}\|} &= \frac{1}{\varepsilon} \left(\frac{d\hat{T}_\gamma}{dT} \right) \\ \zeta &\geq 0 \\ \Phi \zeta &= 0\end{aligned}\tag{EQ 30}$$

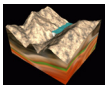
Note that in EQ. 30, the response p has been multiplied by $\|\partial f\|$, in order to use something analogous to the actual contact pressure.

Having defined these quantities, the weighted-residual form with friction can be written

$$\begin{aligned}\sum_{\alpha=1}^2 \int_{\Omega^\alpha} \Omega^\alpha - \sigma^\alpha \cdot \text{grad} \delta x^\alpha + \rho b^\alpha \cdot \delta x^\alpha d\Omega^\alpha - \int_{\Gamma_t^\alpha} i^\alpha \cdot \delta x^\alpha d\Gamma = \\ \int_{\Gamma_k} p \left(\frac{\partial}{\partial g} \hat{g} \delta g + \frac{\partial}{\partial X^2} \hat{g} \delta X^2 + \hat{T}_\gamma [\delta g, \delta X^2]^T \hat{T}^\gamma \right) d\Gamma \\ \int_{\Gamma_k} \delta p \hat{g} d\Gamma \geq 0\end{aligned}\tag{EQ 31}$$

3.6 Modelling the Contraction Joint

Section 3.4 on page 47 provided the general basis for constructing a function \hat{g} . Lau, et. al. [Ref 7] constructed a suitable model for a contraction joint with square keys. This effectively limited the motion (up until complete separation) to purely transverse motion. This paper is concerned with more general forms of the contraction joint, in which partial separation allows for motion in both the lateral and transverse directions.



Concrete arch dams are constructed with vertical contraction joints separating the concrete monoliths that make up the dam Figure 28. The joints are planar, running approximately in the radial direction. In the kinds of joints this paper is concerned with, the contraction joints are beveled structures with the bevels of constant, approximately sinusoidal cross-section when viewed from the top, which allow the concrete monoliths to slide vertically but not laterally (see Figure 29) when the joint is completely closed. However, limited lateral motion is possible if the joint becomes partially open.

The following assumptions will therefore be made regarding \hat{g} . Define T_s (Figure 28) as the direction along which the keys are allowed to slide relative to one another. Define T_k as the direction along which the keys constrain the slide surface (see Figure 29). Note that

- (1) T_s and T_k are referential quantities.
- (2) For each arch dam T_s is a constant, independent of the slideline.
- (3) For each arch dam T_k is constant for each slideline, but T_k for one slideline may be different than T_k for another slideline.

Hence, along each slidesurface one can define at a particular contact point, given the referential coordinates X^1 and X^2 , the quantities

$$\begin{aligned} s_1^\alpha &= X^\alpha \cdot T_s \\ s_2^\alpha &= X^\alpha \cdot T_k \end{aligned} \tag{EQ 32}$$

Then, since the height of the keys is dependent only on the position relative to the T_k direction, one has the general form for \hat{g} as

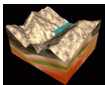
$$\hat{g} = f(g, s_2^1, s_2^2) \tag{EQ 33}$$

Now consider Figure 30, which represents a one-dimensional slice of a particular slidesurface in the reference configuration. Each slidesurface has a sinusoidal variation about the midsurface with amplitude A^α , period $2\frac{\pi}{B}$, and phase C^α , such that the distance d^α above or below the midsurface α is

$$d^\alpha = A^\alpha \cos(B^\alpha s_2^\alpha + C^\alpha) \tag{EQ 34}$$

In the reference configuration, one has $s_2^1 = s_2^2 = s$ and the mid-surfaces of the two slidesurfaces coincide, such that

$$d^\alpha(s) + d^\beta(s) = 0 \forall s \tag{EQ 35}$$



This is true of $A^1 = -A^2 = A$, $B^1 = B^2 = B$, and $C^1 = C^2 = C$. For simplicity, set $C = 0$. Therefore, when the two surfaces are parallel one can write the vertical distance between the two surfaces as

$$d = g - d^1 - d^2 = g - A \cos(Bs_2^1) + A \cos(Bs_2^2) \quad (\text{EQ 36})$$

Note that in the reference configuration $g = d = 0$. This suggests the following restriction for \hat{g}

$$\hat{g}(g, s_2^1, s_2^2) = g \text{ when } s_2^1 = s_2^2 \quad (\text{EQ 37})$$

Now consider Figure 31. The slidesurfaces have moved vertically away from each other but remain parallel, such that their mid-surfaces are a constant distance g away from each other. The mid-surfaces have not stretched, however, they have displaced laterally, such that the value $d = s_2^2 - s_2^1$ is constant. As in the figure, as a first cut, take \hat{g} as equal to d in EQ. 36, that is

$$\hat{g} = g - A(\cos(Bs_2^1) - \cos(Bs_2^2)) \quad (\text{EQ 38})$$

As expected, this function satisfies the requirements of EQ. 33 and EQ. 37.

By inspection it is easy to see that for constant g and parallel surfaces, one cannot have $\hat{g} = \text{constant} = 0$ for \hat{g} of the form of EQ. 38. Given the restriction $\hat{g} = 0$ and assuming constant g , one has as a function of $D = s_2^2 - s_2^1$ that [Figure 32]

$$g = 2A \left| \sin\left(\frac{BD}{2}\right) \right| \quad (\text{EQ 39})$$

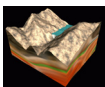
where $\hat{g} = 0$ occurs at $\frac{2\pi}{B}$ intervals of

$$s_1 = \frac{\pm\pi - BD}{2B} \quad (\text{EQ 40})$$

Since the goal of the modelling is to allow for the behavior of the shear keys to in some manner be accounted for even though the contact discretization is much coarser than their frequency, it may not be desirable to use a function \hat{g} of the form of EQ. 38, since for uniform sliding with a coarse mesh, the contact points where EQ. 40 may not be resolved, and hence the uniform g of EQ. 39 may not be determined.

Alternatively, consider the following possibilities

$$\hat{g} = g - 2A \left| \sin(B(s_2^2 - s_1^2)) \right| \quad (\text{EQ 41})$$



$$\hat{g} = g - A(1 - \cos(s_2^2 - s_2^1)) \quad (\text{EQ 42})$$

EQ. 41 identically tracks EQ. 39 for $\hat{g} = 0$, and satisfies restrictions (EQ. 33) and (EQ. 37). However, it has non-smooth derivatives at $s_2^2 = s_2^1$, and hence is difficult to use in implicit calculations where this retards convergence since the stiffness matrix is non-smooth (as numerical experiments have confirmed). The alternative of EQ. 42 provides a rough simulation of the behavior of EQ. 41 without the non-smoothness. The difference between EQ. 42 and EQ. 41 is illustrated by Figure 33. Other possibilities would be smooth approximations (better than EQ. 42) of EQ. 41.

Since in all three cases \hat{g} is a function of s_2^α only, the directions are simplified to

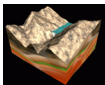
$$\begin{aligned} \hat{T}^1 &= [0, T_s] \\ \hat{T}^2 &= \frac{\left[-\frac{\partial f}{\partial s_2^2}, \frac{\partial f}{\partial g} T_k \right]}{\|\partial f\|} \\ \hat{N} &= \frac{\left[\frac{\partial f}{\partial g}, \frac{\partial f}{\partial s_2^2} T_k \right]}{\|\partial f\|} \end{aligned} \quad (\text{EQ 43})$$

The weighted-residual form can therefore be simplified to

$$\begin{aligned} \sum_{\alpha=1}^2 \int_{\Omega^\alpha} \Omega^\alpha - \sigma^\alpha \cdot \text{grad} \delta x^\alpha + \rho b^\alpha \cdot \delta x^\alpha d\Omega^\alpha - \int_{\Gamma_i^\alpha} i^\alpha \cdot \delta x^\alpha d\Gamma = \\ \int_{\Gamma_k} p \left(\frac{\partial}{\partial g} \hat{g} \delta g + \frac{\partial}{\partial s_2^2} \hat{g} \delta s_2^2 + \hat{T}_1 \delta s_1^2 + \hat{T}_2 [\delta g, \delta s_2^2 T_k]^T \hat{T}^2 \right) d\Gamma \\ \int_{\Gamma_k} \delta p \hat{g} d\Gamma \geq 0 \end{aligned} \quad (\text{EQ 44})$$

3.7 Finite Element Implementation

The formulation was implemented into NIKE3D and DYNA3D as an option to slideline type 3. Users input T_s , A , B , and whether they wish to use \hat{g} of the form of EQ. 42 (method 1), EQ. 41 (method 2), or EQ. 38 (method 3). For each slideline a two-pass algorithm is used, where contact is calculated alternatively taking the master or the slave surface as surface 1.



As described in [Ref 14], contact in NIKE3D is enforced via a penalty method. The same penalty method is used here, except that \hat{g} is substituted for g , that is

$$p = \epsilon_N \langle \hat{g} \rangle \quad (\text{EQ 45})$$

Nodal collocation is used for the integrals along the surface Γ_k such that for N_c the number of contact nodes

$$\int_{\Gamma_k} p \left(\frac{\partial}{\partial g} \hat{g} + \frac{\partial}{\partial s_2^2} \hat{g} \delta s_2^2 + \hat{T}_1 \delta s_1^2 + \hat{T}_2 [\delta g, \delta s_2^2 T_k]^T \hat{T}^2 \right) d\Gamma =$$

$$\sum_{I=1}^{N_c} w^I \left\{ p \left(\frac{\partial}{\partial g} \hat{g} \delta g + \frac{\partial}{\partial s_2^2} \hat{g} \delta s_2^2 + \hat{T}_1 \delta s_1^2 + \hat{T}_2 [\delta g, \delta s_2^2 T_k]^T \hat{T}^2 \right) \right\} \Big|_{\text{node I}} \quad (\text{EQ 46})$$

where the weight functions w^I are arbitrarily taken to be 1.

As in [Ref 14], the frictional stress is updated in NIKE3D and DYNA3D using a predictor-corrector algorithm. One first computes a trial state

$$p_{n+1} = \epsilon_N \langle \hat{g}_{n+1} \rangle$$

$$[\hat{T}_\gamma]_{n+1} = [\hat{T}_\gamma]_n + \epsilon [(g_{n+1} - g_n), ([X^2]_{n+1} - [X^2]_n)^T [\hat{T}^\gamma]_n] \quad (\text{EQ 47})$$

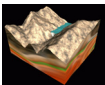
$$(\Phi_{n+1})^{\text{trial}} = \|\hat{T}\| - \mu \|\partial f\|_n p_{n+1}$$

Note that \hat{T}^γ and $\|\partial f\|$ are calculated with respect to time n to simplify the resulting equations and provide for better linearization. It should be noted that in the standard contact algorithm it is necessary to project T_T calculated at time n onto the new metric at time $n+1$. Since T_s and T_k remain constant across a slideline, this is not necessary here.

The slip condition $(\Phi_{n+1})^{\text{trial}}$ is then checked. If it is not violated, the trial values of \hat{T}_γ are accepted, else the following return-mapping algorithm is implemented for the slip state

$$\hat{T}_\gamma = \frac{\mu \|\partial f\|_n p_{n+1}}{(\|\hat{T}\|_{n+1})^{\text{trial}}} (\hat{T}_\gamma)^{\text{trial}} \quad (\text{EQ 48})$$

The contact residual and stiffness follow from the developments in [Ref 14] with the following notes



$$\begin{aligned}
\delta s_1^2 &= T_s \cdot \frac{\partial X^2}{\partial \xi^\alpha} \delta \xi^\alpha \\
\delta s_2^2 &= T_k \cdot \frac{\partial X^2}{\partial \xi^\alpha} \delta \xi^\alpha \\
\Delta \delta s_1^2 &= T_s \cdot \frac{\partial X^2}{\partial \xi^\alpha} \Delta(\delta \xi^\alpha) + T_s \cdot \frac{\partial^2 X^2}{\partial \xi^\alpha \partial \xi^\beta} \delta \xi^\alpha \Delta \xi^\beta \\
\Delta \delta s_2^2 &= T_k \cdot \frac{\partial X^2}{\partial \xi^\alpha} \Delta(\delta \xi^\alpha) + T_k \cdot \frac{\partial^2 X^2}{\partial \xi^\alpha \partial \xi^\beta} \delta \xi^\alpha \Delta \xi^\beta
\end{aligned}
\tag{EQ 49}$$

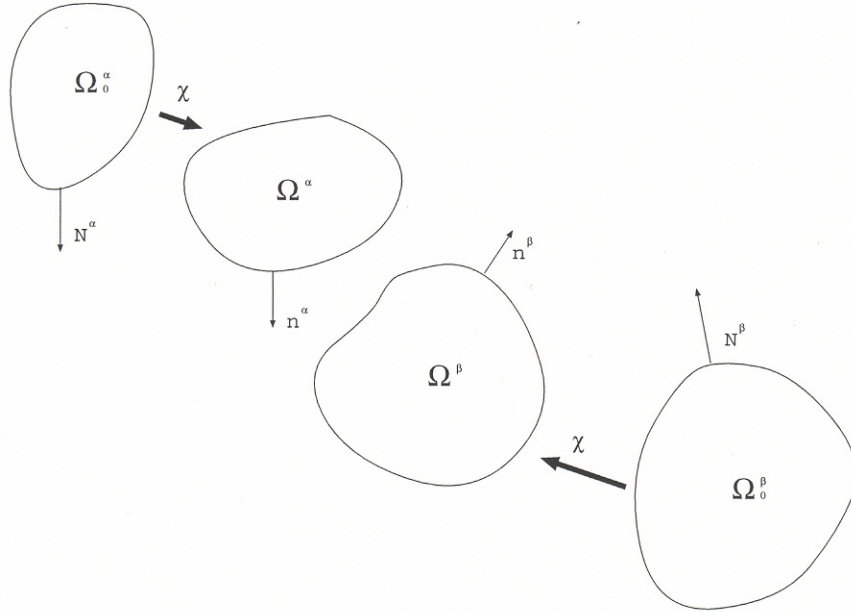
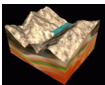


FIGURE 24. Reference and Current Configurations for Two-Body Contact.



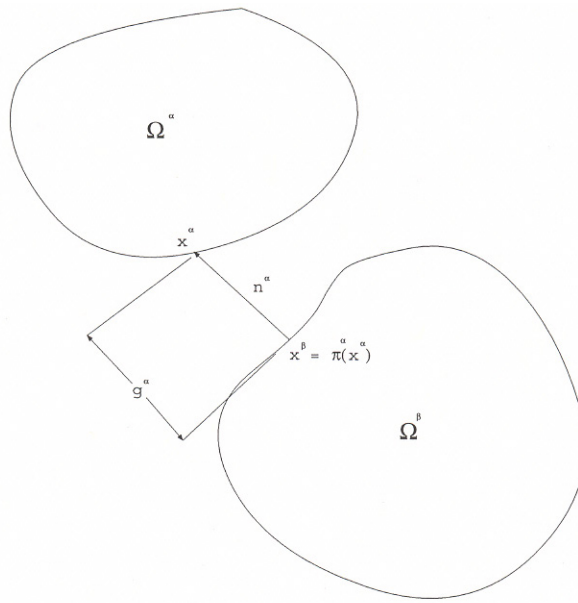


FIGURE 25. Closest-point projection.

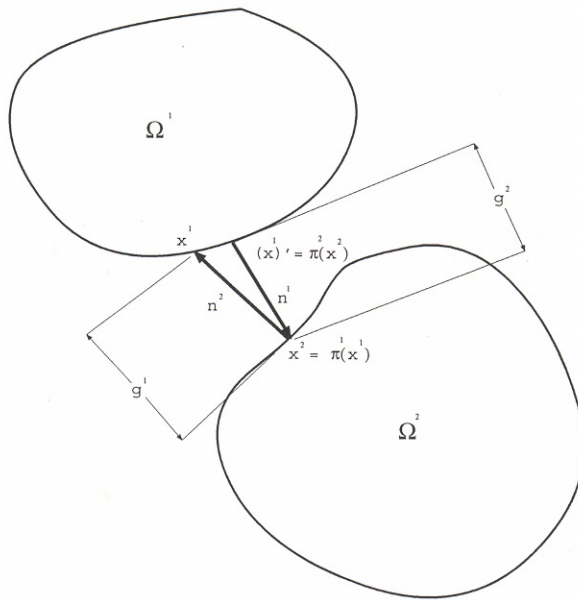
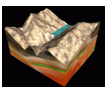


FIGURE 26. Closest-point projection $g^1 \neq g^2$.



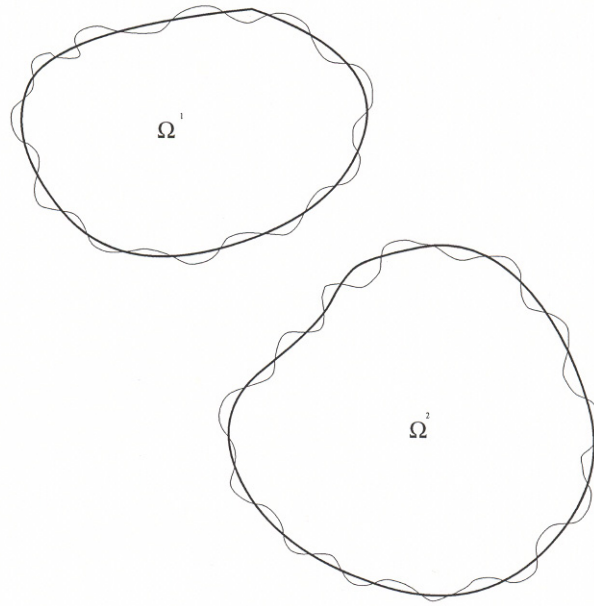


FIGURE 27. Small-scale surface kinematics.

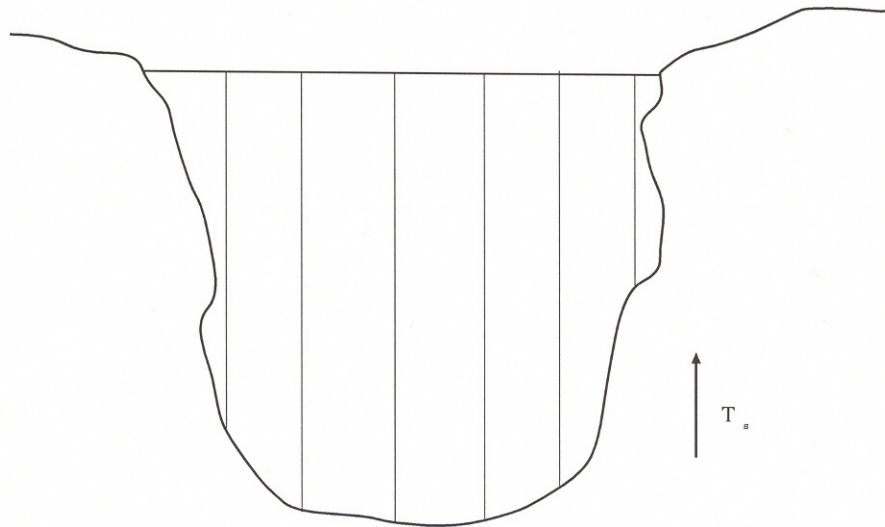
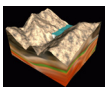


FIGURE 28. Typical arch dam, front, showing vertical contraction joints and direction T_s .



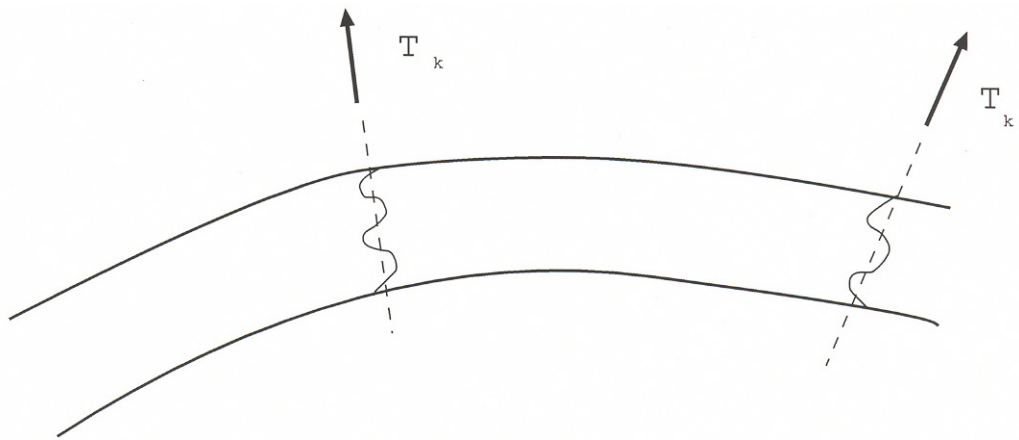


FIGURE 29. Typical arch dam contraction joints, view from top, showing direction T_k .

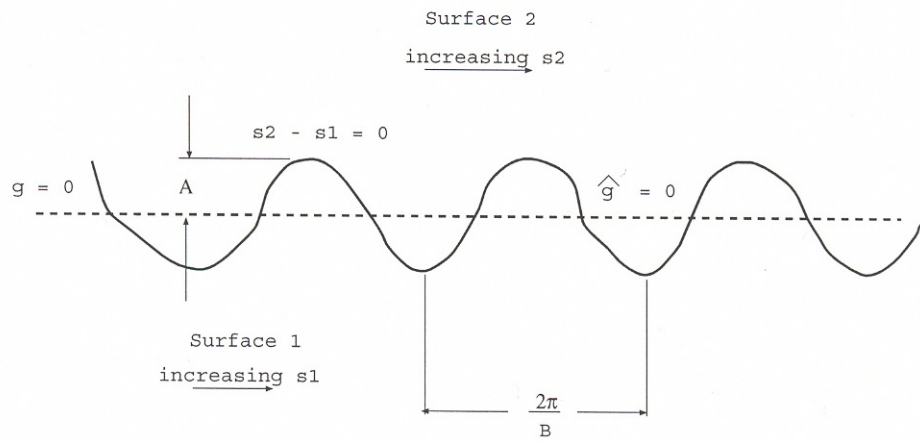


FIGURE 30. Arch dam contraction joint, reference configuration.

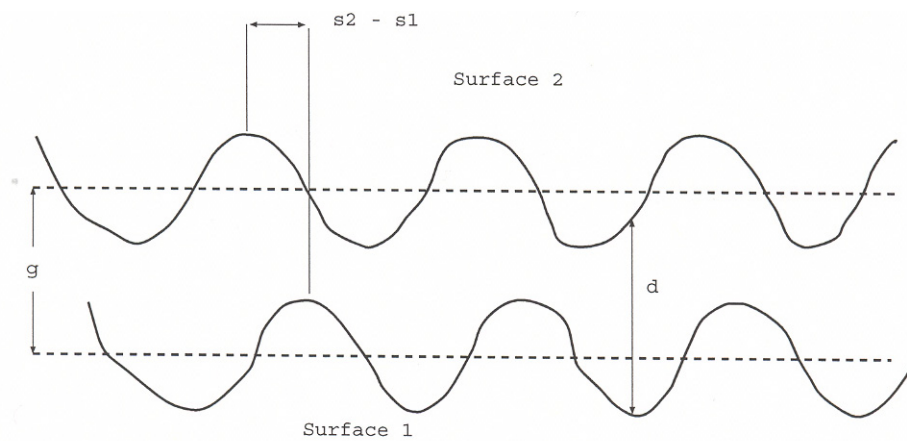
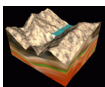


FIGURE 31. Arch dam contraction joint, displaced vertically by g and horizontally by $s_2^2 - s_1^1$.



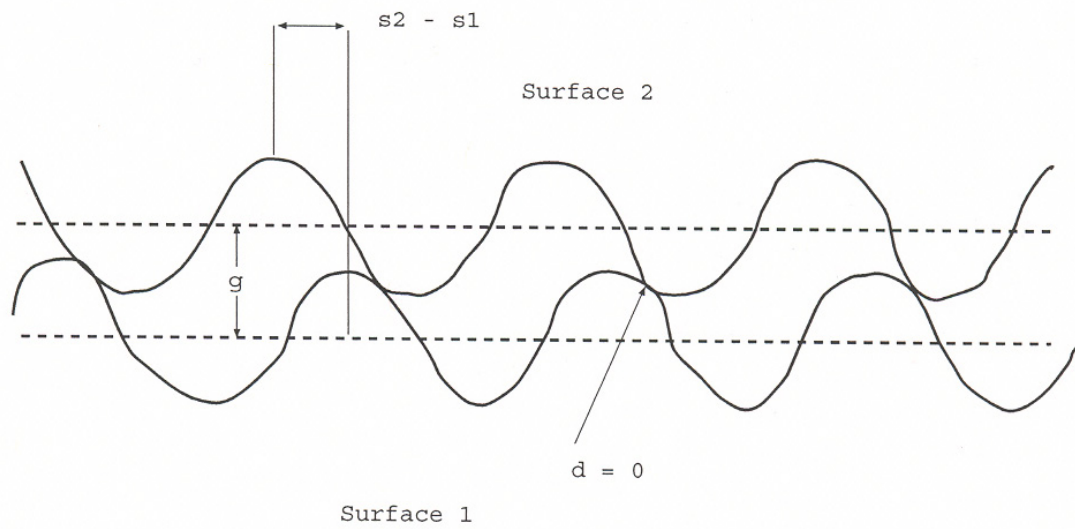


FIGURE 32. Arch dam contraction joint, displaced vertically by g and horizontally by $s_2^2 - s_1^1$ such that $d = 0$ at certain points.

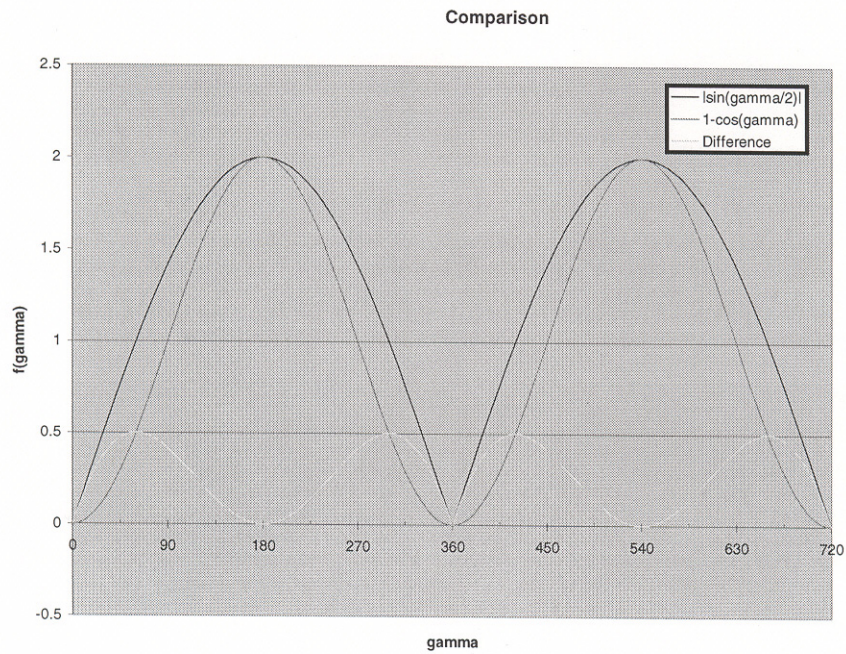
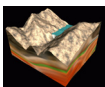


FIGURE 33. Comparison of two different possibilities for \hat{g} .



4.0 Finite Element Verification Studies

One of the main concerns during this project, which the second phase of the study addressed, was that LLNL was using an extremely complex finite element model with some features that hadn't been widely used in NIKE3D or DYNA3D. To verify that the finite element model would be providing a reasonable estimation of the response, verification studies were completed for various aspects of the analysis.

4.1 Fluid Modeling

To ensure that we could model the water explicitly, instead of using a hydrostatic load and a Westergaard Added Mass approach, two verification problems were studied - one for NIKE3D and one for DYNA3D. The NIKE3D fluid modeling verification problem consisted of a steel rectangular box filled with water. Both the box and the water were modeled using 8-node hexahedral elements. The goal of this problem was to verify that we would indeed get the correct hydrostatic loading on the steel box. If the hydrostatic loading is placed on the structure using a linearly varying pressure boundary condition, the maximum effective stress of the box is 42.3 psi. If NIKE3D "water type" elements are used, the maximum effective stress of the box is 42.1 psi. To model the water in NIKE3D, an elastic material (material type 1 in NIKE3D) was used with the following material properties:

TABLE 2. Material properties of NIKE3D fluid elements

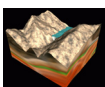
Material Property	Value (lbs, sec, in)
Elastic Modulus	189.7
Poisson's Ratio	0.4999
Mass Density	9.333E-05

Using the definition for the bulk modulus

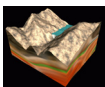
$$K = \frac{E}{3(1 - 2\nu)} \quad (\text{EQ 50})$$

the bulk modulus results in a value of 316,166.67 psi, where the true bulk modulus of fresh water is 316,100 psi. Figure 34 shows the box and the stresses caused by a pressure boundary condition or by using a "nearly incompressible" fluid element.

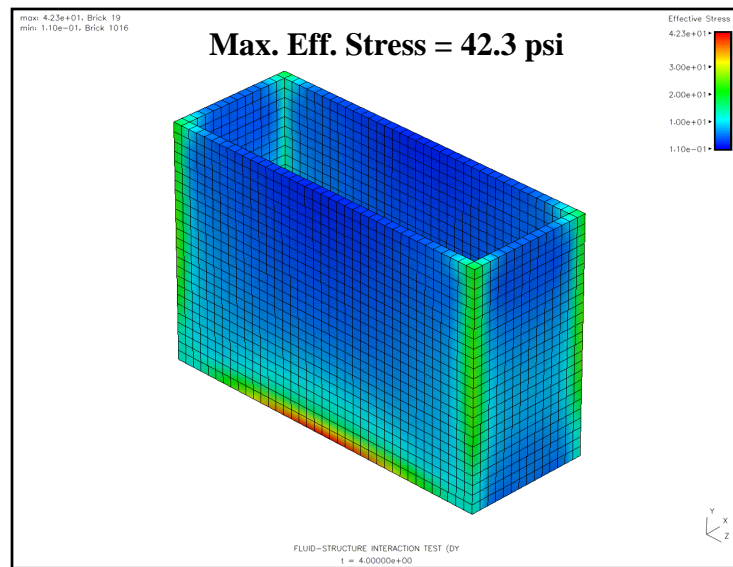
In order to verify that DYNA3D could reasonably model the sloshing of the water within the canyon during an earthquake using the fluid material in DYNA3D, R.D. Blevins provides analytical solutions to the sloshing modes of water in a rectangular tank in his book "Formulas for Natural Frequency and Mode Shape"[Ref 1]. For a rectangular tank filled



with the water shown in Figure 35, the fundamental period of the water is calculated (using Blevins' formulas) to be 2.74 seconds. By sloshing a box filled with water in DYNA3D, a time history of the vertical displacement of the water can be gathered. This is shown in Figure 35. By measuring the time between peaks, one can determine the fundamental period to be approximately 2.5 seconds, which is in reasonable agreement with the analytical solution.

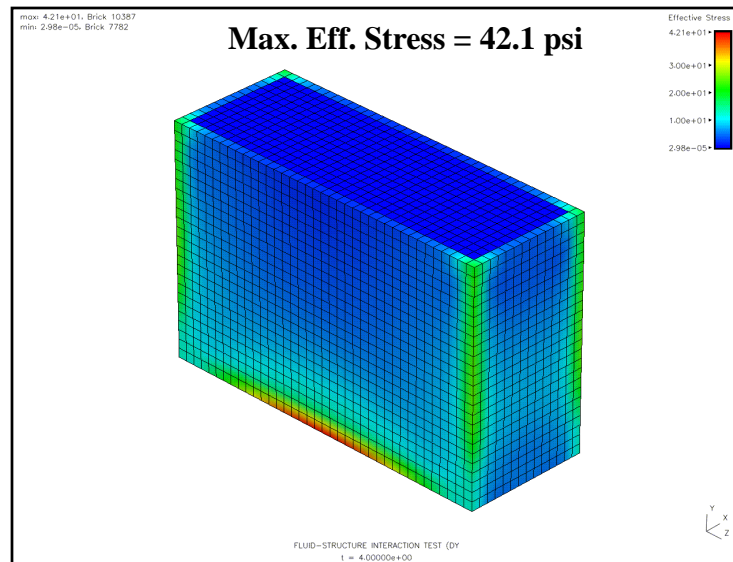


a.)



Hydrostatic Pressure Loading

b.)



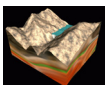
NIKE3D Water Type Elements

K = 316,166.67 psi

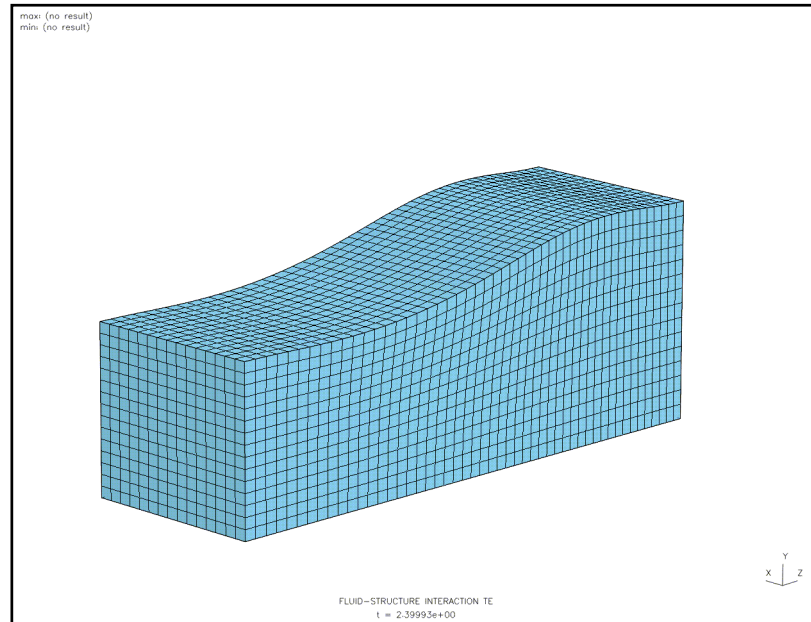
E = 189.7 psi

$\nu = 0.4999$

FIGURE 34. a.) Von Mises stress of steel box loaded with a hydrostatic pressure; b.) von Mises stress of steel box loaded using NIKE3D water type elements



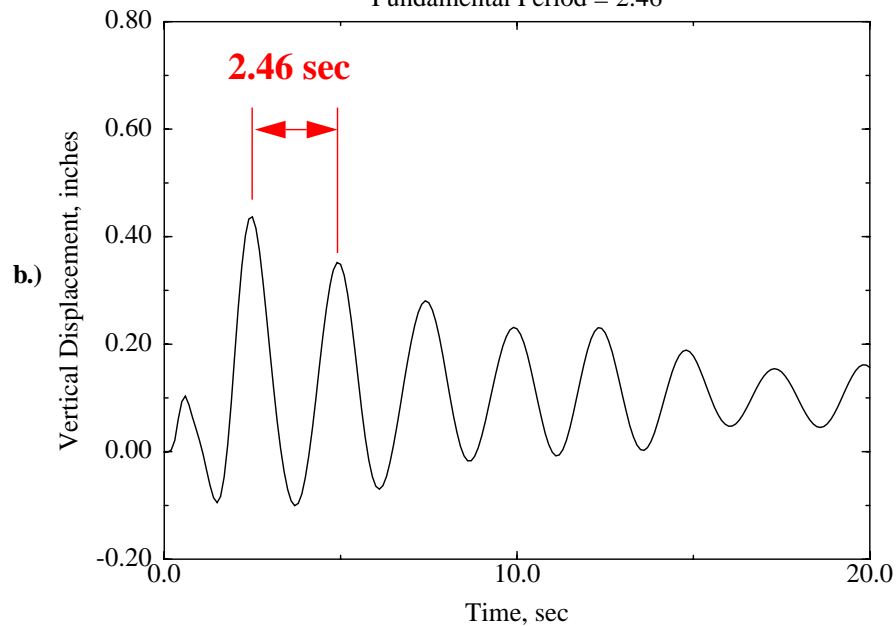
a.)



Fundamental Sloshing Mode

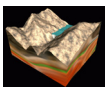
Vertical Displacement of Water

Fundamental Period = 2.46



Fundamental Period = 2.74 sec, Formulas for Natural Frequency and Mode Shape, Robert D. Blevins, Ph.D.

FIGURE 35. a.) Fundamental sloshing mode in DYNA3D finite element analysis; b.) vertical displacement time history of water in DYNA3D finite element analysis.



4.2 Block Sliding Test

Because contact surfaces are used extensively in every finite element model, it was important to validate the DYNA3D contact surfaces against either experimental results or against an analytical solution. The USBR supplied LLNL with a contact problem that could be solved analytically. Figure 36 shows the finite element model of the verification problem. This problem consists of a 10 ft. by 10ft. 150,000 lb. block resting against two planar surfaces that have different friction angles. A 270 kip load is applied to the centroid of the block for 0.5 seconds and the block is allowed to come to rest. The same loading condition is applied in the reverse direction. The block should come to rest at the same location it started from.

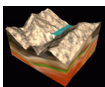
By using the following equations:

$$a = \frac{(F_1 - F_2)}{m} \quad \text{Newtons Second Law}$$

$$x_f = x_o + v_o t + \frac{1}{2} \frac{(F_1 - F_2)t^2}{m} \quad \text{One Dimensional Motion of Particle} \quad (\text{EQ 51})$$

$$F_1 d_1 = F_2 d_2 \quad \text{Conservation of Work}$$

one can calculate a maximum displacement of the block to be 9.15 feet, a maximum calculated velocity of 16.2 ft/sec, and a maximum calculated initial acceleration of 32.4 ft/sec². The results of the finite element analysis are shown in Figure 37. The maximum displacement from the finite element analysis was 9.26 ft, a 1.2% difference. In addition, the block came back to a displacement of -1.49E-02 ft, very close to the expected value of 0.0 ft. The velocities and accelerations were also very close to the analytical results.



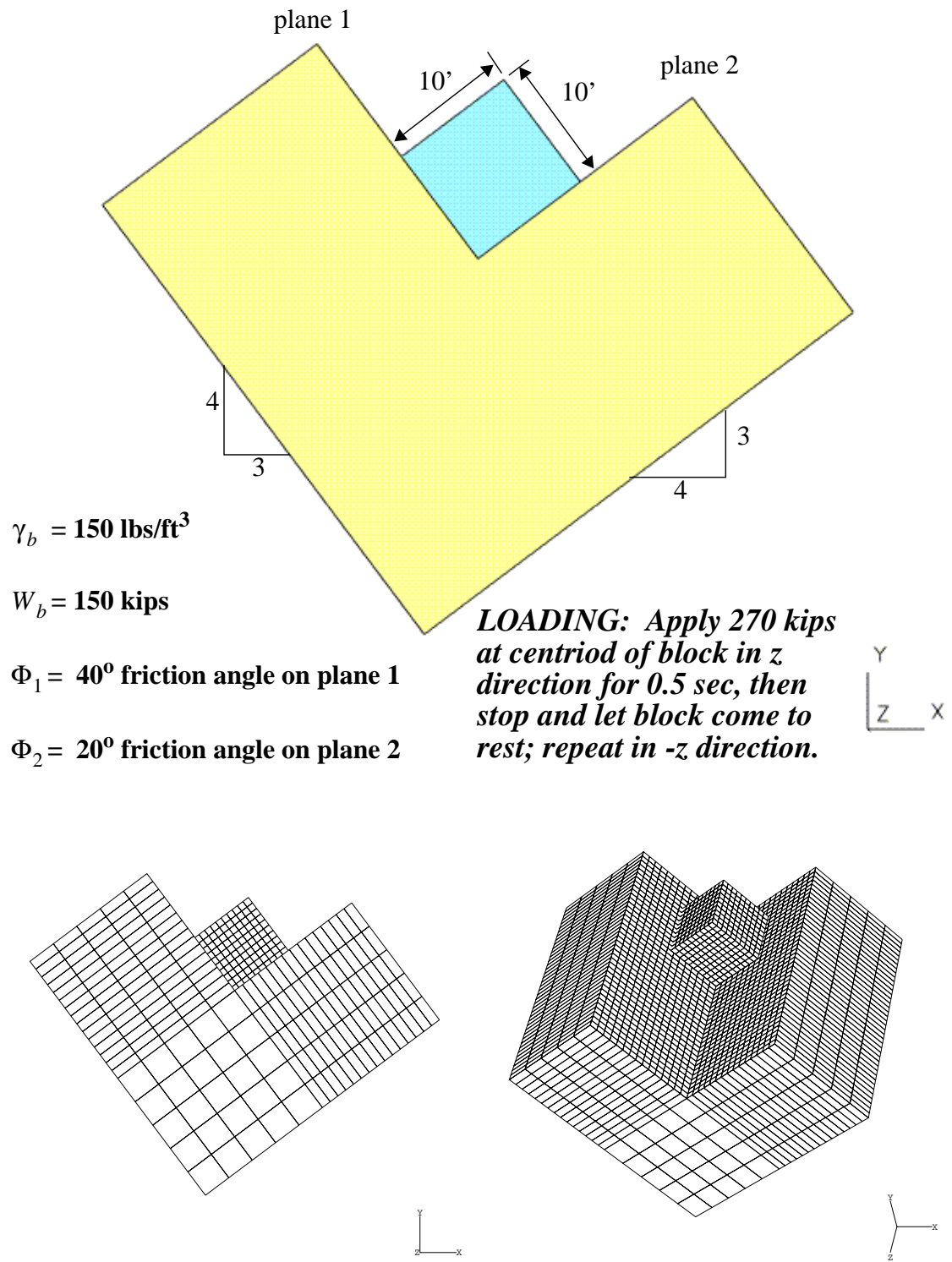
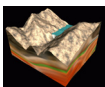


FIGURE 36. Finite element model of block sliding verification test.



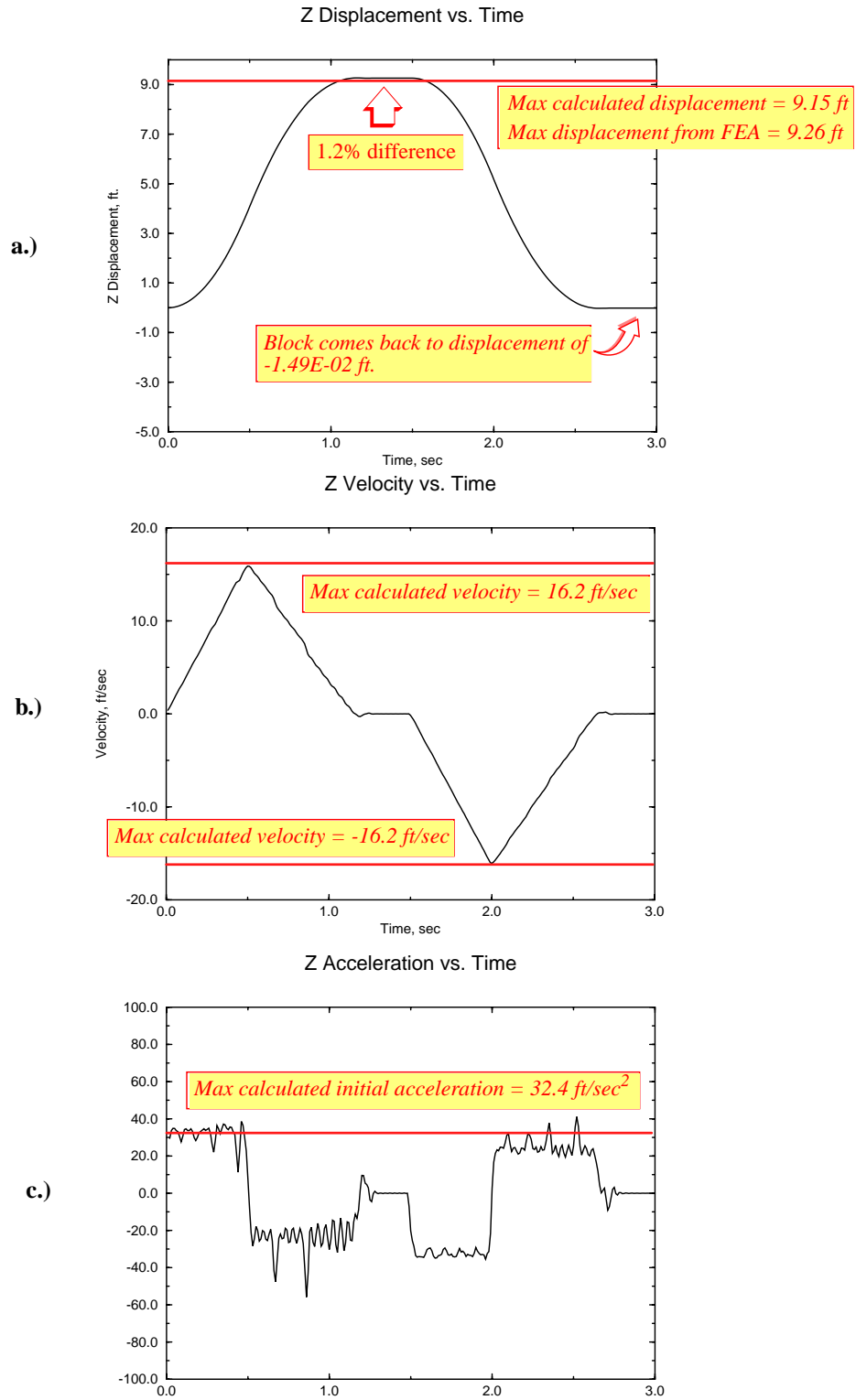
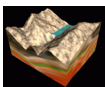


FIGURE 37. a.) z displacement time history of block; b.) z velocity time history of block; c.) z acceleration time history of block.

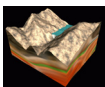


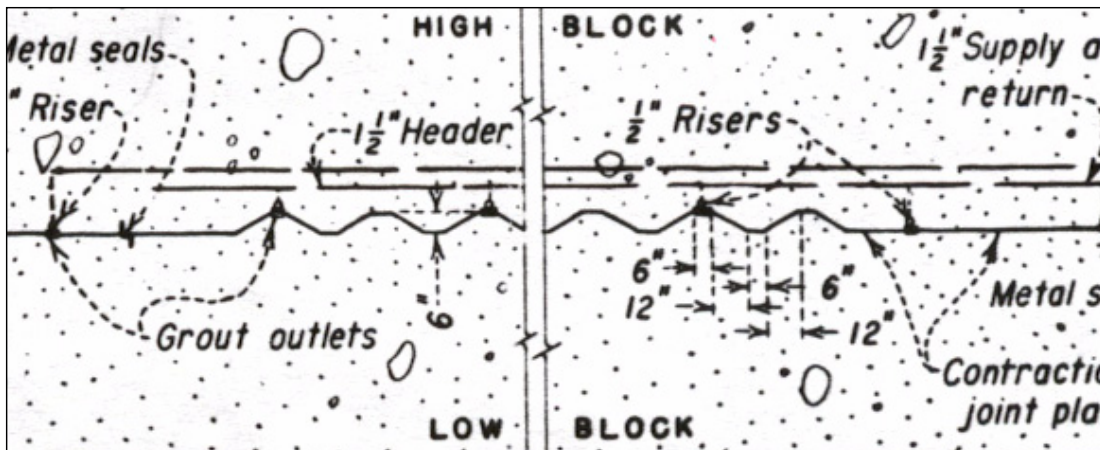
4.3 Contraction Joint Model Tests

Two more tests were completed to determine if the new contraction joint sliding interfaces were indeed working as intended. The first test studied two dam-size blocks, of similar size to that of Morrow Point Dam, where one block was pushed past the other block. The second test compared the stress states in the Morrow Point Dam finite element model. One model used the well-verified discrete elements between the contraction joints, and the second model used the contraction joint sliding interfaces for every vertical joint surface in Morrow Point Dam.

4.3.1 Two (dam-size) blocks sliding past each other

Figure 39 shows a pictorial time history of the one block sliding past the other block. As the one block is being pushed past the other, the shear keys cause the block to be pushed outward. Because of the transverse pressure placed on the block being pushed, it is allowed to slide back into another shear key and contact the adjacent block. The time history of the transverse displacement plotted against the upstream-downstream displacement as well as a pictorial description of the Morrow Point shear keys is shown in Figure 38. By comparing the plan view of the shear keys and the displacement time history, the sliding interface does a good job of representing the behavior of the shear keys without having to explicitly model them using finite elements.





Transverse Displacement vs. Upstream-Downstream Displacement

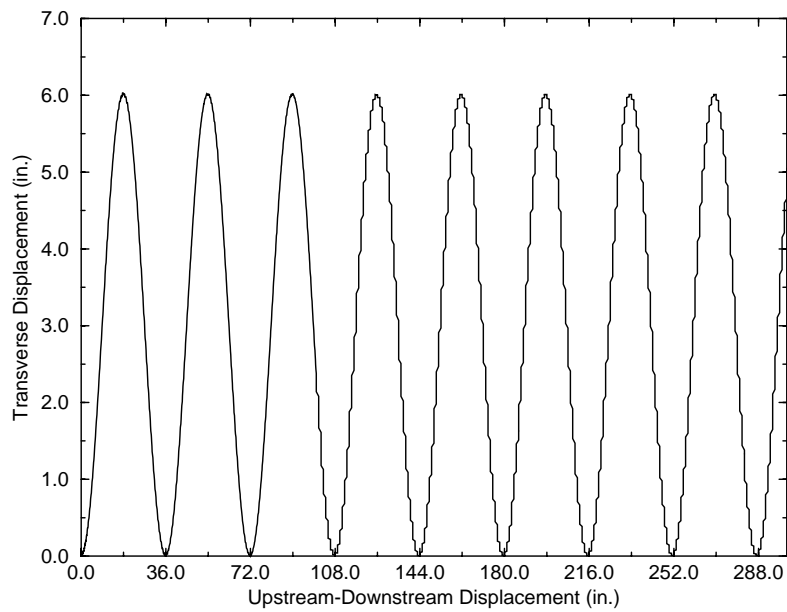
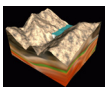


FIGURE 38. a) Plan view of Morrow Point Dam shear keys; b) transverse displacement vs upstream-downstream displacement time history for contraction joint test problem.



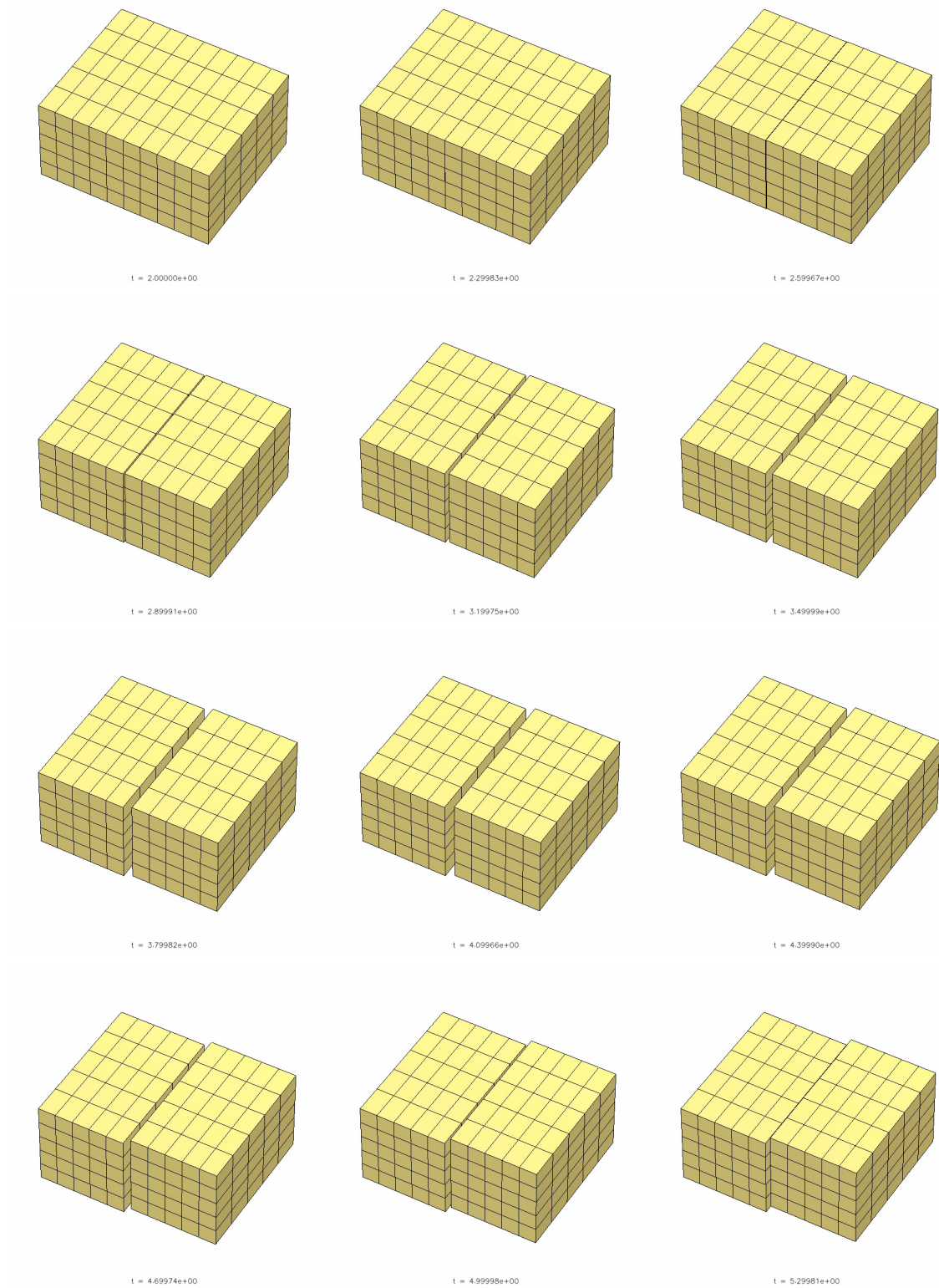
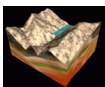
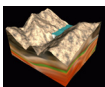


FIGURE 39. Time history of dam-size blocks moving past each other (displacement scale factor in transverse direction = 5.0).



4.3.2 Comparison between discrete springs and contraction joint slide surface

During the first phase of this study, the discrete springs that were used to model the contraction joints were examined closely to verify that they reproduced reasonable results (Section 3.1 on page 29). Another test problem to verify whether the new contact interface was calculating good results, was to compare the Morrow Point Dam model that used discrete elements to a model that used the new contact surfaces. The loading on the model consisted of gravity and hydrostatic loads with the base of the dam fixed in all three coordinate directions. The resulting first principal stresses for both models are compared in Figure 40. As you can see from the figure, there is not much difference in stress between the two models.



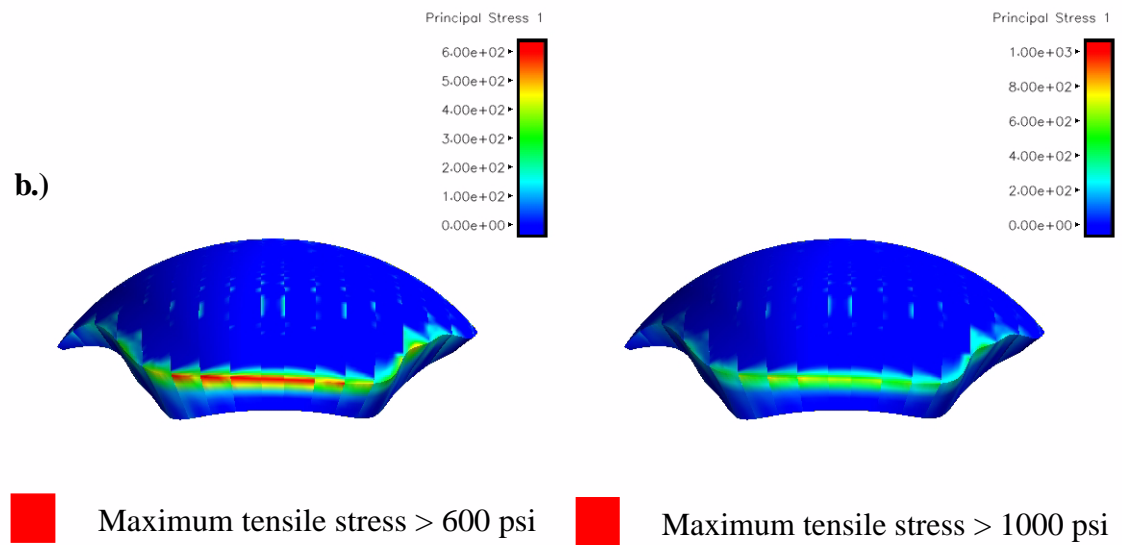
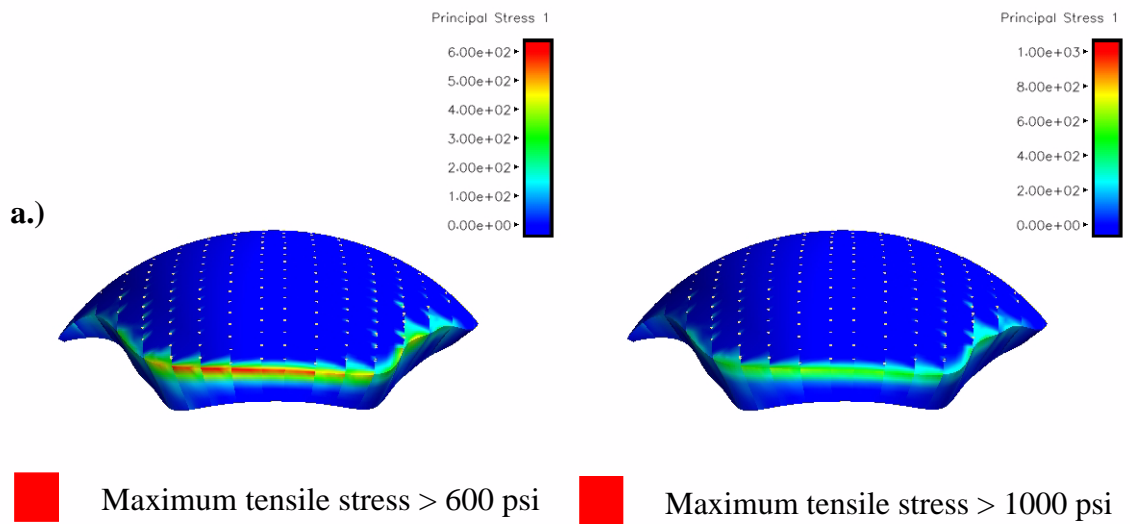
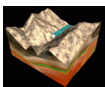


FIGURE 40. a.) NIKE3D static initialization with discrete springs; b.) NIKE3D static initialization with contraction joint slide surface.



5.0 Nonlinear Finite Element Model of Morrow Point Dam

A wide variety of finite element models were used for this study. The following is a brief list of some of the features used in the finite element models (Note: not all of these features were used in every finite element model):

1. Westergaard added mass for fluid-structure interaction
2. Water explicitly modeled using an elastic material in NIKE3D and a fluid material in DYNA3D
3. Vertical contraction joints
4. Topographically accurate flexible foundation
5. Left abutment wedge explicitly represented
6. Ground motions input as either base accelerations or force time histories
7. Non-reflecting boundaries
8. Sliding contact between reservoir/foundation and reservoir/dam
9. Transmitting boundary on upstream side of reservoir
10. Hydrostatic uplift along wedge and foundation contacts
11. Thermal load applied to dam to represent a low-temperature condition
12. Concrete damage plasticity model used for dam
13. Tied with failure slide surface for dam/foundation contact interface

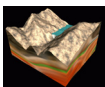
Figure 42 shows the construction plans of Morrow Point Dam, which assisted LLNL in constructing the finite element model geometry in the TrueGrid mesh generator.

5.1 Fluid Modeling in NIKE3D and DYNA3D

In 1933, professor H.M. Westergaard first established a rational standard procedure to take into account the hydrodynamic loadings on gravity dams during earthquakes [Ref 6]. The concept of added mass, which he introduced for the incompressible water reservoir, greatly simplified the analysis procedure of the response of a dam considering hydrodynamic effects during earthquakes. Westergaard's assumptions were the following:

- dam was idealized as a 2-dimensional rigid monolith with vertical upstream face;
- the reservoir extends to infinity in the upstream direction;
- displacements of fluid particles are small;
- surface waves are ignored;
- only horizontal ground motion in the upstream-downstream direction is considered.

He approximated the pressure solution for an incompressible reservoir with a parabola. He observed that the "pressures are the same as if a certain body of water were forced to



move back and forth with the dam while the remainder of the reservoir is left inactive”. Westergaard suggested that the dynamic pressure could be expressed as:

$$p_z = \frac{7}{8}aw\sqrt{H(H-z)} = \frac{7}{8}\rho\ddot{r}_g\sqrt{H(H-z)} \quad (\text{EQ 52})$$

where

a = horizontal ground acceleration, in units of g

w = unit weight of water

\ddot{r}_g = horizontal ground acceleration

ρ = unit mass of water

H = depth of reservoir above the base of the dam

z = distance from the base of the dam

p_z = hydrodynamic pressure at height z from the base of the dam, applied normally to the dam face.

EQ. 52 indicates that the hydrodynamic pressure exerted normally on the upstream face of the dam, is equivalent to the inertia force of a prismatic body of water of unit cross-section and length $\frac{7}{8}\sqrt{H(H-z)}$ attached firmly to the face of the dam, and moving with the dam back and forth in the direction normal to the face of the dam. This body of water is the “added mass” applied by the reservoir to the dam (Figure 41).

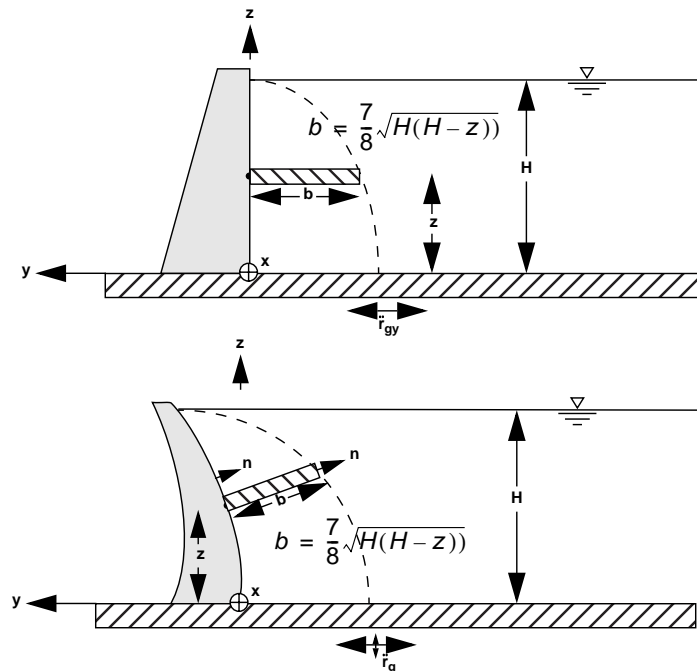
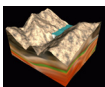
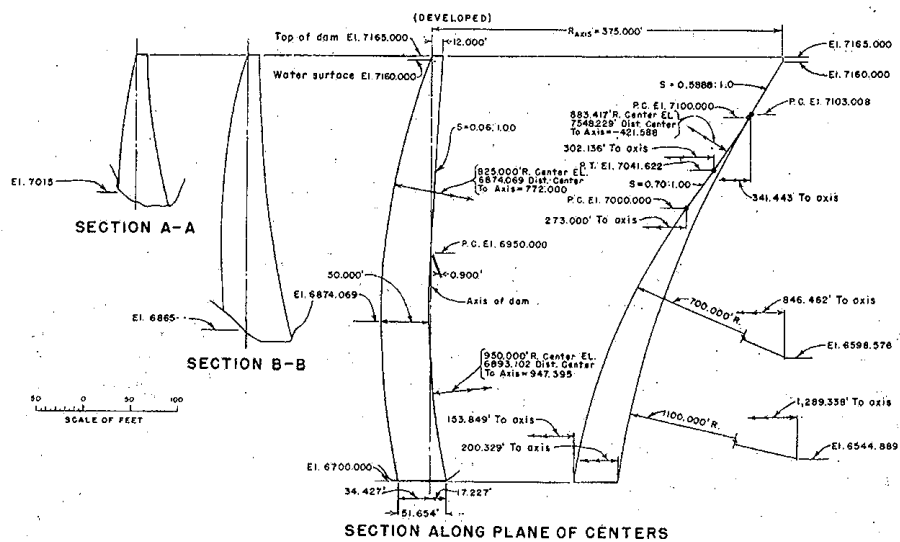
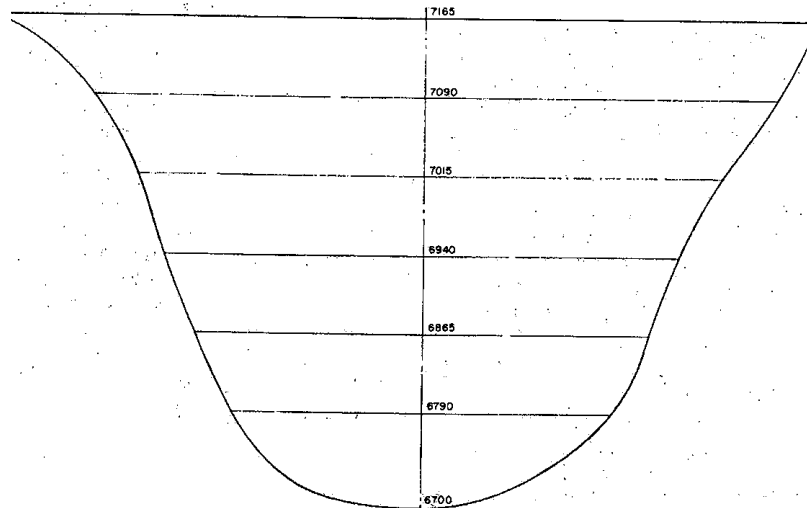
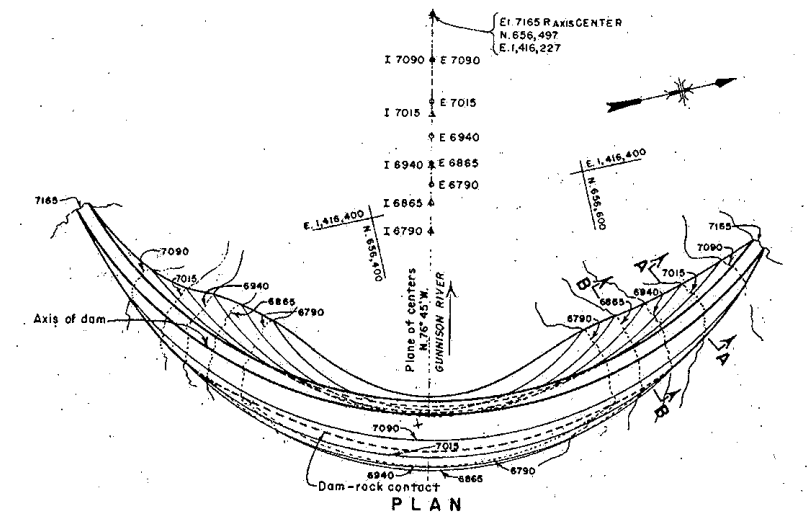


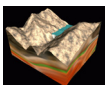
FIGURE 41. a.) Pictorial added mass for gravity dam; b). pictorial added mass for double-curvature arch dam.





MORROW POINT DAM-AS CONSTRUCTED

FIGURE 42. Construction Plans of Morrow Point Dam.



5.2 Contraction Joint Finite Element Model with Rigid Foundation and Westergaard Added Mass

For this finite element model, the base of the dam is considered fixed in all three directions. This finite element model consists of 23,195 brick elements and either 1,640 discrete elements to model the contact and connectivity across the expansion joints or it can use the contraction joint contact surfaces (see Figure 43). A requirement of the contraction joint model was that the contraction joints allow free relative motion in a vertical direction between adjacent dam segments as the gravity dead load was applied. This relative motion prevents the generation of large vertical direction shear stresses which transfer large loads to the upper abutment region of the dam - which the actual construction process of the dam prevents. The contraction joints were modeled with frictionless contact surfaces for the NIKE3D static initialization. This prevents friction between adjacent blocks as the dead loads are applied and does not allow inter-block vertical shears to develop. During the seismic analysis stage, an assumed coefficient of friction value of 0.3 is added to the contraction joint contact surfaces. To simulate the influence of the fluid on the dam structure, Westergaard added mass was included into this finite element model.

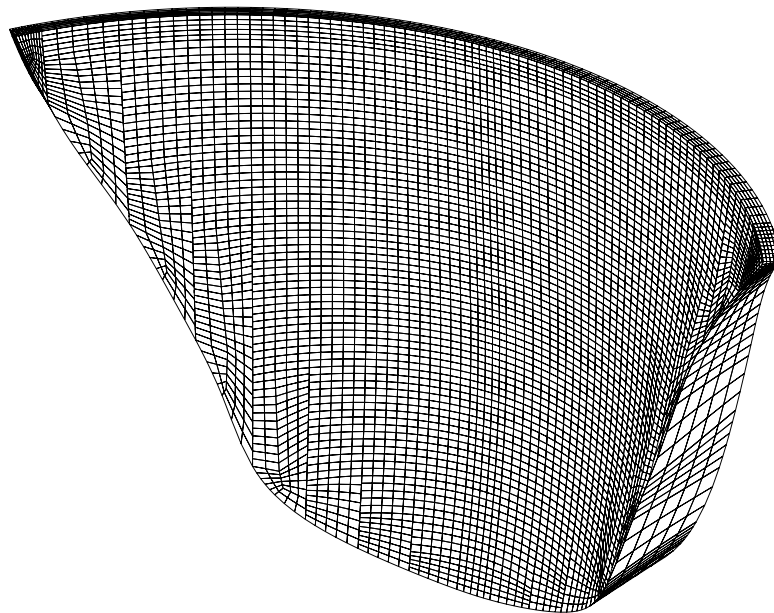
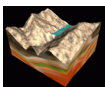


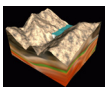
FIGURE 43. Contraction joint finite element model with rigid foundation.

5.3 Contraction Joint Finite Element Model with Flexible Foundation and Westergaard Added Mass

This model consists of the same dam model as that described in Section 5.2, but instead of having a fixed base it has a flexible foundation. To achieve an accurate geology topography for the finite element model, a 1983 USGS topographic map was scanned and used to generate an IGES surface for the TrueGrid mesh generator. Figure 44 shows the topo-



graphic map used and the generated three-dimensional IGES surface. This model consists of approximately 101,000 brick elements and 1,640 discrete elements (see Figure 45). To connect the dam model to the foundation model, a tied slide surface was used. This model also used Westergaard added mass to simulate the fluid-structure interaction.



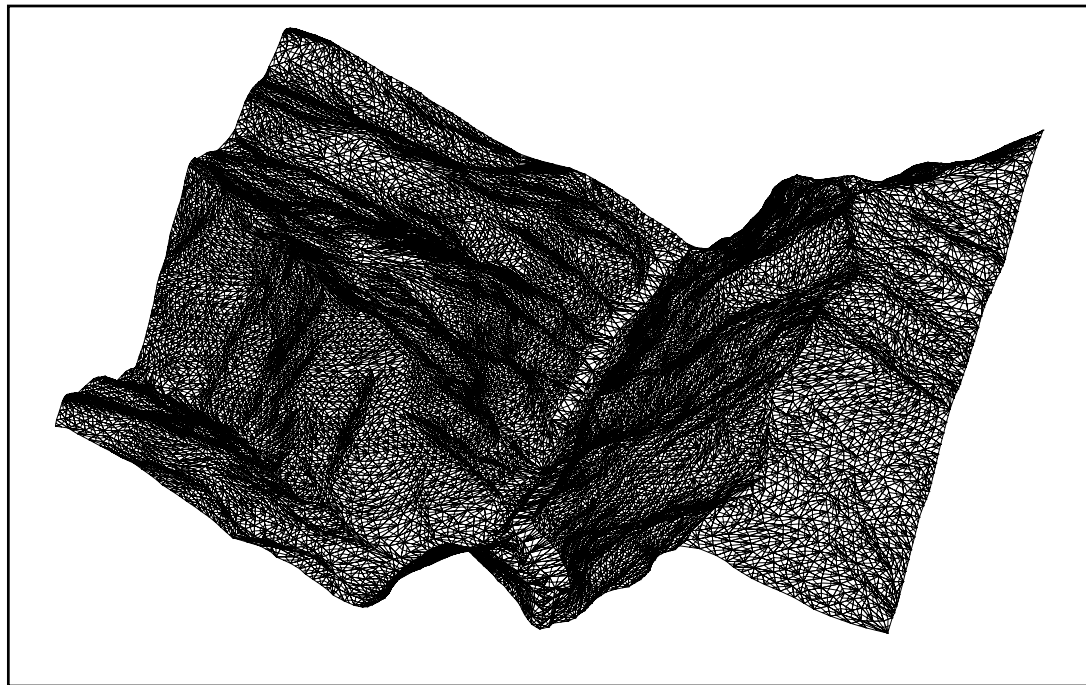
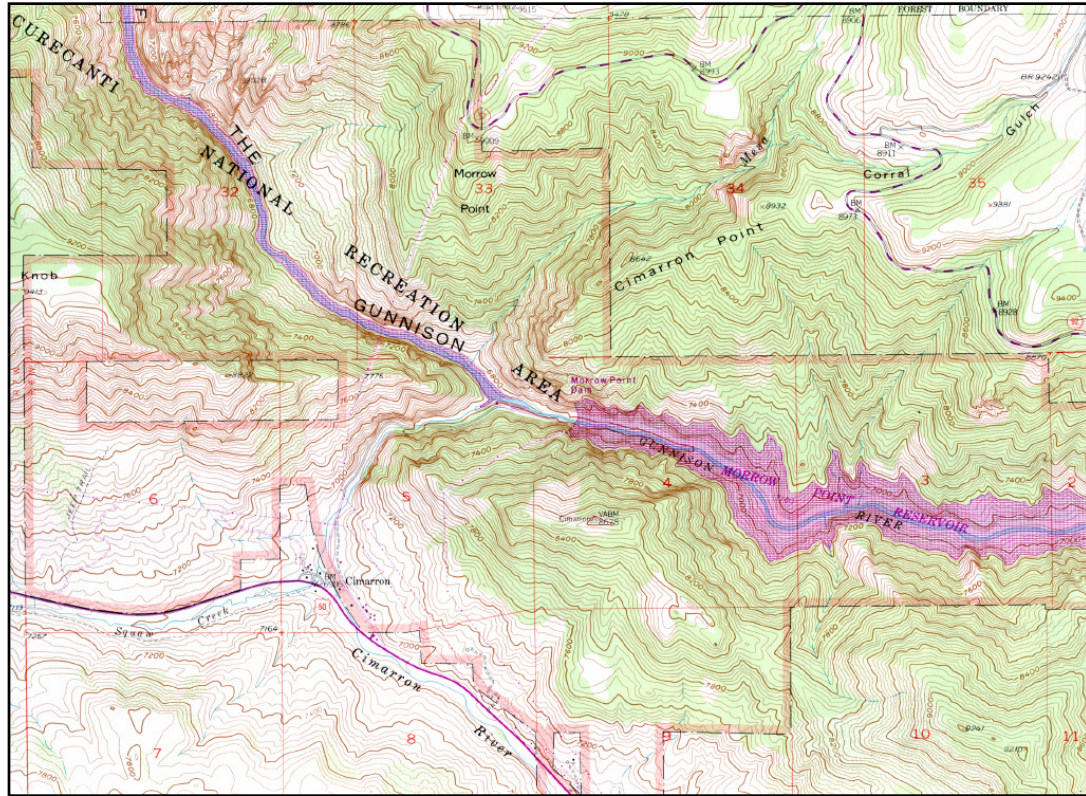


FIGURE 44. IGES surface for TrueGrid mesh generation used USGS 1983 topographic map.

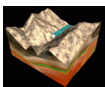
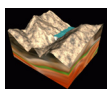




FIGURE 45. Contraction joint finite element model with Westergaard added mass and flexible foundation.

5.4 Contraction Joint Finite Element Model with Flexible Foundation and Water Explicitly Modeled

Figure 46 and Figure 47 shows this finite element model, which is the same as that in Section 5.3, except the water is now explicitly modeled instead of using Westergaard added mass for the fluid-structure interaction. For the static initialization in the NIKE3D implicit finite element program, an elastic material was used to model the water. A low elastic modulus of 189.7 psi and a high poisson's ratio of 0.4999 were used to achieve a low shear modulus and the bulk modulus of fresh water. For the seismic analysis, which was done using the DYNA3D explicit finite element program, the fluid material (Material 9) and an equation of state, which specified the bulk modulus, were used to model the

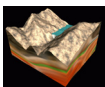


water. A pressure cutoff and viscosity coefficient of 0.0 were assumed. A complete listing of all of the material properties used are given in Table 3 on page 80.

TABLE 3. Material Properties for finite element models

<i>Material Property</i>	<i>Value (lbs, in, sec)</i>
Elastic Modulus of Concrete	4.769E+06 psi
Poisson's Ratio of Concrete	0.15
Mass Density of Concrete	2.2500E-04 lbs-sec ² /in ⁴
Elastic Modulus of Foundation for Models 2 and 3	4.769E+06 psi
Poisson's Ratio of Foundation for Models 2,3, and 4	0.2
Elastic Modulus of Water for NIKE3D Program	189.7 psi
Poisson's Ratio of Water for NIKE3D Program	0.4999
Mass Density of Water	9.3330E-05 lbs-sec ² /in ⁴
Bulk Modulus of Water	316,100 psi
Elastic Modulus of Foundation for Model 4	3.338E+06

To connect the water to the foundation in this model, a tied slide surface was used. A sliding with voids slide surface, however, was used between the water and the dam. This was done so that the water could slide downwards next to the dam during the gravity initialization, preventing any unwanted stresses to be formed on the dam surface. During the second phase of this project, both the reservoir/foundation and reservoir/dam contact surfaces were changed to a sliding only (with no gaps) slide surface for both the static and seismic analyses. The finite element model does a good job of representing the actual reservoir/foundation contact geometry, as is shown in Figure 48.



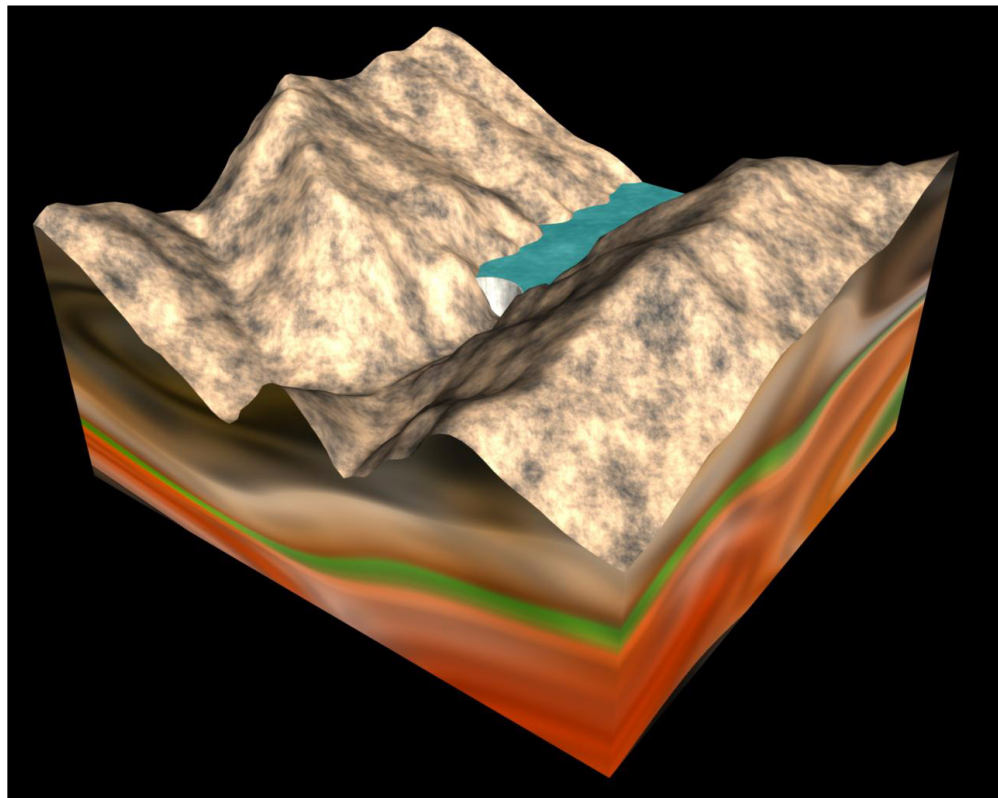
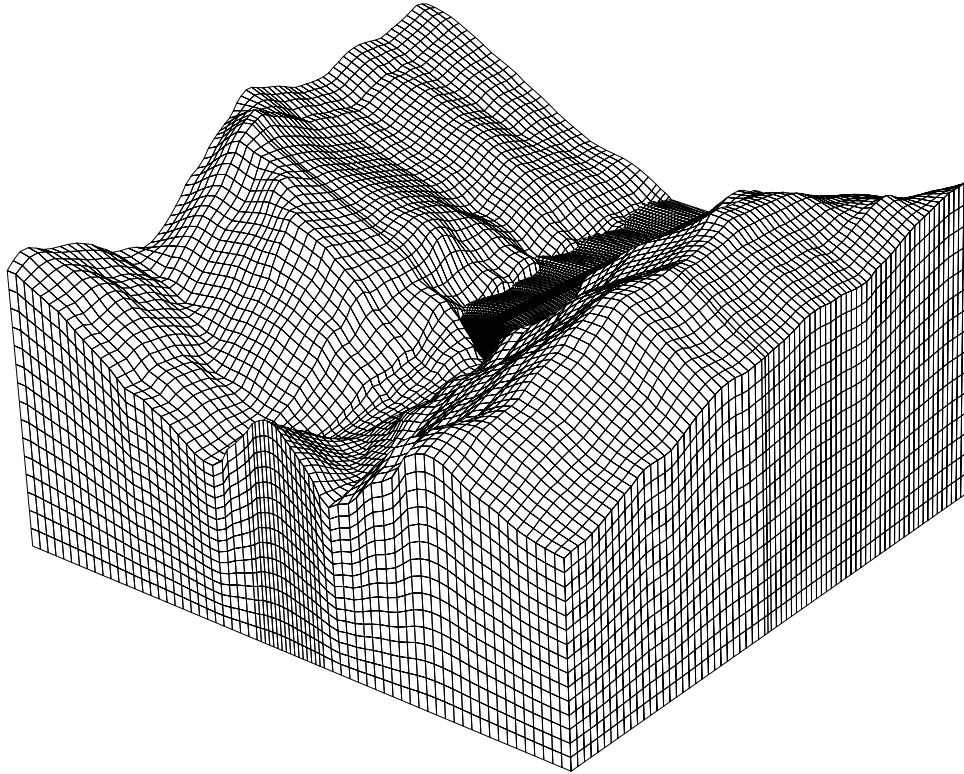
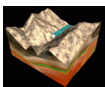


FIGURE 46. Contraction joint finite element model with flexible foundation and water explicitly modeled.



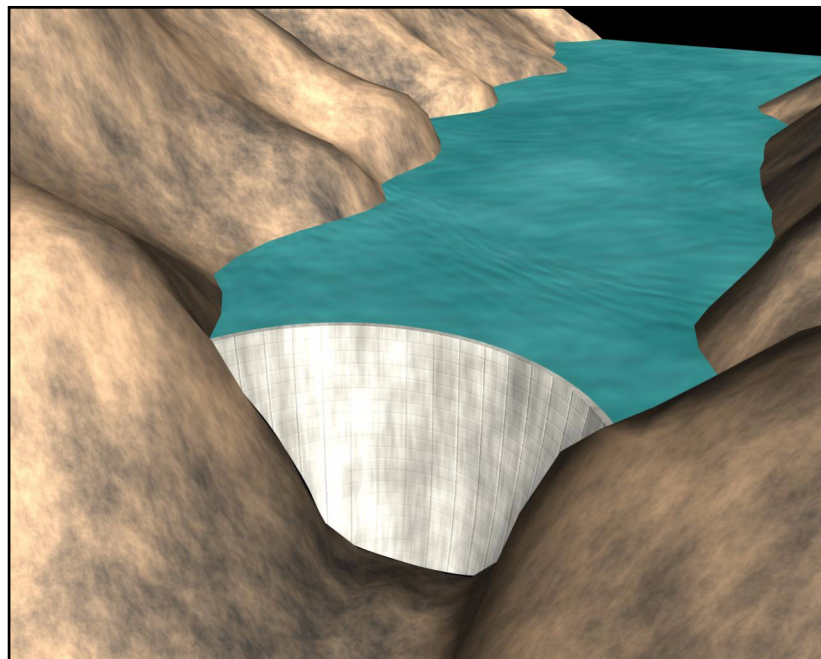
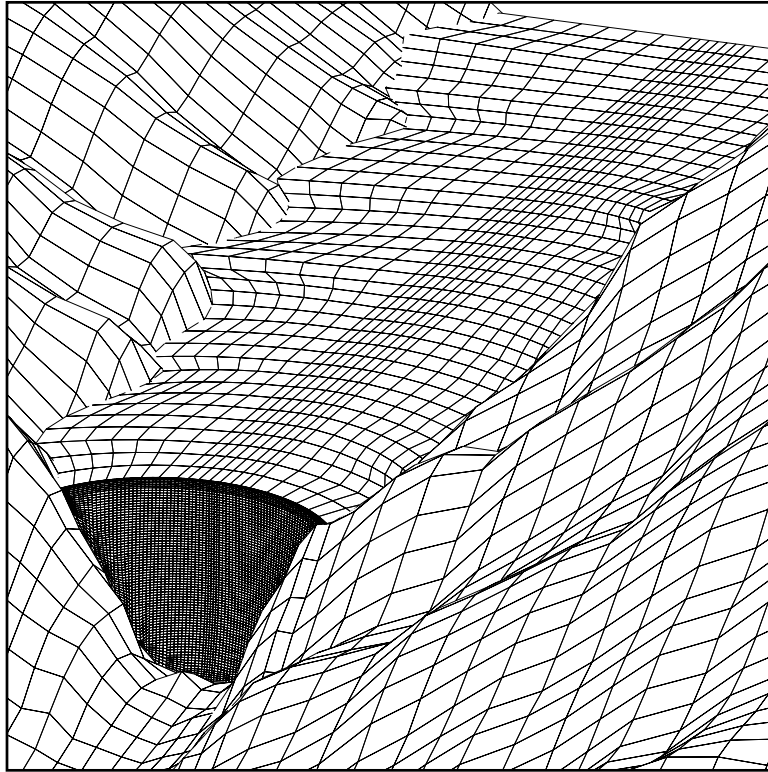
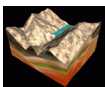


FIGURE 47. Close-up view of contraction joint finite element model with flexible foundation and water explicitly modeled.



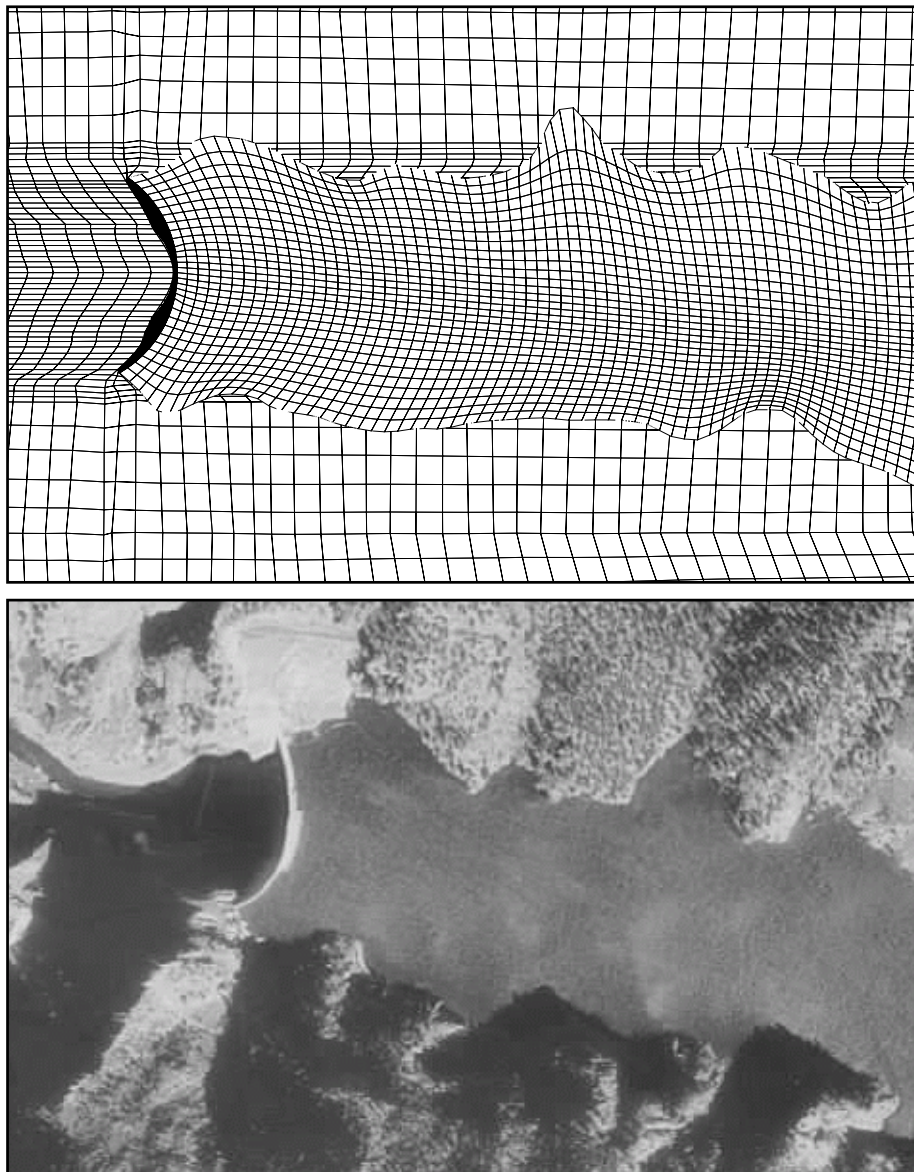
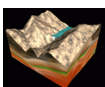


FIGURE 48. a.) Plan view of contraction joint finite element model with flexible foundation and water explicitly modeled; b) aerial photograph of Morrow Point Dam and Reservoir.

5.5 Contraction Joint Finite Element Model with Flexible Foundation, Water Explicitly Modeled, and Left Abutment Wedge

This finite element model is similar to that described in Section 5.4, except that it now includes a new feature called an abutment wedge. This wedge, or large rock, in the foundation is defined by three foliation planes - a base plane, side plane, and release plane. A plan view of the left abutment wedge in relation to the footprint or foundation of Morrow



Point Dam is given in Figure 49. Table 4 and Table 5 detail the features used to define the left abutment wedge and the wedge plane orientations. To assist in modeling the abutment wedge, the USBR provided LLNL with coordinates and unit normals (see Table 6) to be used in TrueGrid for defining the foliation planes or the contact surfaces this abutment wedge slides along. Figure 50 shows the finite element model with the abutment wedge modeled. A transition region was used to connect the larger elements of the foundation with the smaller elements of the abutment wedge. A tied slide surface was used between the foundation and transition region. During the static initialization in NIKE3D, a tied slide surface was used between the wedge and transition region. For the seismic analysis in DYNA3D, this slide surface was changed to a sliding with voids surface with a high coefficient of friction. The coefficient of friction values used are given in Table 6.

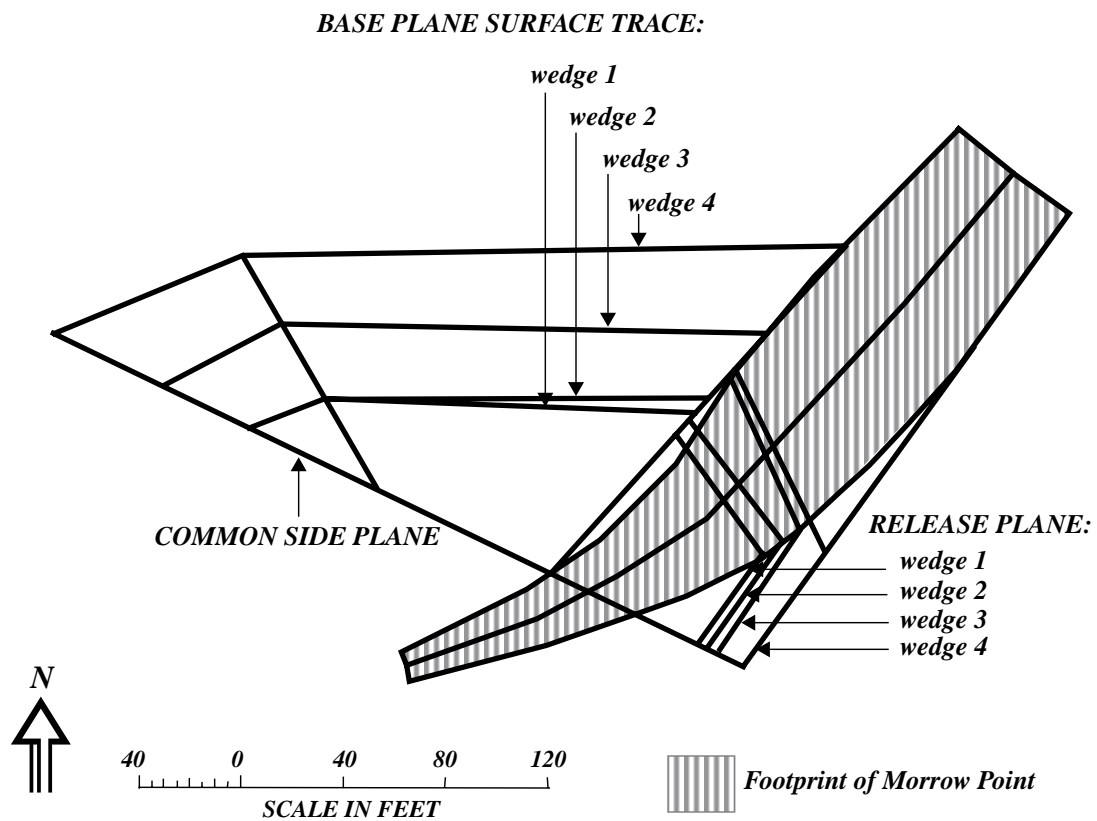


FIGURE 49. Plan view of left abutment wedge 3.

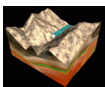


TABLE 4. Left Abutment Wedge Boundaries

Wedge	Features Used to Define Left Abutment Wedges		
	Base Plane	Side Plane	Release Plane
1	Foliation 3	Joint 2	Joint Set B
2	Foliation 3A	Joint 2	Joint Set B
3	Foliation 4	Joint 2	Joint Set B
4	Foliation 5	Joint 2	Joint Set B

TABLE 5. Left Abutment Wedge Plane Orientations

Wedge	Plane Type ^a	Wedge Plane Orientation	
		Strike-Dip	Dip/Dip-Direction
1	BASE	N25°E30°SE	30/115
	SIDE	N65°W90°	90/25
	RELEASE	N36°E90°	90/306
2	BASE	N25°E35°SE	35/115
3	BASE	N30°W34°NE	34/60
4	BASE	N33°E39°SE	39/123

a. The plane types in red define left abutment wedge 3.

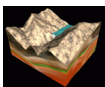
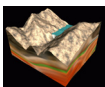


TABLE 6. NIKE3D and DYNA3D Left Abutment Wedge Definitions.^a

Plane	Unit Normal (LLNL coordinates)			DYNA3D Friction
	transverse direction	upstream-downstream direction	vertical direction	
SIDE	-0.97905	0.20364	0.0	0.84
RELEASE	-0.38672	-0.92221	0.0	0.84
BASE	-0.04874	0.24731	0.96771	0.51

a. Apex Coordinates: (286.33, -75.29, 188.3)



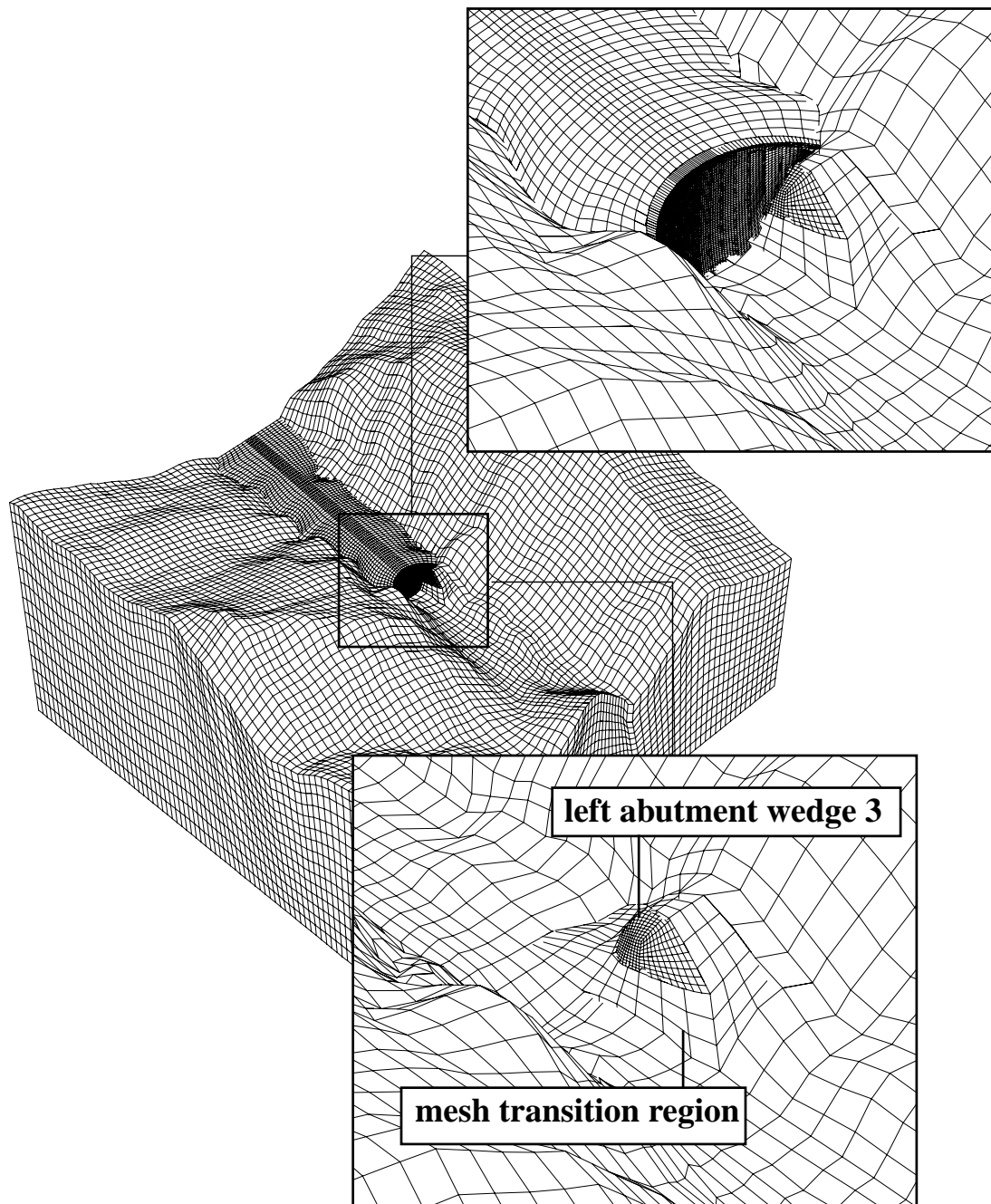
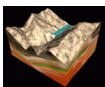


FIGURE 50. Morrow Point Dam finite element model with flexible foundation, water explicitly modeled, and left abutment wedge.



5.6 Homogeneous Finite Element Model

Figure 51 shows a homogeneous finite element model of Morrow Point Dam, or a model that does not include the vertical contraction joints. This model was used in conjunction with the water explicitly modeled and a flexible foundation to assist in validation and comparison with other finite element programs, such as EACD.

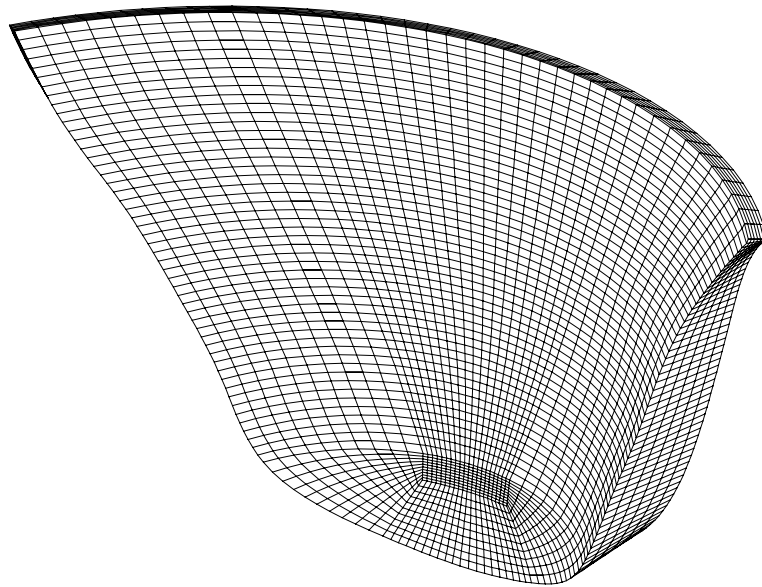


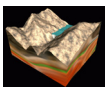
FIGURE 51. Homogeneous finite element model.

6.0 Finite Element Analysis Procedures of Morrow Point Dam

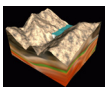
Two finite element analysis procedures were employed for this study. The first procedure was the base acceleration method. This used a fixed bottom boundary and base accelerations to excite the earthquake motions. The second method, the force time history method, used a non-reflecting boundary condition at the bottom boundary and force time histories instead of base accelerations to excite the structural models. Force time histories were used because base accelerations and non-reflecting boundaries cannot be used in conjunction with each other.

7.0 Procedure for Base Acceleration Method

The finite element procedure for the base acceleration method is graphically presented in Figure 52. First, the NIKE3D and DYNA3D finite element models are generated using the TrueGrid mesh generator. Once the models are generated, a static gravity initialization is performed using the NIKE3D implicit finite element program. The bottom of the foundation has been fixed in the vertical direction for this analysis and the sides of the foundation have been given a zero displacement controlled boundary condition in the direction



normal to the foundation. NIKE3D computes reaction forces for nodal degrees of freedom with prescribed displacement boundary conditions. The reason for using boundary conditions on the sides of the foundation is that the canyon would open up during the gravity initialization without them, resulting in very high stresses in the dam. Displacement boundary conditions were used instead of fixed boundary conditions, because the DYNA3D model uses nonreflecting boundary conditions on these same sides. Nonreflecting boundary conditions do not work with fixed boundary conditions, but will work if reaction forces have been placed at the same location as the nonreflecting boundary conditions. After the static initialization, the reaction forces from the zero displacement boundary conditions are gathered and imported into the DYNA3D finite element model. The seismic analyses are run using the DYNA3D explicit finite element program. The foundation has been completely fixed in all directions at the bottom of the dam. 3.3% mass proportional damping for the fundamental mode has been assumed for all analyses presented in this study. Once the analyses are complete, the post-processor GRIZ is used to view and analyze the results.



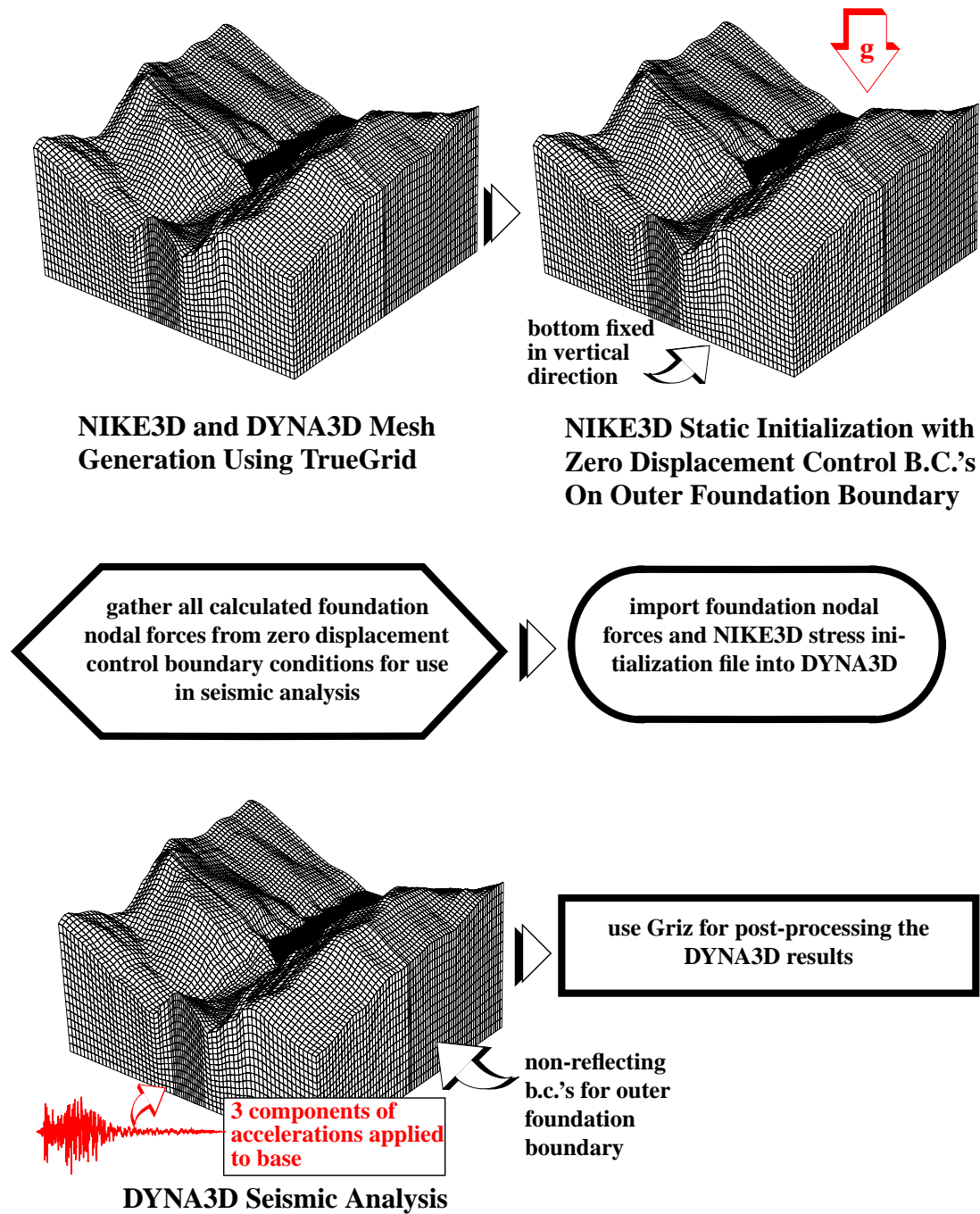
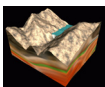


FIGURE 52. Morrow Point Dam finite element analysis procedure for base acceleration method.

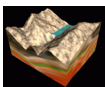
7.1 Procedure for Force Time History Method

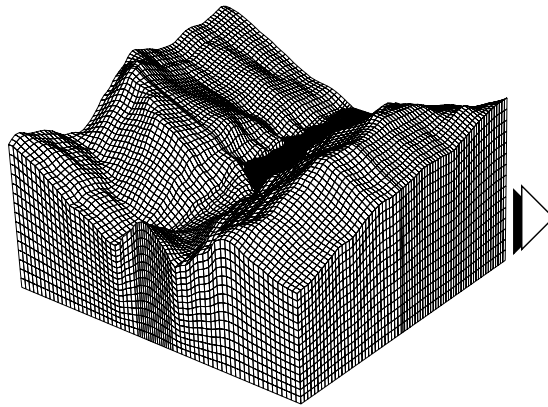
This procedure, as already discussed, is primarily the same as the base acceleration method except for the following:



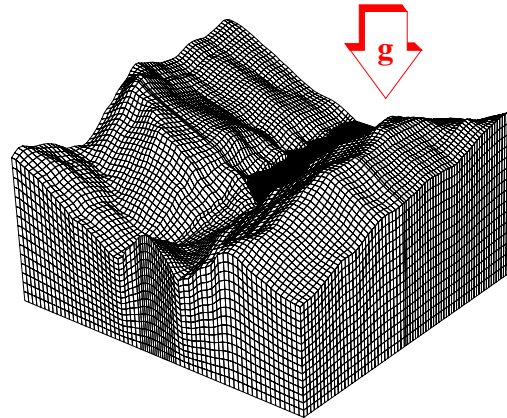
- zero displacement control boundary conditions were used on the entire outer foundation boundary (including the bottom surface)
- non-reflecting boundary conditions were used on the entire outer foundation boundary in DYNA3D
- the nodal forces from NIKE3D's displacement control boundary conditions were imported into DYNA3D and implemented on the bottom surface as well as the sides of the foundation mesh
- 3 components of force time histories were applied to the base, instead of base accelerations, for the seismic analysis in DYNA3D

Please review Section 2.1 on how to calculate the force time histories used for this procedure. It should be noted that because the non-reflecting boundary conditions resist the forces being applied at the base of the foundation, an additional force was applied to the base in order to take that into account.

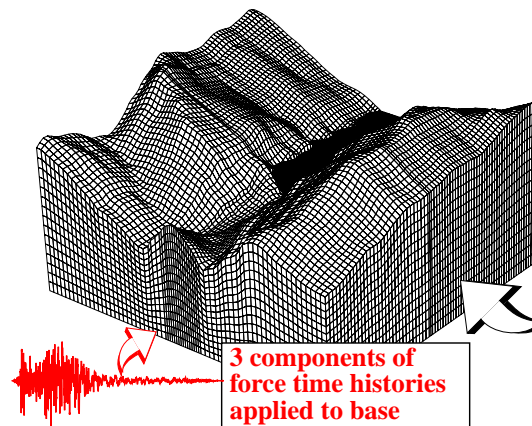
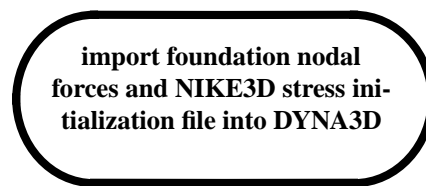
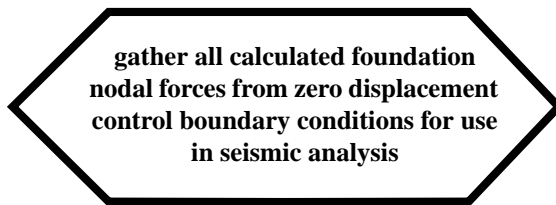




NIKE3D and DYNA3D Mesh Generation Using TrueGrid



NIKE3D Static Initialization with Zero Displacement Control B.C.'s On Entire Outer Foundation Boundary

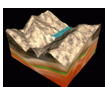


DYNA3D Seismic Analysis



non-reflecting
b.c.'s for entire
outer foundation
boundary

FIGURE 53. Morrow Point Dam finite element analysis procedure for force time history method.

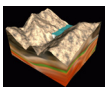


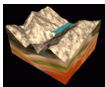
8.0 Natural Modeshapes and Frequencies of Morrow Point Dam

To assist in validating the finite element models, a number of eigenanalyses were completed and the results were compared with those computed by Fenves et al [Ref 5], Tan and Chopra [Ref 16], and Duron and Hall [Ref 4]. Furthermore, Duron and Hall performed forced vibration tests on Morrow Point Dam using two Kinemetrics vibration generators (5000 lb force capacity each) placed side by side on the dam crest at the center of the dam. Symmetric responses were obtained by shaking in the upstream-downstream direction, and antisymmetric responses were obtained by shaking in the cross canyon direction. The modal results from the literature and Duron and Hall's experimental data along with LLNL's eigenvalue analyses are compared in Figure 54. To calculate the mode shapes and frequencies, gravity and hydrostatic loads were placed on the structural model using NIKE3D. Once the static initialization was complete, an eigenanalysis could be completed using NIKE3D and the stress and displacement fields calculated by the static analysis. It should be noted that the coefficient of friction for the contraction joints was 0.0 for the static initialization and 0.3 for the eigenvalue analysis. Three finite element models were studied

1. contraction joint slide surface model with empty reservoir and fixed base
2. contraction joint slide surface model with diagonal added mass and fixed base
3. homogeneous/monolithic model with diagonal added mass and fixed base

The modeshapes and frequencies for both the contraction joint slide surface model with diagonal added mass and the homogeneous/monolithic model with diagonal added mass are given in Figure 55 and Figure 56. Table 7 compares the frequencies of four different NIKE3D finite element models and Table 8 compares the NIKE3D results with the experimentally determined frequencies. The "S" and "A" determinations on the values given in the table correspond to a symmetric or an antisymmetric response. By examining the data, it can be concluded that the contraction joint slide surfaces have the effect of lowering the frequencies in comparison to the results from a model that uses discrete elements. By comparing the contraction joint models to that of the homogeneous/monolithic model, the contraction joints appear to make the structure more flexible. In addition, the homogeneous model appears to match the experimentally determined fundamental model, whereas the contraction joint model more closely matches better with the second symmetric mode. Finally, the reservoir has the effect of lowering the natural frequencies of the structure.





Vibration Frequency ^a (hz)									
Fennes et al			Tan and Chopra		Duron and Hall			NIKE3D [†]	
Empty Reservoir	Full Reservoir		Empty Reservoir	Full Reservoir	Experimental	Computed with Incompressible Water	Computed with Compressible Water	Contraction Joint Slide Surface Model with Empty Reservoir	Contraction Joint Slide Surface Model with Diagonal Added Mass
	Full Added Mass	Diagonal Added Mass							
3.23	2.80	2.5	4.27	2.82	S ^b : 2.95 A ^c : 3.3	S: 3.29 A: 3.31	S: 3.05 A: 3.31	3.75	2.51
3.56	3.02	2.61	-	-	S: 3.95 A: 6.21	S: 5.33 A: 6.76	S: 4.21 A: 6.35	4.4	2.59
5.63	5.63	3.64	-	-	S: 5.4	S: 6.11	S: 5.96	6.4	3.9
5.96	4.82	3.98	-	-	-	-	-	6.7	4.2
6.43	5.78	4.38	-	-	-	-	-	7.4	4.8
									5.76

a.All computed frequencies used a rigid foundation.

b.The 'S' corresponds to a symmetric shake.

c.The 'A' corresponds to an antisymmetric shake.

FIGURE 54. Comparison between measured and computed resonant frequencies for Morrow Point Dam.

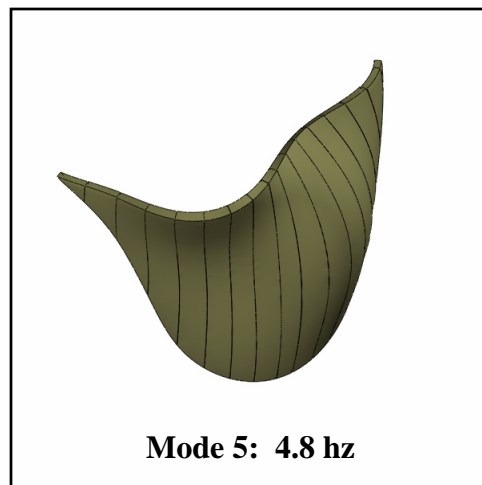
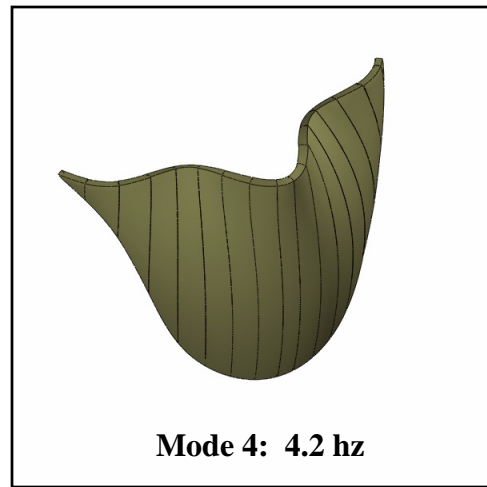
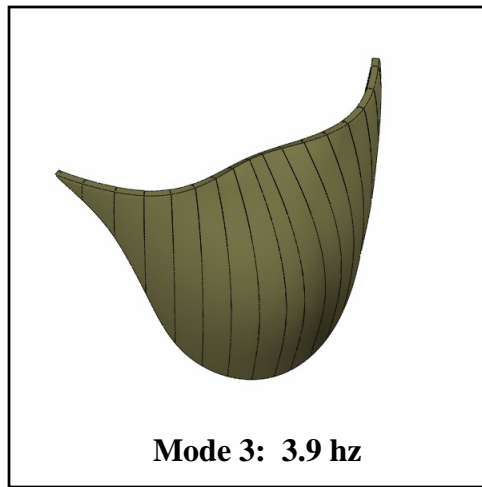
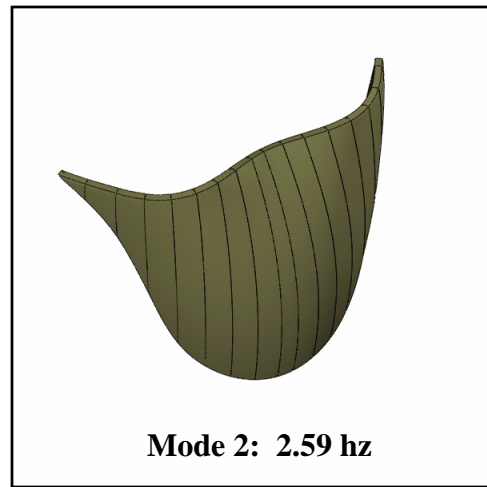
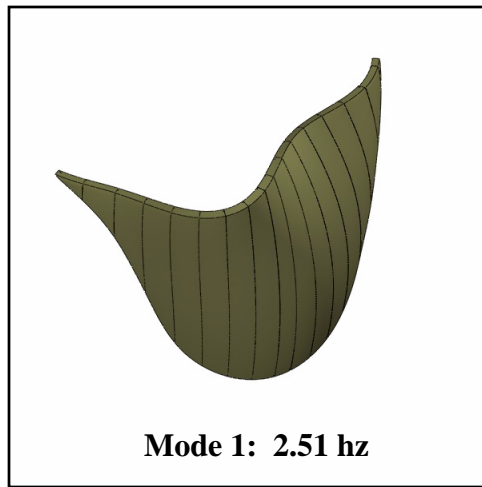
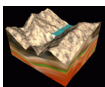


FIGURE 55. Modeshapes for contraction joint slide surface model with diagonal added mass.



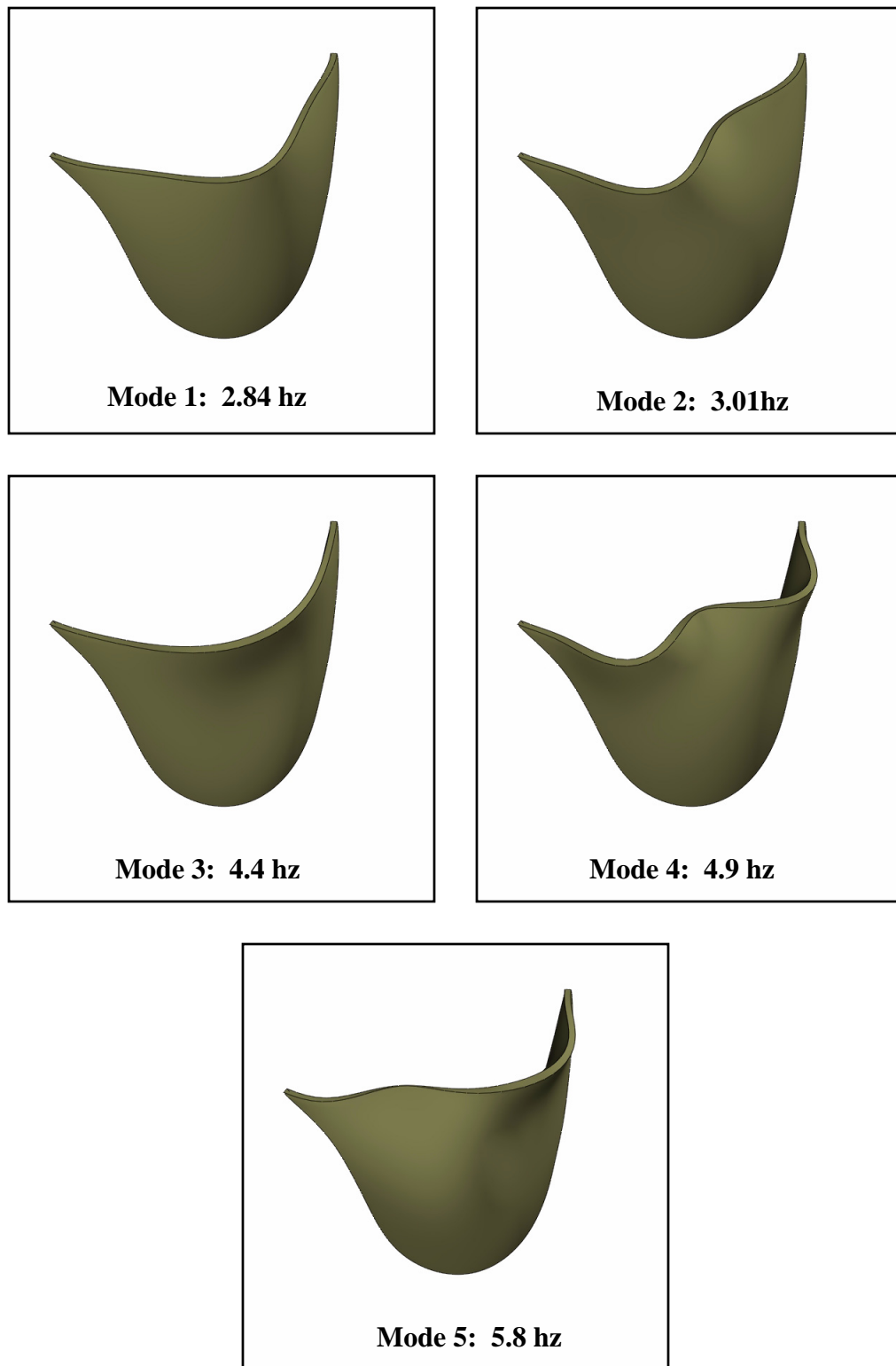


FIGURE 56. Modeshapes for homogeneous/monolithic model with diagonal added mass.

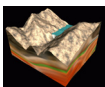
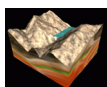


TABLE 7. Comparison of NIKE3D calculated modeshapes and frequencies.

NIKE3D Frequencies (hz)				
Mode	Model with Discrete Elements and No Added Mass	Model with Discrete Elements and Added Mass	Model with Contraction Joint Slide Surfaces and Added Mass	Homogeneous/ Monolithic Model and Added Mass
1	4.2 (A)	2.56 (S)	2.51 (A)	2.84 (S)
2	4.4 (S)	2.76 (A)	2.59 (S)	3.01 (A)
3	6.4 (S)	3.9 (S)	3.9 (S)	4.4 (S)
4	6.9 (S)	4.3 (S)	4.2 (S)	4.9 (S)
5	8.2 (A)	5.3 (A)	4.8 (A)	5.76 (A)

TABLE 8. Comparison of NIKE3D models with experimental data.

Mode	Duron and Hall Experimental Data	Homogenous/ Monolithic Model with Added Mass	Model with Contraction Joint Slide Surfaces and Added Mass
1	2.95 (S)	2.84 (S)	2.59 (S)
2	3.3 (A)	3.01 (A)	2.51 (A)
3	3.95 (S)	4.4 (S)	3.9 (S)
4	5.4 (S)	4.9 (S)	4.2 (S)
5	6.21	5.76 (A)	4.8 (A)



9.0 Free Vibrational Studies of Morrow Point Dam

A NIKE3D eigenvalue analysis was performed on the homogeneous/monolithic finite element models that included both the water explicitly modeled and the flexible foundation; however, the water modes were the most dominant modes and it became too difficult to find the important structural modes. Therefore, the fundamental frequencies (of this model) were attempted to be found by exciting a free vibrational response of the dam. The first and second symmetric mode are extremely similar, and it became difficult to excite the first symmetric mode. Two analyses were completed. The first was able to recover the second symmetric mode and because of the very clean response of the top center of the dam, the damping in the structural model was easily verified. The second free vibration analysis was able to show the first mode of the structure. Figure 57 shows the response shapes for the first three symmetric modes that were experimentally and computationally observed by Duron and Hall. Note the similarities between the first and the second modes.

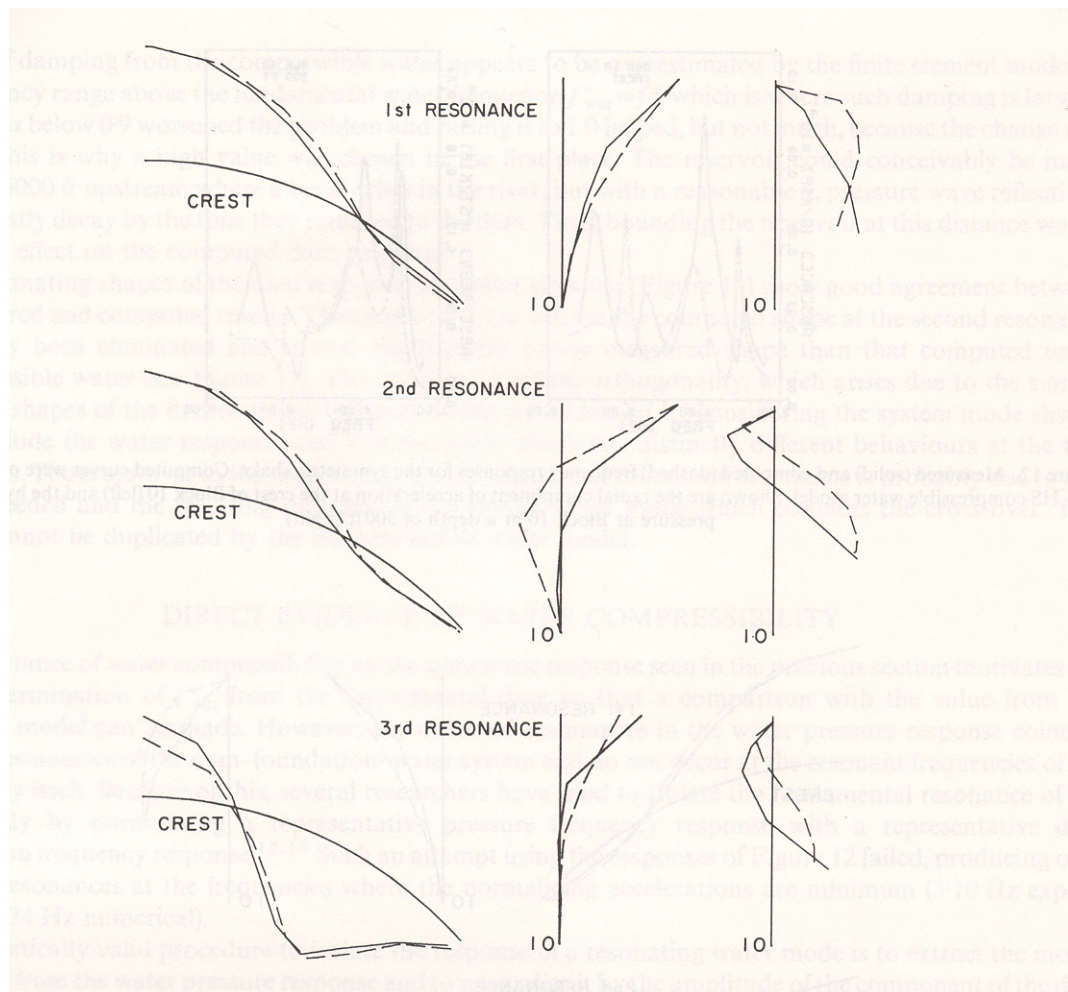
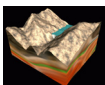


FIGURE 57. Measured (solid) and computed (dashed) response shapes at the first three resonances of the symmetric shake. Shown are the radial component of acceleration at the dam crest (left) and center cantilever (middle) and the hydrodynamic pressure at center block (right) [Ref 4].



9.1 Line forces ramped up over 4 seconds

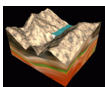
The finite element model for this free vibration test is the homogeneous/monolithic dam model with the water explicitly modeled and a flexible foundation. The left abutment wedge was tied to the foundation with a tied contact surface for this analysis. To achieve a free vibrational response of the dam, forces were applied at the centerline of the dam and ramped up over 4 seconds and then released (see Figure 58). The upstream-downstream displacement time history for a node at top center is shown in Figure 59. For lightly damped systems the damping ratio can be determined from [Ref 2]

$$\zeta = \frac{1}{2\pi j} \ln \frac{u_i}{u_{i+1}} \quad (\text{EQ 53})$$

By placing the displacements at the different peaks into this equation, the damping for the first two cycles were 5.1%, a reasonable damping value for this type of motion. A Fast Fourier Transform (FFT) was also completed on the upstream-downstream displacement time history (Figure 59). The first mode that appears is a mode at 4.37 hz. This correlates well with the second symmetric mode of the homogeneous/monolithic model that had a fixed base and diagonal added mass. A comparison of the mode shapes for the homogeneous model with Westergaard added mass and the free vibrational response is shown in Figure 60. The free vibrational response was scaled by 1500 and the mode shapes were scaled by 1.5. The free vibrational response appears to more closely resemble the third mode of the homogeneous model with Westergaard added mass and a fixed base. Therefore, the objective of the second free vibration test was to excite more of the first mode.

9.2 Pressure at top of dam ramped up over 4 seconds

In an attempt to excite more of the first mode, a region that encompasses the top center of the dam was loaded with a pressure ramped up over 4 seconds and then released (Figure 61). An FFT was also calculated for the upstream-downstream displacement time history at the top center node of the model. Four peaks were observed at 2.73 hz, 3.1 hz, 3.6 hz, and 4.4 hz. The 2.73 hz mode could easily correspond to the first mode observed in the homogeneous/monolithic model with Westergaard added mass. The fundamental frequency calculated using this model was 2.84 hz. The 3.1 hz and 4.4 hz peak could also correspond with the first antisymmetric mode and the second symmetric mode from the monolithic Westergaard added mass model. The Westergaard added mass model calculated these frequencies to be 3.01 and 4.4 hz.



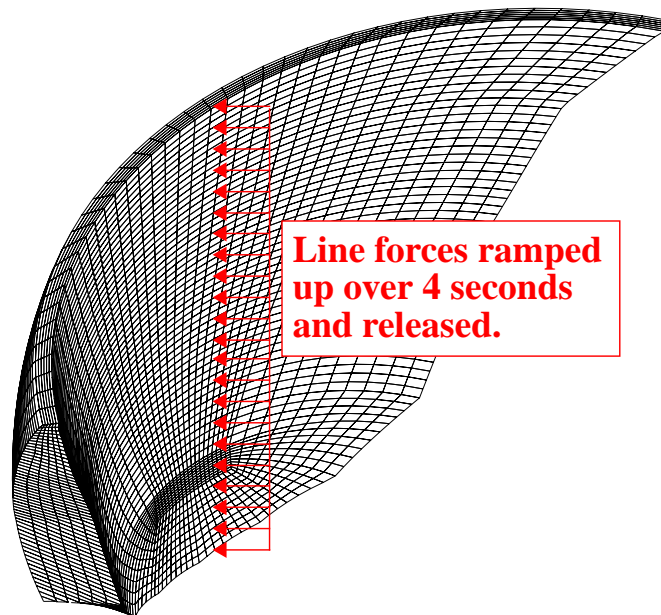
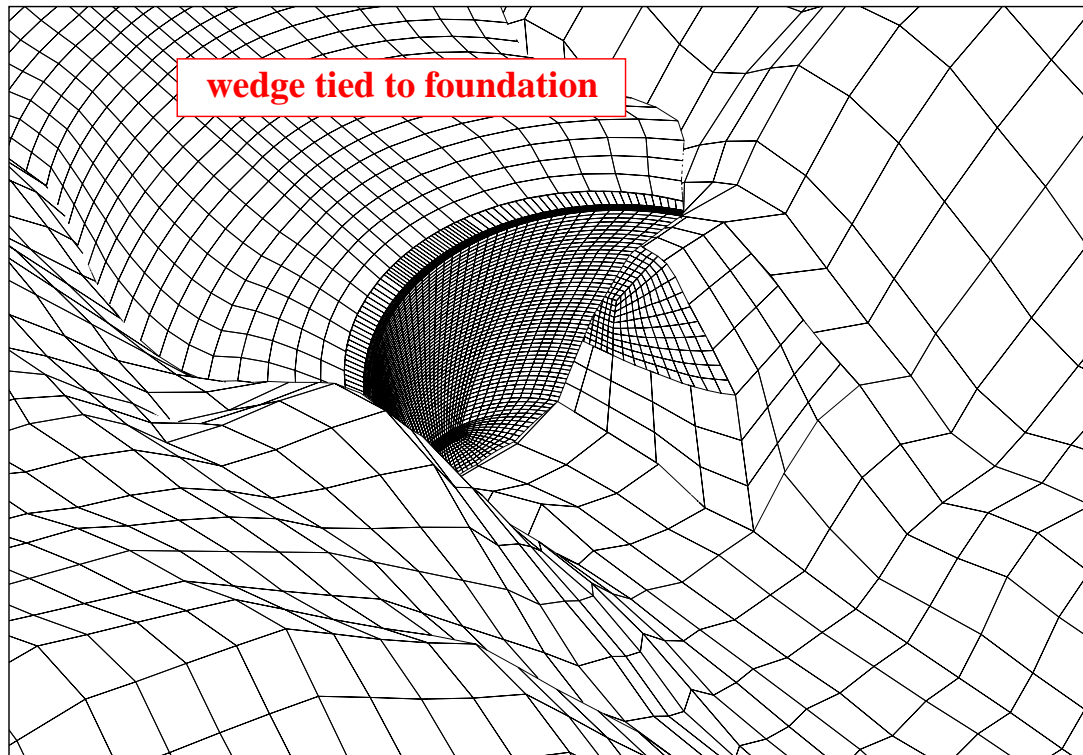
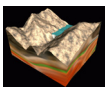


FIGURE 58. Finite element model and loading condition for first free vibrational analysis.



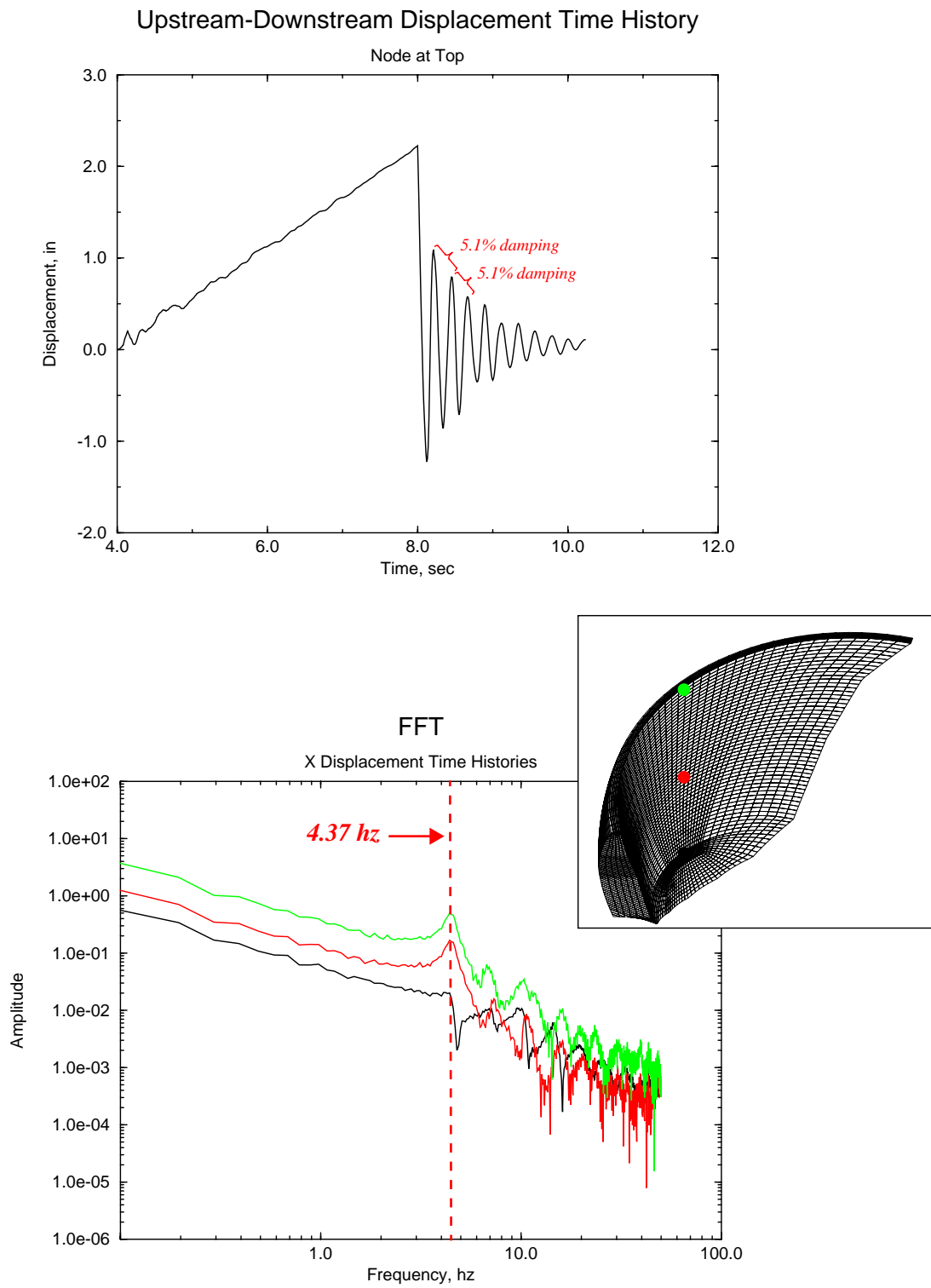
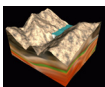
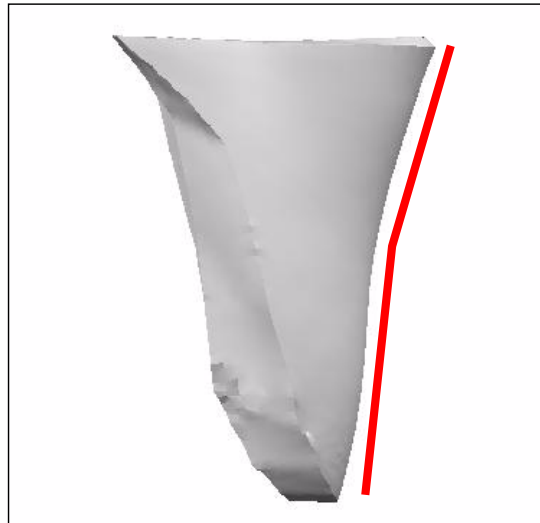


FIGURE 59. Upstream-downstream displacement time history of node at top center of dam (top) and the FFT of the upstream-downstream displacement time histories at three locations of the dam at center (bottom).

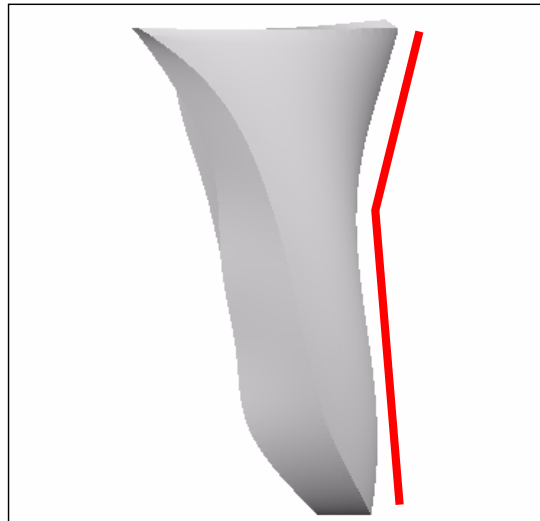


dsf = 1500.



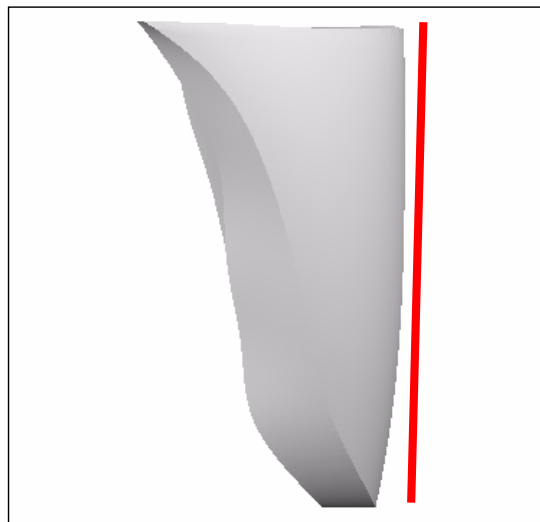
Line forces ramped
up over 4 seconds
and released

dsf = 1.5



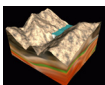
Eigenvalue analysis
of homogeneous
model with
Westergaard added
mass: Mode 3
(4.37 hz)

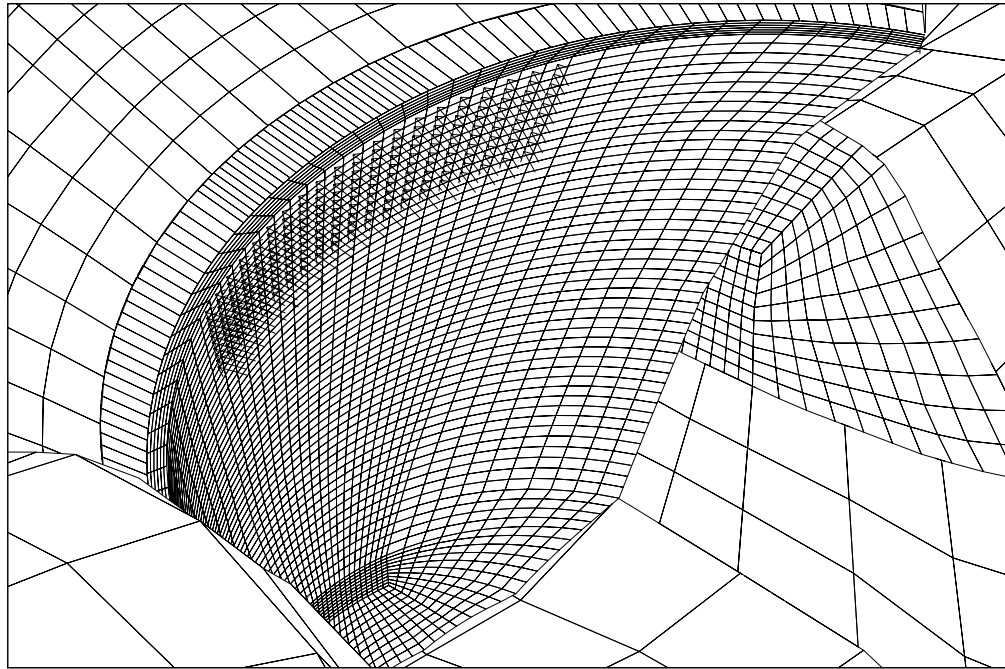
dsf = 1.5



Eigenvalue analysis
of homogeneous
model with
Westergaard added
mass: Mode 1
(2.84 hz)

FIGURE 60. Comparison of modeshapes between eigenvalue analyses and free vibrational response.





FFT

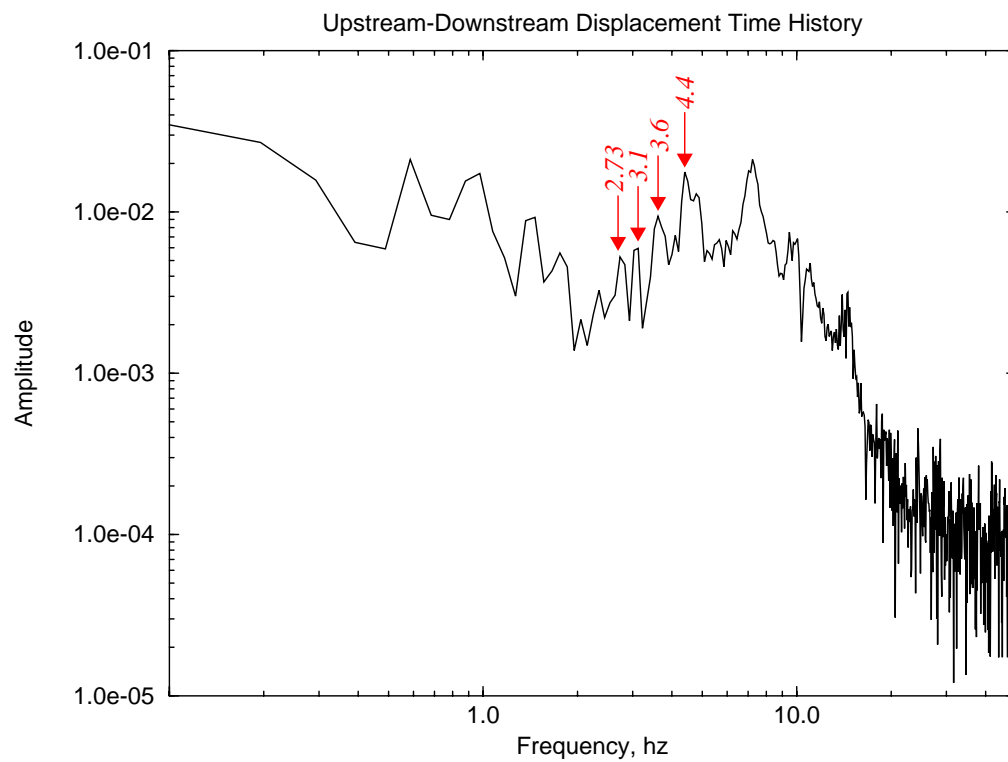
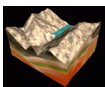


FIGURE 61. Pressure loading at top of dam for second free vibration test and the corresponding FFT of the upstream-downstream displacement time history from top center of dam.



10.0 NIKE3D Static Initialization

The gravity initialized model serves as the starting point for any additional simulations of the dam structure. The gravity initialization results in a static stress field and deformed geometry in the dam structure. Simple diagnostics of the initialized dam model, including the dam states of stress and natural vibrational characteristics, can be examined for a reality check. The entire dam structure is nominally in a state of high compression, with evidence of some tensile stresses at the upstream toe of the dam. With the expansion joint idealization explained in a previous section, the dam stresses resulting from gravity and hydrostatic loading for five different finite element models are as shown in Figure 62. The peak tensile stresses in the structure are near the unconfined tensile strength of concrete, but the area over which this is the case is very limited, and the stresses appear nominally. In addition, the static initialization stress state for the discrete element models and the models that use the contraction joint slide surface are very similar. It is also interesting to note that the region of high stresses seem to decrease when using a flexible foundation rather than a fixed base foundation.

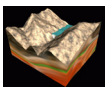
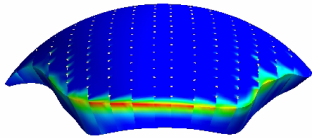
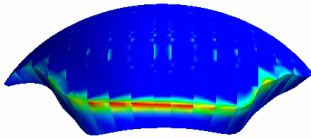
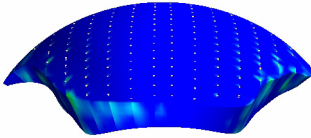
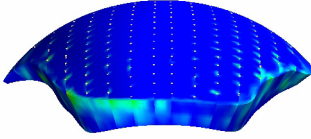
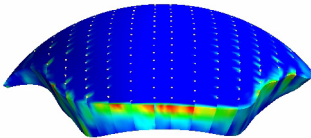
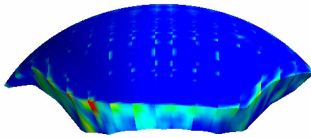
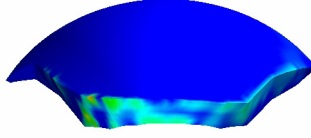


TABLE 1. Comparison of NIKE3D static initialization stress state.

Finite Element Model	NIKE3D stress state using discrete elements	NIKE3D stress state using contraction joint interface
Contraction Joint Finite Element Model with Rigid Foundation and Westergaard Added Mass		
Contraction Joint Finite Element Model with Flexible Foundation and Westergaard Added Mass		Simulation Not Analyzed
Contraction Joint Finite Element Model with Flexible Foundation and Water Explicitly Modeled		Simulation Not Analyzed
Contraction Joint Finite Element Model with Flexible Foundation, Water Explicitly Modeled, and Left Abutment Wedge		
Homogeneous/Monolithic Finite Element Model with Flexible Foundation, Water Explicitly Modeled, and Left Abutment Wedge		


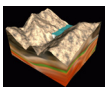
 Maximum tensile stress > 600 psi

FIGURE 62. Tensile stresses at the toe of the dam after gravity initialization of the model.



11.0 Transient Response of Morrow Point Dam to Earthquake Ground Motions

For the following transient analyses, the Cerro Prieto earthquake ground motions were used [Ref 12]. Each analysis was statically initialized using the NIKE3D implicit finite element program for both gravity and hydrostatic loads. Once the NIKE3D analyses was complete, a NIKE3D stress binary file, which contained stresses and displacements from the static initialization, was used as input into DYNA3D. This statically initialized state would be the first state in the DYNA3D explicit analysis. For each model described, a mass proportional damping of 3.3-3.4% for the first mode was used. It should be noted that NIKE3D and DYNA3D both output an extensive amount of data for each analysis. The following is a list of the data that was compiled for each analysis:

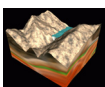
- maximum principal stresses (principal stress 1 and 3) and maximum arch and cantilever stresses
- peak displacements in the upstream-downstream, cross canyon, and vertical directions for the top center node of the dam
- peak contraction joint openings for two locations on the dam - the dam center and dam quarter point (NOTE: the gap openings were calculated by differencing the cross canyon component of displacement and only gives an approximation of the gap openings.)
- displacement time histories for the top center node of the dam and gap opening time histories for the dam center and dam quarter point.

11.1 Phase 1 Models

As discussed previously, there were two phases to this seismic study. The phase 1 finite element models focused on studying the differences between using a fixed base approach or a flexible foundation and also using Westergaard added mass versus modeling the reservoir explicitly. In addition, the phase 1 models allowed the opportunity to study the differences in using deconvolved ground motions as well as the response of the left abutment wedge. For the finite element models that explicitly modeled the reservoir, the reservoir was considered tied to the foundation with a sliding with voids slide surface between the reservoir and dam. In addition, the reservoir was restrained at the edge of the finite element model using a translational boundary condition; hence, there was a non-transmitting boundary at the far upstream side of the reservoir.

11.1.1 Rigid Foundation with Westergaard Added Mass

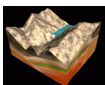
This model had a rigid foundation modeled by fixing the base of the dam finite element model and used Westergaard added mass for the fluid structure interaction. Because the base of the dam was fixed, the base accelerations given to LLNL by USBR could be used directly without deconvolving them or changing them to force time histories. This model also included discrete springs to model the behavior of the contraction joints. The peak upstream-downstream displacement was determined to be 3.5 inches. The maximum contraction joint opening was 0.29 inches at the dam quarter point. Table 2 lists the peak



stresses for both the static and dynamic analyses and the peak displacements. Figure 62 shows the gap opening time histories for the dam center and dam quarter point and shows the displacement time histories for the top center node of the dam. It should be noted that for all of the analyses considered here, the majority of the peak stresses occurred at the base or toe of the dam along the dam/foundation boundary. These stresses are highly localized and are not indicative of the stress field in the entire dam structure. For complete understanding of the stresses within the structure, it is important to review the stress time histories graphically.

TABLE 2. Seismic Analysis Results for Model with Rigid Foundation and Westergaard Added Mass

Analysis Type	Description		Value (lbs, in, sec)
Static	Cantilever	Tension	495
		Compression	1250
	Arch	Tension	596
		Compression	710
	Max Principal Stress 1		676
	Max Principal Stress 3		1690
Static & Dynamic	Cantilever	Tension	1840 (t=6.09 sec)
		Compression	2050 (t=7.32 sec)
	Arch	Tension	1580 (t=6.09 sec)
		Compression	2700 (t=5.43 sec)
	Max Principal Stress 1		2210 (t=6.09 sec)
	Max Principal Stress 3		2960 (t=7.32 sec)
Dynamic	Max Upstream-Downstream Displacement		3.5 (5.34 sec)
	Max Cross Canyon Displacement		-0.27 (t=7.34 sec)
	Max Vertical Displacement		0.85 (t=5.35 sec)
	Max Contraction Joint Opening at Dam Center		0.17 (t=5.82 sec)
	Max Contraction Joint Opening at Dam Quarter Point		0.29 (t=5.81 sec)



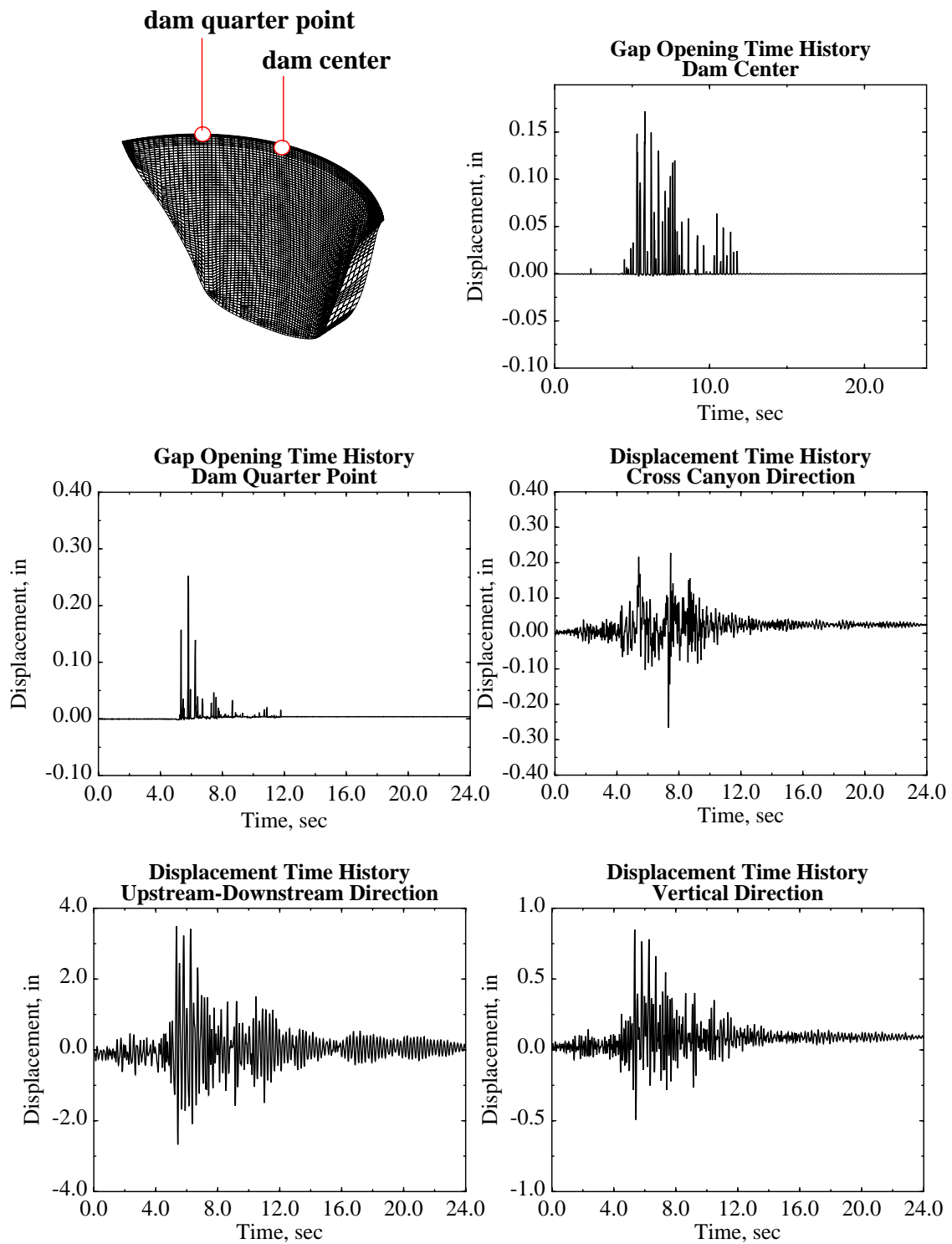
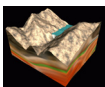


FIGURE 62. Displacement time histories for rigid foundation model with Westergaard added mass.



11.1.2 Flexible Foundation with Westergaard Added Mass

This model consisted of the dam finite element model tied to a flexible foundation using a tied contact surface in both NIKE3D and DYNA3D and used Westergaard added mass. This simulation also used the discrete springs to model the contraction joint behavior and used the base acceleration procedure; therefore, it had a reflecting boundary at the base of the foundation. Deconvolved ground motions were not used for this simulation. The peak displacement in the upstream-downstream direction was 7.4 inches and the peak contraction joint opening was 0.61 inches at the dam quarter point. The peak displacement is much larger than the analysis in Section 11.1.1 due to the use of a reflective boundary at the base and the use of non-deconvolved ground motions. A summary of the displacements and stresses are given in Table 3 and Figure 63.

TABLE 3. Seismic Analysis Results for Model with Flexible Foundation and Westergaard Added Mass

Analysis Type	Description		Value (lbs, in, sec)
Static	Cantilever	Tension	368
		Compression	1260
	Arch	Tension	623
		Compression	910
	Max Principal Stress 1		647
	Max Principal Stress 3		1630
Static & Dynamic	Cantilever	Tension	2050 (t=7.32 sec)
		Compression	4120 (t=7.33 sec)
	Arch	Tension	1690 (t=6.72 sec)
		Compression	3540 (t=6.52 sec)
	Max Principal Stress 1		2800 (t=5.33 sec)
	Max Principal Stress 3		4460 (t=7.33 sec)

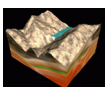
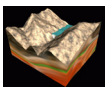


TABLE 3. Seismic Analysis Results for Model with Flexible Foundation and Westergaard Added Mass

Analysis Type	Description	Value (lbs, in, sec)
Dynamic	Max Upstream-Downstream Displacement	7.4 (t=6.33 sec)
	Max Cross Canyon Displacement	1.8 (t=6.76 sec)
	Max Vertical Displacement	1.4 (t=6.33 sec)
	Max Contraction Joint Opening at Dam Center	0.58 (t=7.69 sec)
	Max Contraction Joint Opening at Dam Quarter Point	0.61 (t=6.77 sec)



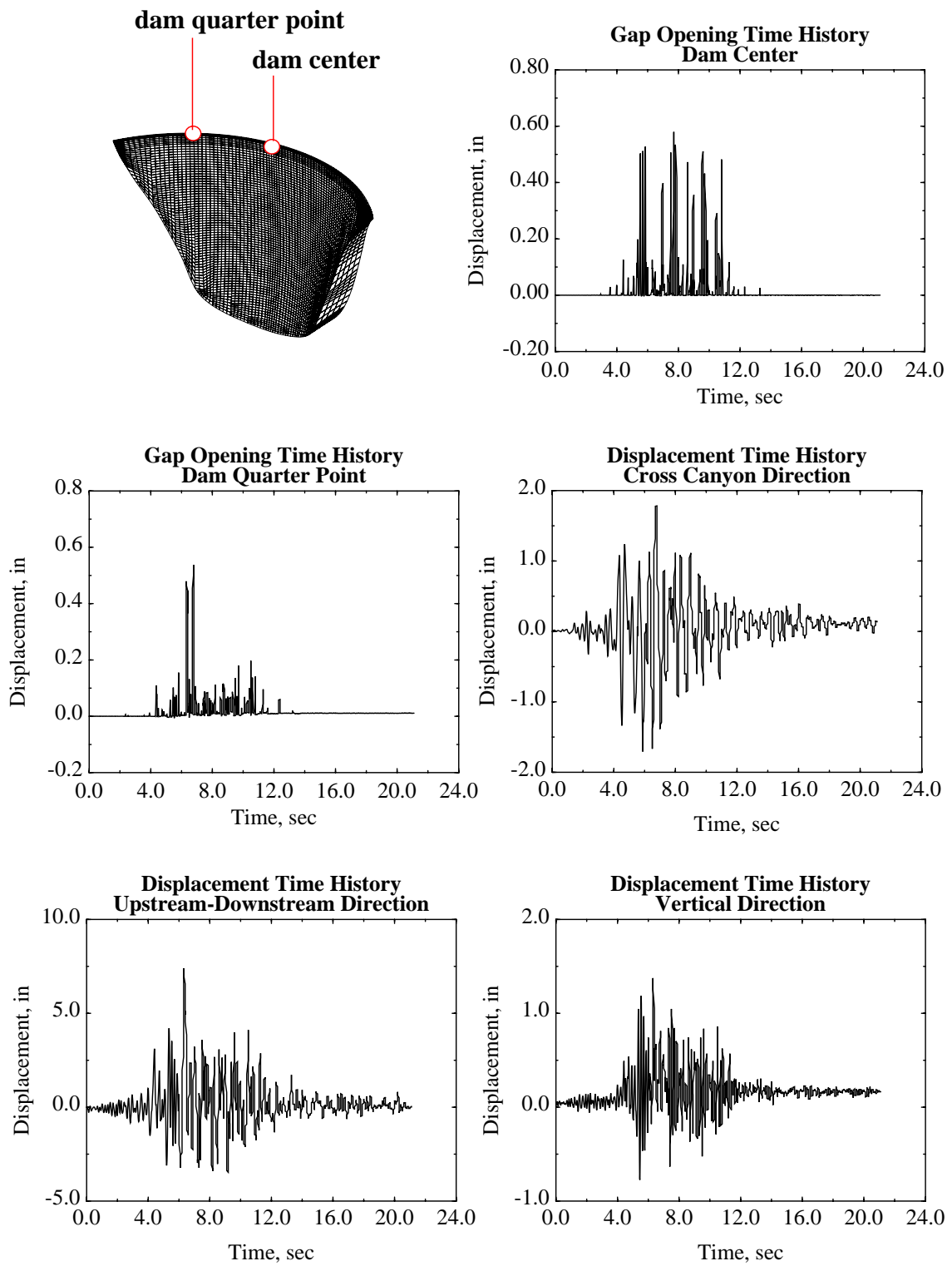
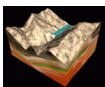


FIGURE 63. Displacement time histories for flexible foundation model with Westergaard added mass.

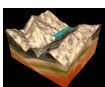


11.1.3 Flexible Foundation with Water Explicitly Modeled

This analysis is primarily the same as in Section 11.1.2 except that the reservoir effects are simulated by explicitly modeling the reservoir. The peak displacement is 14.1 inches and the maximum contraction joint opening is 4.97 inches at the dam quarter point (Table 4 and Figure 64). The much larger displacements appear to be caused by both the non-transmitting boundary at the base and the non-deconvolved ground motions with the fluid material enhancing these large displacements further than that seen in Section 11.1.2.

TABLE 4. Seismic Analysis Results for Model with Flexible Foundation and Water Explicitly Modeled

Analysis Type	Description		Value (lbs, in, sec)
Static	Cantilever	Tension	454
		Compression	1360
	Arch	Tension	505
		Compression	1020
	Max Principal Stress 1		620
	Max Principal Stress 3		1790
Static & Dynamic	Cantilever	Tension	3060 (t=7.69 sec)
		Compression	5610 (t=7.67 sec)
	Arch	Tension	3520 (t=1.57 sec)
		Compression	5770 (t=7.98 sec)
	Max Principal Stress 1		3770 (t=1.57 sec)
	Max Principal Stress 3		6100 (t=7.67 sec)
Dynamic	Max Upstream-Downstream Displacement		14.1 (t=7.78 sec)
	Max Cross Canyon Displacement		3.8 (t=6.6 sec)
	Max Vertical Displacement		1.66 (t=6.64 sec)
	Max Contraction Joint Opening at Dam Center		0.84 (t=7.8 sec)
	Max Contraction Joint Opening at Dam Quarter Point		4.97 (t=7.78 sec)



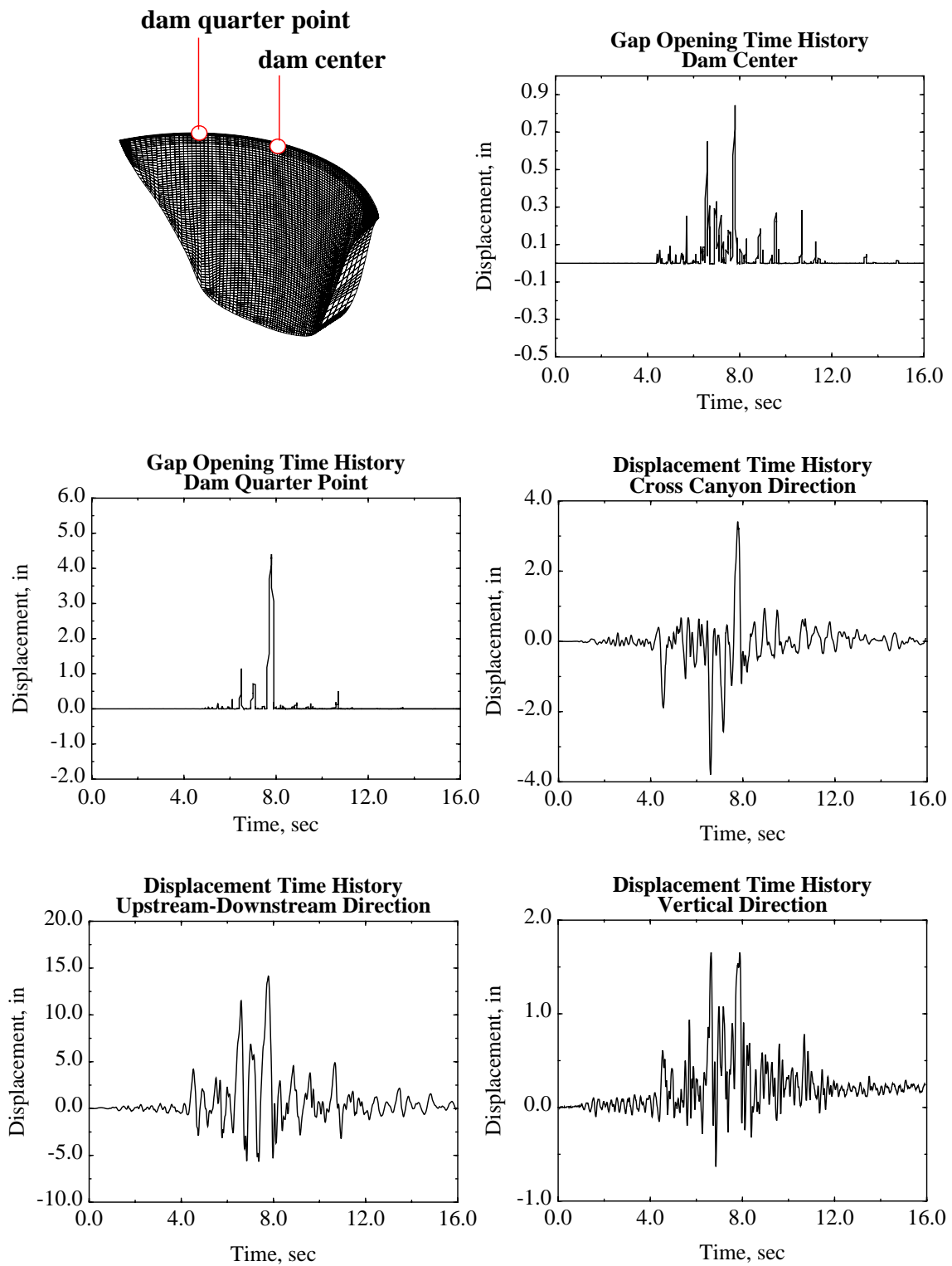
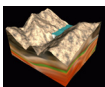


FIGURE 64. Displacement time histories for rigid foundation model with water explicitly modeled.



11.1.4 Flexible Foundation with Water Explicitly Modeled, Abutment Wedge Modeled, and Using Deconvolved Ground Motions

The finite element model for this analysis consisted of the dam (contraction joints modeled using discrete springs) tied to a flexible foundation, with the water explicitly modeled using a fluid material, and the left abutment wedge modeled. It should be noted that the left abutment wedge in this model used an older definition of the geometry or foliation planes than that described in Section 5.5 [Ref 13]. The coefficient of friction values did remain the same between the older definition and the updated definition of the abutment wedge. In addition, this model used the deconvolved ground motions determined by USBR [Ref 12]. However, this model used the base acceleration procedure and therefore had a reflective boundary at the base, which could amplify the dam motions somewhat. The stresses and displacements from this analysis are shown in Table 5 and Figure 65. The peak displacement was determined to be 5.27 inches and the peak contraction joint opening was 0.46 inches (dam quarter point). The deconvolved ground motions appear to have reduced the response of the dam, but the response is still greater than the fixed base model. This is most likely due to the non-transmitting boundary at the base.

The permanent wedge displacement in the cross canyon direction is 0.51 inches. To analyze the wedge, the wedge is considered tied to the foundation and dam in the NIKE3D static initialization. When the seismic analysis begins in DYNA3D, the wedge is released from the foundation by using a sliding with voids sliding interface at the three foliation planes. The friction values are also added at this point in the analysis. For this DYNA3D simulation, the wedge remains to be tied to the dam structure with a tied contact surface. Phase 2 will show simulations where the wedge is allowed to move freely from both the foundation and the dam structure. Figure 66 shows the wedge displacement time histories for the downstream corner of the abutment wedge.

TABLE 5. Seismic Analysis Results for Model with Flexible Foundation, Water Explicitly Modeled, and Left Abutment Wedge

Analysis Type	Description		Value (lbs, in, sec)
Static	Cantilever	Tension	531
		Compression	1610
	Arch	Tension	590
		Compression	2110
	Max Principal Stress 1		927
	Max Principal Stress 3		2430

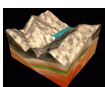
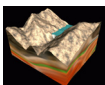


TABLE 5. Seismic Analysis Results for Model with Flexible Foundation, Water Explicitly Modeled, and Left Abutment Wedge

Analysis Type	Description		Value (lbs, in, sec)
Static & Dynamic	Cantilever	Tension	1440 (t=6.73 sec)
		Compression	2530 (t=6.53 sec)
	Arch	Tension	1210 (t=1.51 sec)
		Compression	3430 (t=6.83 sec)
	Max Principal Stress 1		2590 (t=6.71 sec)
	Max Principal Stress 3		3640 (t=6.82 sec)
Dynamic	Max Upstream-Downstream Displacement		5.27 (t=6.64 sec)
	Max Cross Canyon Displacement		0.79 (t=6.98 sec)
	Max Vertical Displacement		0.78 (t=6.4 sec)
	Max Contraction Joint Opening at Dam Center		0.45 (t=6.62 sec)
	Max Contraction Joint Opening at Dam Quarter Point		0.46 (t=6.62 sec)
	Permanent Wedge Displacement in Upstream-Downstream Direction		0.07
	Permanent Wedge Displacement in Cross Canyon Direction		0.51
	Permanent Wedge Displacement in Vertical Direction		0.06



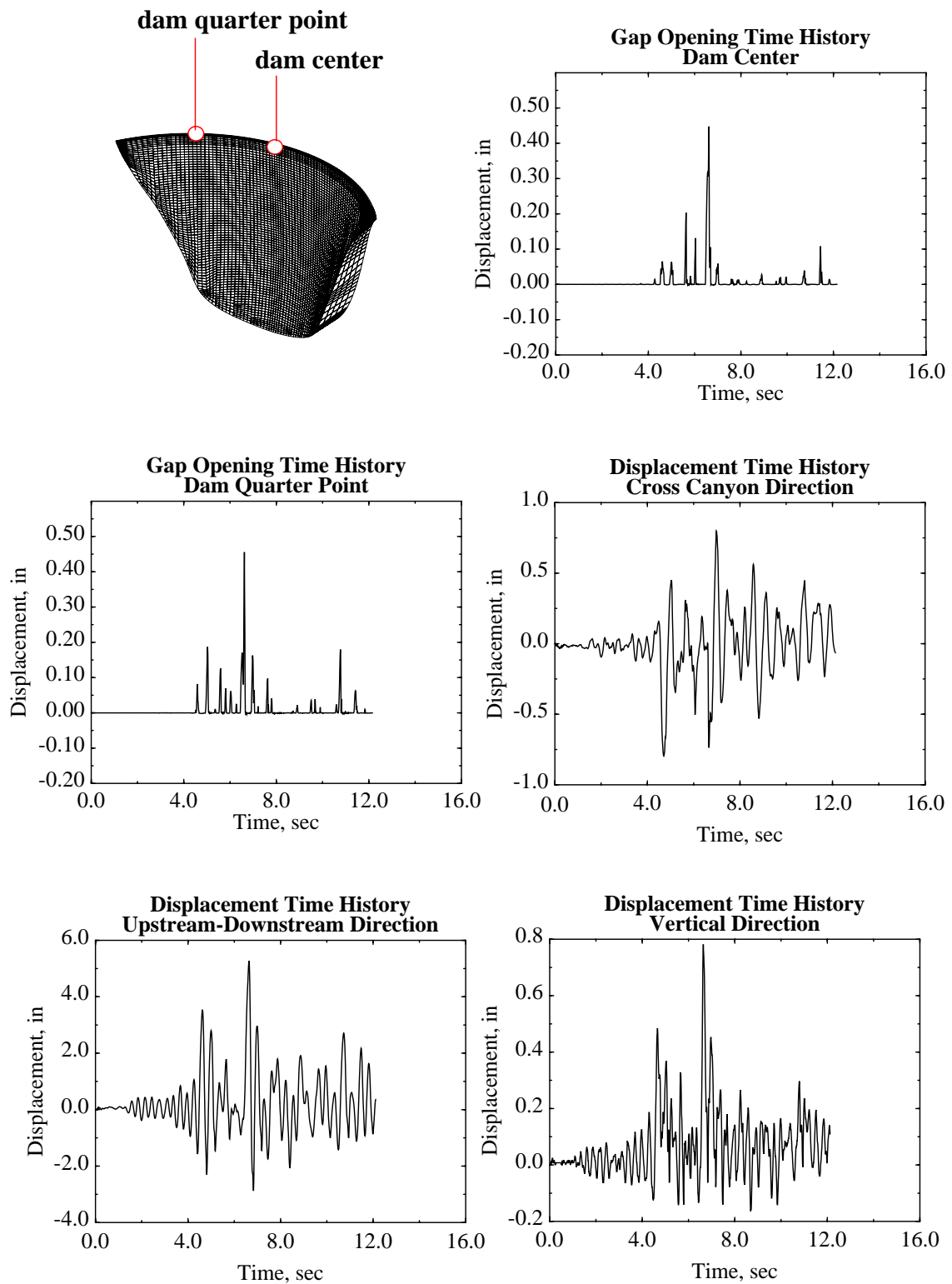
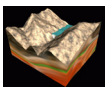


FIGURE 65. Displacement time histories for flexible foundation model and water explicitly modeled.



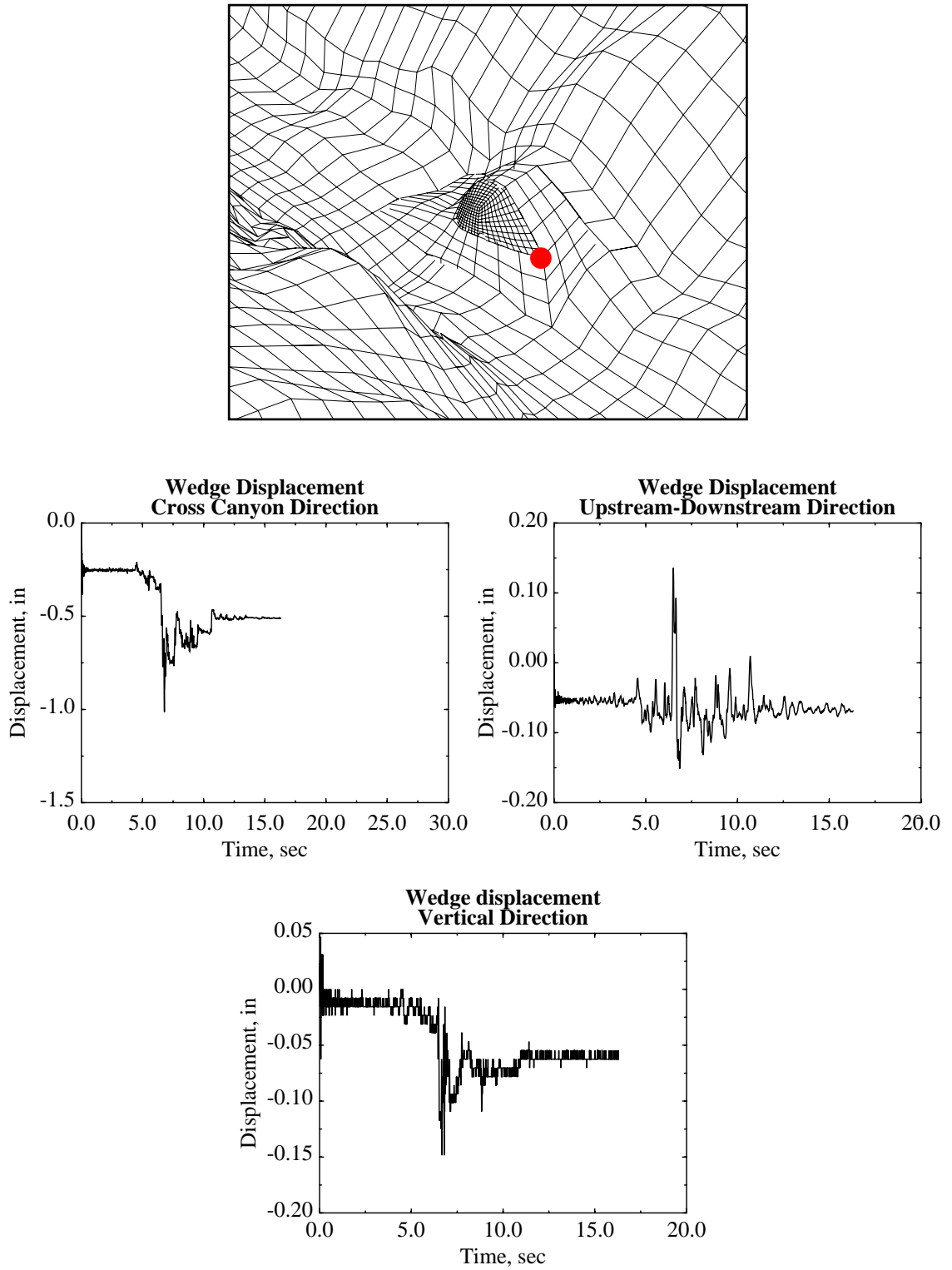
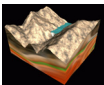


FIGURE 66. Wedge displacement time histories for model with flexible foundation and water explicitly modeled.



11.2 Phase 2 Models

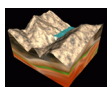
All of the phase 2 models incorporated a flexible foundation and an explicit reservoir model. One of the objectives of this second phase of the study was to start with a simple model and include more features or complexity in each analysis after the first in order to analyze the effects of each model feature. The left abutment wedge model for all of the phase 2 models was defined by the updated geometry, which is described in more detail in Section 5.5. Furthermore, all of the phase 2 models used the deconvolved ground motions and the force time history analysis procedure. Therefore, the reflecting boundary at the base has been effectively removed from these models. In contrast to the phase 1 models, a non-transmitting boundary was placed at the far upstream side of the reservoir and a sliding only contact was used between the reservoir/dam and reservoir/foundation surfaces. For the phase 2 analyses that model the contraction joints, the joints are modeled using the contraction joint interface and not the discrete springs.

11.2.1 Model 1: Homogeneous/Monolithic Dam

This model consisted of a homogeneous/monolithic dam model tied to a flexible foundation with the water explicitly modeled. In addition, the abutment wedge was tied to the foundation and tied to the dam. The peak displacement in the upstream-downstream direction is 2.76 inches, which is lower than the phase 1 model that used a rigid foundation and Westergaard added mass. Table 6 shows the peak displacements and stresses and Figure 67 shows the displacement time histories of the top center dam node.

TABLE 6. Seismic Analysis Results for Model 1

Analysis Type	Description	Value (lbs, in, sec)
Static	Max Principal Stress 1	613
	Max Principal Stress 3	2270
Static & Dynamic	Max Principal Stress 1	1580 (t=6.73 sec)
	Max Principal Stress 3	3810 (t=6.14 sec)
Dynamic	Max Upstream-Downstream Displacement	2.76 (t=6.49 sec)
	Max Cross Canyon Displacement	-0.7 (t=8.78 sec)
	Max Vertical Displacement	0.26 (t=7.4 sec)



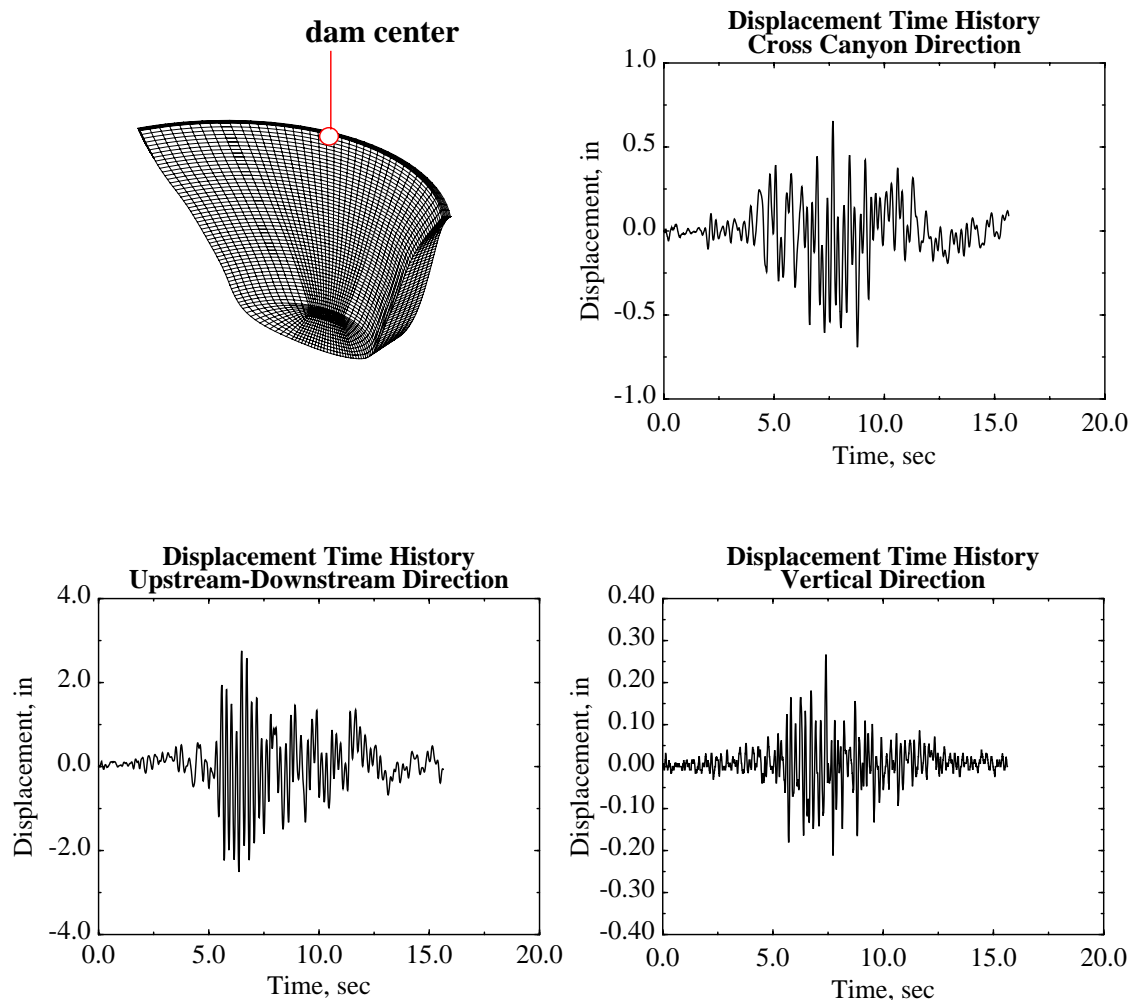
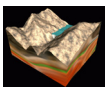


FIGURE 67. Displacement time histories for model 1.

11.2.2 Model 2: Model with Contraction Joints and Wedge Fixed

Model 2 consists of the contraction joint dam model with a flexible foundation, the water explicitly modeled and the abutment wedge fixed to the foundation and tied to the dam. Essentially this analysis is the same as that described in Section 11.2.1 except that the contraction joints are modeled using the new contraction joint slide surface. The peak upstream-downstream displacement is 2.6 inches and the peak contraction joint opening at the dam quarter point is 0.052 inches. Analyzing the simulation carefully, however, revealed a peak contraction joint opening near the left abutment of 0.375 inches. Table 7 and Figure 68 show the stresses and displacements from this analysis. As one may notice from the gap opening time histories, there appears to be a “gap” in both the negative and positive directions. This is mainly due to an artifact of how the gaps were calculated. Because the gaps were calculated simply by taking the difference in cross canyon dis-



placements from two coincident nodes on a contraction joint along the upstream side of the dam, the response of the nodes can be one of two things:

- the two nodes along the contraction joint separate giving either a positive or negative number (depending on the coordinate system being used and which node is differenced from the other).
- or the two nodes can slide past each other in the upstream-downstream direction and therefore it can appear that one node (because of the curved geometry of the dam) has moved more in the cross canyon direction than the other, giving a gap of opposite sign than if the two nodes had actually separated.

TABLE 7. Seismic Analysis Results for Model 2

Analysis Type	Description		Value (lbs, in, sec)
Static	Cantilever	Tension	1500
		Compression	2470
	Arch	Tension	615
		Compression	3540
	Max Principal Stress 1		2110
	Max Principal Stress 3		4230
Static & Dynamic	Cantilever	Tension	1410 (t=6.6 sec)
		Compression	2830 (t=6.64 sec)
	Arch	Tension	2280 (t=1.84 sec)
		Compression	2710 (t=4.76 sec)
	Max Principal Stress 1		2540 (t=1.84 sec)
	Max Principal Stress 3		3780 (t=4.7 sec)

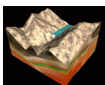
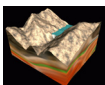


TABLE 7. Seismic Analysis Results for Model 2

Analysis Type	Description	Value (lbs, in, sec)
Dynamic	Max Upstream-Downstream Displacement	2.6 (t=6.55 sec)
	Max Cross Canyon Displacement	0.97 (t=6.62 sec)
	Max Vertical Displacement	0.51 (t=6.61 sec)
	Max Contraction Joint Opening at Dam Center	0.0425 (t=6.59 sec)
	Max Contraction Joint Opening at Dam Quarter Point	0.052 (t=7.77 sec)
	Max Contraction Joint Opening Near Left Abutment	0.375 (t=6.58 sec)



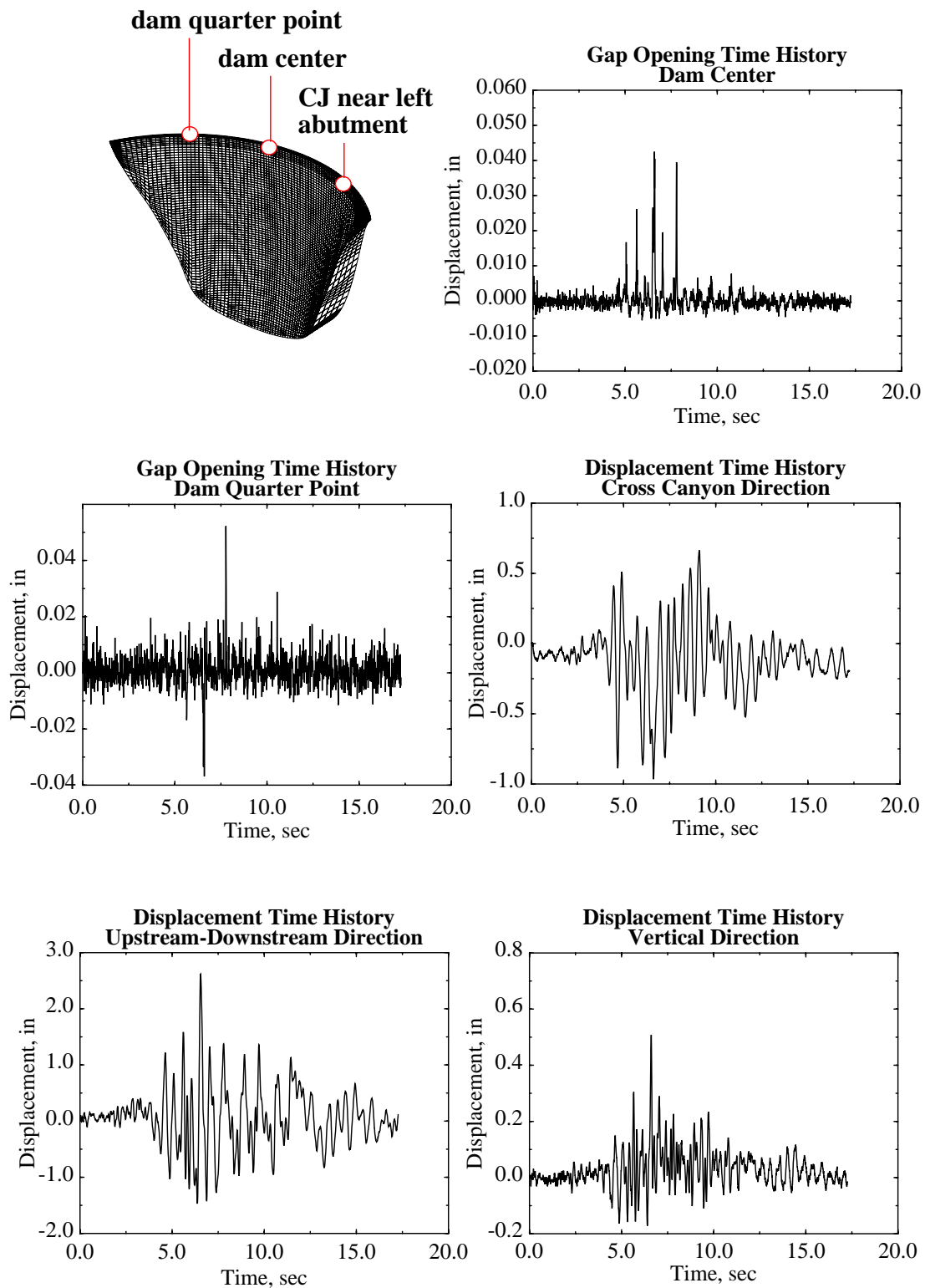
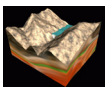


FIGURE 68. Displacement time histories for model 2.



11.2.3 Model 3: Model with Contraction Joints and Wedge Not Fixed to Foundation

The only difference between model 3 and model 2 is that the left abutment wedge was allowed to slide freely from the foundation, but not the dam. In other words, there were sliding with voids sliding interfaces between the wedge and the foundation and a tied contact surface between the dam and abutment wedge. The peak upstream-downstream displacement was 2.73 inches and the peak contraction joint opening was 0.054 inches. In addition, the permanent wedge displacement in the cross canyon direction was 0.4 inches, which is less than that calculated from the phase 1 model (Section 11.1.4). The stresses and displacement are shown in Table 8 and Figure 69. The abutment wedge corner displacements are given in Figure 70.

TABLE 8. Seismic Analysis Results for Model 3

Analysis Type	Description		Value (lbs, in, sec)
Static	Cantilever	Tension	1250
		Compression	2310
	Arch	Tension	589
		Compression	3540
	Max Principal Stress 1		1760
	Max Principal Stress 3		3540
Static & Dynamic	Cantilever	Tension	2590 (t=0.13 sec)
		Compression	6630 (t=0.19 sec)
	Arch	Tension	2530 (t=0.13 sec)
		Compression	6660 (t=0.19 sec)
	Max Principal Stress 1		3490 (t=0.13 sec)
	Max Principal Stress 3		6070 (t=0.13 sec)

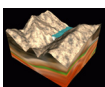
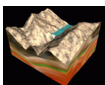


TABLE 8. Seismic Analysis Results for Model 3

Analysis Type	Description	Value (lbs, in, sec)
Dynamic	Max Upstream-Downstream Displacement	2.73 (t=6.55 sec)
	Max Cross Canyon Displacement	0.91 (t=6.63 sec)
	Max Vertical Displacement	0.56 (t=6.61 sec)
	Max Contraction Joint Opening at Dam Center	0.05 (t=6.58 sec)
	Max Contraction Joint Opening at Dam Quarter Point	0.054 (t=6.58 sec)
	Permanent Wedge Displacement in Upstream-Downstream Direction	0.2
	Permanent Wedge Displacement in Cross Canyon Direction	0.4
	Permanent Wedge Displacement in Vertical Direction	0.04



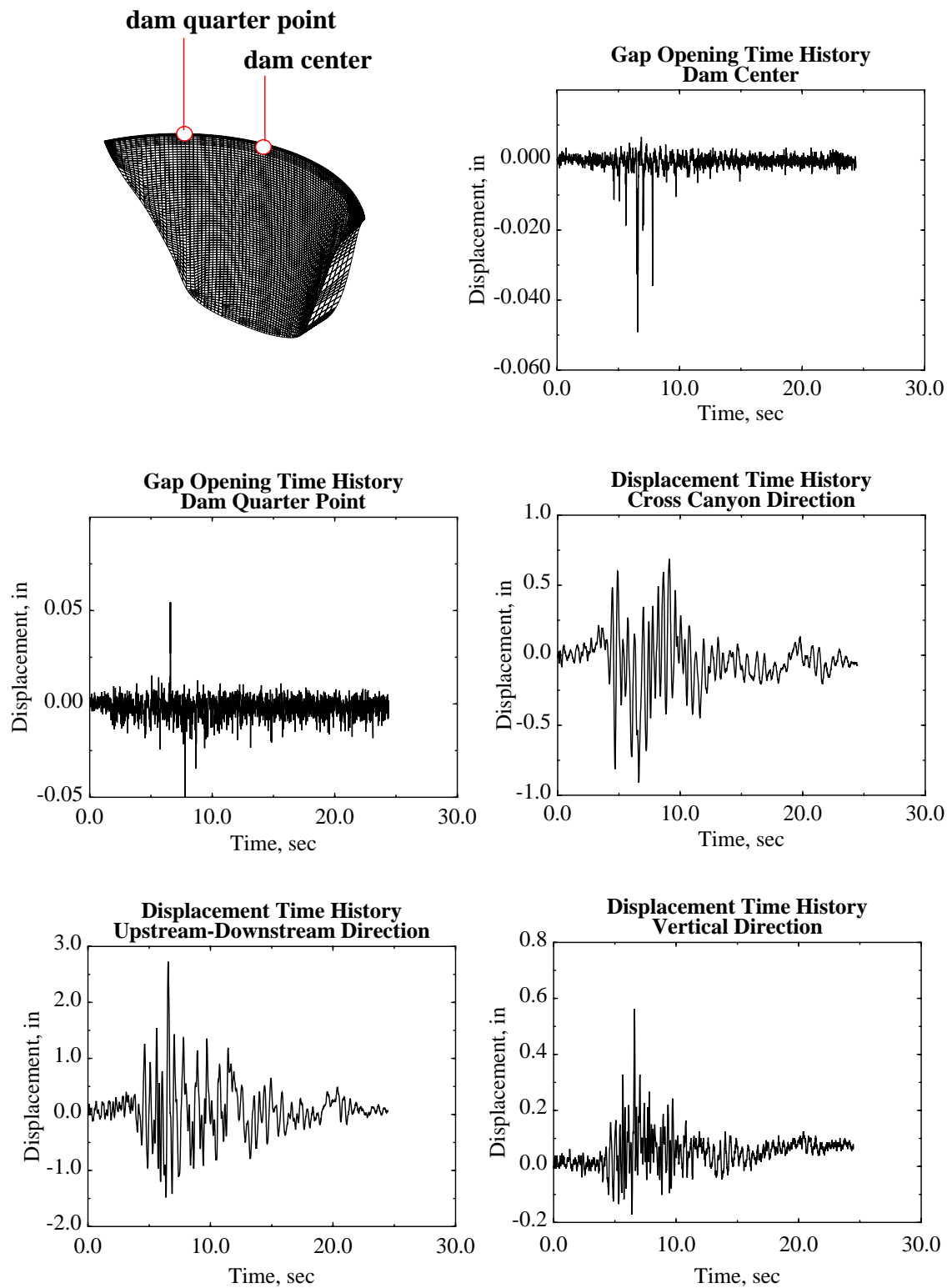
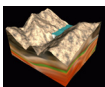


FIGURE 69. Displacement time histories for model 3.



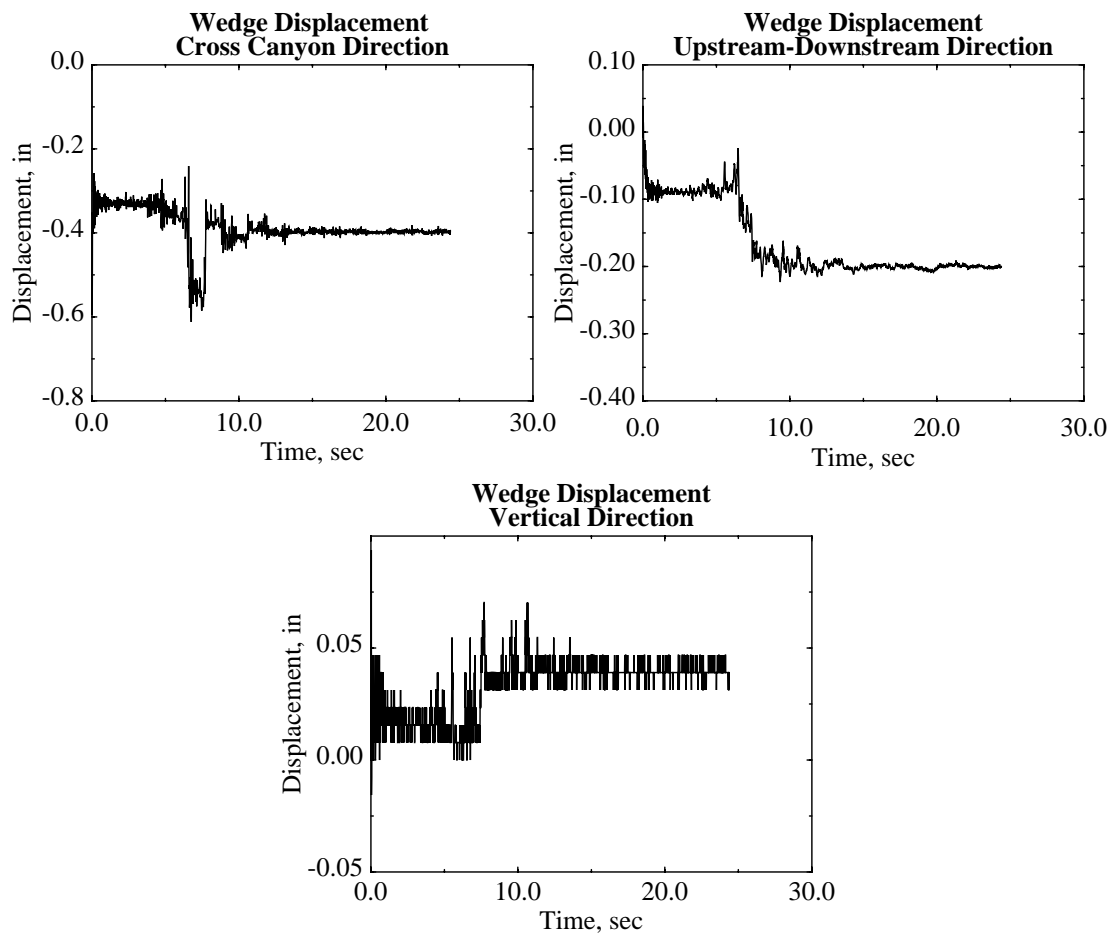
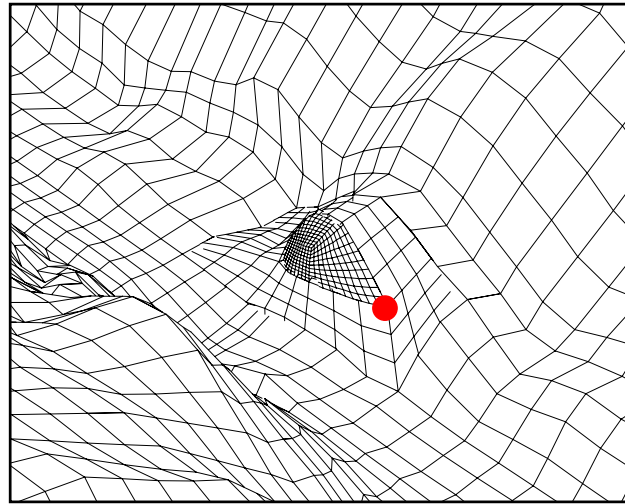
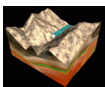


FIGURE 70. Wedge displacement time histories for model 3.



11.2.4 Model 3: Model with Contraction Joints and Wedge Not Fixed to Foundation or Dam

This model studied the effect of providing a sliding with voids slide surface between the dam and the left abutment wedge. Therefore, the wedge in this model was allowed to move freely from the dam and the foundation. A coefficient of friction value of 0.3 was assumed between the dam and the wedge. The peak upstream-downstream displacement of the top center of the dam increased from 2.73 inches to 2.83 inches and the permanent wedge displacement in the cross canyon direction increased from 0.4 inches to 0.83 inches (see Table 9, Figure 71, and Figure 72). By not restricting the wedge by placing a sliding with voids interface between the dam and wedge, the permanent wedge displacement essentially doubled. The peak contraction joint opening near the left abutment was calculated to be 0.65 inches, much larger than the opening calculated in model 2 of 0.375 inches.

TABLE 9. Seismic Analysis Results for Model 3

Analysis Type	Description		Value (lbs, in, sec)
Static	Cantilever	Tension	1100
		Compression	2170
	Arch	Tension	625
		Compression	2210
	Max Principal Stress 1		1560
	Max Principal Stress 3		3180
Static & Dynamic	Cantilever	Tension	1300 (t=6.62 sec)
		Compression	2750 (t=7.45 sec)
	Arch	Tension	958 (t=9.29 sec)
		Compression	2610 (t=4.76 sec)
	Max Principal Stress 1		1940 (t=6.60 sec)
	Max Principal Stress 3		3770 (t=4.76 sec)

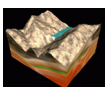
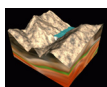


TABLE 9. Seismic Analysis Results for Model 3

Analysis Type	Description	Value (lbs, in, sec)
Dynamic	Max Upstream-Downstream Displacement	2.83 (t=6.55 sec)
	Max Cross Canyon Displacement	0.92 (t=6.63 sec)
	Max Vertical Displacement	0.59 (t=6.61 sec)
	Max Contraction Joint Opening at Dam Center	0.052 (t=6.62 sec)
	Max Contraction Joint Opening at Dam Quarter Point	0.025 (t=6.54 sec)
	Max Contraction Joint Opening Near Left Abutment	0.65 (t=6.56 sec)
	Permanent Wedge Displacement in Upstream-Downstream Direction	0.04
	Permanent Wedge Displacement in Cross Canyon Direction	0.83
	Permanent Wedge Displacement in Vertical Direction	0.008



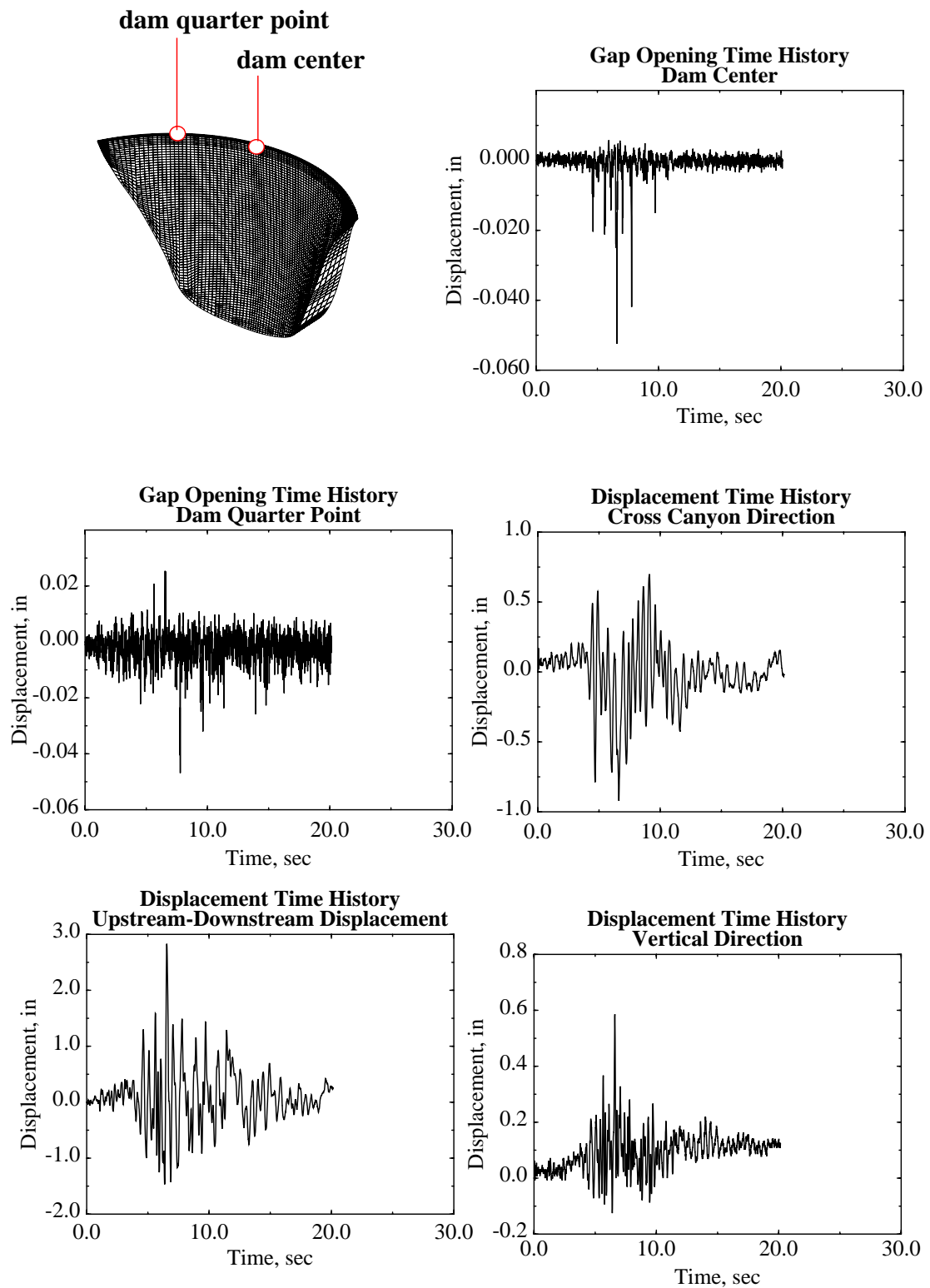
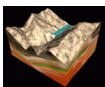


FIGURE 71. Displacement time histories for model 3.



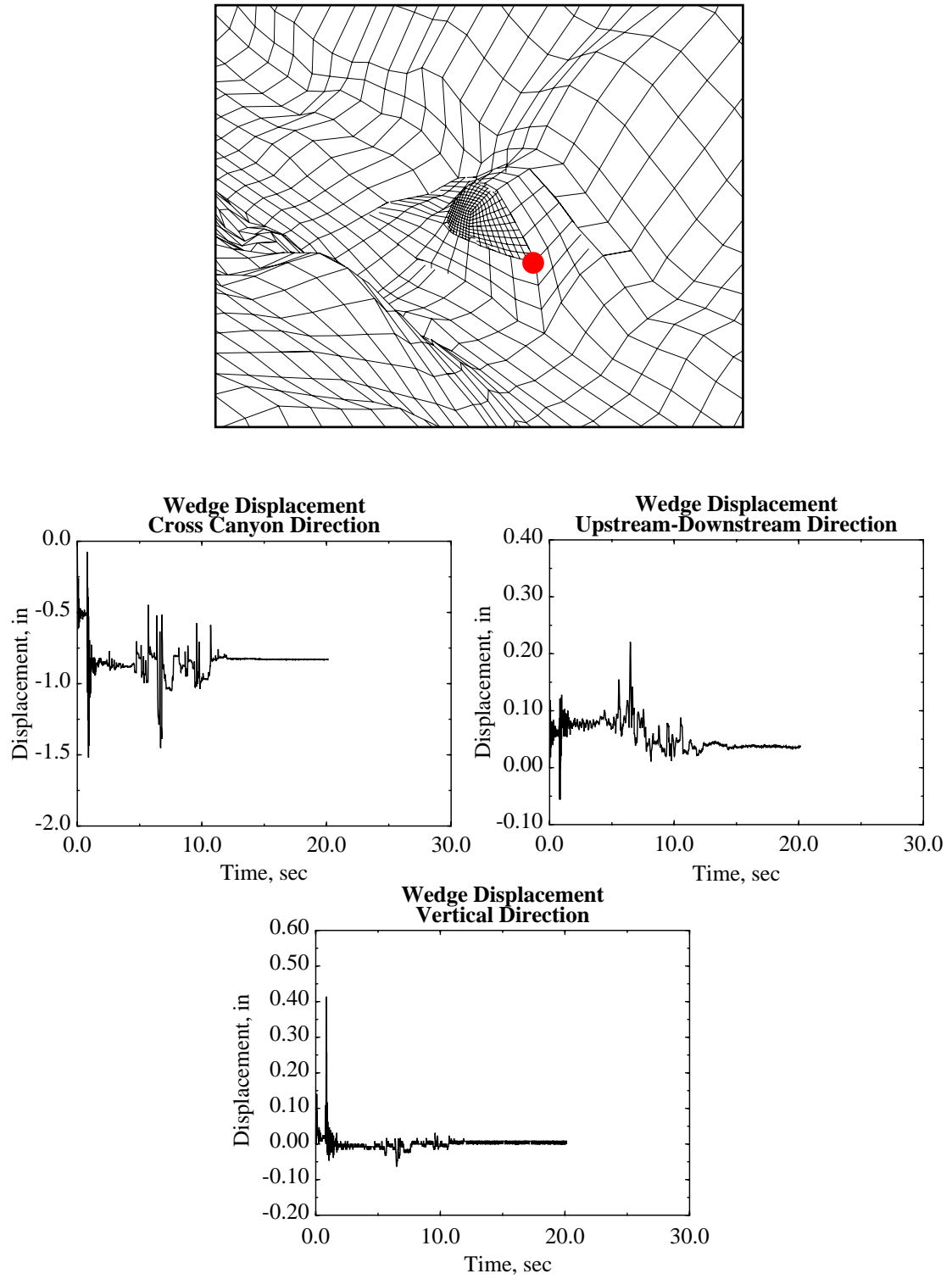
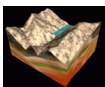
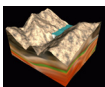


FIGURE 72. Wedge displacement time histories for model 3.



11.2.5 Model 4: Model of Foundation Only with Wedge Fixed

This model was used extensively to verify that the force time history procedure was indeed working as intended. As we saw in Section 2.1, the topography had an effect of reducing the response across the entire spectra at the base of the dam. In addition to verifying that the force time histories applied at the base of the dam would give reasonable motions in comparison to the USBR developed ground motions, a comparison was also completed between using base accelerations, and therefore a non-transmitting boundary at the base of the foundation, and using force time histories and a transmitting boundary at the base. Figure 73 and Figure 74 show an acceleration and an acceleration response spectra comparison (at a node at the base of the dam) between the two procedures. The plots clearly show that the response is higher when using a reflective boundary at the base. The higher response is more pronounced in the upstream-downstream direction, as well.



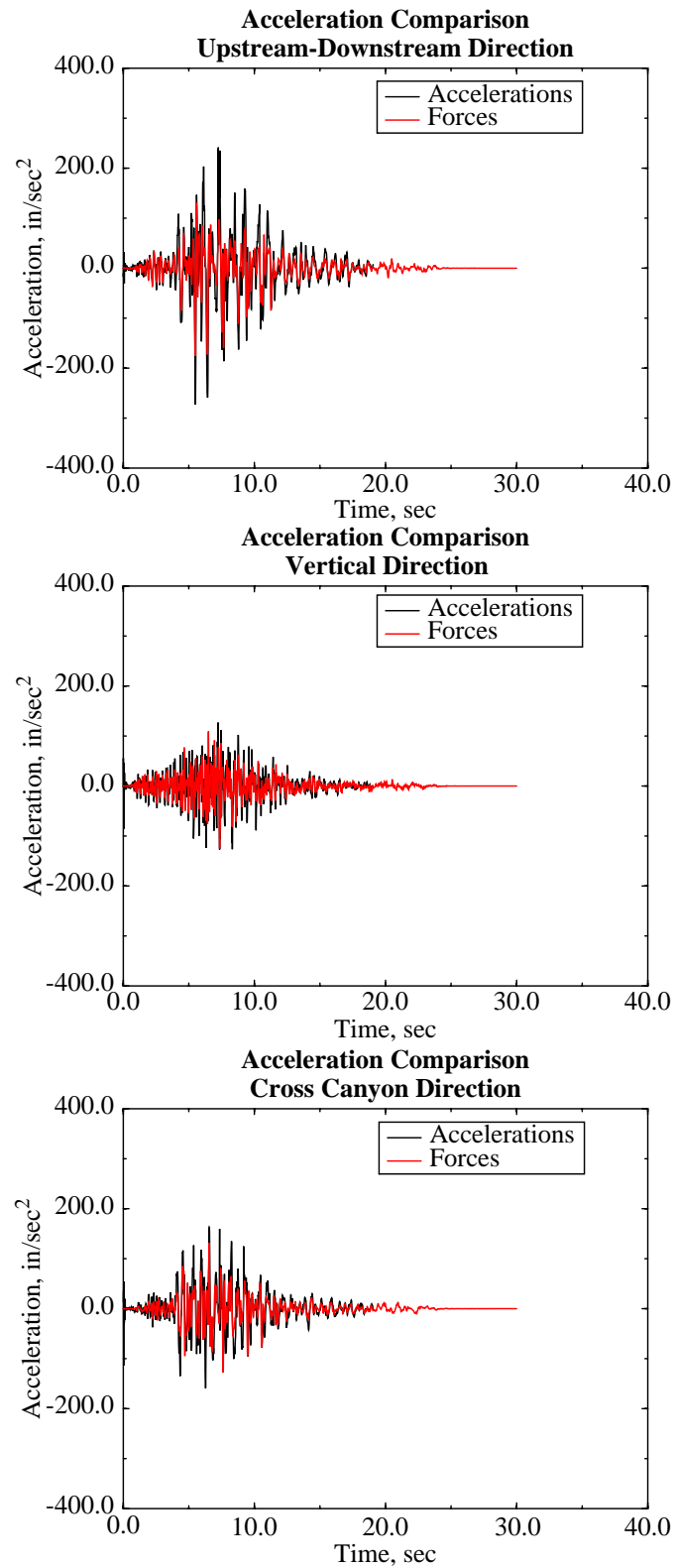
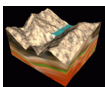


FIGURE 73. Comparison between using force time histories or base accelerations at the base of the foundation. Accelerations taken at dam/foundation interface.



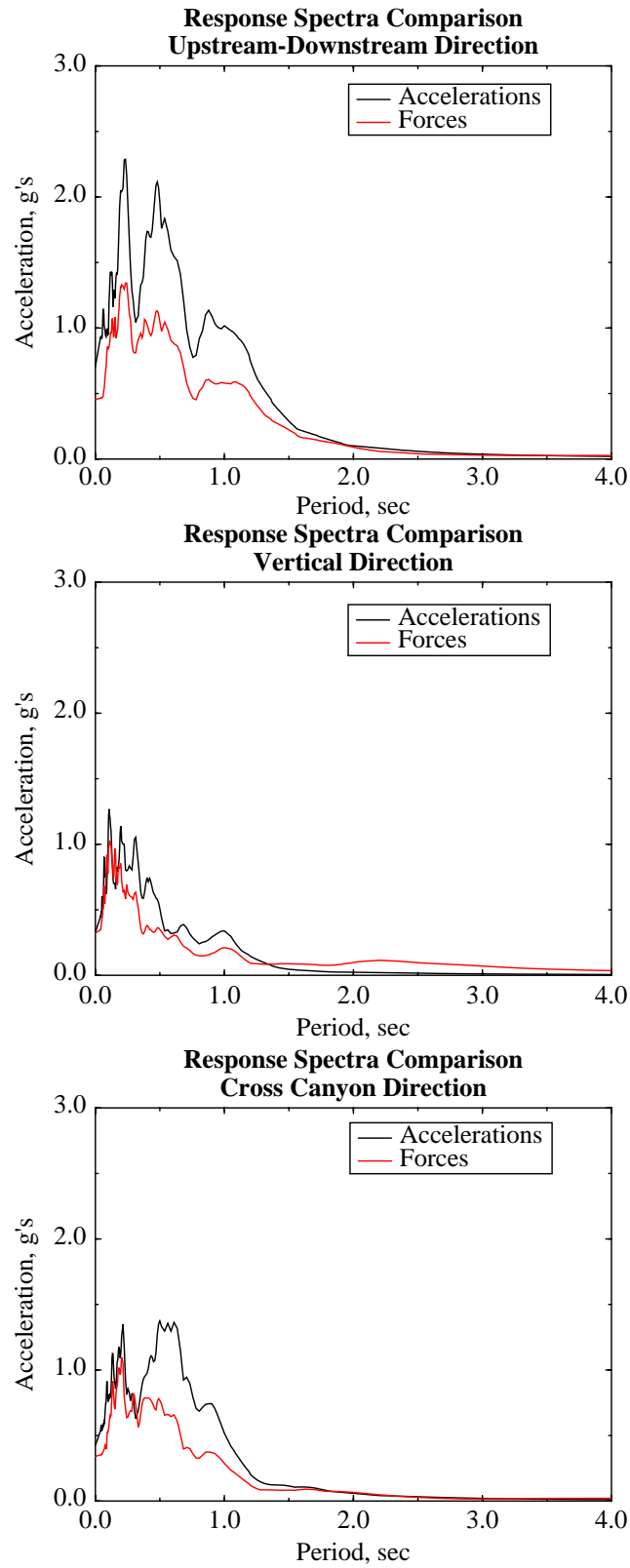
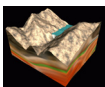
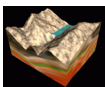


FIGURE 74. Acceleration response spectra comparison between using force time histories or base accelerations at the base of the foundation. Accelerations taken at dam/foundation interface.



11.2.6 Model 5: Model of Foundation Only with Wedge Not Fixed

There was a question as to whether or not the foundation wedge would slide on its own during an earthquake without adding the forces from the dam and the reservoir. Therefore, model 5 includes only the foundation and the left abutment wedge. The permanent wedge displacement is 0.43 inches in the cross canyon direction (as shown in Figure 75 and Table 10).



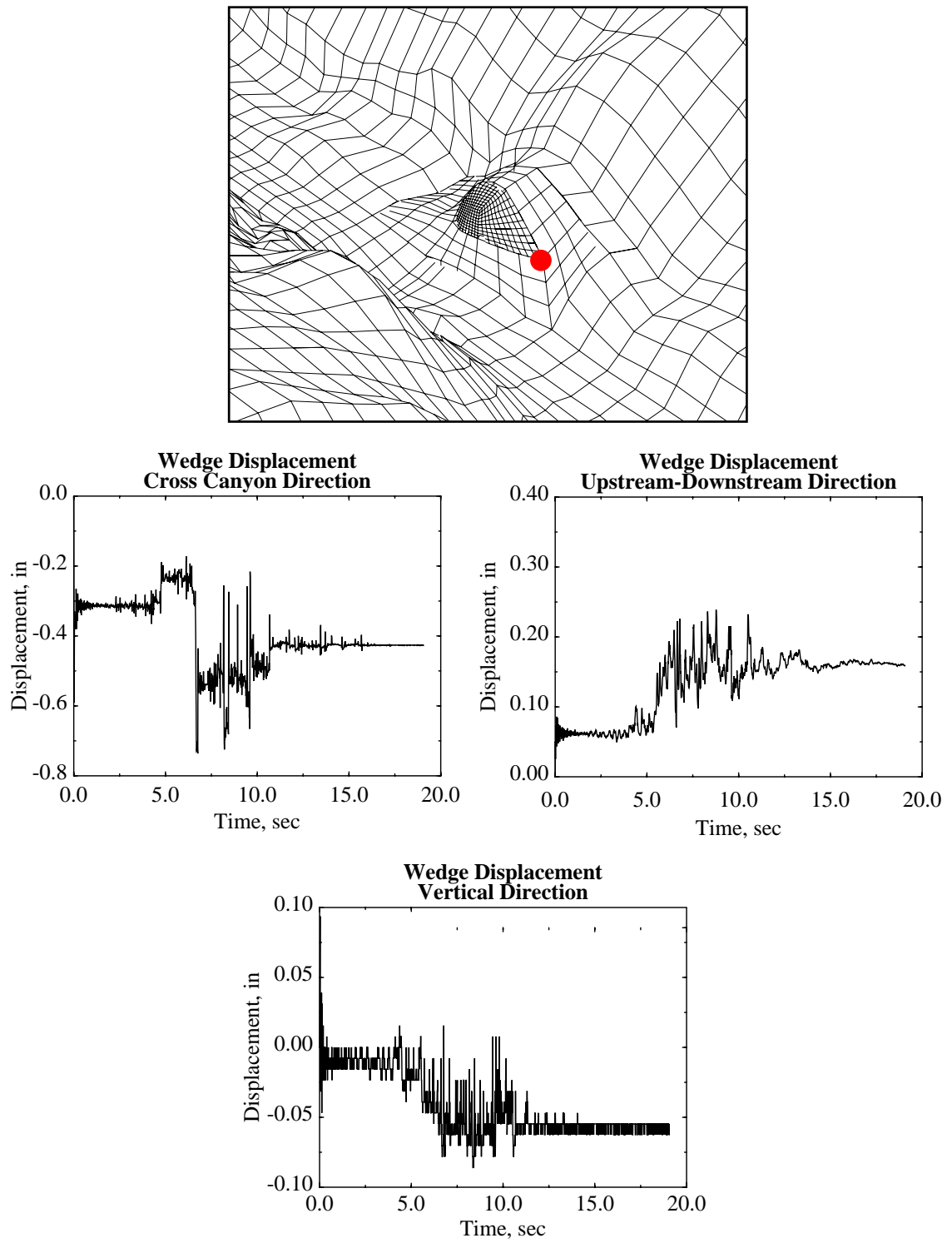


FIGURE 75. Wedge displacement time histories for model 5.

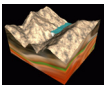
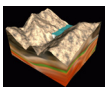


TABLE 10. Seismic Analysis Results for Model 5

Analysis Type	Description	Value (lbs, in, sec)
Dynamic	Permanent Wedge Displacement in Upstream-Downstream Direction	0.16
	Permanent Wedge Displacement in Cross Canyon Direction	0.43
	Permanent Wedge Displacement in Vertical Direction	0.06

11.2.7 Model 6: Model of Foundation and Wedge with Uplift Modeled Between the Wedge and Foundation

Model 6 gave the opportunity to study the effect of hydrostatic uplift forces along the side, release, and base planes of the left abutment wedge. The hydrostatic forces were provided by USBR [Ref 13] and they were input into the finite element model as surface pressures. The hydrostatic uplift pressures were statically initialized in NIKE3D along with the gravity loads for this model. The permanent cross canyon wedge displacement at the corner of the wedge was calculated to be 1.0 inches, much larger than the 0.43 inches calculated using the model without uplift forces. Figure 76 and Table 11 show the displacements of the left abutment wedge.



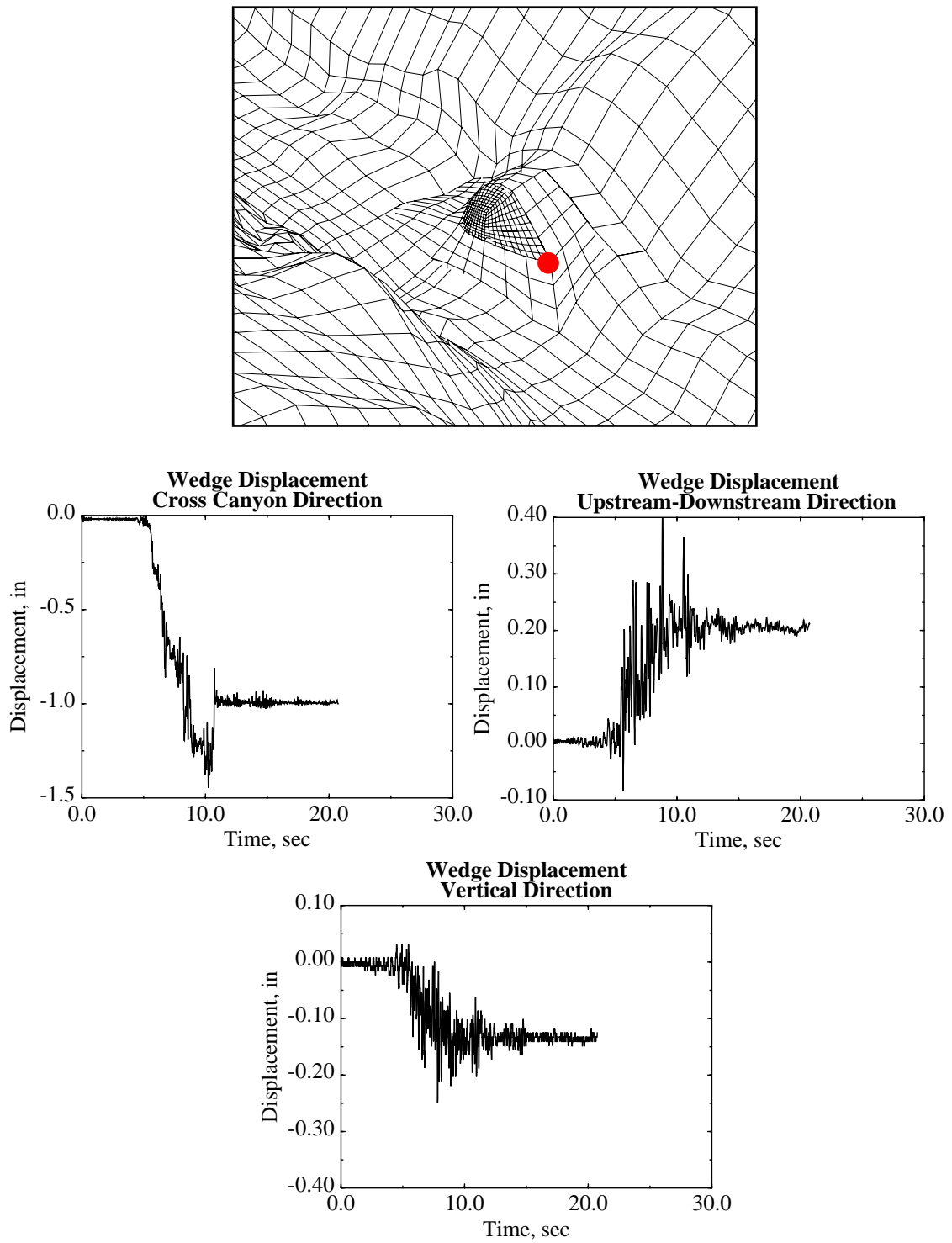


FIGURE 76. Wedge displacement time histories for model 6.

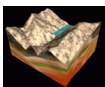


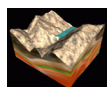
TABLE 11. Seismic Analysis Results for Model 6

Analysis Type	Description	Value (lbs, in, sec)
Dynamic	Permanent Wedge Displacement in Upstream-Downstream Direction	0.21
	Permanent Wedge Displacement in Cross Canyon Direction	1.0
	Permanent Wedge Displacement in Vertical Direction	0.133

11.2.8 Model 7: Concrete Damage Model

The objective of model 7 was to study the severity of concrete damage that may occur during an earthquake of this magnitude. This model is similar to model 3 except that a concrete plasticity constitutive model with damage was used for the concrete in the arch dam. The unconfined compressive strength was chosen to be 6,500 psi and the unconfined tensile strength was chosen to be 464 psi. These values correspond to the properties of the WSMR-5 3/4 concrete material (a material that has been widely tested for use in this material model). Table 12 shows a comparison between the WSMR material properties and the Morrow Point 10 year core samples.

The concrete constitutive model used was DYNA3D's Material Model 45. This concrete model was developed by Javier Malvar, Jim Wesevich, and John Crawford of Karagozian and Case, and Don Simon of Logicon RDA in support of the Defense Threat Reduction Agency's (DTRA) programs. The concrete model uses three independent fixed surfaces to define the plastic behavior of concrete (see Figure 77). The three surfaces are defined by pressure on the horizontal axis and deviatoric stress on the vertical axis. These three surfaces define three important regions of concrete behavior. It can be seen easily if one plots the stress-strain response for a uniaxial unconfined compression test (see Figure 77). The material response is considered linear up until point 1, or first yield. After yielding, a hardening plasticity response occurs until point 2, or maximum strength, is reached. After reaching a maximum strength, softening occurs until a residual strength, which is based on the amount of concrete confinement, is obtained. For this analysis, complete concrete damage will be defined as concrete which has reached the residual strength of the concrete material, or point 3 on the uniaxial stress-strain curve. The post-processor will use the color red to denote concrete which has reached point 3. Furthermore, this concrete material model takes into account strain-rate enhancement. At high strain rates, the apparent strength of concrete and the corresponding strain at peak stress both increase. For a more detailed discussion on this concrete model, please refer to Appendix A. Because of the complex nature of this constitutive model, two sample problems were run for this study to convince the analyst that the model was working accurately. These are a single element tensile test and a uniaxial unconfined compression test on a typical 6 x 12 in. cylinder (see Figure 78). Both tests show that the material model is correctly simulating the input compressive and tensile strengths.



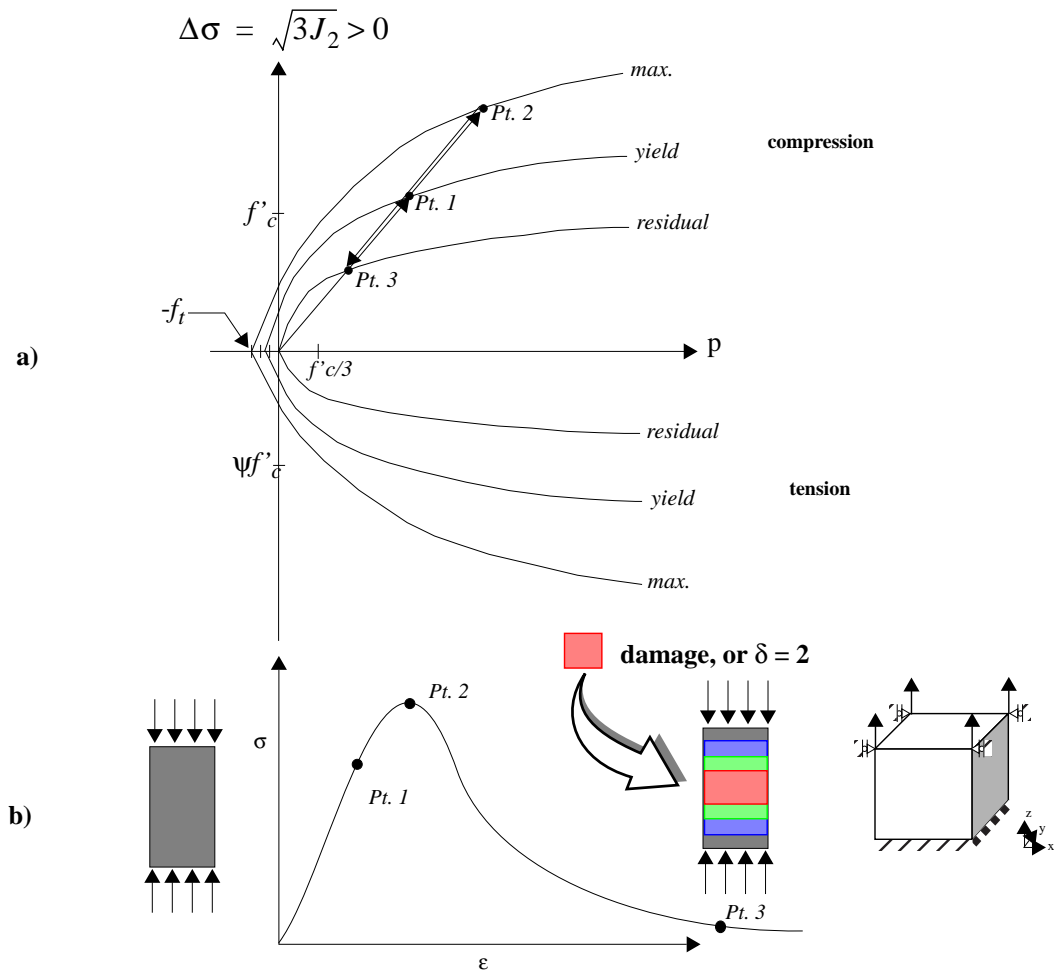
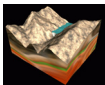


FIGURE 77. a). Three independent fixed failure surfaces for DTRA concrete material model; b). Uniaxial representation of concrete stress-strain curve.



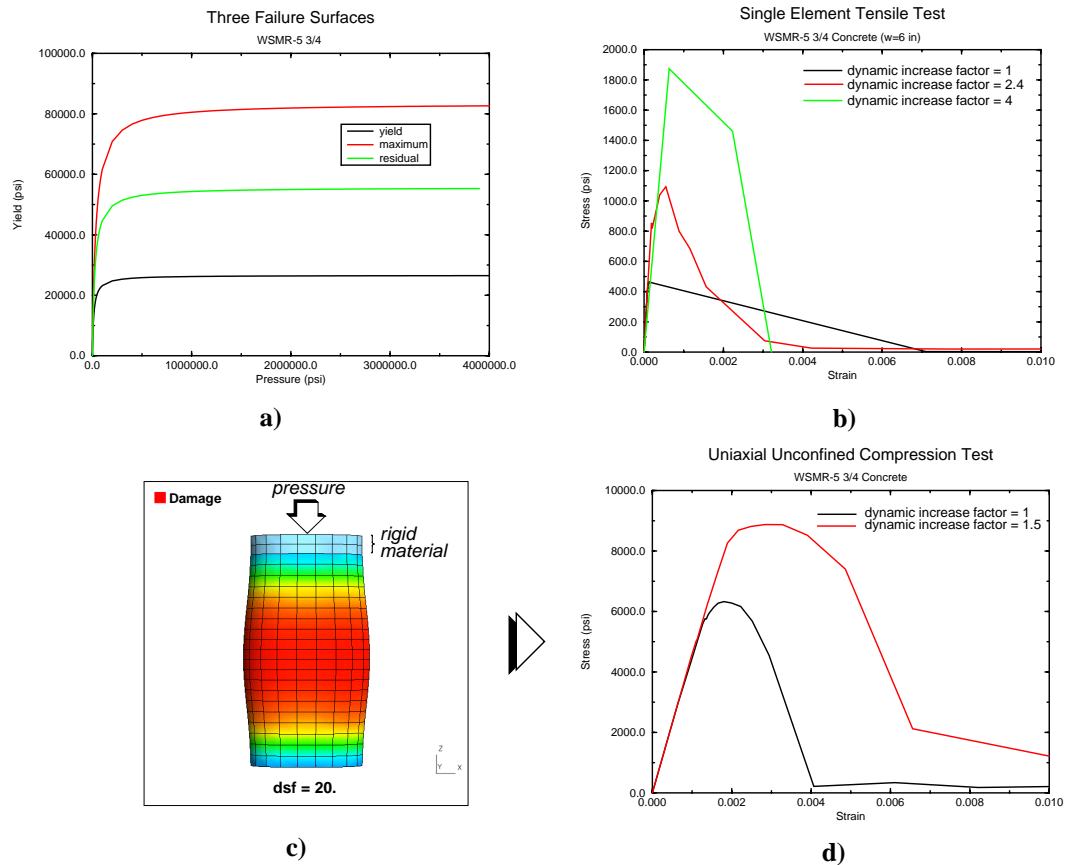


FIGURE 78. WSMR-5 3/4 concrete properties: a) plot of compressive meridians; b) single element uniaxial tensile test with and without rate dependence (tensile strength = 464 psi); c) description of unconfined uniaxial compressive test and plot of damage parameter δ after compressive failure; d) stress-strain plot of UUC test with and without rate dependence (compressive strength = 6500 psi).

TABLE 12. DYNA3D concrete material properties compared with Morrow Point Dam properties.

Concrete Properties	Morrow Point 10 year core samples	WSMR-5 3/4 material
unconfined compressive strength	4590-9610 psi	6250 psi
unconfined tensile strength	106-309 psi	464 psi
elastic modulus	3.9×10^6 - 5.6×10^6 psi	4.6×10^6 psi

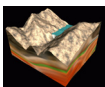


TABLE 12. DYNA3D concrete material properties compared with Morrow Point Dam properties.

Concrete Properties	Morrow Point 10 year core samples	WSMR-5 3/4 material
Poisson's Ratio	0.19-0.36	0.19
density	144.5-152.6 lb/ft ³	141.7 lb/ft ³

The results of this analysis are summarized in Table 13 and Figure 79 through Figure 81. The peak upstream-downstream displacement at the top center point of the dam is 2.8 inches, which compares well with the 2.73 inches that was calculated using model 3. The maximum contraction joint opening was still very low at a value of 0.05 inches and the permanent wedge displacement was calculated to be 0.45 inches. It should be noted that this model did not include a sliding with voids interface between the abutment and the dam. However, if the stresses were large enough, the concrete could fail along the abutment/dam boundary. As you can see from Figure 81, DYNA3D calculated virtually zero damage in the dam.

TABLE 13. Seismic Analysis Results for Model 7

Analysis Type	Description		Value (lbs, in, sec)
Static	Cantilever	Tension	1250
		Compression	2310
	Arch	Tension	589
		Compression	3540
	Max Principal Stress 1		1760
	Max Principal Stress 3		3540

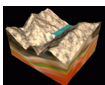
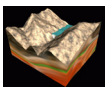


TABLE 13. Seismic Analysis Results for Model 7

Analysis Type	Description	Value (lbs, in, sec)
Dynamic	Max Upstream-Downstream Displacement	2.8 (t= 6.54 sec)
	Max Cross Canyon Displacement	-1.0 (t=6.63 sec)
	Max Vertical Displacement	0.55 (t= 6.61 sec)
	Max Contraction Joint Opening at Dam Center	0.04 (t=6.58 sec)
	Max Contraction Joint Opening at Dam Quarter Point	0.05 (6.59 sec)
	Permanent Wedge Displacement in Upstream-Downstream Direction	0.3
	Permanent Wedge Displacement in Cross Canyon Direction	0.45
	Permanent Wedge Displacement in Vertical Direction	0.06



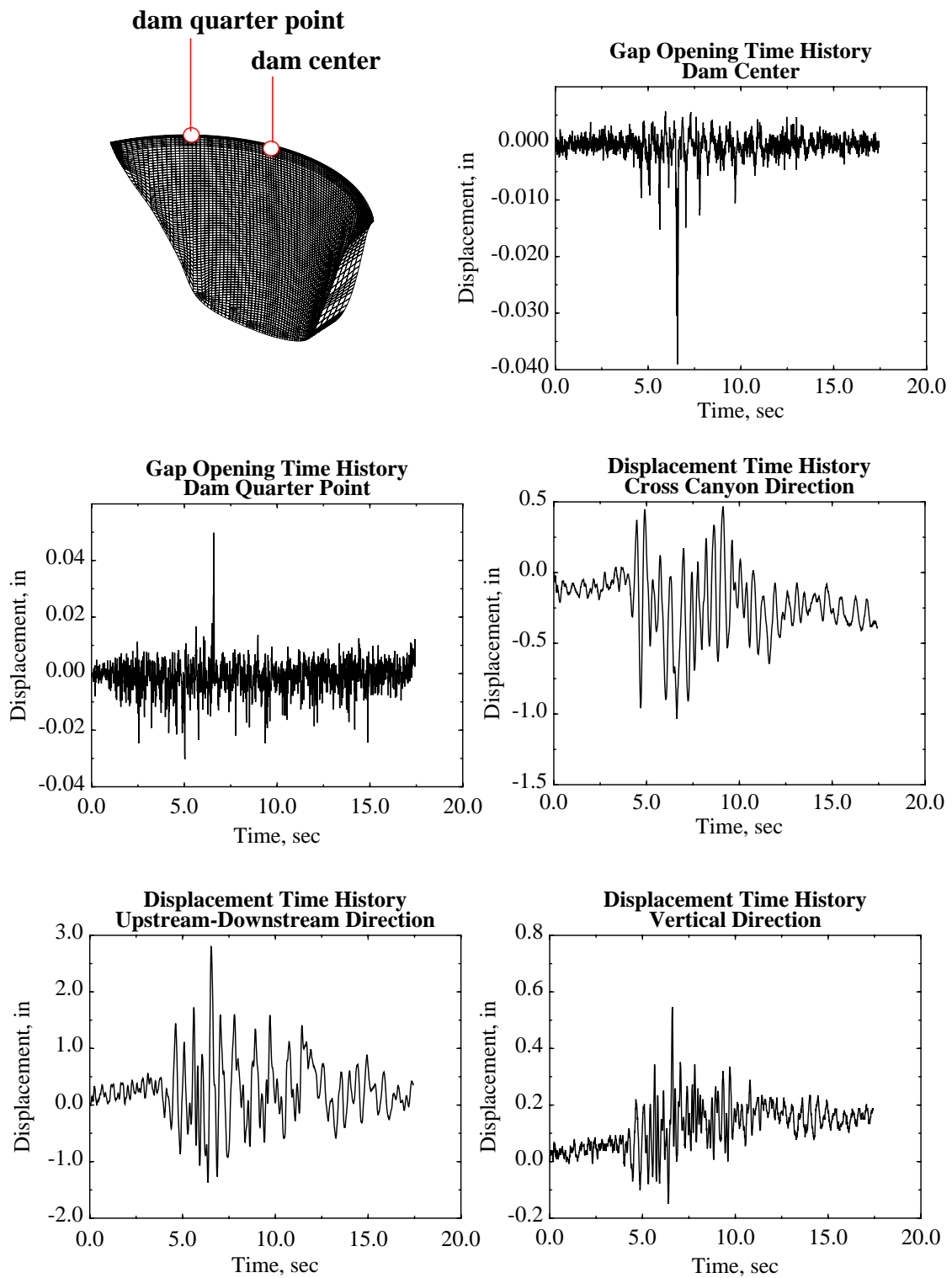
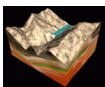


FIGURE 79. Displacement time histories for model 7.



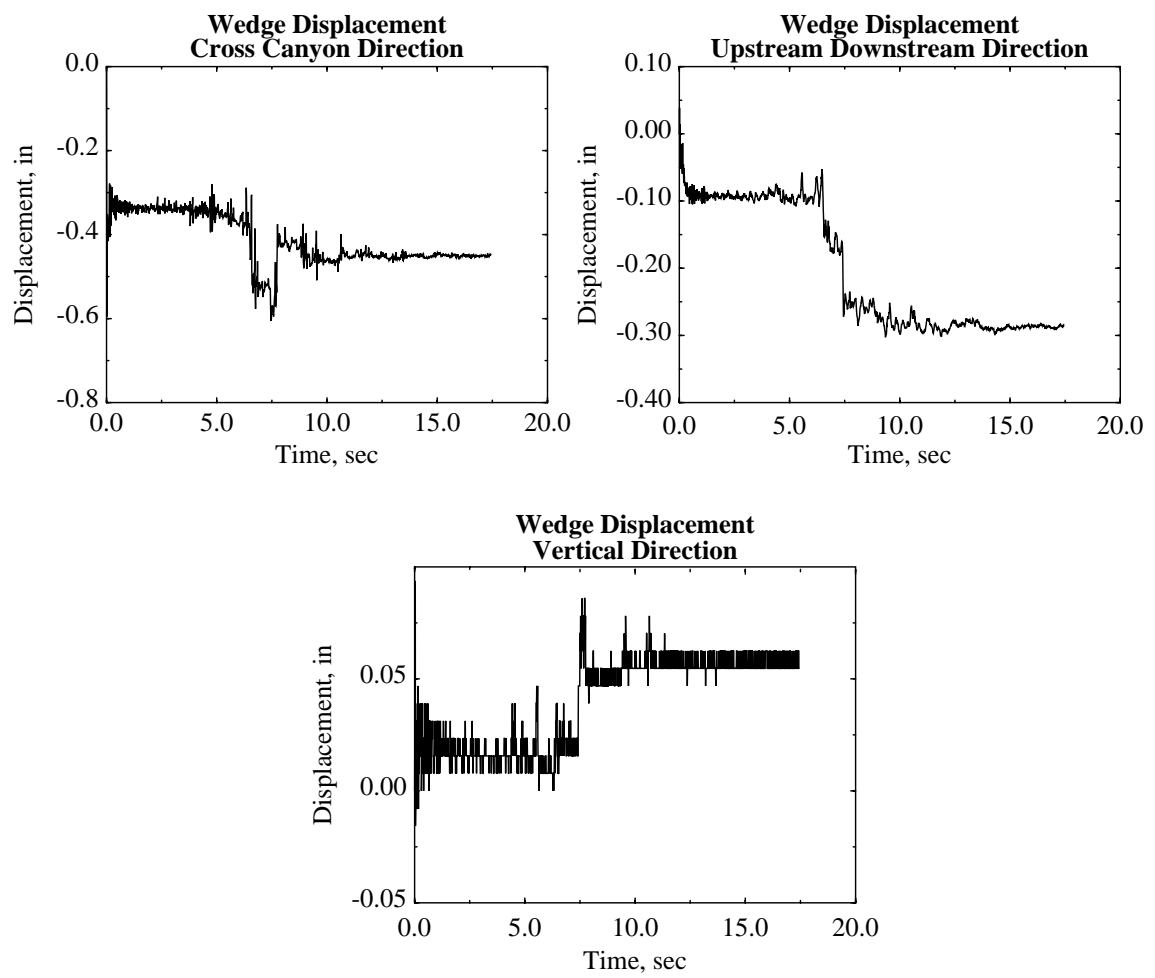
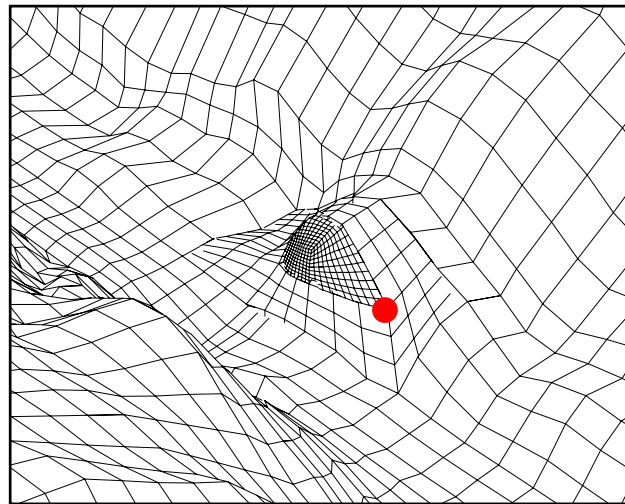
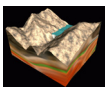


FIGURE 80. Wedge displacement time histories for model 7.



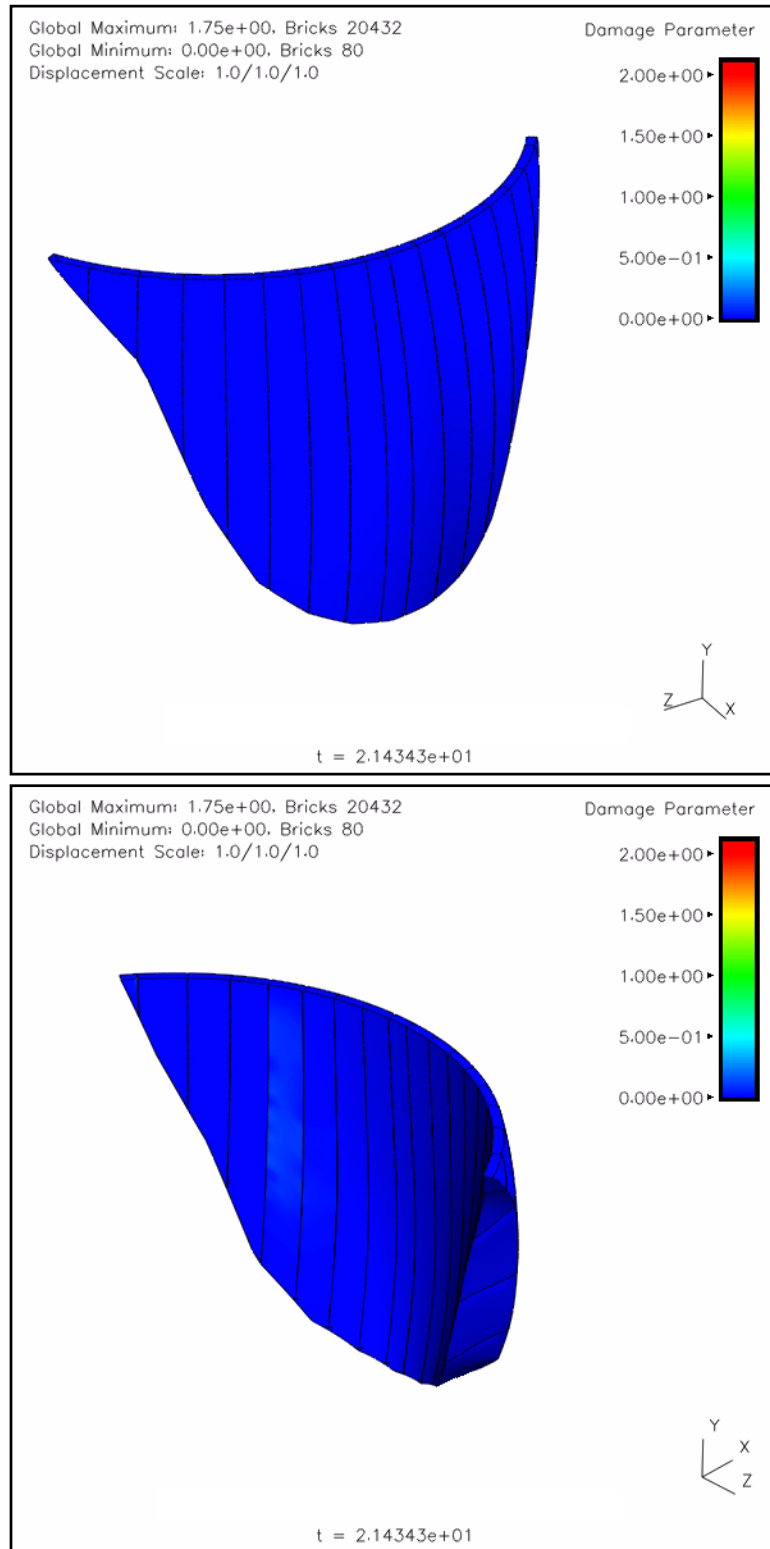
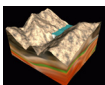


FIGURE 81. Concrete damage after completion of seismic analysis.



11.2.9 Model 8: Model with Tied with Failure Slide Surface at the Foundation/Dam Interface

Model 8 contains the contraction joint dam model with a flexible foundation, the water explicitly modeled, and a tied with failure slide surface at the foundation/dam interface. This model does not include the left abutment wedge. The NIKE3D static initialization used a tied contact surface between the dam and the foundation. When the analysis was restarted in DYNA3D, the contact interface was changed to a tied with failure slide surface. The tied with failure slide surface functions like the tied surface until the user prescribed normal and shear failure stresses are exceeded. Thereafter, the slide surface functions as a sliding with voids slide surface. The normal and shear failure stresses were assumed to be 600 and 1500 psi. The 600 psi normal failure stress was chosen because it is close to the tensile strength of concrete. A slightly larger value than the tensile strength was chosen to account for any slight rate enhancement that may occur during an earthquake. Choosing a shear strength is much harder due to the fact that it is very difficult to measure the strength of concrete in pure shear directly. Mindess and Young suggest a value of 20% of the compressive strength of concrete. However, they also note that “if normal stresses are also acting, the shearing strength can be made to exceed the uniaxial compressive strength” [Ref 9]. Multiplying 0.2 by 6,500 psi gives a value of 1,300 psi. A shear strength value of 1,500 psi was chosen for this analysis. The peak upstream-downstream displacement was determined to be 2.86 inches, which is slightly larger than models 1 through models 7 (see Table 14 and Figure 82). The maximum contraction opening was determined to be 0.076 inches at the dam center.

TABLE 14. Seismic Analysis Results for Model 8

Analysis Type	Description		Value (lbs, in, sec)
Static	Cantilever	Tension	326
		Compression	1400
	Arch	Tension	591
		Compression	1390
	Max Principal Stress 1		1300
	Max Principal Stress 3		3180

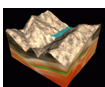
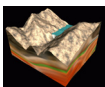


TABLE 14. Seismic Analysis Results for Model 8

Analysis Type	Description		Value (lbs, in, sec)
Static & Dynamic	Cantilever	Tension	1120 (t=7.47 sec)
		Compression	2180 (t= 6.08 sec)
	Arch	Tension	1520 (t=6.92 sec)
		Compression	1890 (t=7.46 sec)
	Max Principal Stress 1		1760 (t=7.48 sec)
	Max Principal Stress 3		3180 (t=0.0 sec)
Dynamic	Max Upstream-Downstream Displacement		2.86 (t=6.57 sec)
	Max Cross Canyon Displacement		1.53 (t=6.63 sec)
	Max Vertical Displacement		0.54 (t=6.62 sec)
	Max Contraction Joint Opening at Dam Center		0.076 (t=7.83 sec)
	Max Contraction Joint Opening at Dam Quarter Point		0.07 (t=8.87 sec)



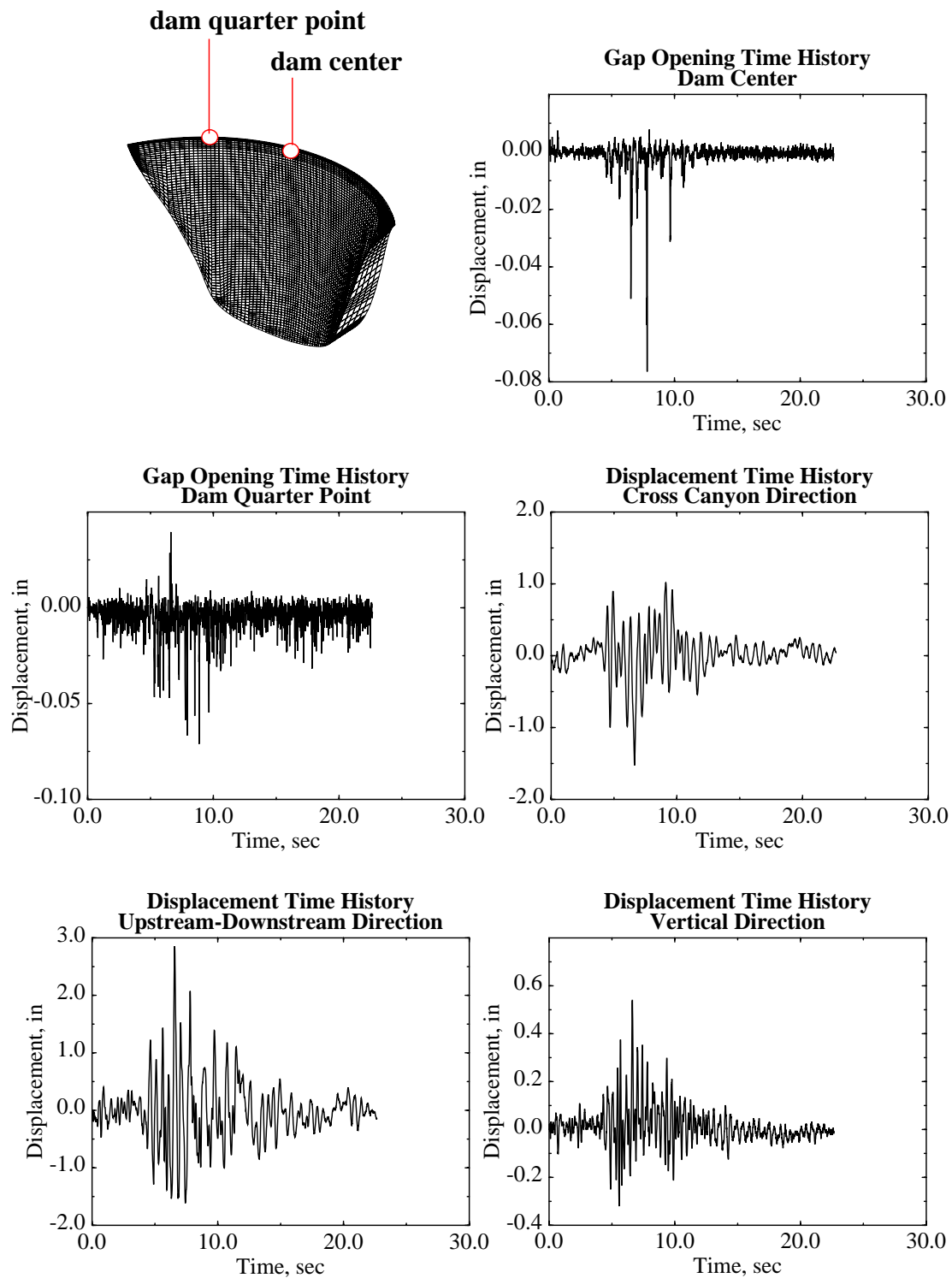
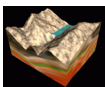


FIGURE 82. Displacement time histories for model 8.



11.2.10 Model 9: Model with Tied with Failure Slide Surface and Uplift at the Foundation/Dam Interface

Model 9 included the flexible foundation, water explicitly modeled, a tied with failure slide surface and uplift pressures modeled at the dam/foundation interface. The peak upstream-downstream displacement was calculated to be 2.84 inches and the maximum contraction joint opening near the left abutment was 0.91 inches. This contraction joint opening is much larger than that seen in model 2. This large value for a contraction joint opening suggests that the tied with failure slide surface and uplift pressures increase the contraction joint openings, especially near the left abutment. Table 15 and Figure 83 summarize the analysis results for this finite element model.

TABLE 15. Seismic Analysis Results for Model 9

Analysis Type	Description		Value (lbs, in, sec)
Static	Cantilever	Tension	376
		Compression	1450
	Arch	Tension	471
		Compression	855
	Max Principal Stress 1		864
	Max Principal Stress 3		1720
Static & Dynamic	Cantilever	Tension	1160 (t=1.94 sec)
		Compression	2030 (t=7.49 sec)
	Arch	Tension	1620 (t=6.91 sec)
		Compression	2040 (t=11.11 sec)
	Max Principal Stress 1		1860 (t=6.74 sec)
	Max Principal Stress 3		3720 (t=14.93 sec)

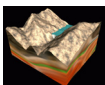
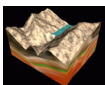


TABLE 15. Seismic Analysis Results for Model 9

Analysis Type	Description	Value (lbs, in, sec)
Dynamic	Max Upstream-Downstream Displacement	2.84 (t=6.57 sec)
	Max Cross Canyon Displacement	-1.44 (t=6.63 sec)
	Max Vertical Displacement	0.48 (t=6.62 sec)
	Max Contraction Joint Opening at Dam Center	0.07 (t=7.83 sec)
	Max Contraction Joint Opening at Dam Quarter Point	0.063 (t=8.92 sec)
	Max Contraction Joint Opening Near Left Abutment	0.91 (t=6.59 sec)



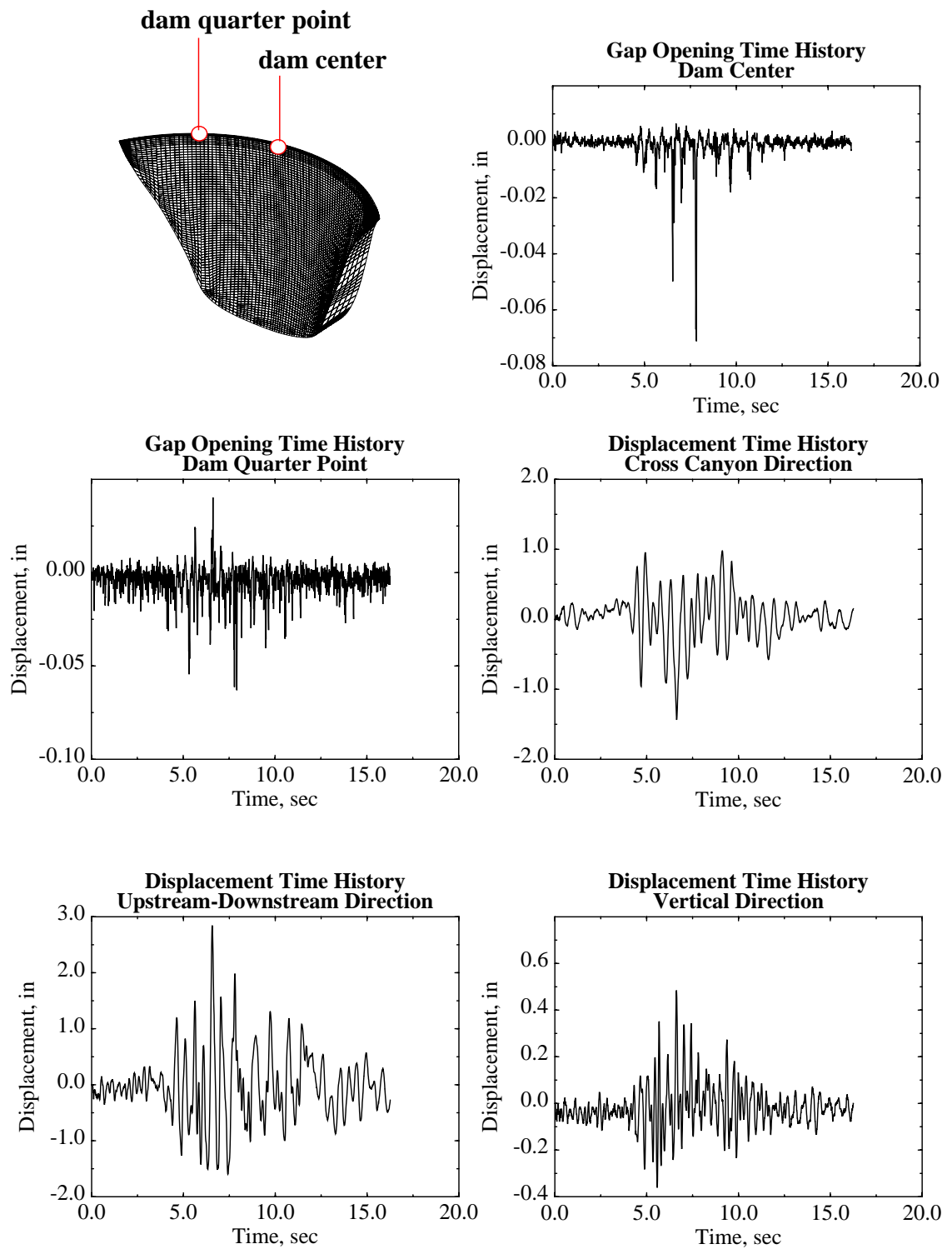
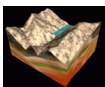
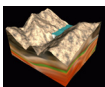


FIGURE 83. Displacement time histories for model 9.



11.2.11 Thermal Analysis

To study the effects of a low temperature condition on the dam during an earthquake, a thermal analysis was completed before running the seismic analysis in DYNA3D. The USBR provided LLNL with nodal temperatures for the low (winter) condition for both the upstream and downstream sides of the dam [Ref 12] and [Ref 10]. Figure 84 shows the temperature variation versus dam height for both the upstream and downstream sides. TOPAZ3D, a three-dimensional implicit finite element code at LLNL, was used to solve the steady state temperature field throughout the dam structure using these temperature variations as boundary conditions. Figure 85 shows the temperature variation on the dam calculated by TOPAZ3D. This temperature field was then used as a temperature profile in NIKE3D, so that NIKE3D could calculate the thermal stresses (along with the gravity and hydrostatic loads). A material reference temperature of 40°F was chosen and the coefficient of thermal expansion used was 0.0000056 in/in/°F. The thermal loading virtually caused no change in the peak upstream-downstream displacement, which was calculated to be 2.8 inches. The maximum gap opening was 0.05 inches at the dam center and the permanent wedge displacement was 0.72 inches compared to 0.83 inches computed in model 3 (see Table 16, Figure 86, and Figure 87). Note that the finite element model used for this analysis was the same as model 3 with the left abutment wedge allowed to move freely from the dam and the foundation.



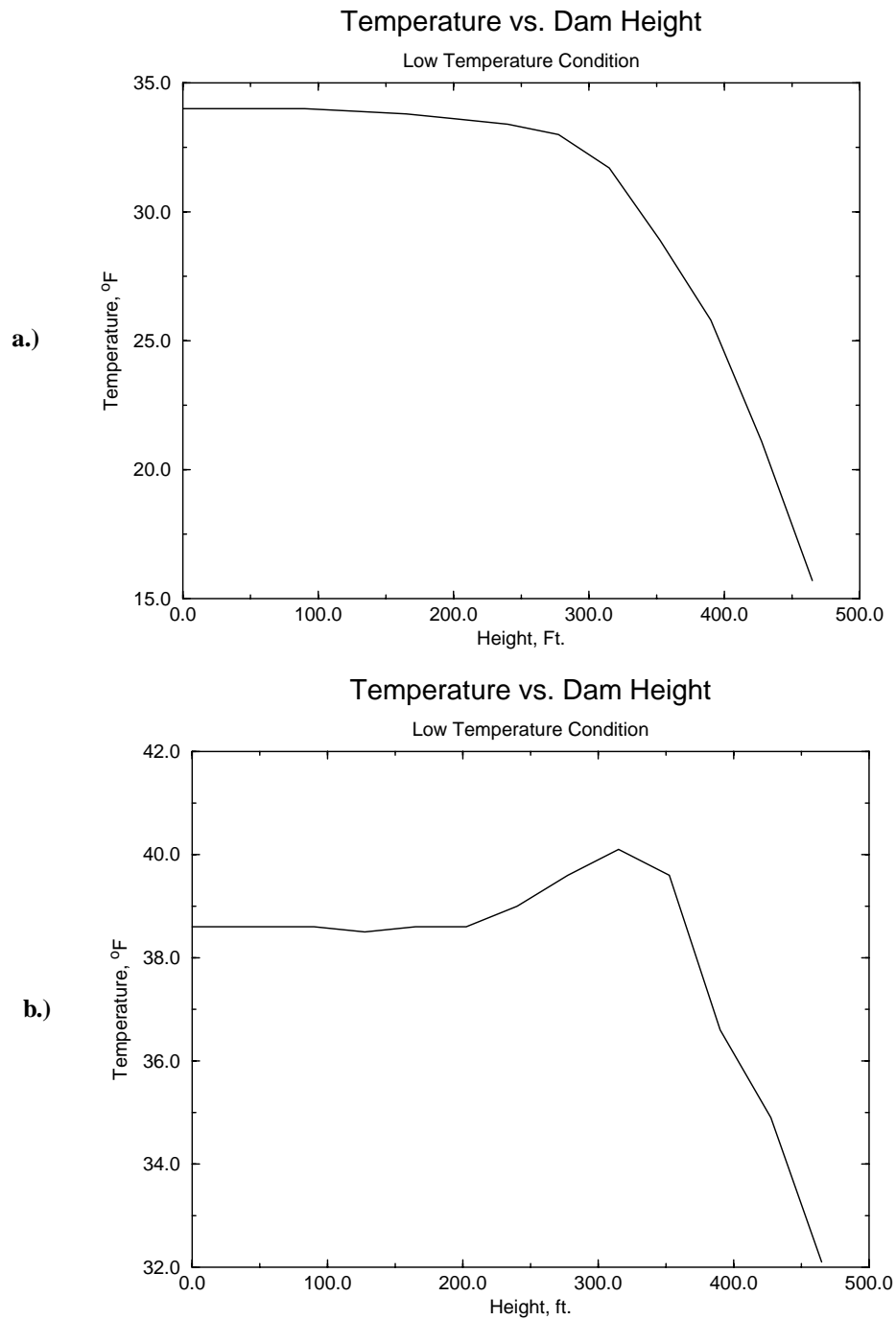
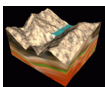
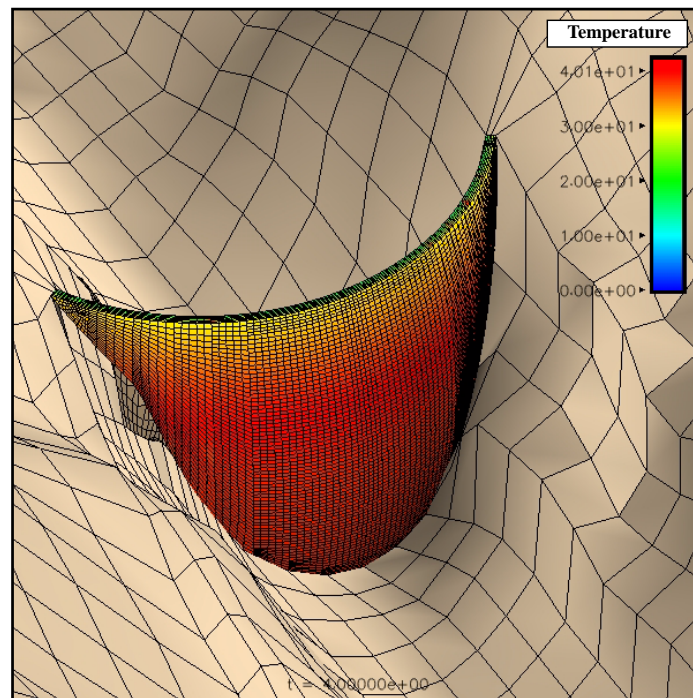


FIGURE 84. a.) Upstream temperature variation; b) downstream temperature variation.



a.)



b.)

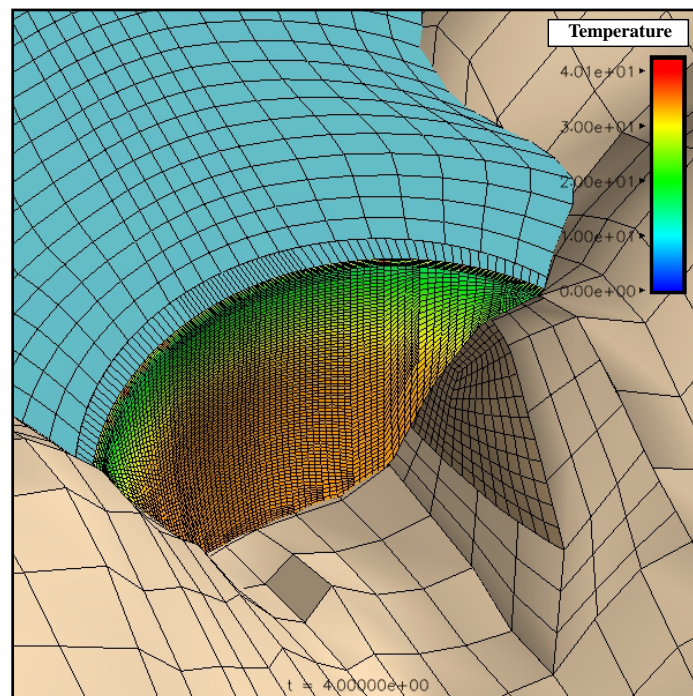


FIGURE 85. a). Upstream temperature variation ; b). downstream temperature variation.

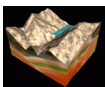


TABLE 16. Seismic Analysis Results for thermal model

Analysis Type	Description		Value (lbs, in, sec)
Static	Cantilever	Tension	1100
		Compression	2140
	Arch	Tension	626
		Compression	2190
	Max Principal Stress 1		1560
	Max Principal Stress 3		3130
Static & Low Temperature	Cantilever	Tension	1080
		Compression	2070
	Arch	Tension	626
		Compression	2150
	Max Principal Stress 1		1540
	Max Principal Stress 3		3090
Static & Dynamic	Cantilever	Tension	1240 (t=0.02 sec)
		Compression	2560 (t=7.43 sec)
	Arch	Tension	868 (t= 10.85 sec)
		Compression	2700 (t= 4.76 sec)
	Max Principal Stress 1		2000 (t=6.61 sec)
	Max Principal Stress 3		3760 (t=4.76 sec)

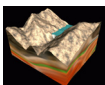
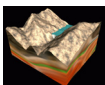


TABLE 16. Seismic Analysis Results for thermal model

Analysis Type	Description	Value (lbs, in, sec)
Dynamic	Max Upstream-Downstream Displacement	2.8 (6.55 sec)
	Max Cross Canyon Displacement	-0.85 (t=6.63 sec)
	Max Vertical Displacement	0.51 (t=6.61 sec)
	Max Contraction Joint Opening at Dam Center	0.05 (t=7.79 sec)
	Max Contraction Joint Opening at Dam Quarter Point	0.04 (t=7.77 sec)
	Permanent Wedge Displacement in Upstream-Downstream Direction	0.04
	Permanent Wedge Displacement in Cross Canyon Direction	0.72
	Permanent Wedge Displacement in Vertical Direction	0.04



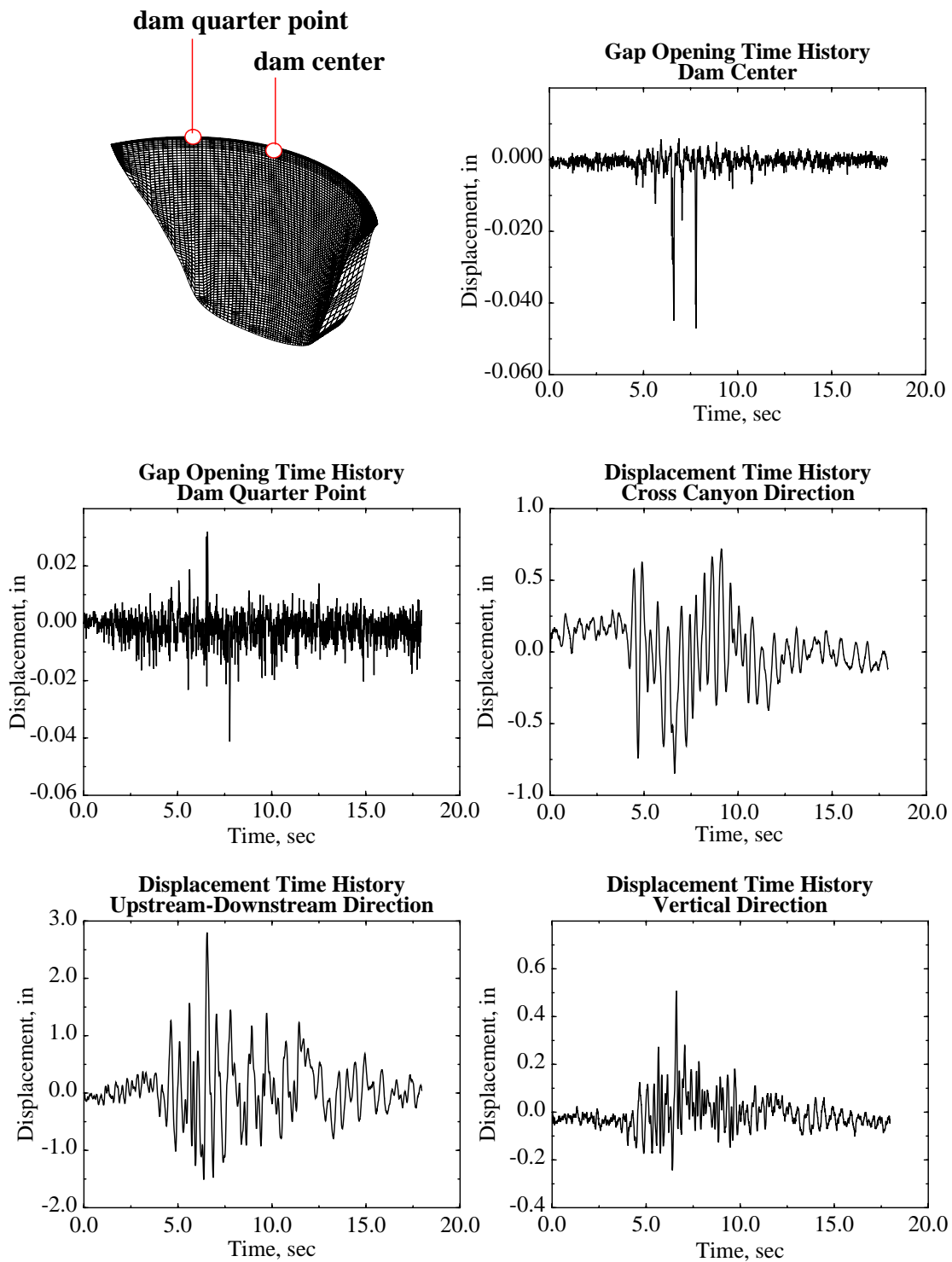
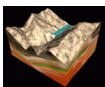


FIGURE 86. Displacement time histories for thermal model.



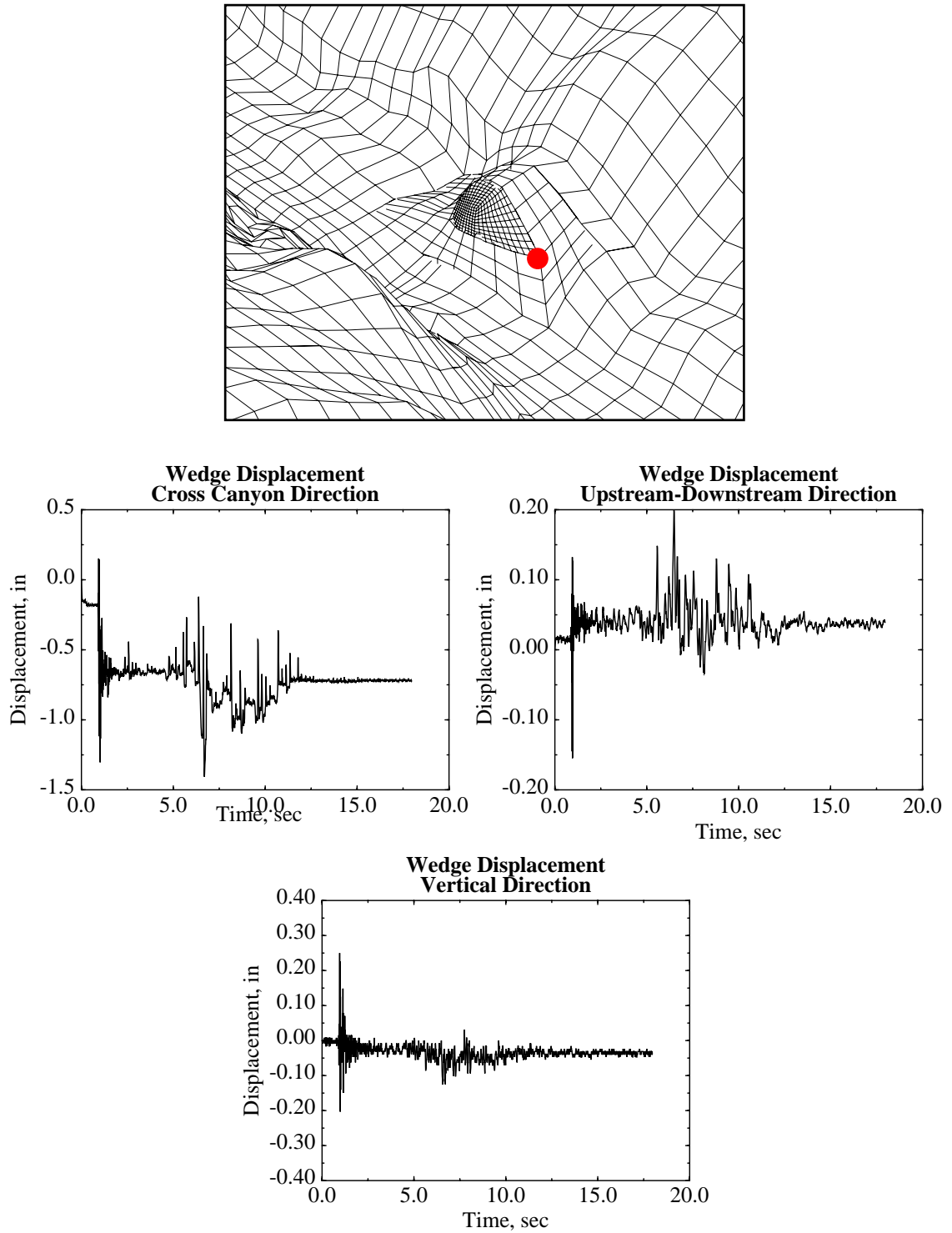
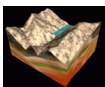


FIGURE 87. Wedge displacement time histories for thermal model.



12.0 Conclusions

A summary of the upstream-downstream displacements for all of the analyses are provided for comparison in Table 17. Based on the extensive analyses performed, a number of conclusions can be stated:

- When modeling a foundation, it is important to deconvolve the ground motions to the base of the foundation model. By not deconvolving the ground motions, the earthquake accelerations may be larger than wanted at the dam/foundation interface.
- When modeling a flexible foundation, it is also important to use non-reflecting boundaries along all sides of the finite element mesh. If a reflecting boundary was placed at the base of the foundation, for example, it was seen that the response was greater across the entire acceleration response spectra in comparison to the response that would be calculated if a non-reflecting boundary was used.
- The topography had an effect of reducing the ground motions seen by the dam structure.
- By placing a sliding with voids interface between the dam and wedge instead of a tied contact surface, the permanent wedge displacements doubled in value.
- The USBR calculated peak displacement compared very well to the models that used non-reflecting boundaries throughout the finite element model and deconvolved ground motions.
- It can be concluded from model 7, that the damage to the concrete for this magnitude earthquake would be minimal.
- The tied with failure surface models suggest that the concrete dam structure is very stable throughout the earthquake loading.
- Hydrostatic uplift pressures at the dam/foundation interface has little effect on the peak upstream-downstream displacement. It may have an effect on the peak contraction joint gap opening near the left abutment.
- The low temperature condition analysis caused minimal differences in peak upstream-downstream displacements.
- The contraction joint openings are more severe when the wedge is not restricted or tied to the dam or foundation and when a tied with failure slide surface and uplift is modeled between the dam/foundation interface.

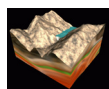
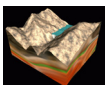


TABLE 17. Upstream-Downstream Displacement Comparison

Study	Finite Element Model	Maximum Upstream-Downstream Displacement (in.)
USBR	EACD3D96	2.9
LLNL (Phase 1)	Rigid Foundation and Westergaard Added Mass	3.5
	Flexible Foundation and Westergaard Added Mass	7.4
	Flexible Foundation and Water Explicitly Modeled	14.1
	Flexible Foundation, Water Explicitly Modeled, Wedge 3	5.27
LLNL (Phase 2)	Model 1	2.76
	Model 2	2.6
	Model 3	2.73
	Model 3 (wedge free)	2.83
	Model 4	N/A
	Model 5	N/A
	Model 6	N/A
	Model 7	2.8
	Model 8	2.86
	Model 9	2.84
	Thermal	2.8



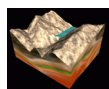
13.0 Acknowledgements

This study was supported by the United States Bureau of Reclamation and the support and guidance of Mr. Larry Nuss is gratefully acknowledged. Dr. Mike Puso, Dr. Edward Zywickz, and Dr. Jerome Solberg of LLNL's Methods Development Group made modifications to NIKE3D and DYNA3D programs for this study and their timely help is greatly appreciated.

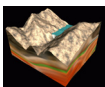
This work was performed at the Lawrence Livermore National Laboratory under the auspices of the United States Department of Energy, contract W-7405-Eng-48.

14.0 References

1. Blevins, R.D., Formulas for Natural Frequency and Mode Shape, Krieger Publishing Company, Malabar, Florida, 1993.
2. Chopra, A.K., Dynamics of Structures: Theory and Applications to Earthquake Engineering, Prentice-Hall, Inc., 1995.
3. Clough, R.W. (1980), Nonlinear Mechanisms in the Seismic Response of Arch Dams, Proc., Int. Res. Conf., on Earthquake Engrg., Skopje, Yugoslavia.
4. Duron, Z.H., Hall, J.F., Experimental and Finite Element Studies of the Forced Vibration Response of Morrow Point Dam, Earthquake Engineering and Structural Dynamics, Vol. 16, 1021-1039, March 1988.
5. Fenves, G.L., Mojtahedi, S., and Reimer, R.B., Effect of Contraction Joints on Earthquake Response of an Arch Dam, Journal of Structural Engineering, Vol. 118, No. 4, 1039-1055, April 1992.
6. Kuo J.S., Fluid-Structure Interactions: Added Mass Computations for Incompressible Fluid, Earthquake Engineering Research Center, Report No. UCB/EERC-82/09, August 1982.
7. Lau, D.T., Noruziann, B., and Razaqpur, A.G. Modelling of contraction joint and shear sliding effects on earthquake response of arch dams. *Earthquake Engineering and Structural Dynamics*, 27:1013 - 1029, 1998.
8. Maker, B.N., Ferencz, R.M., and Hallquist, J.O., NIKE3D: A Nonlinear, Implicit, Three-Dimensional Finite Element Code for Solid and Structural Mechanics, Lawrence Livermore National Laboratory Report UCRL-MA-105268.
9. Mindess, S., Young, J.F., Concrete, Prentice-Hall, Inc., 1981.
10. Nuss, L.K., Static and Dynamic Structural Linear Elastic Structural Analysis (EACD3D96) Morrow Point Dam, Technical Memorandum No. MP-D8110-IE-2002-2, Technical Service Center, U.S. Department of the Interior, Bureau of Reclamation, Denver, CO, September 2002.
11. Personal communication between J. Hall (CalTech) and C. Noble (LLNL).
12. Personal communication between L. Nuss (USBR) and C. Noble (LLNL).

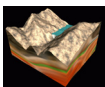


13. Personal communication between C. Powell (USBR) and C. Noble (LLNL).
14. Puso, M., Laursen, T., and Weiss, J., Contact improvements in nuke3d. UCRL-JC Report 125876, Lawrence Livermore National Laboratory, 1996.
15. Shapiro, A., TOPAZ3D: A Three-Dimensional Finite Element Heat Transfer Code, UCID-20484, Lawrence Livermore National Laboratory, August 1985.
16. Tan, H., Chopra, A.K., Dam-Foundation Rock Interaction Effects in Earthquake Response of Arch Dams, Journal of Structural Engineering, May 1996.
17. Whirley, R.G., DYNA3D: A Nonlinear, Explicit, Three-Dimensional Finite Element Code for Solid and Structural Mechanics, Lawrence Livermore National Laboratory Report UCRL-MA-107254-REV-1.



Appendix A

DYNA3D Concrete Model 45



15.0 Background

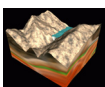
Concrete is perhaps one of the most widely used construction materials in the world. Engineers use it to build massive concrete dams, concrete waterways, highways, bridges, and even nuclear reactors. The advantages of using concrete is that it can be cast into any desired shape, it is durable, and very economical compared to structural steel. The disadvantages are its low tensile strength, low ductility, and low strength-to-weight ratio. Concrete is a composite material that consists of a coarse granular material, or aggregate, embedded in a hard matrix of material, or cement, which fills the gaps between the aggregates and binds them together. Concrete properties, however, vary widely. The properties depend on the choice of materials used and the proportions for a particular application, as well as differences in fabrication techniques. Table 1 provides a listing of typical engineering properties for structural concrete.

TABLE 18. Typical Engineering Properties of Structural Concrete

Compressive strength	5000 lb/in. ²
Tensile strength	400 lb/in. ²
Modulus of Elasticity	4×10^6 lb/in. ²
Poisson's Ratio	0.18
Failure Strain for Unconfined Uniaxial Compression Test	0.002
Failure Strain for Unconfined Uniaxial Tensile Test	0.00012
Coefficient of Thermal Expansion	5.6×10^{-6} / °F
Normal Weight Density	145 lb/ft. ³
Lightweight Density	110 lb/ft. ³

Properties also depend on the level of concrete confinement, or hydrostatic pressure, the material is being subjected to. In general, concrete is rarely subjected to a single axial stress. The material may experience a combination of stresses all acting simultaneously. The behavior of concrete under these combined stresses are, however, extremely difficult to characterize. In addition to the type of loading, one must also consider the stress history of the material. Failure is determined not only by the ultimate stresses, but also by the rate of loading and the order in which these stresses were applied.

The concrete model described herein accounts for this complex behavior of concrete. It was developed by Javier Malvar, Jim Wesevich, and John Crawford of Karagozian and Case, and Don Simon of Logicon RDA in support of the Defense Threat Reduction



Agency's programs. The model is an enhanced version of the Concrete/Geological Material Model 16 in the Lagrangian finite element code DYNA3D. The modifications that were made to the original model ensured that the material response followed experimental observations for standard uniaxial, biaxial, and triaxial tests for both tension and compression type loading. A disadvantage of using this material model, however, is the overwhelming amount of input that is required from the user. Therefore, the goal of this report is to provide future users with the tools necessary for successfully using this model.

15.1 Terminology

Before discussing the details of this model, it is instructive to provide an overview of some of the key terminology and nomenclature that will be used extensively later on in this description.

15.1.1 Volumetric and Deviatoric Stresses and Strains

As you may recall, stress can be broken up into its volumetric and deviatoric parts as follows,

$$\boldsymbol{\sigma} = \boldsymbol{\sigma}_M + \boldsymbol{s} \quad (\text{EQ 54})$$

In indicial form,

$$\sigma_{M_{ij}} = \frac{1}{3}\sigma_{kk}\delta_{ij} \quad \text{or} \quad \sigma_{M_{ij}} = p\delta_{ij} \quad (\text{EQ 55})$$

where

$$p = \frac{1}{3}\sigma_{kk} \quad \text{or} \quad p = \frac{1}{3}(\sigma_{11} + \sigma_{22} + \sigma_{33}) \quad (\text{EQ 56})$$

and

$$s_{ij} = \sigma_{ij} - \frac{1}{3}\sigma_{kk}\delta_{ij} \quad (\text{EQ 57})$$

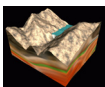
However, in DYNA3D, pressure is defined as the negative of the one defined above,

$$p = -\frac{1}{3}(\sigma_{11} + \sigma_{22} + \sigma_{33}) \quad (\text{EQ 58})$$

so that pressure is positive in compression.

In addition, for a principal coordinate system that coincides with the directions of the principal stresses, all the σ_{ij} , with $i \neq j$, terms vanish so that

$$p = -\frac{1}{3}(\sigma_1 + \sigma_2 + \sigma_3) \quad (\text{EQ 59})$$



and

$$s_1 = \max\{\sigma_1 - p, \sigma_2 - p, \sigma_3 - p\} \quad (\text{EQ 60})$$

Finally, volumetric and deviatoric strains are commonly written as,

$$\begin{aligned} \epsilon_v &= \epsilon_1 + \epsilon_2 + \epsilon_3 \\ \epsilon_q &= \frac{2}{3}(\epsilon_1 - \epsilon_3) \end{aligned} \quad (\text{EQ 61})$$

15.1.2 Stress Invariants

Scalar quantities may also be constructed out of the tensor σ_{ij} , that is,

$$\begin{aligned} P_1 &= \sigma_{ii} \\ P_2 &= \sigma_{ij}\sigma_{ij} \\ P_3 &= \sigma_{ij}\sigma_{jk}\sigma_{ki} \end{aligned} \quad (\text{EQ 62})$$

These scalar quantities constructed from a tensor are independent of any particular coordinate system and are therefore known as invariants. In the principal coordinate frame, these quantities are usually written as,

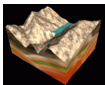
$$\begin{aligned} P_1 &= \sigma_1 + \sigma_2 + \sigma_3 \\ P_2 &= \sigma_1^2 + \sigma_2^2 + \sigma_3^2 \\ P_3 &= \sigma_1^3 + \sigma_2^3 + \sigma_3^3 \end{aligned} \quad (\text{EQ 63})$$

In this particular model description, however, the stress invariants are defined as follows,

$$\begin{aligned} I_1 &= 3p = (\sigma_1 + \sigma_2 + \sigma_3) \\ J_2 &= \frac{1}{2}(s_1^2 + s_2^2 + s_3^2) \quad \text{or} \\ \sqrt{J_2} &= \frac{\sqrt{(\sigma_1 - \sigma_2)^2 + (\sigma_1 - \sigma_3)^2 + (\sigma_2 - \sigma_3)^2}}{\sqrt{6}} \\ J_3 &= s_1 s_2 s_3 \end{aligned} \quad (\text{EQ 64})$$

15.1.3 Triaxial Compression and Extension

The triaxial compression test provides the means for defining the effect of confinement on the strength of the concrete. When a lateral confining pressure is applied, the increase in compressive strength can be very large. In addition, the application of a lateral confining pressure leads to a large increase in the compressive strain at failure. The effect of a con-



fining pressure on strength is, however, more beneficial for weak than for strong concretes. In the case of tension plus biaxial compression, the tensile strength is reduced by the application of lateral compressive stresses.

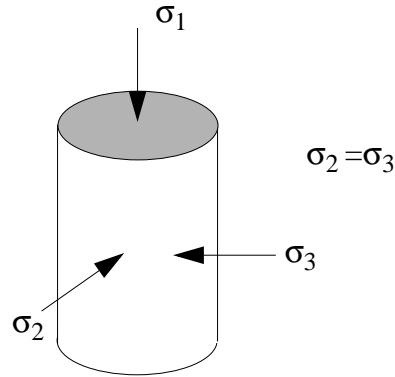


FIGURE 88. Description of triaxial test

A typical triaxial compression test is defined as follows:

18. at the beginning of the test, $\sigma_1 = \sigma_2 = p$.

19. during test, σ_1 increased until failure.

20. At failure, the concrete strength is defined as $\Delta\sigma_c = |\sigma_1 - \sigma_2|$.

A typical triaxial extension test is defined as follows:

1. at the beginning of the test, $\sigma_1 = \sigma_2 = p$.

2. during test, σ_1 increased until failure.

3. At failure, the concrete strength is defined as $\Delta\sigma_t = |\sigma_1 - \sigma_2|$.

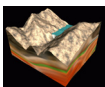
A comparison of the concrete strengths may be computed as

$$\psi = \frac{\Delta\sigma_t}{\Delta\sigma_c} \quad (\text{EQ 65})$$

The value, ψ , usually varies from $0.5 \leq \psi \leq 1.0$, depending on the amount of confining pressure the material is subjected to.

The $\Delta\sigma$ value defined above will be used throughout the material description as a way of referring to the shear strength of concrete. The $\Delta\sigma$ can also be related to the second invariant of the deviatoric stress by

$$\Delta\sigma = \sqrt{3J_2} \quad (\text{EQ 66})$$



16.0 Nonlinear Concrete Model Description

The Karagozian & Case concrete model decouples the volumetric and deviatoric responses. The model also uses an Equation of State (EOS). The Equation of State prescribes a user-defined set of pressures, unloading bulk moduli, and volumetric strains. Once the pressure has been determined from the EOS, a movable surface, or failure surface, limits the second invariant of the deviatoric stress tensor (i.e. $\Delta\sigma$). In addition, the model is strain rate dependent, which is extremely important for accurately simulating blast effects.

16.1 Failure Surfaces

The model uses three independent fixed surfaces to define the plastic behavior of concrete. The surfaces, which define three important regions of concrete behavior, can be seen easily if one plots the stress-strain response from an unconfined uniaxial compression test (see Figure 89). The material response is considered linear up until point 1, or first yield. After yielding, a hardening plasticity response occurs until point 2, or maximum strength, is reached. After reaching a maximum strength, softening occurs until a residual strength, which is based on the amount of confinement, is obtained. The three surfaces are defined by the following equations:

$$\Delta\sigma_y = a_{oy} + \frac{P}{a_{1y} + a_{2y}P} \quad (\text{yield failure surface}) \quad (\text{EQ 67})$$

$$\Delta\sigma_m = a_o + \frac{P}{a_1 + a_2P} \quad (\text{maximum failure surface}) \quad (\text{EQ 68})$$

$$\Delta\sigma_r = \frac{P}{a_{1f} + a_{2f}P} \quad (\text{residual failure surface}) \quad (\text{EQ 69})$$

where a_{oy} , a_{1y} , a_{2y} , a_o , a_1 , a_2 , a_{1f} , and a_{2f} are all user-defined parameters which change the shape of the failure surface.

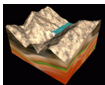
The current failure surface is calculated from the three fixed surfaces using a simple linear interpolation technique:

1. if the current state lies between the yield surface and the maximum surface, the failure surface is calculated using

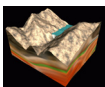
$$\Delta\sigma_f = \eta(\Delta\sigma_m - \Delta\sigma_y) + \Delta\sigma_y \quad (\text{EQ 70})$$

2. if, on the other hand, the current state is located between the maximum surface and the residual surface, the failure surface is defined by

$$\Delta\sigma_f = \eta(\Delta\sigma_m - \Delta\sigma_r) + \Delta\sigma_r \quad (\text{EQ 71})$$



where η varies between 0 and 1, and depends on the accumulated effective plastic strain parameter λ . The current value of λ - calculated using an equation that will be discussed later - is compared to a set of 13 user-defined (η, λ) pairs, which are usually determined from experimental data. The η value is 0 when $\lambda = 0$, 1 at some value $\lambda = \lambda_m$, and again 0 at some larger value of λ . Therefore, if $\lambda \leq \lambda_m$, the current failure surface is calculated using EQ. 70, and if $\lambda \geq \lambda_m$, the current failure surface is calculated using EQ. 71. In essence, the (η, λ) values define where the current failure surface is in relation to the three fixed surfaces for different values of plastic strain.



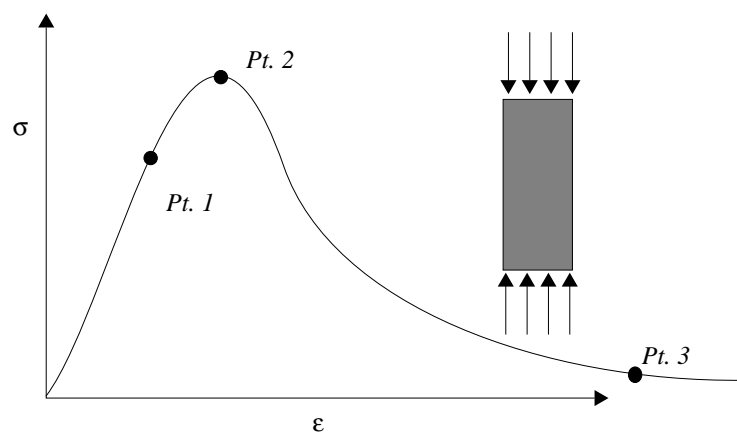
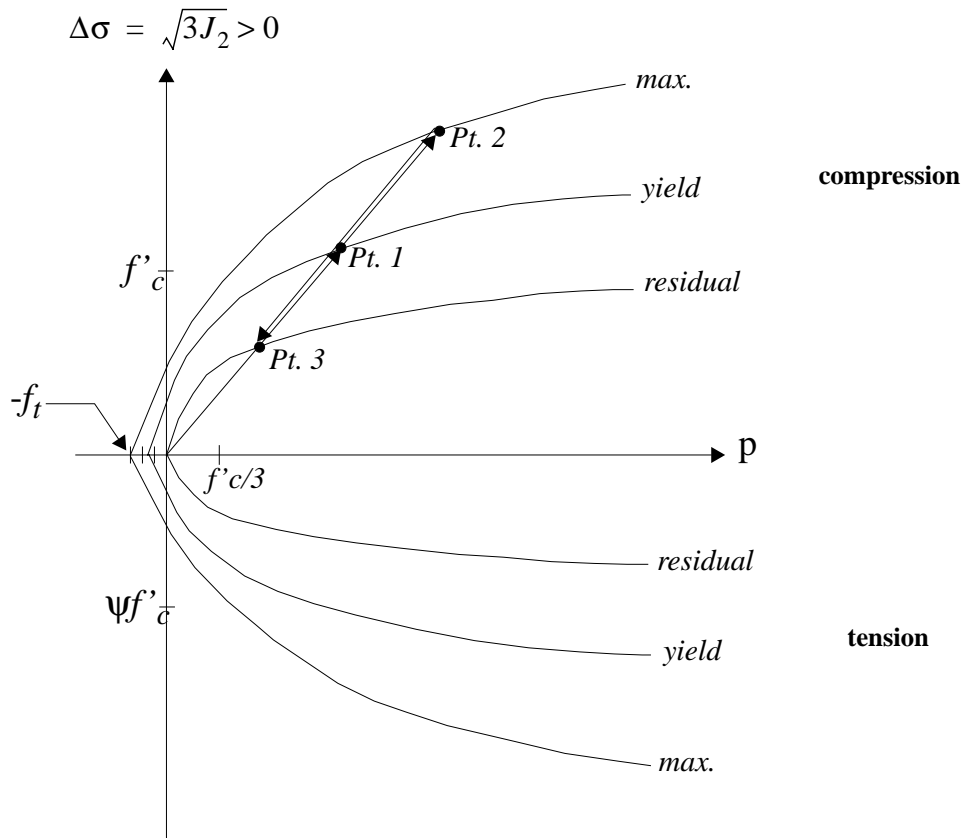
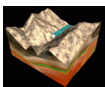


FIGURE 89. Model failure surfaces and uniaxial stress-strain response



16.2 Pressure Cutoff

The pressure cutoff was modified from the original DYNA3D material model 16 to prevent the pressure from being lower than the maximum tensile strength f_t , instead of $f_t/3$. This allows for correct values of $\Delta\sigma$ for both the biaxial and triaxial tensile tests (see Figure 90). For example, the uniaxial, biaxial, and triaxial $\Delta\sigma$ values are calculated as follows:

1. *Uniaxial:* ($\sigma_1 = f_t, \sigma_2 = 0, \sigma_3 = 0$)

$$\sqrt{J_2} = \frac{\sqrt{(\sigma_1 - \sigma_2)^2 + (\sigma_1 - \sigma_3)^2 + (\sigma_2 - \sigma_3)^2}}{\sqrt{6}} = \frac{f_t}{\sqrt{3}}$$

$$\Delta\sigma = f_t$$

$$p = -\frac{f_t}{3}$$

2. *Biaxial:* ($\sigma_1 = f_t, \sigma_2 = f_t, \sigma_3 = 0$)

$$\sqrt{J_2} = \frac{\sqrt{(\sigma_1 - \sigma_2)^2 + (\sigma_1 - \sigma_3)^2 + (\sigma_2 - \sigma_3)^2}}{\sqrt{6}} = \frac{f_t}{\sqrt{3}}$$

$$\Delta\sigma = f_t$$

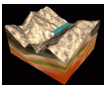
$$p = -\frac{2f_t}{3}$$

3. *Triaxial:* ($\sigma_1 = f_t, \sigma_2 = f_t, \sigma_3 = f_t$)

$$\sqrt{J_2} = \frac{\sqrt{(\sigma_1 - \sigma_2)^2 + (\sigma_1 - \sigma_3)^2 + (\sigma_2 - \sigma_3)^2}}{\sqrt{6}} = 0$$

$$\Delta\sigma = 0$$

$$p = -f_t$$



1. p_c is equal to $-f_t$ if the maximum failure surface has not yet been reached.
2. p_c is equal to $-\eta f_t$ if the maximum failure surface has already been reached.

[illegible]

16.3 Damage Evolution

$$\lambda = \int_0^{\bar{\epsilon}^p} \frac{d\bar{\epsilon}^p}{r_f \left(1 + \frac{p}{r_f f_t}\right)^{b_1}} \quad \text{when} \quad p \geq 0 \quad (\text{EQ 72})$$

$$\lambda = \int_0^{\bar{\epsilon}^p} \frac{d\bar{\epsilon}^p}{r_f \left(1 + \frac{p}{r_f f_t}\right)^{b_2}} \quad \text{when} \quad p < 0 \quad (\text{EQ 73})$$

where the effective plastic strain increment is given by:

$$d\bar{\epsilon}^p = \sqrt{\left(\frac{2}{3}\right) d\epsilon_{ij}^p d\epsilon_{ij}^p} \quad (\text{EQ 74})$$

It is instructive to mention that this effective plastic strain increment is the one commonly used for a von Mises isotropic hardening model for metals. In a more general case, the effective plastic strain increment is defined as:

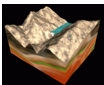
$$d\bar{\epsilon}^p = \sqrt{\left(\frac{2}{3}\right) d\epsilon_{ij}^p d\epsilon_{ij}^p} \quad \text{or in the longer format} \quad (\text{EQ 75})$$

$$\left(d\bar{\epsilon}^p = \left\{ \frac{2}{9} \left[(d\epsilon_{11}^p - d\epsilon_{22}^p)^2 + (d\epsilon_{22}^p - d\epsilon_{33}^p)^2 + (d\epsilon_{33}^p - d\epsilon_{11}^p)^2 \right] + \frac{4}{3} \left[(d\epsilon_{23}^p)^2 + (d\epsilon_{31}^p)^2 + (d\epsilon_{12}^p)^2 \right] \right\}^{\frac{1}{2}} \right)$$

where e_{ij} is the deviatoric part of strain and can be written,

$$e_{ij}^p = \epsilon_{ij}^p - \frac{1}{3} \delta_{ij} \epsilon_{kk}^p \quad (\text{EQ 76})$$

The reasoning behind writing the effective plastic strain increment as in EQ. 74, is that when modeling metals, it is postulated that the plastic deformation occurs under constant volume (i.e. $\epsilon_{kk}^p = 0$). This assumption forces $e_{ij}^p = \epsilon_{ij}^p$. The drawback of using a deviatoric damage criterion for concrete, is that the material cannot accumulate damage under a pure volumetric extension, or triaxial tensile test, because the second deviatoric stress invariant remains zero. Therefore, a volumetric damage increment was added to the deviatoric damage whenever the stress path was “close” to the triaxial tensile test path. The closeness to this path is calculated from the ratio $|(\sqrt{3J_2})/p|$, which is 1.5 for the biaxial tensile test, as you may recall from the pressure cutoff examples. The volumetric damage increment is limited by a closeness parameter f_d given by



$$f_d = \begin{cases} 1 - \frac{|(\sqrt{3}J_2)/p|}{0.1} & , 0 \leq |(\sqrt{3}J_2)/p| < 0.1 \\ 0 & , |(\sqrt{3}J_2)/p| \geq 0.1 \end{cases} \quad (\text{EQ 77})$$

Then the modified effective plastic strain damage parameter is incremented by

$$\Delta\lambda = b_3 f_d k_d (\epsilon_v - \epsilon_{v, yield}) \quad (\text{EQ 78})$$

where b_3 is a user-defined parameter that prescribes the rate of damage primarily in the triaxial tensile regime, k_d is an internal scalar multiplier, and ϵ_v and $\epsilon_{v, yield}$ are the volumetric strain and volumetric strain at yield.

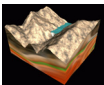
The user-defined parameters b_1 and b_2 , located in EQ. 72 and EQ. 73, also change the rate at which damage occurs, and the r_f value is a dynamic increase factor that accounts for strain rate effects. It is important to note that the DYNA3D manual states EQ. 72 and EQ. 73 as follows:

$$d\lambda = \frac{\overline{d\epsilon^p}}{\left[1 + \left(\frac{s}{100}\right)(r_f - 1)\right] \left(1 + \frac{p}{r_f f_t}\right)^{b_1}} \quad \text{when} \quad p \geq 0 \quad (\text{EQ 79})$$

$$d\lambda = \frac{\overline{d\epsilon^p}}{\left[1 + \left(\frac{s}{100}\right)(r_f - 1)\right] \left(1 + \frac{p}{r_f f_t}\right)^{b_2}} \quad \text{when} \quad p < 0 \quad (\text{EQ 80})$$

If the user defines $s = 0$, the strain-rate effects have been toggled off, and if $s=100$, the strain-rate effects are included.

In addition, the values b_2 and b_3 , which govern the softening part of a tensile stress-strain response, are mesh-size dependent. For example, this means that the softening response for a 6 x 6 x 6 in. cube element will likely be different for a 1 x 1 x 1 in. cube element, if the same values of b_2 and b_3 are used to define both element sizes. Therefore, different material definitions should be used for different regions of the finite element model. It is highly recommended that the user perform a series of single element tensile tests to view whether the material model is indeed yielding the desired softening response. If the analysis does not give a realistic stress-strain curve, the b_2 and b_3 parameters should be modified and the tensile test restarted. This iterative procedure should be continued until the



desired result is achieved. Figure 91 shows the variation that can occur for WSMR-5 3/4 concrete.

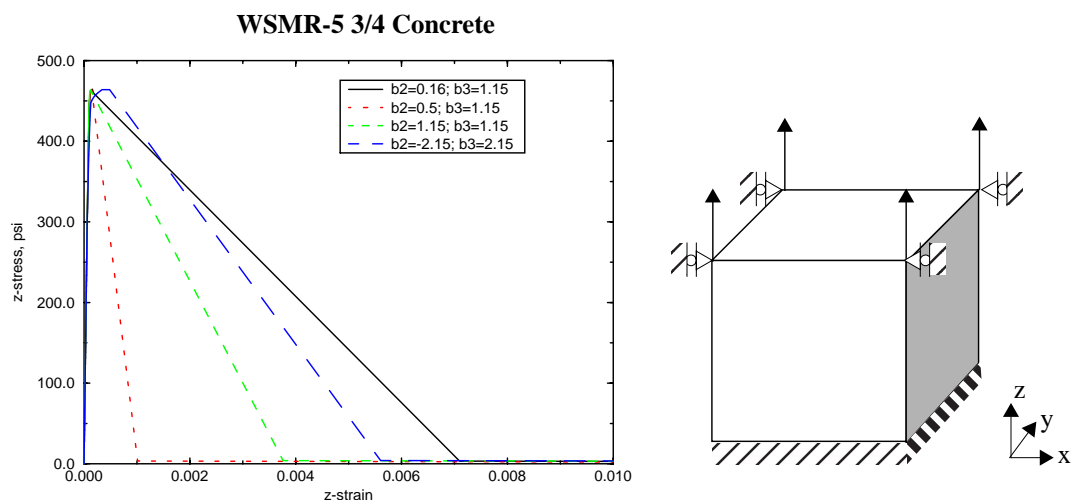


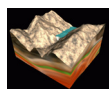
FIGURE 91. Effects of parameters b_2 and b_3 on softening for a single element tensile test.

The user may also track the failure surface evolution by specifying a value of 2 for the emr output on card 4 of the DYNA3D material deck. This parameter tells the subroutine to calculate a “damage” parameter δ , which is calculated in the following manner:

$$\delta = \frac{2\lambda}{\lambda + \lambda_m} \quad (\text{EQ 81})$$

This parameter will be a value of 0 until the initial yield surface has been reached, a value of 1 when the failure surface reaches the maximum surface, and a value of 2 at the residual surface.

In addition, an element deletion criteria was added recently. During extreme loading conditions, some elements, after failing in tension, would stretch or deform continuously without any limits. As a result, the time step would decrease until it was no longer feasible to run the simulation. This can be a problem when the user wants to run the simulation out to a far enough time to see the global response of the structure being analyzed. Therefore, the element deletion criterion that seemed to give the best results for this type of situation, was one that was based on a tensile volumetric strain. To use this feature, the user places a volumetric strain value in row 4 of card 4 in the DYNA3D material deck. Once this volumetric strain has been reached, the element is deleted from the simulation. It is recommended that a relatively high value be used, however, otherwise the element may be deleted too soon. Furthermore, if the element being deleted is subjected to a pressure loading at the time of deletion, that pressure loading will not transfer to the surrounding elements.



16.4 Description of Third Invariant

As you may recall, in a three-dimensional principal stress space, the yield surface may be visualized as a prism with the axis along the space diagonal $\sigma_1 = \sigma_2 = \sigma_3$, which is the ray OC shown in Figure 92.

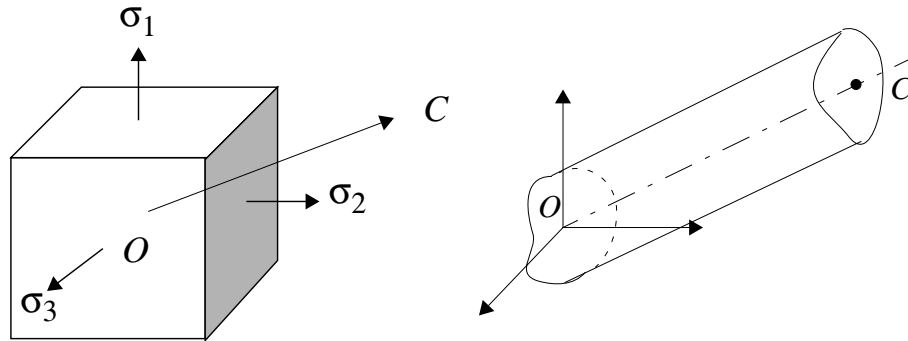


FIGURE 92. Three-dimensional state of stress and space diagonal

Since the stress state may be resolved into a volumetric component and a stress deviator component, the cross section of the prism represents the deviatoric plane. The cross section of the prism may be plotted on any plane perpendicular to the space diagonal. The deviatoric planes have the following equation:

$$\sigma_1 + \sigma_2 + \sigma_3 = \text{constant} \quad (\text{EQ 82})$$

where the π -plane is the deviatoric plane that passes through the origin.

As you know, the yield condition attributed to R. von Mises is represented by a circle on the π -plane (see Figure 93). The circle is the intersection of a sphere of radius r

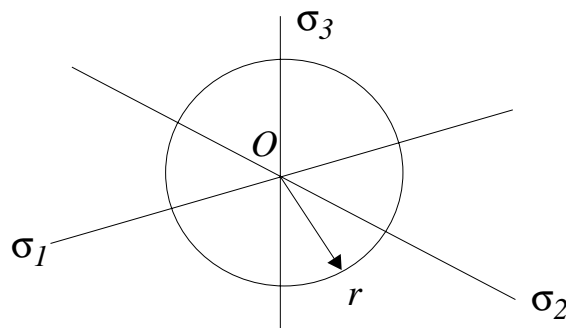
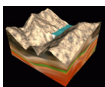


FIGURE 93. Von Mises yield surface (plan view of π -plane).



$$\sigma_1^2 + \sigma_2^2 + \sigma_3^2 = r^2 \quad (\text{EQ 83})$$

in the stress space and the plane

$$\sigma_1 + \sigma_2 + \sigma_3 = 0 \quad (\text{EQ 84})$$

where r is defined by

$$r = \sigma_y \sqrt{\frac{2}{3}} \quad (\text{EQ 85})$$

Since EQ. 84 is satisfied by strain deviator components, the equation for a von Mises yield surface becomes

$$s_1^2 + s_2^2 + s_3^2 = \frac{2}{3} \sigma_y^2 \quad (\text{EQ 86})$$

which may also be written as

$$[\sigma_1 - \sigma_2]^2 + [\sigma_2 - \sigma_3]^2 + [\sigma_3 - \sigma_1]^2 = 2\sigma_y^2 \quad (\text{EQ 87})$$

Furthermore, written in terms of the stress deviator invariant, the yield surface becomes

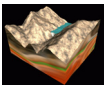
$$\sigma_y = \sqrt{3J_2}. \quad (\text{EQ 88})$$

Therefore, the von Mises yield condition is based on the stress deviator and thus are essentially independent of the hydrostatic pressure. This is appropriate for ductile materials, but is not adequate enough to describe all isotropic materials, specifically materials which are dependent on the hydrostatic pressure and the third stress invariant, such as plain concrete and sand.

If a third invariant is included, the circles used to describe the yield condition on the deviatoric plane for the von Mises surface, can become triangular curves with smooth corners. Based on experimental results of concrete, the intersection with the deviatoric plane is triangular at low pressures and circular at higher pressures (see Figure 94).

A model was proposed by William and Warnke, which yields a smooth, convex triangular surface (see Figure 94). If r_c is the coordinate of the surface at the compressive meridian, and r_t the one at the tensile meridian, any intermediate position r may be calculated as follows:

$$r = \frac{2r_c(r_c^2 - r_t^2)\cos\theta + r_c(2r_t - r_c)\sqrt{4(r_c^2 - r_t^2)(\cos\theta)^2 + 5r_t^2 - 4r_tr_c}}{4(r_c^2 - r_t^2)(\cos\theta)^2 + (r_c - 2r_t)^2} \quad (\text{EQ 89})$$



By dividing both sides by r_c and dividing the numerator and denominator of the right hand side by r_c^2 , the equation now becomes

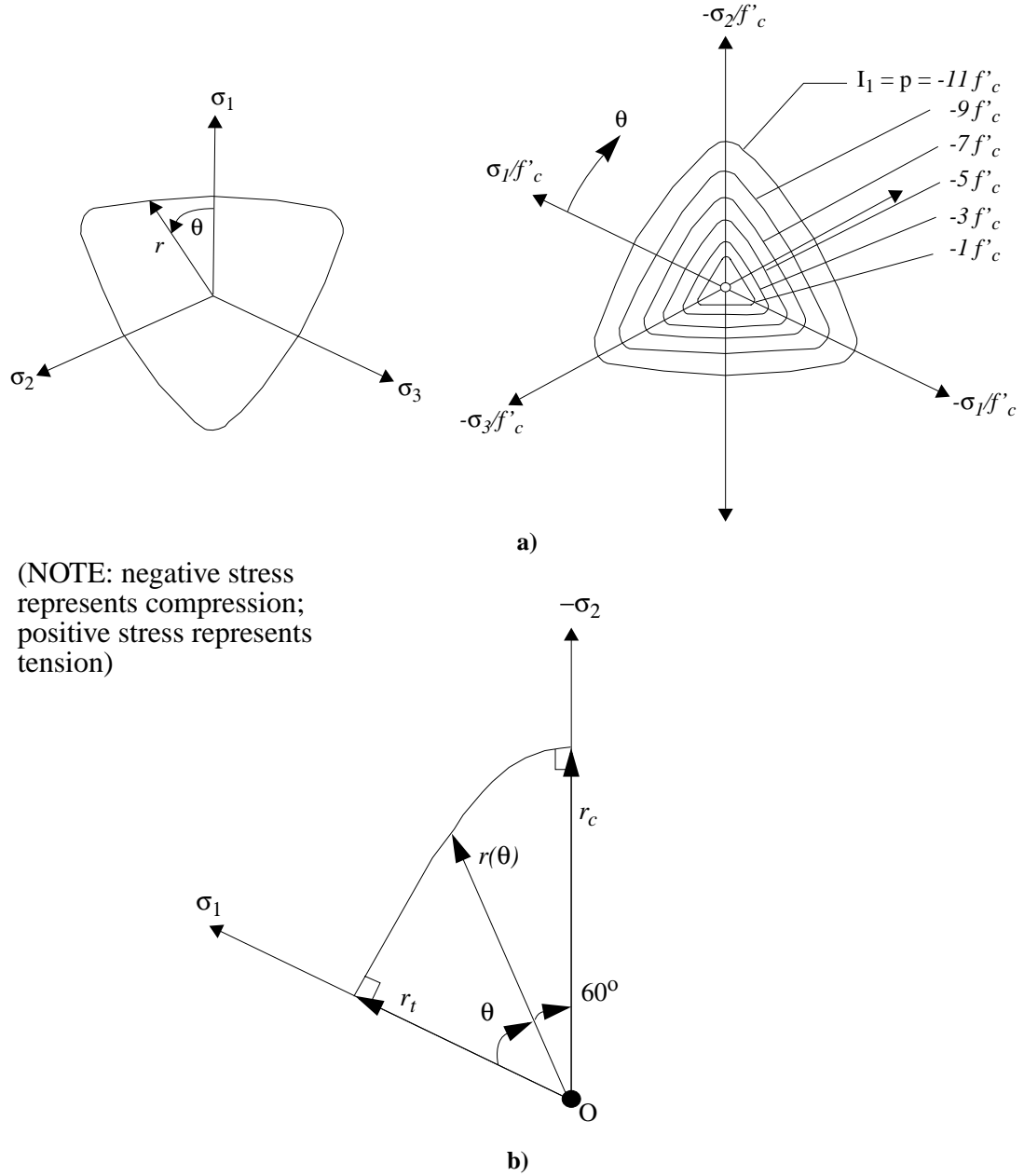
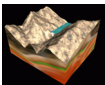


FIGURE 94. a) Concrete deviatoric sections for increasing pressure; b) William and Warnke model.

$$r' = \frac{2(1 - \psi^2)\cos\theta + (2\psi - 1)\sqrt{4(1 - \psi^2)(\cos\theta)^2 + 5\psi^2 - 4\psi}}{4(1 - \psi^2)(\cos\theta)^2 + (1 - 2\psi)^2} \quad (\text{EQ 90})$$



where $\psi = r_t/r_c$ and $r' = r/r_c$. Note the similarity between our definition ψ here and the one defined by EQ. 65. For $\theta = 0^\circ$, the formula yields $r' = \psi$, and for $\theta = 60^\circ$ it yields $r' = 1$, where the value of θ can be obtained from the following relationships,

$$\cos \theta = \frac{\sqrt{3}}{2} \frac{s_1}{\sqrt{J_2}} \quad \text{or} \quad \cos 3\theta = \frac{3\sqrt{3}}{2} \frac{J_3}{J_2^{3/2}} \quad (\text{EQ 91})$$

Once the value of r' is known, the original compressive meridians are multiplied by r' at that location. By doing this, we obtain separate tensile meridians and compressive meridians as was shown in Figure 89.

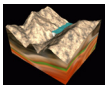
Up to this point, it has been said that the compressive meridian is known and the tensile meridian is found by multiplying the compressive meridian by ψ . However, the actual material model, in certain regions, uses the tensile meridian to determine the compressive one. For pressures greater than $f'_c/3$, the input compressive meridians are based on the input parameters a_o , a_1 , and a_2 , as already stated. For pressures below $f'_c/3$ and above $-f_t$, the tensile meridian is given by

$$\Delta\sigma = \frac{3}{2}(p + f_t) \quad (\text{EQ 92})$$

which passes through both the triaxial tensile test failure point and the uniaxial tensile test point (See “Pressure Cutoff” on page 171.) At $p = f'_c/3$, the two meridians are forced to coincide by determining an appropriate value of ψ . The compressive meridian for pressures below $f'_c/3$ then follows as the image of the tensile meridian, which can be calculated by dividing the tensile meridian by $\psi(p)$ at every pressure p . The determination of $\psi(p)$ is fully discussed in [Ref 2], and will not be discussed in this report. However, it will suffice it to say that the function $\psi(p)$ is determined from experimental data, and are used internally by the code. Therefore, no input is required from the user.

16.5 Strain Rate Effects

In the analysis of concrete structures subjected to blast loading, the concrete may be subjected to strain rates on the order of $10s^{-1}$ to $1000s^{-1}$. At these high strain rates, the apparent strength of concrete and the corresponding strain at peak stress both increase. The fracture energy, or the area under the tensile load-deflection curve, is also believed to increase. Since concrete strain rate effects are generally thought to be dependent on the rate of crack propagation, the elastic modulus is assumed to be rate independent, because at low stress levels no cracking is present. It has been shown by experimental tests that there are different rate enhancements for tensile and compressive loading (see Figure 95). The tensile strength increases by a larger factor than does the compressive strength. Fur-



thermore, the tensile strength rate enhancements have a larger slope than the compressive strength rate effects.

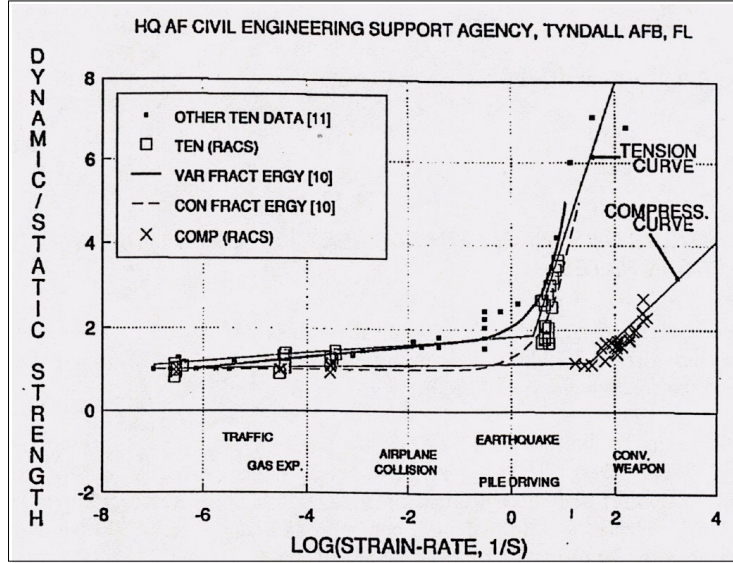


TABLE 19. DYNA3D input

Strain Rate	Strength Factor
-1.000E+02	7.960E+00
-1.000E+01	4.040E+00
-1.000E+00	1.890E+00
-1.000E-01	1.780E+00
-1.000E-02	1.670E+00
-1.000E-03	1.560E+00
0.000E+00	1.000E+00
1.000E-03	1.119E+00
1.000E-02	1.150E+00
1.000E-01	1.200E+00
1.000E+00	1.300E+00
1.000E+01	1.375E+00
1.000E+02	2.000E+00
1.000E+03	3.000E+00

FIGURE 95. Strain rate effects on tensile and compressive strengths ([Ref 3] and [Ref 4]).

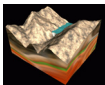
The DYNA3D model has the capability of using different strain rate enhancement factors for tension and compression. These factors are input into a DYNA3D via the use of a load curve (see Table 19). Please note that if strain rate effects are to be included in the calculation properly, one must specify a load curve number and also use $s = 100$ on card 4 of the material deck. In addition, the negative values tell the code that those strength factors are to be used for tensile strength, while the positive ones are to be used for compressive strength.

The material model uses the negative values if $p < f_t/3$ and the positive values if $p > f_c/3$. For pressures that lie between these values, a linear interpolation is used. The rate effects are calculated by obtaining an enhanced $\Delta\sigma_e$ of the failure surface at some pressure p . This calculation is represented by the following:

$$\Delta\sigma_e = r_f \Delta\sigma\left(\frac{p}{r_f}\right) \quad (\text{EQ 93})$$

r_f = rate enhancement factor; p = pressure calculated by EOS

First, an unenhanced pressure, p/r_f , is calculated. This allows the code to obtain an unenhanced strength at $\Delta\sigma(p/r_f)$ from the compressive meridians. Then the unenhanced



strength is multiplied by the strength factor to give the enhanced failure surface. This is graphically represented by Figure 96.

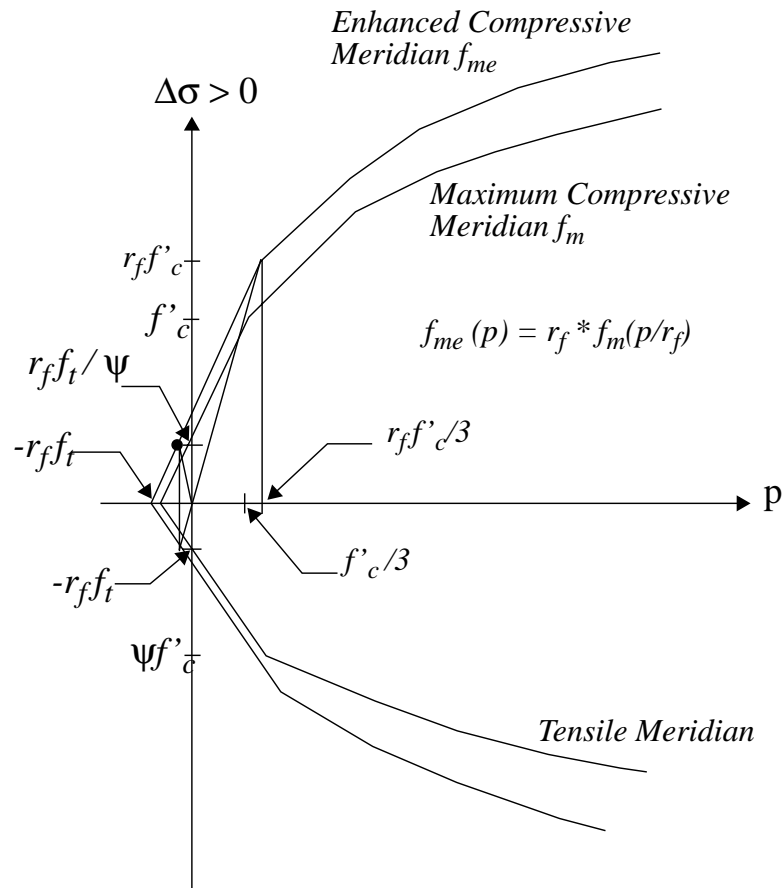
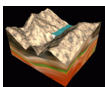


FIGURE 96. Description of strength enhancement calculation.

16.6 Shear Dilation

Dilatancy is a term used to describe the volume increase which may result from the formation and growth of cracks parallel to the direction of the greatest compressive stress. Shear dilation is the volume increase which may occur when concrete is subjected to shear stresses (see Figure 97). When the material is cracking, the dilation continues until the crack opening is large enough to clear the aggregates. At this point, dilatancy does not continue.

To include the effects of shear dilatancy and to make sure that too much shear dilation does not occur, a proper flow rule must be used. As you may recall, in a simple von Mises isotropic hardening law for metals, the plastic flow develops along the normal to the yield surface. This is known as an associative flow rule. If an associative flow rule is used for the concrete model, too much shear dilation tends to occur. In DYNA3D material model 16, the original version of this model, instead used a constant volume Prandtl- Reuss model, which is a non-associative flow rule. This rule, however, has the drawback of not being



able to represent any shear dilation. Therefore, a partial associative flow rule is used, where the amount of associativity is prescribed by the user input value ω , where a value of 0 indicates no change in volume during plastic flow and a value of 1 indicates shear dilation occurs according to an associative flow rule (see Figure 97). Typical concrete experiments show that the value of ω should range from 0.5 to 0.7.

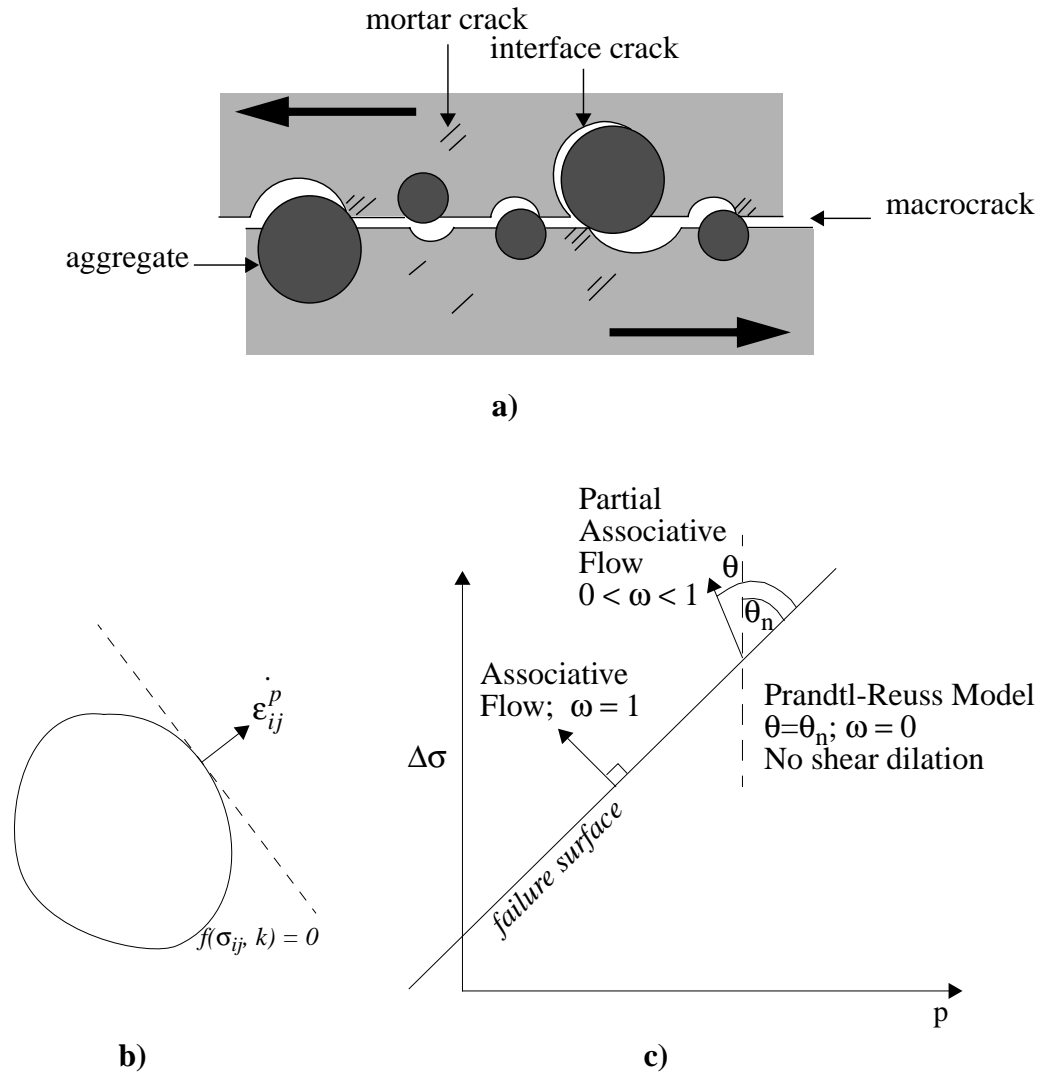
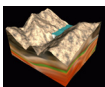


FIGURE 97. a) graphical representation of shear dilation; b) yield surface with associated flow rule; c) description of associative, non-associative, and partial associative flow rules.

16.7 Equation of State

The DYNA3D equation of state form 8 (similarly form 12), prescribes the relationship between pressure and volumetric strain. In addition, it also includes a tabulation of the unloading bulk modulus at peak volumetric strains. Please note that volumetric strain is positive in tension, and pressure is positive in compression. In general, the pressure vs.



volumetric strain may have a cubic spline representation; however, the concrete data that will be supplied in this report consist of a linear pressure vs. volumetric strain relationship see Figure 98, Table 20, and Table 21).

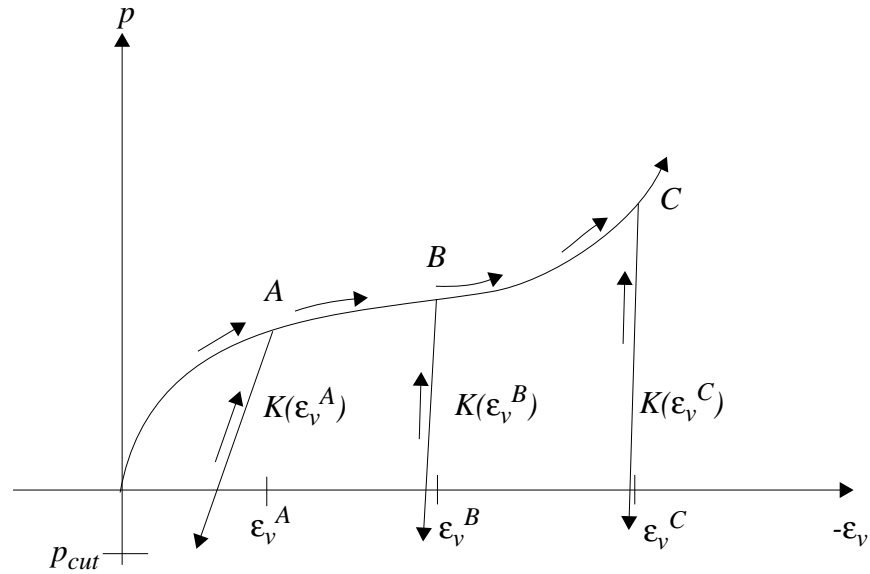


FIGURE 98. Pressure vs. volumetric strain curve for equation-of-state Form 8 with compaction (similarly Form 12).

TABLE 20. Input for equation-of-state form 12: WSMR-5 3/4 concrete

COLUMN 1	COLUMN 2	COLUMN 3	COLUMN 4	COLUMN 5
0.000000000E+00	-1.466000000E-03	-1.000000000E-02	-4.000000000E-02	-7.000000000E-02
-1.000000000E+00	0.000000000E+00	0.000000000E+00	0.000000000E+00	0.000000000E+00
0.000000000E+00	3.625000000E+03	1.513800000E+04	4.437000000E+04	8.076500000E+04
1.032110000E+06	0.000000000E+00	0.000000000E+00	0.000000000E+00	0.000000000E+00
0.000000000E+00	0.000000000E+00	0.000000000E+00	0.000000000E+00	0.000000000E+00
0.000000000E+00	0.000000000E+00	0.000000000E+00	0.000000000E+00	0.000000000E+00
2.472250000E+06	2.472250000E+06	4.437000000E+06	4.437000000E+06	4.437000000E+06
4.437000000E+06	0.000000000E+00	0.000000000E+00	0.000000000E+00	0.000000000E+00
0.000000000E+00	0.000000000E+00	0.000000000E+00	0.000000000E+00	0.000000000E+00

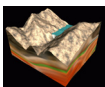
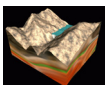


TABLE 21. Input for equation-of-state form 12: SAC5 concrete

COLUMN 1	COLUMN 2	COLUMN 3	COLUMN 4	COLUMN 5
0.000000000E+00	-4.760000000e-03	-1.004760000e+00	0.000000000e+00	0.000000000e+00
0.000000000e+00	0.000000000E+00	0.000000000E+00	0.000000000E+00	0.000000000E+00
0.000000000E+00	1.015000000e+04	7.351500000e+05	0.000000000E+00	0.000000000E+00
0.000000000E+00	0.000000000E+00	0.000000000E+00	0.000000000E+00	0.000000000E+00
0.000000000E+00	0.000000000E+00	0.000000000E+00	0.000000000E+00	0.000000000E+00
0.000000000E+00	0.000000000E+00	0.000000000E+00	0.000000000E+00	0.000000000E+00
2.131500000e+06	2.131500000e+06	2.131500000e+06	0.000000000e+00	0.000000000e+00
0.000000000e+00	0.000000000E+00	0.000000000E+00	0.000000000E+00	0.000000000E+00
0.000000000E+00	0.000000000E+00	1.000000000E+00	0.000000000E+00	0.000000000E+00



17.0 Concrete Material Properties

There are two concrete materials which have been used extensively with the DYNA3D material model. These materials include the WSMR-5 3/4 concrete and the SAC5 concrete. Because having only two sets of material data is rather limiting to the user, a procedure for scaling known data to another material is also presented.

17.1 WSMR-5 3/4 Concrete

This material model was used primarily for all of the Morrow Point Dam simulations presented. The primary reason for this is that the unconfined compressive strength of WSMR-5 3/4 concrete is approximately 6500 psi, which is similar to the compressive strength of the cylinder tests conducted on the Morrow Point concrete. The corresponding tensile strength of this material is approximately 465 psi. Figure 99 shows a plot of the compressive meridians, a single element tensile test, and a uniaxial unconfined compressive test.

17.2 SAC5 Concrete

The SAC5 concrete material was used for the DYNA3D/ALE3D concrete wall benchmark experiment presented earlier in the report. This material has an unconfined compressive strength of approximately 5500 psi and a tensile strength of 365 psi. Furthermore, a comparison of the (η, λ) pairs of SAC5 concrete to those of WSMR-5 3/4 concrete, reveals that the failure surface of SAC5 concrete is reached at a later damage value λ than for the WSMR-5 3/4 concrete. Figure 100 similarly shows a plot of the failure surfaces, a single element tensile test, and a uniaxial unconfined compressive test.

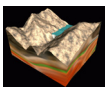


TABLE 22. DYNA3D input for WSMR-5 3/4 concrete: mesh size (6 x 6 x 6 in. cube)

CARDS	COLUMN 1	COLUMN 2	COLUMN 3	COLUMN 4	COLUMN 5	COLUMN 6	COLUMN 7	COLUMN 8
3	1.900E-01	4.640E+02	1.946E+03	4.463E-01	1.228E-05	1.500E+00	5.000E-01	4.417E-01
4	s=0 or 100	2.000E+00	0.000E+00	volumetric strain at failure	0.000E+00	load curve giving rate sensitivity	0.000E+00	0.000E+00
5	0.000E+00	1.000E-05	3.000E-05	5.000E-05	7.000E-05	9.000E-05	1.100E-04	2.700E-04
6	5.800E-04	7.800E-04	1.331E-02	5.000E-01	6.000E-01	1.150E+00	1.469E+03	6.250E-01
7	0.000E+00	8.500E-01	9.600E-01	9.900E-01	1.000E+00	9.900E-01	9.600E-01	5.000E-01
8	5.000E-02	1.000E-02	0.000E+00	0.000E+00	0.000E+00	1.600E-01	1.797E-05	3.981E-05

NOTE: all units in lbs, sec, in.

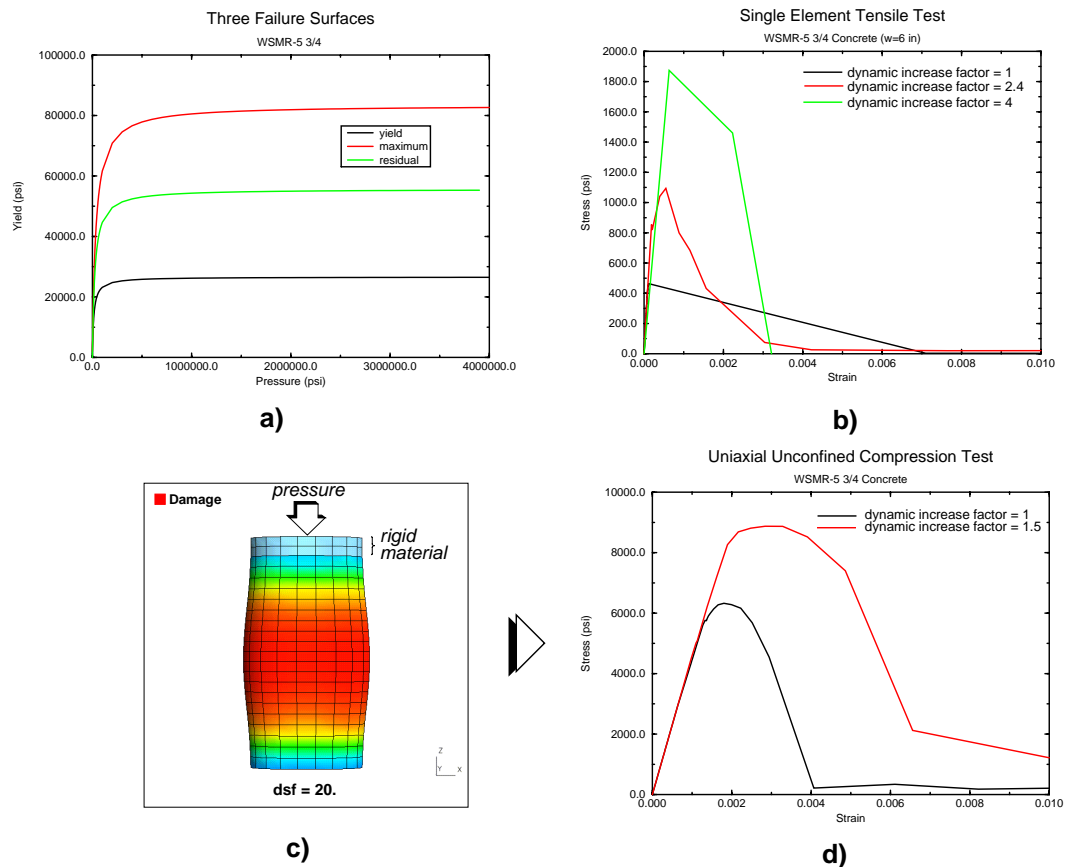


FIGURE 99. WSMR-5 3/4 concrete properties: a) plot of compressive meridians; b) single element uniaxial tensile test with and without rate dependence (tensile strength = 464 psi); c) description of unconfined uniaxial compressive test and plot of damage parameter δ after compressive failure; d) stress-strain plot of UUC test with and without rate dependence (compressive strength = 6500 psi).

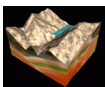


TABLE 23. DYNA3D input for SAC5 concrete: mesh size (6 x 6 x 6 in. cube)

CARDS	COLUMN 1	COLUMN 2	COLUMN 3	COLUMN 4	COLUMN 5	COLUMN 6	COLUMN 7	COLUMN 8
3	1.900E-01	3.625E+02	2.192E+03	4.910E-01	1.246E-05	1.400E+00	0.000E+00	4.417E-01
4	s=0 or 100	2.000E+00	0.000E+00	volumetric strain at failure	0.000E+00	load curve giving rate sensitivity	0.000E+00	0.000E+00
5	0.000E+00	1.500E-04	2.800E-04	1.200E-03	0.100E+00	0.200E+00	0.300E+00	0.400E+00
6	5.000E-01	6.000E-01	7.000E-01	8.000E-01	9.000E-01	0.400E+00	1.560E+03	7.414E-01
7	0.000E+00	1.000E+00	2.400E-01	0.000E+00	0.000E+00	0.000E+00	0.000E+00	0.000E+00
8	0.000E+00	0.000E+00	0.000E+00	0.000E+00	0.000E+00	1.500E+00	1.797E-05	3.569E-05

NOTE: all units in lbs, sec, in.

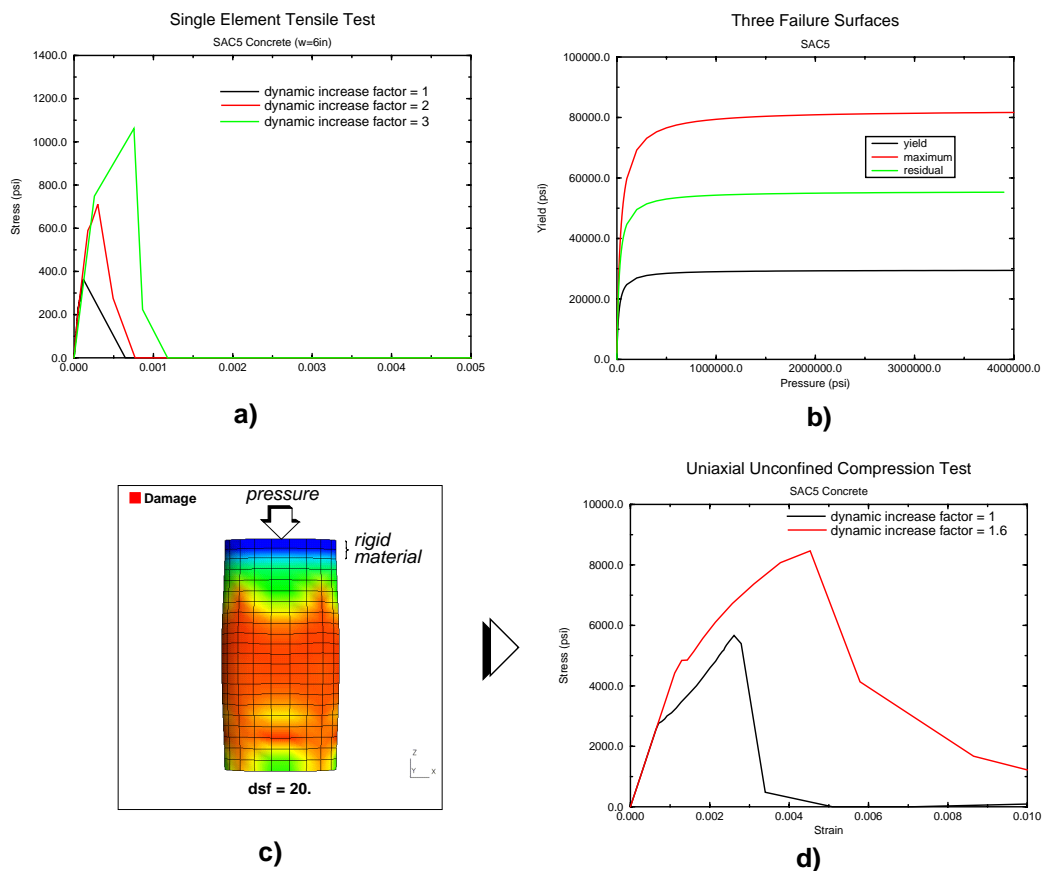
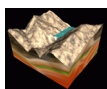


FIGURE 100. SAC5 concrete properties: a) plot of compressive meridians; b) single element uniaxial tensile test with and without rate dependence (tensile strength = 363 psi); c) description of unconfined uniaxial compressive test and plot of damage parameter δ after compressive failure; d) stress-strain plot of UUC test with and without rate dependence (compressive strength = 5500 psi).



17.3 Scaling of Existing Data

A disadvantage to using this particular material model is the large amount of data that is required for one type of concrete. Therefore, it is useful to discuss briefly the methods required to scale the known data, such as the data given for WSMR-5 3/4 concrete and SAC5 concrete, so that it can be used for a different material [Ref 3]. The user input that requires scaling are the failure surfaces and the equation of state.

The following steps are used to scale the failure surfaces:

1. If $f'_{c_{new}}$ is the unconfined compression strength of the new material to be modeled, and $f'_{c_{old}}$ is the unconfined compression strength of a previous modeled concrete material, then a ratio, r , may be calculated as

$$r = \frac{f'_{c_{new}}}{f'_{c_{old}}} \quad (\text{EQ 94})$$

2. New coefficients for the failure surfaces may be calculated by

$$\begin{aligned} a_{0n} &= a_0 r \\ a_{1n} &= a_1 \\ a_{2n} &= a_2 / r \end{aligned} \quad (\text{EQ 95})$$

where the subscript n represents the new material's coefficients.

The equation of state needs modification to both the input pressures and input bulk moduli. The new pressures and moduli may be calculated by the two following relationships:

$$p_{new} = p_{old} \sqrt{r} \quad (\text{EQ 96})$$

$$K_{new} = K_{old} \sqrt{r} \quad (\text{EQ 97})$$

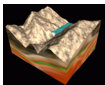
These relationships stem from the fact that the bulk modulus is calculated by

$$K = \frac{E}{3(1-2\nu)} \quad (\text{EQ 98})$$

where the modulus of elasticity, E , is related to the unconfined concrete compressive strength by

$$E = 57000 \sqrt{f'_c}. \quad (\text{EQ 99})$$

Please note that the empirical relationship for E requires that the units be in (lbs, sec, in).



18.0 References

1. Attaway, S.W., Matalucci, R.V., Morrill, K.B., Malvar, L.J., and Crawford, J.E., Enhancements to PRONTO3D to Predict Structural Response to Blast, Sandia National Laboratories Draft Copy, October 15, 1999.
2. Malvar, L.J., Crawford, J.E., Wesevich, J.W., A New Concrete Material Model For DYNA3D, Karagozian and Case, Report No. TR-94-14.1, June 1, 1994.
3. Malvar, L.J., Crawford, J.E., Wesevich, J.W., A New Concrete Material Model For DYNA3D Release II: Shear Dilation and Directional Rate Enhancements, Karagozian and Case, Report No. TR-96-2.2, February 8, 1996.
4. Ross, C.A., Kuennen, S.T., Tedesco, J.W., "Effects of Strain Rate on Concrete Strength," Session on Concrete Research in the Federal Government, ACI Spring Convention, Washington, D.C., March 1992.
5. Whirley, R.G., DYNA3D: A Nonlinear, Explicit, Three-Dimensional Finite Element Code for Solid and Structural Mechanics, Lawrence Livermore National Laboratory Report UCRL-MA-107254-REV-1.

